NTNU – Trondheim
Norwegian University of
Science and Technology

Coupled Analysis of a Spar Floating Wind Turbine considering both Ice and Aerodynamic Loads

Marine Yvette Josette
Saccoman

Maritime Engineering
Submission date: May 2015
Supervisor: Torgeir Moan, IMT
Co-supervisor: Pentti Kujala, Aalto University
Zhen Gao, IMT
Wei Shi, IMT

Norwegian University of Science and Technology
Department of Marine Technology

NTNU

TMR 4930 - Marine Technology,
Master's Thesis

Master's Thesis

Coupled Analysis of a Spar Floating Wind Turbine considering both Ice and Aerodynamic Loads

Marine Saccoman

01/06/2015

NTNU Trondheim
Norwegian University of Science and Technology
Department of Marine Technology – Group of Marine Structures

MSC THESIS IN MARINE TECHNOLOGY

SPRING 2015

FOR

STUD.TECHN. Marine Saccoman

Coupled Analysis of a Spar Floating Wind Turbine considering both Ice and Aerodynamic Loads

Background:
In certain geographic locations around the globe, ice load on offshore wind turbines might be an important design concern. Ice loads on the cylindrical hull of a spar wind turbine might be in the same order of aerodynamic or hydrodynamic loads. Drifting ice creates large mean loads on the spar hull and this is particularly challenging for mooring system design.

On the other hand, the drifting ice sheet will also induce dynamic loads on floaters due to the periodical ice breaking. This will result in dynamic motions of the spar and also introduce dynamic tension in mooring lines. Ice loads in thin ice sheet are normally small and have a random nature. But, ice loads in thick ice sheet will typically be periodical impulse loads. In addition to rigid-body motions, the first flexible bending mode of wind turbines might be excited by these loads and significant dynamic structural responses might be induced. On the other hand, aerodynamic loads on the wind turbine rotor will cause similar dynamic effects on floater motions and vibrations. In numerical models, it is then important to consider a coupled analysis model of spar wind turbines in both wind and level ice. Different from a bottom-fixed wind turbine, the contact between the drifting ice sheet and the spar will be largely influenced by the motions of the spar. This creates numerical problems when coupling the ice load module to a global aerodynamic model of wind turbines. A convergence study should be performed.

In the project work, the candidate did a literature review on ice load calculation for cylindrical and coned structures, and also carried out uncoupled numerical simulations to study the behaviour of a spar floating wind turbine in drifting level ice. The ice loads were obtained using a Fortran code, while the global responses of the spar floating wind turbine were obtained in HAWC2 using the time series of ice loads as input.

In the thesis work, the candidate should work on the coupling between the Fortran module and the HAWC2 code, and in particular, perform a convergence study to understand the necessary analysis settings to obtain reliable results. In addition, coupled analysis with both ice and wind loads should be performed, to investigate the relative importance of rotor aerodynamic loads and ice loads on the floater.

Assignment:
The following tasks should be addressed in the thesis work:
1. Complete the literature review on ice load calculation and response analysis of floating wind turbines. In addition, the literature review should be extended to numerical procedures for ice load and response analysis.

2. Study and develop the coupling between the ice load DLL and HAWC2. The effect of initial conditions, transient phases, as well as time steps and iterations should be investigated in detail via a convergence study.
3. Based on the existing data of the 5MW spar wind turbine, perform coupled time-domain simulations considering only ice loads and a sensitivity study for different ice drift speed and thickness. Compare the results of uncoupled and coupled analyses.

4. Perform analyses with both ice and wind turbine loads, considering random variation of ice thickness as well as turbulent wind field. Compare the dynamic responses (such as spar motions, tower base bending moment and mooring line tension) via spectral and statistical analyses.

5. Conclude the work and give recommendations for future work.

6. Write the MSc thesis report.

In the thesis the candidate shall present his personal contribution to the resolution of problem within the scope of the thesis work.

Theories and conclusions should be based on mathematical derivations and/or logic reasoning identifying the various steps in the deduction.

The candidate should utilize the existing possibilities for obtaining relevant literature.

The thesis should be organized in a rational manner to give a clear exposition of results, assessments, and conclusions. The text should be brief and to the point, with a clear language. Telegraphic language should be avoided.

The thesis shall contain the following elements: A text defining the scope, preface, list of contents, summary, main body of thesis, conclusions with recommendations for further work, list of symbols and acronyms, reference and (optional) appendices. All figures, tables and equations shall be numerated.

The supervisor may require that the candidate, in an early stage of the work, present a written plan for the completion of the work. The plan should include a budget for the use of computer and laboratory resources that will be charged to the department. Overruns shall be reported to the supervisor.

The original contribution of the candidate and material taken from other sources shall be clearly defined. Work from other sources shall be properly referenced using an acknowledged referencing system.

The thesis shall be submitted in two copies as well as an electronic copy on a CD:

- Signed by the candidate
- The text defining the scope included
- In bound volume(s)
- Drawings and/or computer prints which cannot be bound should be organized in a separate folder.

Supervisors:
Torgeir Moan
Zhen Gao
Wei Shi

Deadline for thesis report: 10.06.2015

Abstract

In this thesis a model is proposed for establishing the coupled analysis of a spar floating wind turbine considering both ice and aerodynamic loads. This topic is important within the field of renewable energies research given that wind energy has known one of the fastest growths among renewable energies. And, in the case of cold climate regions such as the Baltic Sea, ice loads become an important point to consider in the design of offshore wind turbines. The central issue to be addressed within this work is the action of ice and aerodynamic loads on a spar floating wind turbine which is of relevance in determining the design requirements for structural checking of such structure. The aim is the diagnosis of the factors relevant to the spar floating wind turbines design and the investigation of their potential for inducing significant dynamic structural responses.

A numerical model for ice loads calculations has been implemented in the aero-hydro-servo-elastic simulation tool HAWC2 using a Fortran module. The work has been derived from Xian Tan's thesis and papers (Tan, et al., 2013) and Wei Shi's work (Shi, et al., November 24-26, 2014). The ice loads are determined by defining the structure and ice sheet geometry at the mean sea level and then by integrating the contact loads over the waterline.

First, an eigenfrequency analysis and a convergence study have been conducted to gain knowledge on the system and the simulation settings. Then, the developed model was applied in order to determine the coupled action of wind and ice loads along with the effect of ice drifting speed and thickness variations. The simulations were defined for ice conditions corresponding to the ones encountered in the Baltic Sea. These results are compared to the results obtained with a decoupled analysis realized in a previous work to state on the goodness of the model applied.

The application of the developed model to the coupled analysis of a spar floating wind turbine considering both ice and aerodynamic loads has shown that ice thickness is of critical importance in the determination of the dynamic response while ice drifting speed does not seem to have a significant influence. It is explained by the direct link between the ice loads value and the contact area between the ice sheet and the structure. Indeed, thicker ice will leads to a larger contact area for the same ice drifting speed and as a result

to higher loads. Thus, these results are in agreement with the accepted knowledge within ice loads studies. Coupled and decoupled models present similar output shapes but they differ in magnitude. This difference increases for increasing ice drifting speed and ice thickness. However, a trend in the divergence is hard to identify. Then, the simulations performed including both ice and wind loads have shown that the wind has a predominant influence on the loads. But, ice loads participate to the dynamic component of the response by causing amplified oscillations around the mean value. Thus, this could have a significant influence in the lifetime of the wind turbine by accelerating fatigue damages. However, the power production does not seems to be significantly impacted, at the rated speed at least. The results achieved are not providing an extensive enough basis to state on the relative importance of ice loads in regards to aerodynamic loads. However, it is a good first insight of the subject and knowledge was gained in the simulation settings that will be a good asset in the future.

Due to convergence problems in the module and the time needed to run a full simulation, only a restricted number of cases where tested and this work should be continued to obtain more extensive data and thus draw more accurate conclusions. During this investigation, the possibility offered by the coupled model to run analysis of a spar floating wind turbine considering both ice and aerodynamic loads where demonstrated. Moreover, this work has given a first validation on the settings to apply through a convergence study on both simulation time and time step influences. The cases including both wind and ice should be investigated further to allow longer simulations. It would be necessary to also complete the Fortran code to include randomly varying ice conditions. This way, the simulations would be run in more realistic conditions – varying ice properties along the ice sheet and turbulent wind. A possible continuation of this work could be to include a fatigue module and look more closely on the influence of the ice loads in the energy production. Besides, now that the model gives long enough time simulations and thus stable results, it would be necessary to assess the real quality of this model by comparing the numerical results to model tests or full scale data. Nonetheless, this work demonstrate that future modelling design improvements for floating wind turbines are possible.

Acknowledgements

First I would like to thank Torgeir Moan, Zhen Gao and Wei Shi for giving me the opportunity to realize my MSc thesis under their supervision and having always found time to advise me. I want to also thank the Ecole Centrale de Nantes and the Nordic Master in Maritime Engineering committee for the opportunity that was given to me to realize this double diploma in both Aalto University and NTNU. It has been two wonderful and very formative years that have confirmed my interest for maritime engineering and that gave me the chance to discover new countries, cultures and people.

To Prof. Poul Andersen for the energy he puts in the Nordic Master in Maritime Engineering programme and the annual social gathering that is always giving a nice start to the coming academic year and gives the great opportunity to meet our fellows.

To Prof. Torgeir Moan who helped me find a subject that match my interests and to Prof. Pentti Kujala who took the time to advise me from afar.

To Prof. Zhen Gao who took the time to give me precious advice and explanations all along this work.

Special thanks must be given to Wei Shi for his precious help whether by getting me started with the different software or by recommending literature, for the advice he gave me all along my MSc thesis and for his patience to answer all of my (numerous) questions.

I would also like to thanks Torben J. Larsen, Anders Yde and Anders Melchior Hansen from DTU for their help in handling HAWC2.

Finally, I would like to thanks my parents, family and friends for their constant support.

Trondheim, May 21, 2015

Contents

List of figures

List of tables

Abbreviations

Abbreviation	*Definition*
API	*American Petroleum Institute*
BEM	*Blade Element Momentum*
CAE	*Computer-aided engineering*
CDF	*Cumulative Distribution Function*
CM	*Center of Mass*
cf.	*Confer*
DLL	*Dynamic Link Library*
DNV-OS	*Det Norsk Veritas – Offshore Standards*
DOF	*Degree of Freedom*
e.g.	*exempli gratia (for example)*
FA	*Fore-Aft*
FEM	*Finite Elements Method*
Fortran	*FORmula TRANslating System*
FSICR	*Finnish Swedish Ice Class Rules*
GDW	*Generalized Dynamic Wake*
GL	*Germanischer Lloyd*
HAWC2	*Horizontal Axis Wind turbine simulation Code 2nd generation*
HAWT	*Horizontal Axis Wind Turbine*
i.e.	*id est (it is; in other words)*
IEA	*International Energy Agency*
IEC	*International Electronical Commission*
ISO/FDIS	*International Organization for Standardization / Final Draft International Standard*
LC	*Load Case*
mps	*Meters Per Second*
MSL	*Mean Sea Level*
NREL	*National Renewable Energy Laboratory*
OC3	*Offshore Code Comparison Collaboration*
OC5	*Offshore Code Comparison Collaboration Continuation, with Correlation*
PDF	*Probability Distribution Function*
PSD	*Power Spectral Density*
SS	*Side-to-Side*
STD	*Standard Deviation*
SWL	*Static Water Level*
TLP	*Tension Leg Platform*
vs.	*Versus*
WT	*Wind Turbine*

List of symbols

Roman Characters

A	*Added mass matrix (§3.2)*
A	*Rotor area (§2.6.2)*
A_{cr}	*Ice-structure contact area*
A_i	*Area corresponding to the nodal force in the the Määttänen ice loads model*
a	*Axial induction factor, tower radius*
a'	*Tangential induction factor*
B	*Damping matrix (§3.2)*
B	*Number of blades (§2.6.2)*
C	*Restoring force matrix*
C_D	*Viscous coefficient on the specific direction that has projected area Ddz*
$C_d(\alpha)$	*Drag coefficient*
$C_l(\alpha)$	*Lift coefficient*
C_n	*Normal load coefficient*
C_t	*Tangential load coefficient*
c	*Chord*
D	*Cylinder diameter*
D_n	*Goodness of fitting (cumulative value of the data and fitted distributions are compared)*
$D_t(z)$	*Tower diameter at elevation z*
$E(x)$	*CDF of extreme value distribution*
$E[y_n]$	*Mean value of the data serie y_n*
e	*PDF of extreme value distribution*
$F(t)$	*Excitation force and moment vector*
$\boldsymbol{F}$	*Ice force*
$\boldsymbol{F}$	*Cumulative Distribution Function for normal distribution*
F_{cr}	*Local ice crushing force*
F_i	*Nodal force from the Määttänen ice loads model*
F_y	*Fore-aft force*
$F_{y,i}$	*Fore-aft force at the simulation step i*
$F_{y,mean}$	*Fore-aft force final value in the ramp function utilized to introduce the ice loads*
F^{-1}	*Inverse function of the Cumulative Distribution Function for normal distribution*
f	*The frequency (in Hz)*
$G(y_n)$	*Cumulative Distribution Function (CDF) of Gumbel 1 function*
$H(y_n)$	*CDF of the truncated Gumble I*
$h(y_n)$	*PDF of the truncated Gumble I*
h_i	*Level ice thickness*
I	*Turbulence intensity*
k	*Ratio between ice broken length and ice thickness from field measurement result (from 4 to 7 from field measurement results in the Bohai Bay) (§2.2)*
k	*Empirical parameters in the determination of average contact pressure (§3.3)*
L	*Length scales in the PSD models*
L_B	*Breaking length of the ice sheet*

L_d	*Ice-structure indentation length*
L_h	*Ice-structure contact length*
M	*Mass matrix*
M_x	*Fore-aft moment*
n	*Empirical parameters in the determination of average contact pressure (§3.3)*
n	*Number of observations (§2.5)*
p_{av}	*Average contact pressure*
Δp	*Pressure drop over the rotor*
R	*Rotor Radius*
r	*Radius [wind turbine control volume]*
S	*The longitudinal velocity spectrum*
T	*Ice force period (§2.22.6.2)*
T	*Thrust force (§2.6.2)*
t	*Ice thickness*
U	*Randomly generated number between 0 and 1*
U_n	*Gumbel 1 function parameter*
$\overline{U}$	*Mean wind speed (from synoptic and diurnal data) (usually 10 min average)*
$\overline{U}_{ref}$	*Wind speed at reference height* z_{ref}
u	*Undisturbed fluid velocity*
u	*Wind speed at the rotor plane (§2.6.2)*
u_1	*Wind speed in the wake of the rotor*
$u'(t)$	*Wind speed variation over time (turbulence)*
V	*Ice velocity*
V_0	*Wind speed*
V_0	*Wind speed far upstream of the rotor (§2.6.2)*
w	*Induced velocity (§2.6.2)*
w	*Wave frequency (§3.2)*
z_{ref}	*Reference height in wind shear model*

Greek Characters

α	*Local angle of attack (§2.6.2)*
α	*Vertical shear exponent (§2.6.2)*
α_n	*Gumbel 1 function parameter*
β	*Newmark method parameter*
γ	*Newmark method parameter (§3.2)*
γ	*Euler's constant (equals 0.577) (§2.5)*
η	*Position vector*
$\dot{\eta}$	*Velocity vector*
$\ddot{\eta}$	*Acceleration vector*
$\dot{\eta}_1$	*Velocity of the body*
θ	*Local pitch of the blade*
ρ	*Density of sea water*
ρ_a	*Air density*
σ	*Solidity (§2.6.2)*
σ	*Standard deviation of the variation of wind speed around* $\overline{U}$ *(§ 2.6.1)*
σ_c	*Crushing strength in the Määttänen ice loads model*
σ_f	*Ice flexural strength*

$\dot{\sigma}$	*Stress rate in the Määttänen ice loads model*
φ	*Frame angle*
ϕ	*Flow angle*

1. Introduction

In the past years, the energy consumption has increased along with Global warming concerns while fossil-based energy resources have been depleting. In this context, thorough investigations have been run to find ways to counter the energy problem by exploiting renewable energies and develop their use. Among those renewable energies, wind energy has known one of the fastest growths. Indeed, it has been highlighted that wind energy production has increased at an annual rate of 25-30% (Muliawan, et al., 2012).

To obtain this energy production, different types of wind turbines have been developed throughout the years in order to convert wind energy into electricity as efficiently as possible. All these types present their respective advantages and drawbacks but so far, the main part of the production was ensured by onshore wind turbines: up to 2013 in EU, 110.7GW were produced onshore versus 6.6GW offshore. The main reason for this difference was the installation and production costs -way inferior in the case of onshore farms. However, onshore wind turbines development is reaching its limit due to the impossibility to find optimal sites because of noise and visual disturbances linked to their installation and operation. Moreover, onshore wind turbines have a capacity factor of 25-30%, while offshore wind turbines capacity factor attains 35-45% and improvements have been met to reduce their exploitation costs – i.e. increased turbine size, improved manufacturing and improved infrastructure. So, offshore wind turbines are now the preferred solution because of their more important production capacity and the possibility offered to tackle visual and noise related limitations. And, several types of offshore wind turbines have been developed to ensure the production needs such as monopile, gravity-based, TLP or semi-submersible wind turbines.

Among all the types of offshore wind turbine developed so far, the present study will focus on a single one: the spar floating wind turbine. A spar wind turbine presents good heave motions performances, small wave forces and is, among other things, easy to install and cheap to build and maintain compared to other types of wind turbines (Biswajit, et al., 2013). All of these features make this type of structure well suited for deep water operations where the production is the most promising given the encountered wind conditions i.e. strong and constant wind.

Floating wind turbines can be really challenging structures for modelling processes due to, among other things, large rotational and translational motions of the structure and modeling of mooring and anchoring systems. However, they have been studied extensively in the literature due to their suitability for wind energy production in deep water. Nevertheless, the most suited sites to install offshore wind farms might potentially be subjected to ice conditions and so far few researchers have studied the importance of these loads compared to the aerodynamic ones in the case of spar wind turbines. Indeed, for thin ice, ice loads might be -and were- considered small but it is not the case for thick ice conditions. Ice loading will also, due to its time variation, trigger dynamic effects as well as motions of spar and thus tension in mooring lines. As a major part of the literature focuses on the study of monopile wind turbine the question remains about the relative importance of ice loads compared to aerodynamic loads in the case of a spar wind turbine. So, it seemed to us to be important to develop a numerical model considering the coupled influence of ice and wind loads in order to run design checks, hence additional studies are needed.

The purpose of this project is to study the ice loads on a spar wind turbine, to perform dynamic response analyses of a spar wind turbine under ice loads for design check, and to investigate the importance of ice loads on the floater. As a start, we have realized in a previous work an uncoupled analysis considering only ice loading and not taking into account wind effects. We will now extend this analysis to a coupled model including both wind and ice loads. Indeed, in numerical models, it is important to consider a coupled analysis model for spar wind turbines in both wind and level ice. Different from a bottom-fixed wind turbine, the contact between the drifting ice sheet and the spar will be largely influenced by the motions of the spar. This creates numerical problems when coupling the ice load module to a global aerodynamic model of the wind turbine. A convergence study should also be performed to gather information on the accuracy of the implementation.

To do so, we have implemented a semi-empirical ice load model into the aero-hydro-servo-elastic tool HAWC2 (Larsen, et al., 2007). The structure is fitted with an inverted cone at the mean sea level (MSL) to mitigate the ice loads. A rigid model is implemented to study the influence of ice drifting speed, ice thickness and study the relative importance of aerodynamic and ice loads in the case of a coupled analysis.

This paper is thus divided as follows. In a first part, we realize a literature review on ice loads on conical structures and ice failure mechanism. Then we describe the numerical model implementation and the case that are studied. Finally the results are presented and discussed.

2. Literature review

The system studied in this report is a spar floating wind turbine with a conical shape around mean water level operated in ice conditions. Due to the nature of the problem, the structure will thus be submitted to 4 different types of loads:

- Aerodynamics loads;
- Hydrodynamic loads;
- Hydrodynamic loads on mooring lines;
- Ice loads.

These different loads are depicted in Figure 2.1, as per below:

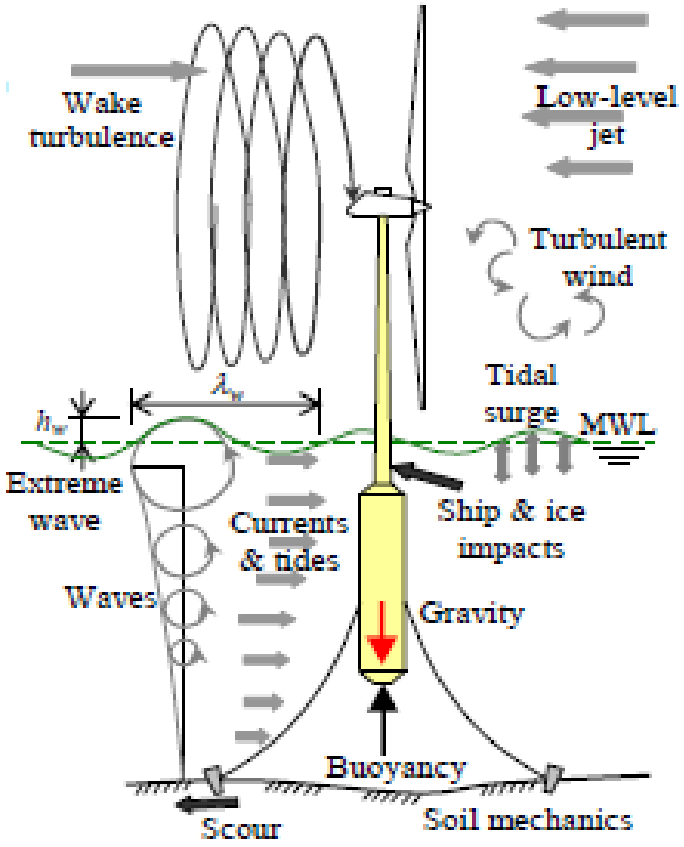

Figure 2.1 : Operating conditions of a floating wind turbine (Biswajit, et al., 2013)

The three firstly mentioned types of loads - i.e. aerodynamics, hydrodynamics, and hydrodynamic loads on mooring lines - are the ones commonly considered when analyzing a spar floating wind turbine dynamic response and most of the time ice loads are not taken into account. That is why it has been chosen to focus in this work on the

influence of ice loads on the structure. Thus, the present literature review will focus on ice failure mechanisms and ice loads on conical structures. Indeed, the studied structure is designed with a conical shape around mean water level. Moreover, the different numerical procedures used so far for ice loads analysis will be reviewed along with the identified influence of ice thickness and ice drifting speed. A particular attention will be drawn to randomly varying ice conditions simulations. Finally, a brief part will be dedicated to aerodynamic loads representation and estimation.

When referring to ice loads, we will refer here to level ice conditions. Icebergs or ridges are not considered in the present model. The standard we will refer to will be (ISO/FDIS19906, 2010). Indeed, after a comparison of several standards, the conclusions drawn by (Popko, et al., 2012) show that some of them give only approximate results and that the *" most comprehensive assessment of ice loads applicable to an offshore wind turbine support structure"* is given by (ISO/FDIS19906, 2010). And, several others standards, such as (DNV-OS-J101, May, 2014), give direct reference to (ISO/FDIS19906, 2010), hence our choice.

2.1. Ice failure mechanism

As highlighted in (ISO/FDIS19906, 2010) [A.8.2], in the case of arctic offshore structures, a first step in the estimation of ice loads is to determine what are the main modes of ice failures against the structure. Indeed, ice failure under compression is a complicated process where several ice failure modes can be encountered and the predominant ones for a given structure will depend on criterions such as the structure geometry, the ice properties i.e. ice thickness, presence of ridges, ice velocity or ice temperature. The failure modes for sea ice can be:

- Creep;
- Crushing;
- Bending;
- Buckling;
- Splitting.

Here, the hull of the structure considered is designed to have a conical shape at the mean sea level (MSL). Hence, as highlighted in (ISO/FDIS19906, 2010), (Xu, et al., 2014), (Barker, et al., 2005), (Gravesen, et al., 2005), (Xu, et al., 2010), (Kärnä, et al., 2004) and (Mroz, et al., 2008) the ice failure mode more likely to happen is a flexural failure in the case of a structure presenting a conical shape around the mean water level. This is explained by the fact that the force between the structure and the ice will now have a vertical component which triggers the bending failure (Mroz, et al., 2008). Thus, it will be the only failure mode considered throughout the tests. So, this conical shape allows invoking the bending failure mode. This is a design choice as it globally leads to smaller ice actions than for structures presenting vertical walls. Indeed, in the latter case, crushing failure can also occurs and the ice loads are more important for this failure mode than in flexural failure. A typical failure mechanism cycle in our case can be described as follows (see also Figure 2.2 and Figure 2.3) (ISO/FDIS19906, 2010), (Xu, et al., 2014):

- The ice sheet approaches the structure till contact with the structure;
- The ice sheet will be in compression against the structure and is lifted up along the surface
- Radial and circumferential cracks appear. They interact with each other and their shape and size depend on several ice properties. Their propagation leads to an increase of the ice force till the ice breaks downward in bending (c.f. downward cone in the model utilized) ;
- The ice will then ride up face of the structure;
- The ice pieces will accumulate on the slope;
- Finally, they will be cleared by the sides of the cone.

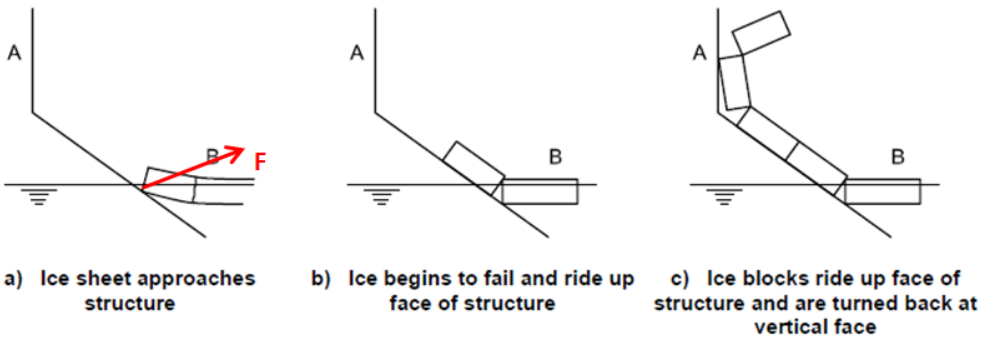

a) Ice sheet approaches structure

b) Ice begins to fail and ride up face of structure

c) Ice blocks ride up face of structure and are turned back at vertical face

Key
A sloping structure
B encroaching ice sheet

Figure 2.2: Processes in the interaction between a sloping structure (here upwards cone) and sheet ice (ISO/FDIS19906, 2010)

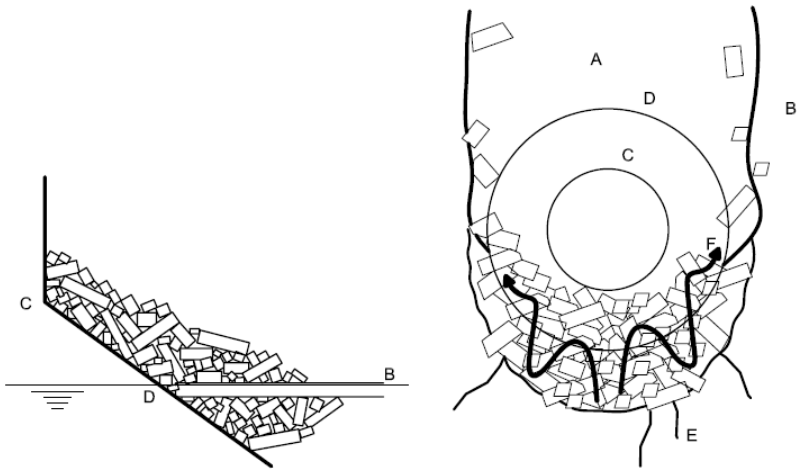

a) Ice rubble pile-up against a sloping structure

b) Ice failure and clearing of rubble around an upward breaking conical structure

Key
A open water in wake of structure
B encroaching ice sheet
C top of sloping face of structure
D waterline of structure
E cracks forming in encroaching ice sheet
F clearing of ice rubble blocks around structure

Figure 2.3: Ice rubble pile-up and clearing around a sloping structure (here upwards cone) (ISO/FDIS19906, 2010)

It should be noted that we will consider in the numerical model that after it breaks all the ice pieces are cleared away of the structure before the next ice-structure contact and will not accumulate around the cone.

2.2. Ice loads on conical structures

From the ice breaking cycle, it is then possible to identify 3 different steps in the ice force time history (Xu, et al., 2014) that are (See Figure 2.4):

- First, a loading process occurring till the ice breaks;
- Then, there is a period of time of unloading process triggered by the broken ice pieces riding up the surface of the cone. The ice force decreases during this stage as, while they are riding further down, the velocity of the broken ice pieces is slowing down. The decay time is longer than the force rise up;
- Finally there is a phase with no more loading as the ice broken pieces are cleared up from the structure before a new contact with the ice cover occurs.

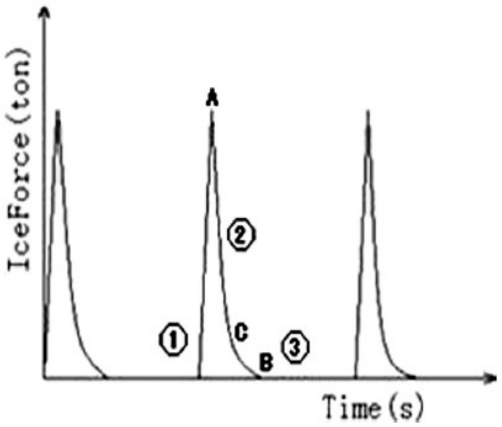

Figure 2.4: Ice force variation during the interaction between the ice and cone (Xu, et al., 2014)

This periodical ice breaking process will thus leads to ice-induced vibrations on the structure. Nevertheless, (Xu, et al., 2010), (Barker, et al., 2005) and (Gravesen, et al., 2005) have shown that the magnitude of the ice-induced vibrations is significantly reduced when adding a cylindrical shape around the mean waterline compared to a structure with vertical walls. This is one more time due to the different failure modes – respectively flexural and crushing failure mode - involved in the 2 cases.

However, as mentioned before, there are still ice-induced vibrations. They can be separated in 3 types (Xu, et al., 2010):

- Damping vibration under quasi-static ice force;
- Steady state vibration under ice-excited force ;
- Highly random vibration under random ice force.

These 3 types of ice-induced vibrations can also be found in the literature under different names (Heinonen, et al., 2011): intermittent crushing, lock-in vibration and continuous brittle crushing (ISO/DIS19906, 2008). The predominant ones will depend on the dynamic properties of the structure.

So, the structure will still experience ice-induced vibrations even if it is fitted with a conical shape at the mean sea level and this type of load has proven, in the past, its severeness (Määttänen, 1999). Thus, the dynamic response of the structure to ice loads should be thoroughly studied and the vibration frequencies due to ice-induced vibrations compared to the eigenfrequencies of the structure to avoid strong self-excited vibration.

Now that that the main steps of the process have been identified, the ice force applied on the structure should be estimated. Both static and dynamic analysis of the ice loads should be considered given the previously described load history. The first step of a typical ice force implementation described in the literature is to find the structure characteristics (ISO/FDIS19906, 2010), (Xu, et al., 2010), (Kärnä, et al., 2004), (Mroz, et al., 2008) and (Qu, et al., 2006). As the structure is submitted to vibrations, the relevant components to calculate first are the eigenfrequencies and eigenmodes. From them it will be possible to identify the most critical loadings for the structure. These critical loadings are described by 2 parameters:

- Ice drifting speed;
- Ice thickness.

For the definition of the loading case, from a chosen ice velocity the ice breaking length can be estimated. It has been done in the past from either analytical estimation or empirical formulation (Yu, et al., 2014). For example, (Qu, et al., 2006), (Xu, et al., 2010) define the breaking length with the following relation:

$$T = \frac{L_B}{V} \quad [1]$$

With: T : *Ice force period*

L_B : *Breaking length of the ice sheet*

V : *Ice velocity*

To find the critical loading, the ice force period is set equal to the eigenperiods of the structure. Then for the chosen ice velocity it is possible to estimate the breaking length of the ice sheet. From there, using one of the various relations published in the literature, the ice thickness corresponding to the applied force can be derived from the breaking length. For example, (Kärnä, et al., 2004) use a procedure given by Ralston while (Kärnä, et al., 2004) and (Xu, et al., 2010) use the formulas derived from field test measurements in the form:

$$L_B = kt \quad [2]$$

With: t : ice thickness

k : *Ratio between ice broken length and ice thickness from field measurement result (from 4 to 7from field measurement results in the Bohai Bay).*

With the ice conditions defined, it is then possible to calculate the static loads. To do so, several models have been developed through the years. Among them, 2 are cited in our chosen standard reference – (ISO/FDIS19906, 2010):

- A plastic method;
- An elastic beam bending method.

The Ralston's method is also commonly employed in the literature (Popko, et al., 2012), (Kärnä, et al., 2004), (DNV-OS-J101, May, 2014). It is based on plastic limit analysis and as the two previously cited methods it can be utilized for both upward and downward cone structures. Numerical methods utilizing finite-element methods are also sometimes applied (Yu, et al., 2014). The peak values of the ice forces are obtained then and by using probability distributions for the force and the breaking length it is possible to simulate dynamic ice forces (Kärnä, et al., 2004), (ISO/FDIS19906, 2010), (Qu, et al., 2006). These distributions are extrapolated from field measurement data.

Moreover, it should be noted that even if the ice breaks in bending failure mode, local crushing will appear at isolated contact points. The ice crushes locally against the structure for a short duration, and then it reaches a point where the ice fails in large-scale behavior (Barker, et al., 2005). This local crushing will increase the local area (Kärnä, et al.). And a dependency exists between the pressure and the area of ice-structure contact. This relation is commonly called *(p-a)* curve and exhibits a power law form (Tan, et al., 2013). So, as the local area is increasing the local loads will too. This increase will last until, as explain before, the ice breaks in bending. This breaking point can be predicted using bending failure criterion. Different criterions have been developed in previous studies (Tan, et al., 2013) ; both static and dynamic as experiments and theories have shown that the ice speed indentation will influence the stress rate and thus the ice bending failure load.

2.3. Numerical procedures for ice loads analysis

Different numerical models have been developed throughout the years. First, we can cite the recommendations from the different standards which aim at giving a guideline to simulate ice loads. A first method suggested in the IEC and DNV standards and employed in (Popko, 2014) is to apply on the numerical model of the wind turbine ice loading time series recorded on the full scale installation. In this case the 3D numerical model of the structure was implemented in Abaqus and the full scale loading time series were processed in the Abaqus model through a Python script. The ice loads were then applied to areas on the model simulating the load panels from the full scale installation. So, as highlighted in (Popko, 2014), this method presents several shortcoming:

- The ice loading cases are restricted to the ones recorded on the full scale installation;
- As the ice loads applied only concerned the areas covered with load panels, this method does not give an accurate representation of the full ice loading and breaking pattern;
- The interaction ice-structure cannot be simulated in the 3D model.

Moreover, in (Popko, et al., 2012), the different available guidelines are compared. The paper states that in GL guideline the importance of dynamic ice loads is underlined but no clear method to calculate them is included in the document. On the contrary, IEC, DNV and ISO standards provide ice loads curve to estimate the ice loads given a chosen location. The shape of the curve changes from one standard to another. For example, ISO provides a triangular shaped ice loading curve while IEC standard suggest a shifted sinusoidal curve and a serrated function. These curves definitions depend then on the structure natural frequencies, its shape at the waterline and ice properties. These ice loads curves were for example exploited in (Hendrikse , et al., 2014). The point highlighted in this work is that employing such ice loads curves will result in conservative results and it is suggested using a coupled method based on phenomenological models instead to obtain realistic and reliable results. They applied, for example, the model developed by (Määttänen, 1999). This model was also applied for ice loads numerical model in (Hetmanczyk, et al., 2011) and (Heinonen, et al., 2011). In these works, the well-established empirical model for ice loads developed by (Määttänen, 1999) was

implemented in the aero-hydro-servo-elastic simulation tool OnWind on a simplified model of wind turbine. To do so, Modelica language was employed to develop a model simulating the ice loads and linking these calculations to the features of OnWind. The ice loads model was also implemented in Abaqus in order to compare the result to a reference model for the wind turbine. And, basically, the ice loads obtained with the ice model were transferred as nodal loads in the FEM model based on the following formula:

$$F_i = A_i \sigma_c(\dot{\sigma}) \quad [3]$$

With: F_i: *Nodal force*

A_i: *Corresponding area*

σ_c: *Crushing strength that depends on the stress rate* $\dot{\sigma}$

$\dot{\sigma}$: *Stress rate that depends on the ice drifting velocity and the velocity of structure at the waterline*

These 2 articles highlight the limits of phenomenological models. Indeed, as pointed out in section 2.1, the ice breaking mechanism is a complicated process where several ice failure modes can be encountered depending on a rather large number of factors whether they are linked to the ice properties or the structure geometry. Thus, to obtain a reliable model, several ice breaking scenarios should be included using as many sub-models as necessary to describe a wide range of ice conditions and structure geometries. And, in all the previously mentioned methods, the system studied was a bottom fixed structure with vertical sides which triggers dominantly crushing failure. While here we are interested by a floating wind turbine fitted with a cone at the waterline. So, the dominant ice failure mode to consider is bending failure and not crushing failure. So, the model applied should include a sub-model predicting bending failure.

As conical structures are more and more added at the waterline of wind turbine to reduce the ice forces on the structures it is possible to find some studies that include ice bending failure mechanism to their numerical models. For example, in (Yu, et al., 2013), (Yu, et al., 2014) and (Yu, et al., 2014) the progressive refinements done on an ice-structure interaction module are presented. The ice module is included in the FAST software, a commonly utilized CAE software for wind turbines study. The model developed includes constant wind and floating fresh water ice loading and it was gradually refined by adding

new sub-models for different ice conditions scenarios. The ice sheet is defined as "*a rigid-plastic structure supported by an elastic foundation*". It takes into account the 3 different types of ice-induced vibrations mentioned in section 2.2 i.e.:

- Damping vibration under quasi-static ice force;
- Steady state vibration under ice-excited force ;
- Highly random vibration under random ice force.

It also predicts ice failing in multiple zones non-simultaneously and was fitted with a sub-model predicting bending failure on sloping structure. Bending failure on sloping structures was also implemented in (Mroz, et al., 2008). There, a numerical model including ice and wind loads was employed to roughly estimate the goodness of a conical structure design. The ice was included as a simplified material model in a model developed using the FEM software Abaqus. The ice sheet was defined as an elastic-plastic material model and meshed with 4-nodes shell elements. However, the article points out that the model applied is a simplified one and refinements are needed to develop a more accurate method.

So, from this review, it can be seen that phenomenological models give more reliable results and should be employed over ice loads curves provided in the different standards. Indeed, actual measurements give accurate phenomenological information. However, they present a certain number of drawbacks. Among other things, we can cite that they only represent a limited number of environmental conditions – that is the ones encountered at the time of the experiment and their impact on the particular part of the structure where the sensors where positioned. That is why numerical methods should be employed for a complete study of the ice loads impact because of the extensive possibilities offered for a parametric study. And, these methods are cost efficient compared to physical tests and easier to deploy. However, this does not mean that physical tests should never be used. Indeed, thanks to them calibration and validation of the different numerical methods developed can be achieved as per (Tan, et al., 2013).

To simulate ice loads on a floating wind turbine, different approaches are possible. The ice loads module can be either added to a FEM software for a structural check or to an aero-hydro-servo-elastic simulation tool if aerodynamic loads have to be included to the

analysis. Moreover, the ice model applied should represent the appropriate ice failure mechanism relatively to the ice properties and the structure geometry – in the present case bending failure.

2.4. Influence of ice thickness and ice drifting speed

The methods to calculate ice loads cited above i.e. (ISO/FDIS19906, 2010) plastic method and elastic beam bending method and the Ralston's method give the same proportionality between ice force and ice thickness, which is also highlighted in (Barker, et al., 2005). Indeed, in bending failure the ice force is proportional to the product of the bending strength and the thickness squared:

$$F \propto \sigma_f h_i^2 \quad [4]$$

With: σ_f: *Ice flexural strength*

h_i: *Level ice thickness*

So, an increasing ice thickness should induce increasing loads. This effect has been observed in some previous simulations. (Hetmanczyk, et al., 2011) has, for example, found increasing structure displacement at ice level and blade tip with increasing ice thickness. (Shi, et al., November 24-26, 2014) has found that the overturning moment at the mudline increases with increasing ice thickness It is explained by the fact that an increasing ice thickness will increase the contact area, and consequently induces higher ice loads.

As explained in §2.2, locally the ice field will be submitted to local crushing till reaching the bending failure load. The strength has moreover been proven to be dependent on the ice drifting speed. For example, data obtained at the Norströmsgrund lighthouse show a significant speed effect in local panel pressures. However, speed effects are not evident in the directly measured global pressures (Gravesen, et al., 2009). Indeed, with the varying speed the ice failure modes will change. At low velocity, the ice will have a ductile behavior causing high loads due to the ice high strength while at higher velocity the ice will have a continuous brittle crushing behavior. Influence of speed appears in ISO calculations as a coefficient to consider the ice strength in different ice regimes, as well as effect due to ice speed along with waterline displacements of the structure effects

(Gravesen, et al., 2009). And some models have been developed such as the Määttänen-Blenkarn model describing the dynamic loads against a narrow vertical structure ((Määttänen, 1999), (Blenkarn, 1970)), where the crushing strength of ice depends both on the relative velocity between the ice and the structure at the waterline as well as the size of the contact area (Hetmanczyk, et al., 2011). It is therefore employed in (Hetmanczyk, et al., 2011) and differences due to the change in ice failure modes are observed:

- At low speed, the displacements have a nearly constant value as a consequence of the ductile ice behavior and the resulting high loads.
- In an intermediate range, the displacements present high amplitudes and a saw-tooth like shape. The structure also starts to vibrate close to resonance frequency and this vibration occurs independently of the frequency.
- Finally, for higher ice velocity, the ice should exhibit a brittle behavior leading to lower loads. However, the behavior observed in (Hetmanczyk, et al., 2011) was not realistic (sinusoidal displacement) due to assumptions made in the model.

Other simulations also observed this failure mode change such as (Shi, et al., November 24-26, 2014) where at low drifting speed, random response is presented while at higher drifting speed the structural response shows similar periodic loads. In both cases, the response shows a saw-tooth like pattern. Additionally, (Karna, et al., 1990) analysis indicated that when a lock-in condition arises, the structure's velocity amplitude at the waterline is approximately the same as the ice velocity (Barker, et al., 2005). This relation tends to be confirmed by the model tests done in (Barker, et al., 2005).

Additionally, ice thickness and drifting speed have a combined influence on vibrations. (Ziemer, et al., 2014) has observed in ice model tests that thicker ice seems to facilitate the occurrence of ice-induced vibrations. Periodic and straight vibrations are only found in the lower velocity regime while circular vibrations only occurred in thin ice. This influence can also be found in other field measurements such as (Xu, et al., 2010). It explains that the ice thickness and ice drifting velocity will influence the loads frequency. Indeed, the frequency is defined as the ratio between the ice velocity and the ice broken length against the cone. And, it has been observed that the ice broken length against the cone can be simply regarded as linearly increasing with ice thickness. So, for a constant

thickness, the loads frequency will decrease with decreasing ice velocity and for a constant ice drifting velocity the loads frequency will decrease with increasing ice thickness.

2.5. Randomly varying ice conditions

Usually, the ice loads models are implemented using constant level ice/equivalent ice thickness and strength properties as per the Finnish Swedish Ice Class Rules, for example. However, due to the complexity of the ice formation process, these parameters can vary greatly in the same ice sheet as exposed by (Kujala, 1996) and (Su, et al., 2011). Indeed, as explained in these articles, the ice thickness can, for example, varies due to the variation in air temperature or snow cover during the ice formation. Concerning the ice properties, the temperature grain size, crystallographic orientation, porosity, brine content and strain rate are parameters of influence. And, as a direct consequence the ice loading process displays a clear stochastic nature. However, as explained in (Kujala, 1996), few ice loads models include statistics.

Both short terms and long terms ice loads should be considered for a complete design study. First, for the short term predictions, statistical distributions for parameters such as the ice thickness, ice flexural and crushing strength can be derived from field measurements using the Monte Carlo method (Su, et al., 2011). In this work, it is assumed that these parameters follow normal distributions and are independent from each other's. From existing data measurements (here taken from (Kujala, 1994)), the mean value and standard deviation can be obtained for each parameters (see Figure 2.5).

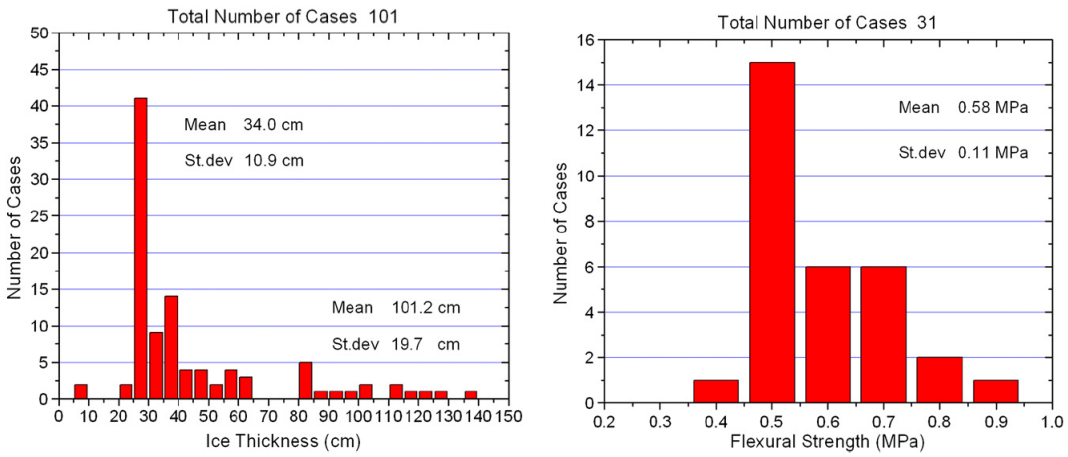

Figure 2.5: Distribution of the ice thickness as measured at 10 m intervals along a line of 1 km length on March 1975 on the Bothnian Bay and Distribution of the measured flexural strength values of Baltic Sea ice (Digitized from (Kujala, 1994)) (Su, et al., 2011)

From the obtained mean values and standard deviations a statistical distribution can be fitted to the data. Here, as the parameters follow normal distributions the Cumulative Distribution Function (CDF) will be as presented in equation [5]. However, in other cases the statistical distribution fitted to data could be theoretical or empirical.

$$F(X) = \frac{1}{\sqrt{2\pi\sigma}} \int_{-\infty}^{X} e^{\left[-\frac{(S-\mu)^2}{2\sigma^2}\right]} ds \qquad [5]$$

With: σ *: Standard deviation of the random variable X*

μ*: Mean value of the random variable X*

Using the inverse function of the defined CDF it is then possible to generate random value *X* as follows:

$$X = F^{-1}(U) \qquad [6]$$

With: *U a randomly generated number between 0 and 1*

So, random values can now be generated for the ice thickness and the strength properties based on the field measurements. Then, to generate a full ice cover sampling points are selected. At these points, the values of the selected parameters are randomized and the intermediate value between two adjacent points is determined by linear interpolation (Su, et al., 2011). Figure 2.6 gives an example of a randomized ice thickness field along a 10 km route.

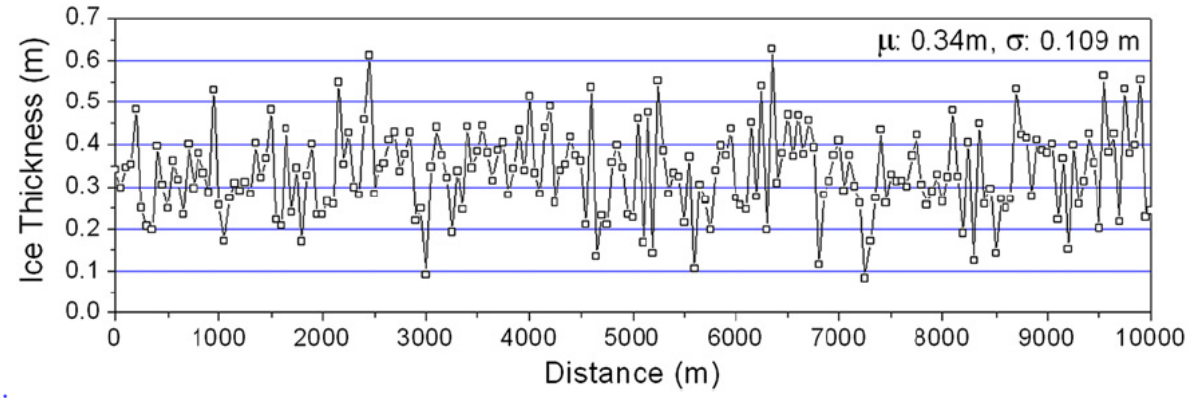

Figure 2.6: Randomized ice thickness along a 10 km route (Su, et al., 2011)

Additionally, long term predictions should be implemented for an accurate design of the structures in ice. That is why in (Kujala, 1996), a semi empirical method is developed to

predict the long term ice loads. This method is based on full scale measurements and on the analysis of the ice edge failure process. The only ice failure mechanism consider is breaking ice in bending like in the present work. The long term predictions are obtained by *"extrapolating 12-hour maximum load values for the life time of the ship"* (Kujala, 1996). The 12 hour period is selected, because this is about the average time required for a ship to pass each sea area in the case of an ice going ship (Kujala, 1996). As explained in (Kujala, 1996) and (Kujala, et al., 2013), first, annual 12 hour maximum values are measured during one winter. For the analysis, the smallest peaks shall be removed because they are due to electronic noise, brash ice … and thus does not fit in the scope of the work. Then, a statistical distribution should be fitted on the ice loads histogram. Long term measurements indicates that a Gumbel I asymptotic extreme value distribution fits well on the measured extreme values (Kujala, 1996). So, the Gumbel I distribution parameters are obtained using the mean value and the standard deviation of the measured 12 hour maximum. By definition we have the following expressions for the mean value and the standard deviation of the measured 12 hours maximum respectively:

$$E[y_n] = \sum_i y_{n_i} . P(y_n = y_{n_i}) \quad \textbf{[7]}$$

$$\sigma = \sqrt{Var[y_n]} = E[(y_n - E[y_n])^2] \quad \textbf{[8]}$$

The Cumulative Distribution Function (CDF) of Gumbel 1 function is defined as follows:

$$G(y_n) = \exp[-e^{-\propto_n (y_n - U_n)}] \quad \textbf{[9]}$$

With:

$$\propto_n = \frac{\pi/\sqrt{6}}{\sqrt{Var[y_n]}} \quad \textbf{[10]}$$

$$U_n = E[y_n] - \gamma \frac{\sqrt{6}}{\pi} \sqrt{Var[y_n]} \quad \textbf{[11]}$$

With: γ *: Euler's constant (equals 0.577)*

Due to the removal of small peaks, the Gumble I distribution starting point does not have a probability equals to 0 for load null. Since the probability of the negative forces is zero,

we have to plot a truncated distribution. A possible way to define the PDF of the truncated Gumble I [*h(x)*] is (Kujala, et al., 2013):

$$h(x) = \begin{cases} 0 & x < 0 \\ \dfrac{g(x)}{\int_0^{\infty} g(x)dx} & x \geq 0 \end{cases} \xrightarrow{\int_0^{\infty} g(x)dx = 1 - \int_{-\infty}^{0} g(x)dx = 1 - G(0)} \begin{cases} 0 & x < 0 \\ \dfrac{g(x)}{1-G(0)} & x \geq 0 \end{cases}$$

So, we obtain for the CDF:

$$H(y_n) = \begin{cases} 0, & y_n < 0 \\ \dfrac{G(y_n) - G(0)}{1 - G(0)}, & y_n \geq 0 \end{cases} \quad [12]$$

Then, the Goodness of fitting should be checked using for example Kolmogorov-Smirnov test i.e. the cumulative value of the data and the fitted distribution are compared. The max difference between these two will determine the Goodness of fit:

$$D_n = \max|F(x) - S_n(x)| \quad [13]$$

D_n values are given in tables with different level of significance α (see Figure 2.7 for an example).

n \ α	0.20	0.10	0.05	0.01
5	0.45	0.51	0.56	0.67
10	0.32	0.37	0.41	0.49
15	0.27	0.30	0.34	0.40
20	0.23	0.26	0.29	0.36
25	0.21	0.24	0.27	0.32
30	0.19	0.22	0.24	0.29
35	0.18	0.20	0.23	0.27
40	0.17	0.19	0.21	0.25
45	0.16	0.18	0.20	0.24
50	0.15	0.17	0.19	0.23
>50	$1.07/\sqrt{n}$	$1.22/\sqrt{n}$	$1.36/\sqrt{n}$	$1.63/\sqrt{n}$

Figure 2.7: Critical values of D_n in the Kolmogorov-Smirnov Test

The CDF of extreme value distribution [*E(x)*] can then be calculated as:

$$E(x) = [H(x)]^n \quad \textbf{[14]}$$

With: *n is the number of observations*

H(x) is the CDF of truncated Gumble I distribution

As an example to grasp the signification of the number of observations, we can focus on a 1C ice class ship. The long term extreme value distribution for a 25 year life time of the ship has to be calculated, assuming that the ship will be in ice 10 days/year. The data measured are annual 12 hour maximum values so the total number of observations is:

$$n = 25[years] * 10[days/year] * 2[observations/day] = 500\ observations$$

Then:

$$E(x) = [H(x)]^n = \begin{cases} 0, & y_n < 0 \\ \left[\dfrac{G(x) - G(0)}{1 - G(0)}\right]^n, & y_n \geq 0 \end{cases} \quad \textbf{[15]}$$

And the Probability Distribution Function (PDF) of the extreme value distribution is:

$$e(x) = \begin{cases} 0, & y_n < 0 \\ n * h(x) * \left[\dfrac{G(x) - G(0)}{1 - G(0)}\right]^{n-1}, & y_n \geq 0 \end{cases} \quad \textbf{[16]}$$

One drawback of this method is that it is area dependent. It can only be applied to a site where full scale measurements have been realized. And, these measurements can be time consuming and tedious to implement. Indeed, we can mention the example of ice thickness measurements done in the Northern Baltic Sea in March 2012 (Kujala, 2013). The goal of the experiment was to develop an automatic ice thickness measurement method using stereo cameras. The thickness is measured when the ice pieces are turning against the hull and the cross-section is defined by detecting the top and bottom layer of the ice sheet (See Figure 2.8).

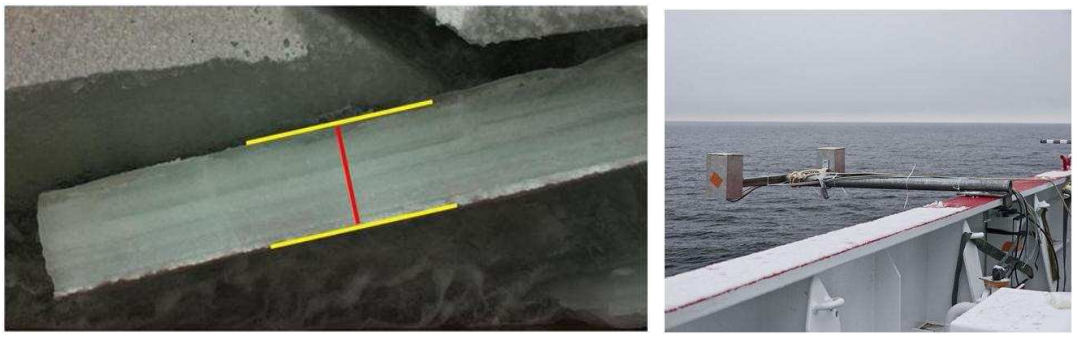

Figure 2.8: Ice thickness measurements by a stereo camera (Kujala, 2013)

However, the definition of the cross section is not always as easy as presented in Figure 2.8. Various phenomenon such as layered ice, irregular shapes, complex ice breaking patterns, and very irregular cross-sections or color variations greatly complicate the process.

Another example that can be mentioned is the flexural strength measurement (Kujala, 2013). Indeed, flexural strength is one of the most important parameter to determine ice-induced loads and, to measure the flexural strength, in situ cantilever beams are typically used. This will cause typically high scatter in the results e.g. due the high stress concentration factor at the root and four point bending is the best way to measure the flexural strength but it is fairly tedious to conduct (See Figure 2.9).

Figure 2.9: Ice flexural strength measurement (Kujala, 2013)

2.6. Aerodynamic loads

The Offshore Code Comparison Collaboration (OC3) for IEA Task 23 was implemented to test different simulations tools developed by universities, industries and research institutions and ensure their capacity to predict coupled dynamic loads and responses in the case of the different offshore wind turbine types. At this occasion, different codes were compared. The participants at phase IV (see § 3.1 for more details) were from the National Renewable Energy Laboratory (NREL), Risø National Laboratory of the Technical University of Denmark (Risø-DTU), MARINTEK, the Norwegian University of Science and Technology (NTNU), the Institute for Energy Technology (IFE), the Norwegian University of Life Sciences (UMB), Garrad Hassan & Partners Limited (GH), the Leibniz University of Hannover (LUH), Acciona Energia, and the Pohang University of Science and Technology (POSTECH). The characteristics of the different codes involved are displayed in Table 2.1.

Table 2.1: Overview of aero-hydro-servo-elastic modeling capabilities of the different codes involved in OC3 (Jonkman, et al., 2010)

FAST	Bladed	ADAMS	HAWC2	3Dfloat	Simo	SESAM/DeepC
Code Developer						
NREL	GH	MSC + NREL + LUH	Risø-DTU	IFE-UMB	MARINTEK	DNV
OC3 Participant						
NREL + POSTECH	GH	NREL + LUH	Risø-DTU	IFE-UMB	MARINTEK	Acciona + NTNU
Aerodynamics						
(BEM or GDW) + DS	(BEM or GDW) + DS	(BEM or GDW) + DS	(BEM or GDW) + DS	(BEM or GDW)	BEM	None
Hydrodynamics						
Airy+ + ME, Airy + PF + ME	(Airy+ or Stream) + ME	Airy+ + ME, Airy + PF + ME	Airy + ME	Airy + ME	Airy + PF + ME	Airy+ + ME, Airy + PF + ME
Control System (Servo)						
DLL, UD, SM	DLL	DLL, UD	DLL, UD, SM	UD	DLL	None
Structural Dynamics (Elastic)						
Turbine: FEMP + (Modal / MBS), Moorings: QSCE	Turbine: FEMP + (Modal / MBS), Moorings: UDFD	Turbine: MBS, Moorings: QSCE, UDFD	Turbine: MBS / FEM, Moorings: UDFD	Turbine: FEM, Moorings: FEM, UDFD	Turbine: MBS, Moorings: QSCE, MBS	Turbine: MBS, Moorings: QSCE, FEM

Airy[+] – Airy wave theory; (+) with free surface connections
BEM – blade-element/momentum
DLL – external dynamic link library
DNV – Det Norsk Veritas
DS – dynamic stall

GDW – generalized dynamic wake
FEM[P] – finite-element method; (P) for mode preprocessing only
MBS – mulibody-dynamics formulation
ME – Morison's Software Corporation

PF – linear potential flow with radiation and diffraction
QSCE – quasi-static catenary equations
SM – interface to Simulink® with MATLAB®
UD – implementation through user-defined subroutine available
UDFD – implementation through user-defined force-displacement relationships

In the present study, we will be using the software HAWC2 (*Horizontal Axis Wind turbine simulation Code 2nd generation*). During OC3, HAWC2 has shown its reliability (see (Jonkman, et al., 2010)). Moreover, HAWC2 goodness has been verified in many articles such as (Karimirad, et al., 2011), (Karimirad, et al., January 2012), (Karimirad, et al., July 2012) and (Karimirad, 2013). To do so, a code-to-code comparison with codes such as USFOS, Simo-Riflex or FAST was conducted for a spar floating wind turbine. At these occasions, the code has shown that it tends to predict higher roll and pitch natural

frequencies than other codes and can display in certain situations different damping values. However, contrary to most of the codes tested in OC3, HAWC2 can model tower and blade bending and drivetrain torsion modes (Jonkman, et al., 2010), (Karimirad, 2013). The goodness of the results were tested for both wave and wind-waves induced load cases.

The detailed features of the code will be described later on (see 3.4 for more details) and we will deal here with the theory behind the aerodynamic loads calculations implemented in HAWC2. The aerodynamic part of the code is based on the blade element momentum (BEM) theory. We will thus introduce the main principles of BEM. First, for a better understanding, we will talk about the different representations of wind loads commonly employed in the literature and implemented in the code. Then, we will move on to the methodology applied in the study to calculate the different aerodynamic loads.

2.6.1. Wind representations

For simpler modelling, constant wind can be applied as input. However, wind velocity is typically not constant but varying over time. These variations can extend on different periods and then define different wind spectra adapted to these particular time intervals. The main variation domains are represented in Figure 2.10 and can be described as follows (Gao, et al., 2014), (Schreck, October 2004):

- Annual and seasonal variations: This concerns wind pattern changes occurring with a time period of around one year. These patterns are influenced by the degree of latitude and variations vanish close to the equator where the variations due to seasons are less sensible.
- Synoptic variations: It concerns wind pattern changes occurring with a time period of around 4 days. It is linked to the cycle between depressions and anticyclones;
- Diurnal variations: These variations have a time period of approximately 1 day and occur due to difference in temperature between day and night. These effects are thus more significant for onshore sites than for offshore ones.
- Turbulent variations: Turbulences correspond to local change in the wind speed over seconds and minutes. It is therefore important to account for this phenomenon as it will have various impacts on the system. First, due to the time

variation of the wind velocity, the energy production will be reduced compare to a simulation with constant wind. Moreover, dynamic loads will increase on the blade and overall the wind fluctuations will trigger dynamic effects. As a consequence, the structure life span will be shortened.

- An additional phenomenon called spectral gap is observed between time periods of 10 min to 2 hours. There, no significant peaks due to wind pattern fluctuation is observed.

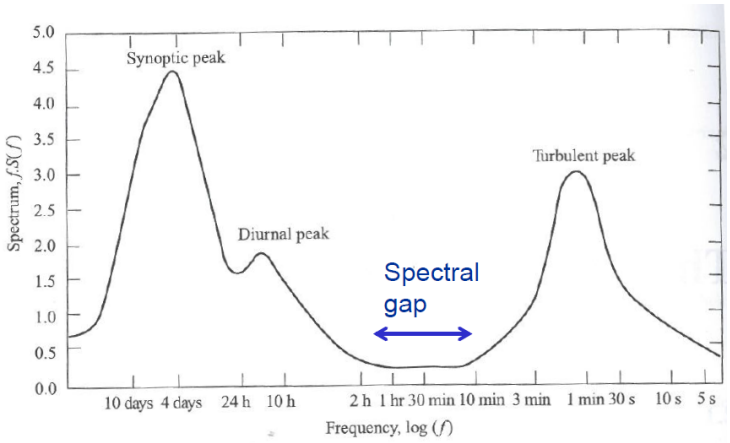

Figure 2.10: Wind spectrum from Brookhaven based on work by van der Hoven (1957) (Gao, et al., 2014)

Once the different wind variations patterns identified, we can easily restrain the study to the one of interest for the present work. Indeed, here we will work with time series of around 1400s. So the only pattern to consider is the turbulent peak. In this case, the wind is described by a mean wind speed $\overline{U}$ (from synoptic and diurnal data) and a variation $u'(t)$ over the time (turbulence) (Gao, et al., 2014):

$$U = \overline{U} + u'(t) \quad [17]$$

The turbulent part is a complex randomly defined phenomenon. Thus, deterministic features cannot be applied to describe it. Stochastic tools are then employed and turbulence is described by two parameters that are the turbulence intensity and the Power Spectral Density (PSD) (Schreck, October 2004). These values should describe both the temporal and the spatial fluctuations in the wind speed. The turbulence intensity is *"a measure of the overall level of turbulence"* (Schreck, October 2004) and is defined as per equation [18] (Hansen, 2008), (Schreck, October 2004):

$$I = \frac{\sigma}{\overline{U}} \quad [18]$$

With: I: *Turbulence intensity*

σ*: Standard deviation of the variation of wind speed around* $\overline{U}$

$\overline{U}$*: Mean wind speed (from synoptic and diurnal data) (usually 10 min average)*

The turbulence intensity depends on the roughness of the surface and on the surrounding environment comprising features such as mountains, hills or trees (Gao, et al., 2014), (Schreck, October 2004). In OC3 work, the turbulence intensity was set to $I = 0.14$ in conformity with IEC61400-1 (Jonkman, et al., 2010).

The two statistical parameters used to describe turbulence are complementary. Indeed, the turbulence intensity does not contain any temporal information (height, roughness at surface, etc.) while the PSD describes the temporal properties of the turbulent wind (data regarding the frequency of wind speed change) (Schreck, October 2004). Different PSD are often applied in the literature and HAWC2 allows the use of the two most common ones i.e. Kaimal spectrum and Von Karman spectrum (Mann model). Their respective expressions are given in equations [19] and [20] (Schreck, October 2004), (Hansen, 2008):

$$S(f) = \sigma^2 \frac{4L_1/\overline{U}}{\left(1 + \frac{6fL_1}{\overline{U}}\right)^{\frac{5}{3}}} \quad [19]$$

$$S(f) = \sigma^2 \frac{4L_2/\overline{U}}{\left(1 + \left(\frac{70.8fL_2}{\overline{U}}\right)^2\right)^{\frac{5}{6}}} \quad [20]$$

With: L*: Length scales in the PSD models (more details in* (Hansen, 2008) *and* (Larsen, et al., 2007)*)*

S*: The longitudinal velocity spectrum*

f*: The frequency (in Hz)*

These two spectra are employed in different configurations. Von Karman spectrum is more suited to represent wind tunnel modelling as it gives an isotropic turbulence model in neutral atmospheric conditions. However, the atmospheric conditions are not isotropic and then the Kaimal spectrum is more adapted to depict the atmospheric boundary layer

(Arany, et al., 2014), (Larsen, et al., 2007). In OC3 project the Mann model is applied and is based on the Von Karman spectrum modified to account for the non-isotropic atmospheric conditions (Jonkman, et al., 2010), (Larsen, et al., 2007). Those spectra are roughly valid in the range going from 0.02 s to 600 s (Arany, et al., 2014). Wind speed time series are then obtained by using inverse discrete Fourier transform. And inversely, a PSD can be derived by using discrete Fourier transform and on-site data (Hansen, 2008).

2.6.2. Estimation of the loads on the structure

From the obtained wind speed time series, loads can be introduced on the structure. They will concern different parts of the structure and in HAWC2 the superposition principle is used (Larsen, et al., 2007). Indeed, the calculations are separated for the rotor, tower and nacelle.

Due to the slender shape of a WT, an important phenomenon to account for is the wind shear i.e. vertical wind profile variations. Typically the wind will increase as the distance to the ground increases. Different models are included in HAWC2: constant, logarithmic, power law, linear. The model most commonly employed in the literature is the power law model transcribed in equation [21] (Larsen, et al., 2007), (Gao, et al., 2014):

$$\overline{U}(z) = \overline{U}_{ref}\left(\frac{z}{z_{ref}}\right)^{\alpha} \quad [21]$$

With: α: *Vertical shear exponent*

$\overline{U}_{ref}$: *Wind speed at reference height* z_{ref}

Once the wind shear has been accounted for it is possible to calculate the loads on the different parts of the structure. It should be noted that in the OC3 simulations wind shear was not taken into account and a constant wind shear (factor 1) was applied along the tower (Jonkman, et al., 2010). It can be justified by the fact that the turbine is meant to be implanted offshore where the wind shear is less important than in rough areas (built-up ones for example).

The loads on the tower and the nacelle are calculated based on the pressure integration method coupled to the Morison's equation (Faltinsen, 1990):

$$dF_{aero} = \frac{1}{2}\rho_a C_{D,t} D_t(z) dz[U(z,t)|U(z,t)|] \quad [22]$$

With: ρ_a = *Air density*

$D_t(z)$ = *Tower/Nacelle diameter at elevation z*

$C_{D,t}$= *viscous coefficient on the specific direction that has projected area* $D_t(z)dz$ *(depends on tower dimensions and wind flow regime; 1.0 by default in HAWC2)*

U = W*ind velocity along the tower/Nacelle height and in time*

Concerning the load calculations on the turbine, the two main methods commonly applied are Generalized Dynamic Wake (GDW) and the Blade Element Momentum (BEM) theory. GDW theory was developed for helicopters – lightly loaded rotors- and is not utilized for wind speed below 8 m/s (Gao, et al., 2014). As in HAWC2 the aerodynamic part of the code is based on the blade element momentum theory, GDW theory will not be developed any further in this work. We will instead develop in the following the basics behind BEM theory and the different corrections that can be implemented on it to obtain the most accurate model possible.

The BEM theory was introduced in 1935 by Glauert. The aim of this theory is to be able to quantify the loads due to aerodynamics i.e. the steady loads but also the thrust and power for different settings of wind speed, rotational speed and pitch angle (Hansen, 2008). To do so, the momentum theory is coupled with the local events at the actual blades (Hansen, 2008). The wind turbine is modelled by discretizing N annular elements of height *dr*, each of which can be studied using the 1D momentum theory as shown in Figure 2.11. Those annular elements are defined based on the following assumptions (Hansen, 2008):

1- *"No radial dependency – in other words what happens at one element cannot be felt by the others.*
2- *The force from the blades on the flow is constant in each annular element; this corresponds to a rotor with an infinite number of blades."*

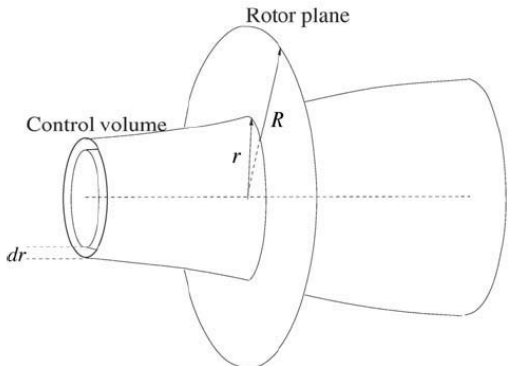

Figure 2.11: Control volume shaped as an annular element exploited in the BEM model (Hansen, 2008)

By coupling 1D results and the integral momentum equation, it is possible to compute the thrust from the disc on the control volume and the torque on the annular element. Thus the local loads can be derived. The different steps of the calculations will not be presented in details here. See (Hansen, 2008) concerning the calculation steps.

The easiest way to understand the foundations of BEM theory formulations is to focus on a 1D model for an ideal rotor. The WT will extract mechanical energy from the kinetic of the wind by creating a force pointing upstream and called thrust. This force is caused by a pressure drop Δp over the rotor and will reduced the wind speed from V_0 – speed far upstream - to u – at the rotor plane – and to u_1 – in the wake (Hansen, 2008), (Gao, et al., 2014). This is illustrated in Figure 2.12 in and equation [23] .

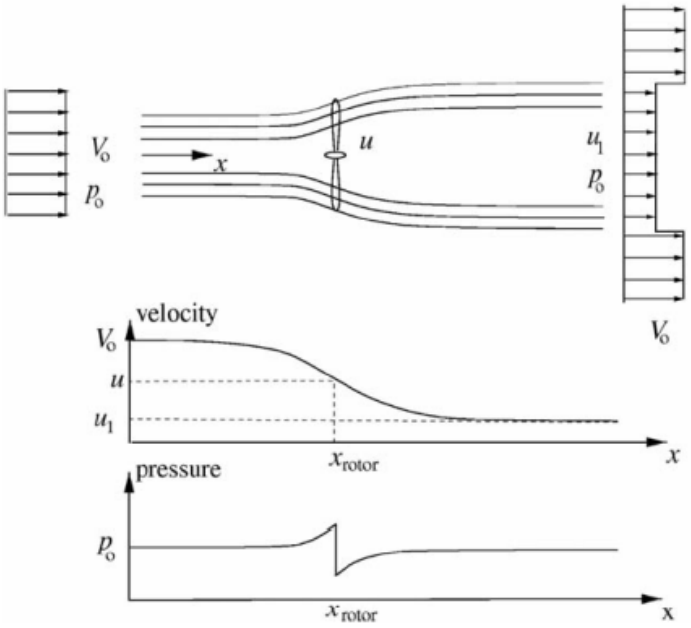

Figure 2.12: Streamlines past the rotor and the axial velocity and pressure up and downstream of the rotor (Hansen, 2008)

$$T = \Delta p A \quad \textbf{[23]}$$

With: $A = \pi R^2$, *the area of the rotor*

By applying Bernoulli equation far upstream and at the rotor plane and far in the wake and at the rotor plane it is possible to express the pressure drop as shown in equation [24]. See (Hansen, 2008) concerning the calculation steps.

$$\Delta p = \frac{1}{2}\rho_a (V_0^2 - u_1^2) \quad \textbf{[24]}$$

Moreover, by combining the momentum equation, the conservation of mass and the axial induction factor a (See definition in equation [25]) we can obtain equation [26] for the thrust.

$$u = (1 - a)V_0 \quad \textbf{[25]}$$

$$T = 2\rho_a V_0^2 a(1 - a)A \quad \textbf{[26]}$$

By extending the results obtained in 1D taking into account the number of blades B, it is possible to derive a formula for the thrust valid for the 3D control volume, see equation [27].

$$dT = \frac{1}{2}\rho_a B \frac{V_0^2 a(1 - a)^2}{\sin^2 \phi} c C_n dr \quad \textbf{[27]}$$

With: ϕ: *Flow angle*

C_n : *Normal load coefficient*

c: *Chord*

Using a similar methodology, the formula for the torque can be also derived for the 3D control volume as per equation [28].

$$dM = \frac{1}{2}\rho_a B \frac{V_0 a(1 - a) w r (1 + a')}{\sin\phi \cos\phi} c C_t r dr \quad \textbf{[28]}$$

With: w: *Induced velocity*

C_t: *Tangential load coefficient*

a': *Tangential induction factor*

Now all the necessary equations are known. So, first the axial and tangential induction factor are determined for each strip of the control volume using the algorithm summarized in Figure 2.13. Once their values satisfy the convergence requirements, the thrust and torque can be calculated using equations [27] and [28].

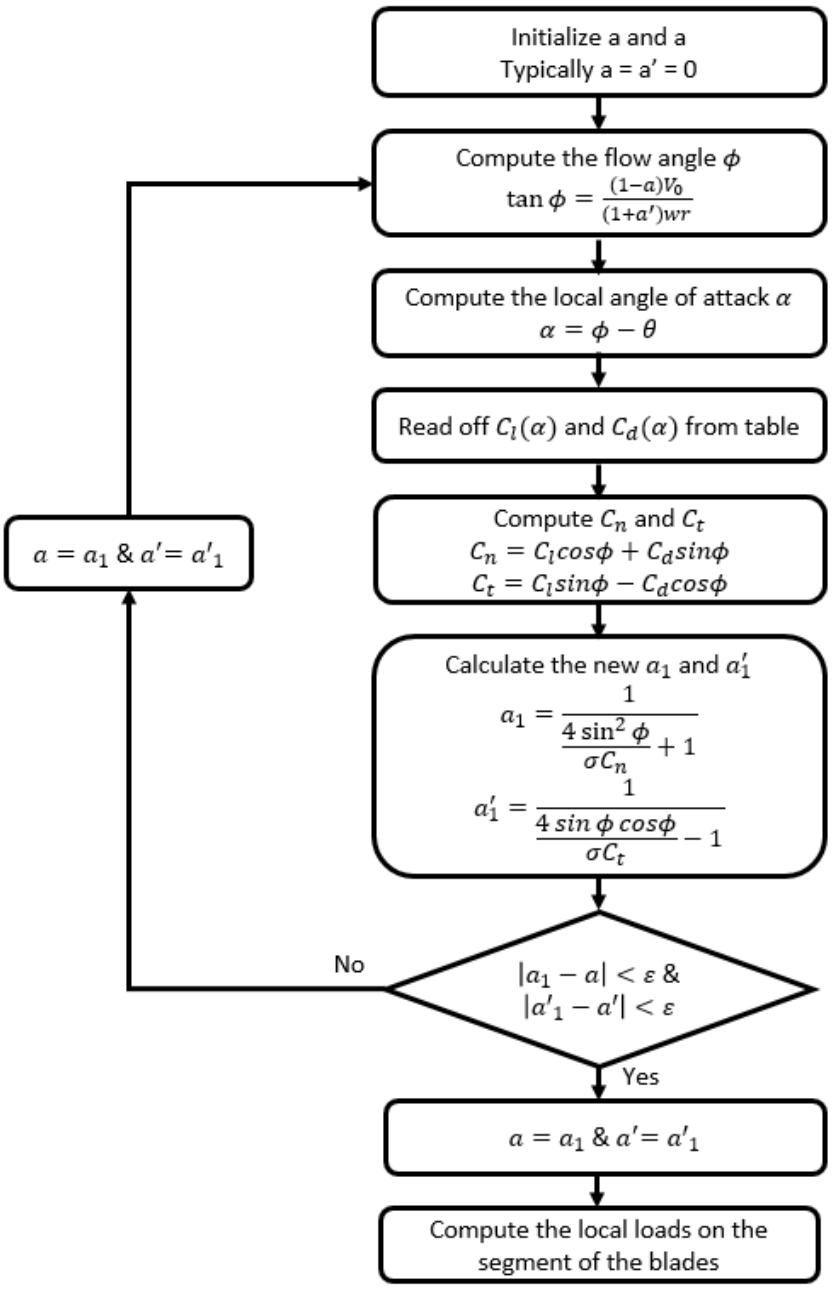

Figure 2.13: Flow chart of the BEM calculations process

With: a: *Axial induction factor (tower radius)*

a': *Tangential induction factor*

V_0: *Wind speed*

w: *Induced velocity*

r: *Radius*

ϕ: *Flow angle*

α: *Local angle of attack*

θ: *Local pitch of the blade*

$C_l(\alpha)$: *Lift coefficient*

$C_d(\alpha)$: *Drag coefficient*

C_n *: Normal load coefficient*

C_t *: Tangential load coefficient*

However, to get good results some corrections need to be implemented and in HAWC2 the classic BEM approach has been extended to handle dynamic inflow, dynamic stall, skew inflow, shear effects on the induction and effects from large deflections (Gao, et al., 2014), (Hansen, 2008):

- The dynamic inflow model will take into account the time delay between the induced velocities attain the equilibrium. This time lag is due to vorticity being shed and convected downstream.
- The dynamic stall model will compensate the fact that the angle of attack will change in time but those change will not be instantaneous and will modify the lift and drag coefficients.
- Finally, a correction should be applied to mitigate the fact that when the axial induction factor becomes greater than 0.4 the simple momentum theory is no longer valid.

The different models applied in the present model will be detailed in later sections (See 3.4).

3. Dynamic analysis implementation using HAWC2

3.1. Wind turbine model

The Offshore Code Comparison Collaboration (OC3) for IEA Task 23 was implemented to test different simulations tools developed by universities, industries and research institutions and ensure their capacity to predict coupled dynamic loads and responses in the case of the different offshore wind turbine types. It is a useful exercise as it helps to work on deficiencies in implemented models and works towards a better accuracy and efficiency of the different codes. The project was thus divided in different phases aiming at testing different types of wind turbines (Jonkman, 2010), (Jonkman, et al., 2010):

- In Phase I, the NREL offshore 5-MW wind turbine was installed on a monopile with a rigid foundation in 20 m of water.
- In Phase II, the foundation of the monopile from Phase I was made flexible by applying different models to represent the soil-pile interactions.
- In Phase III, the water depth was changed to 45 m and the monopile was replaced with a tripod substructure, which is one of the common space-frame concepts proposed for offshore installations in water of intermediate depth
- In Phase IV, the wind turbine was installed on a floating spar-buoy in deep water (320 m).

The model exploited here is taken from HAWC2 website (http://www.hawc2.dk) and corresponds to Phase IV – Floating spar buoy described in OC3 i.e. NREL offshore 5-MW wind turbine is installed on a floating spar-buoy in deep water (320 m). The NREL 5 MW model is an upwind, variable-speed, collective pitch controlled horizontal axis wind turbine (HAWT). See Figure 3.1 below.

Figure 3.1: Phase IV – Floating spar buoy described in the Offshore Code Comparison Collaboration (OC3) for IEA Task 23. In the model Phase IV – Floating spar buoy, NREL offshore 5-MW wind turbine is installed on a floating spar-buoy in deep water (320 m) (from http://www.hawc2.dk)

The model used is derived from *Hywind* developed by Statoil. This particular model was chosen because the shape of the structure is easy to model and a real full scale prototype has been constructed which allows to compare simulation results to field measurements. The model applied in simulations has been slightly modified to adapt to the NREL 5 MW wind turbine which was used throughout all the phases of OC3 but is not the one originally employed by Statoil on the actual wind turbine.

The different characteristics of the model and assumptions applied in phase IV can be found in (Jonkman, 2010) and (Jonkman, et al., 2010), for example, and the main properties of the spar wind turbine are presented in Table 3.1 and Table 3.2 below.

The following section describes the resolution method applied and how different parameters influences are going to be tested.

Table 3.1: Summary of OC3-Hywind spar properties (Jonkman, et al., 2010)

Parameter	Value
Depth to Platform Base Below SWL (Total Draft)	120 m
Elevation to Platform Top (Tower Base) Above SWL	10 m
Depth to Top of Taper Below SWL	4 m
Depth to Bottom of Taper Below SWL	12 m
Platform Diameter Above Taper	6.5 m
Platform Diameter Below Taper	9.4 m
Platform Mass, Including Ballast	7,466,330 kg
CM Location Below SWL Along Platform Centerline	89.9155 m
Platform Roll Inertia about CM	4,229,230,000 kg•m2
Platform Pitch Inertia about CM	4,229,230,000 kg•m2
Platform Yaw Inertia about Platform Centerline	164,230,000 kg•m2
Number of Mooring Lines	3
Angle Between Adjacent Lines	120º
Depth to Anchors Below SWL (Water Depth)	320 m
Depth to Fairleads Below SWL	70.0 m
Radius to Anchors from Platform Centerline	853.87 m
Radius to Fairleads from Platform Centerline	5.2 m
Unstretched Mooring Line Length	902.2 m
Mooring Line Diameter	0.09 m
Equivalent Mooring Line Mass Density	77.7066 kg/m
Equivalent Mooring Line Weight in Water	698.094 N/m
Equivalent Mooring Line Extensional Stiffness	384,243,000 N
Additional Yaw Spring Stiffness	98,340,000 Nm/rad

Table 3.2: Summary of properties for the NREL 5-MW baseline wind turbine (Jonkman, et al., 2010)

Parameter	Value
Rating	5 MW
Rotor orientation, configuration	Upwind, 3 blades
Control	Variable speed, collective pitch
Drivetrain	High speed, multiple-stage gearbox
Rotor, hub diameter	126 m, 3 m
Hub height	90 m
Cut-in, rated, cut-out wind speed	3 m/s, 11.4 m/s, 25 m/s
Cut-in, rated rotor speed	6.9 rpm, 12.1 rpm
Rated tip speed	80 m/s
Overhang, shaft tilt, precone	5 m, 5º, 2.5º
Rotor mass	110,000 kg
Nacelle mass	240,000 kg
Tower mass	347,500 kg
Coordinate location of overall center of mass (CM)	(-0.2 m, 0.0 m, 64.0 m)

3.2. Wind turbine dynamic

The equation of rigid-body motion of the structure can be written as (Gao, et al., 2014):

$$-w^2(M + A(w))\eta + iwB(w)\eta + C(w)\eta = F(w) \quad \textbf{[29]}$$

Where $M, A, B\ and\ C$ are the mass, added mass, linear damping and hydrostatic restoring force matrices. This equation is commonly rewritten by defining the following terms (Gao, et al., 2014):

$$\begin{cases} A(w) = a(w) + A_\infty \\ B(w) = b(w) + B_\infty = b(w) \\ K(w) = iwa(w) + b(w) \end{cases} \quad \textbf{[30]}$$

By introducing in equation [29] the terms presented in equation [30] and using an inverse Fourier transform, equation [29] can be expressed in the time domain as follows:

$$(M + A_\infty)\ddot{\eta}(t) + \int_{-\infty}^{+\infty} k(t-\tau)\,\dot{\eta}(\tau)d\tau + C\eta(t) = F(t) \quad \textbf{[31]}$$

The second term in equation [31] is a convolution integral and k is the retardation function that depicts the memory effects triggered by the free surface. However, "*linear hydrodynamic damping is not included because in ice covered water the ice load is considered to be the most major source of energy consumption*" (i.e. $B = 0$) (Tan, et al., 2013). The convolution integral is also null in this configuration and the added mass matrix is not considered frequency-dependent. For the study cases presented here, it can be justified by the fact that we consider long waves and their influence on the structure can be neglected compared to the ice loads. Indeed, 2 velocity components are needed to generate waves and here, due to the ice cover, the vertical velocity can be considered null. And, the damping matrix values are linked to the square power of the amplitude of the radiated waves which are null for $w \to 0$ (Faltinsen, 1990), (Greco, 2012). So B can be selected null. Moreover, due to finite water depth and 3D effects, the added mass terms will also be finite for $w \to 0$ (Faltinsen, 1990), (Greco, 2012). So, for a structure that present a plane of symmetry and with its center of gravity located at $(0,0,z_G)$ in its mean

oscillatory position, the equation of motion of the structure can be simplified as (Faltinsen, 1990):

$$(M + A)\ddot{\eta}(t) + B\dot{\eta}(t) + C\eta(t) = F(t) \quad [32]$$

Where $M, A\ and\ C$ can be written as (Faltinsen, 1990):

$$M = \begin{bmatrix} M & 0 & 0 & 0 & Mz_G & 0 \\ 0 & M & 0 & -Mz_G & 0 & 0 \\ 0 & 0 & M & 0 & 0 & 0 \\ 0 & -Mz_G & 0 & I_4 & 0 & -I_{46} \\ Mz_G & 0 & 0 & 0 & I_5 & 0 \\ 0 & 0 & 0 & -I_{46} & 0 & I_6 \end{bmatrix} \quad [33]$$

$$A = \begin{bmatrix} A_{11} & 0 & A_{13} & 0 & A_{15} & 0 \\ 0 & A_{22} & 0 & A_{24} & 0 & A_{26} \\ A_{31} & 0 & A_{33} & 0 & A_{35} & 0 \\ 0 & A_{42} & 0 & A_{44} & 0 & A_{46} \\ A_{51} & 0 & A_{53} & 0 & A_{55} & 0 \\ 0 & A_{62} & 0 & A_{64} & 0 & A_{66} \end{bmatrix} \quad [34]$$

$$C = \begin{bmatrix} 0 & 0 & 0 & 0 & 0 & 0 \\ 0 & 0 & 0 & 0 & 0 & 0 \\ 0 & 0 & C_{33} & 0 & C_{35} & 0 \\ 0 & 0 & 0 & C_{44} & 0 & 0 \\ 0 & 0 & C_{53} & 0 & C_{55} & 0 \\ 0 & 0 & 0 & 0 & 0 & 0 \end{bmatrix} \quad [35]$$

And, the acceleration, velocity and position vectors are written as follows:

$$\begin{cases} \ddot{\eta} = [\ddot{\eta}_1, \ddot{\eta}_2, \ddot{\eta}_3, \ddot{\eta}_4, \ddot{\eta}_5, \ddot{\eta}_6] \\ \dot{\eta} = [\dot{\eta}_1, \dot{\eta}_2, \dot{\eta}_3, \dot{\eta}_4, \dot{\eta}_5, \dot{\eta}_6] \\ \eta = [\eta_1, \eta_2, \eta_3, \eta_4, \eta_5, \eta_6] \end{cases} \quad [36]$$

They denoted, per order of notation, the surge, sway, heave, roll, pitch and yaw motions. $F(t)$ is the excitation force and moment vector. As pointed out previously, it should include the following loads:

- Aerodynamics loads;
- Hydrodynamic loads;
- Hydrodynamic loads on mooring lines;

- Ice loads.

The loads implementation will be presented case by case in the next sections. FEM modelling is then used in HAWC2 to determine the deformations of the wind turbine and the floater.

In HAWC2, the resolution of equation [32] is based on Newmark method, a numerical integration method to solve differential equation widely used in numerical evaluation of the dynamic response of structures and solids. It is a step-by-step time integration method and the assumption taken regarding the acceleration between t_i and t_{i+1} is that the acceleration varies linearly between each time step:

$$\ddot{\eta}_{k+1} = \ddot{\eta}_k + (\ddot{\eta}_{k+1} - \ddot{\eta}_k)\gamma \quad \textbf{[37]}$$

The parameters β and γ are fixed as the default ones and ensure unconditional stability of the method. Indeed, the method is unconditionally stable if (Langen, et al., 1977):

$$\begin{cases} \gamma \geq \frac{1}{2} \ (\gamma = 0.51 \ here) \\ \beta \geq \frac{1}{4}\left(\gamma + \frac{1}{2}\right)^2 = 0.255025 \ (\beta = 0.27 \ here) \end{cases} \quad \textbf{[38]}$$

The method is based on the following integral equation for the velocity and the displacement in the $(k+1)^{th}$ time step (Langen, et al., 1977), (Tan, et al., 2013):

$$\dot{\eta}_{k+1} = \dot{\eta}_k + h[\gamma\ddot{\eta}_{k+1} + (1-\gamma)\ddot{\eta}_k] \quad \textbf{[39]}$$

$$\eta_{k+1} = \eta_k + \dot{\eta}_k h + \frac{1}{2}h^2[2\beta\ddot{\eta}_{k+1} + (1-2\beta)\ddot{\eta}_k] \quad \textbf{[40]}$$

With *h* the time step length.

At each time step, the dynamic equilibrium [32] should be satisfied so:

$$(M + A)\ddot{\eta}_{k+1} + B\dot{\eta}_{k+1} + C\eta_{k+1} = F_{k+1} \quad \textbf{[41]}$$

Using equation [40], we can then derive the incremental displacement:

$$\Delta\eta_{k+1} = \dot{\eta}_k h + \frac{1}{2}h^2(1-2\beta)\ddot{\eta}_k + (M+A)^{-1}(F_{k+1} - C\eta_{k+1})2h^2\beta \quad [42]$$

And, the variables can now be updated and used as initial values for the next time step iteration:

$$\ddot{\eta}_{k+1} = \frac{1}{h^2\beta}\left[\Delta\eta_{k+1} - \dot{\eta}_k h - \frac{1}{2}h^2(1-2\beta)\ddot{\eta}_k\right] \quad [43]$$

$$\dot{\eta}_{k+1} = \dot{\eta}_k + \Delta\dot{\eta}_{k+1} \quad [44]$$

$$\eta_{k+1} = \eta_k + \Delta\eta_{k+1} \quad [45]$$

3.3. Ice loads model

HAWC2 is not fitted with an ice loads calculations method. However, it is possible to take them into account by including a DLL. The ice characteristics utilized for the model correspond to the ice conditions encountered in the Baltic Sea (ISO/FDIS19906, 2010). The main parameters values are summarized in Table 3.3 below:

Table 3.3: Ice characteristics utilized in the model (ISO/FDIS19906, 2010)

Parameter	Value
Density [kg.m^{-3}]	880
Crushing strength [MPa]	2.3
Bending strength [kPa]	580
Young modulus [GPa]	5.4
Poisson's ratio	0.33
Coefficient of friction	0.05

The DLL file algorithm is based on the work presented in (Tan, et al., 2013). In this DLL, the ice breaking forces are calculated by integrating the contact forces over the icebreaking waterline. The problem should be studied in time domain given the non-simultaneous failure of the ice around the structure. The numerical procedure to estimate the ice loads can be divided into 6 main steps:

1/ Definition of geometries:

The ice conditions i.e. the ice edge geometry are initialized. Moreover, the rigid body boundary conditions for the ice edge are defined by the wind turbine surface around the waterline. In the definition of this surface, the variations due to the 6 DOFs motions of the wind turbines are taken into account to define the waterline geometry of the wind

turbine. This result is obtained by looking for intersection between the wind turbine surface and the waterplane at each time step.

2/ Contact detection:

The geometries of the ice edge and the wind turbine waterline are now known. So, the algorithm is then looking for overlap between them to determine if there is a contact and where. This procedure is illustrated in Figure 3.2 (local coordinates are depicted there).

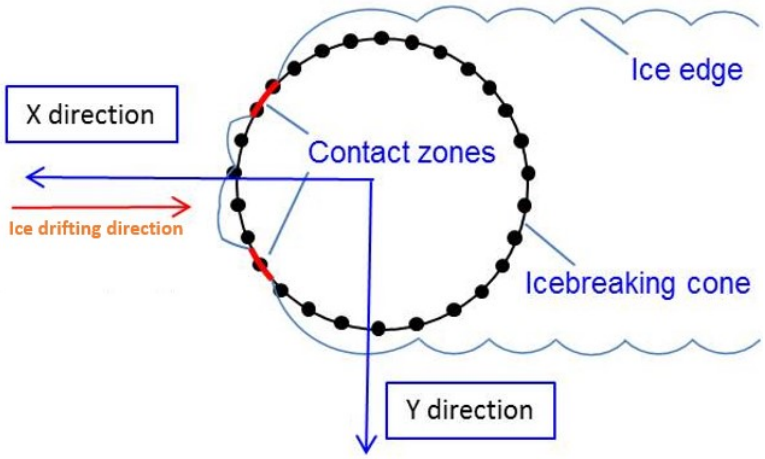

Figure 3.2: Illustration of the contact detection procedure between a wind turbine and ice edge at the waterline

The contact area A_{cr} is then calculated for each contact zone by considering two types of contact interface, see Figure 3.3. For each contact interface type, the contact area is calculated based on the contact length L_h, the indentation length L_d and the frame angle φ as per equation [46] below:

$$A_{cr} = \begin{cases} \frac{1}{2} L_h \frac{L_d}{\cos\varphi}, & L_d \tan\varphi \le h_i \ (type\ I) \\ \frac{1}{2}\left(L_h + L_h \frac{L_d - \frac{h_i}{\tan\varphi}}{L_d} \right) * \frac{h_i}{\sin\varphi}, & L_d \tan\varphi > h_i \ \ (type\ II) \end{cases} \quad \textbf{[46]}$$

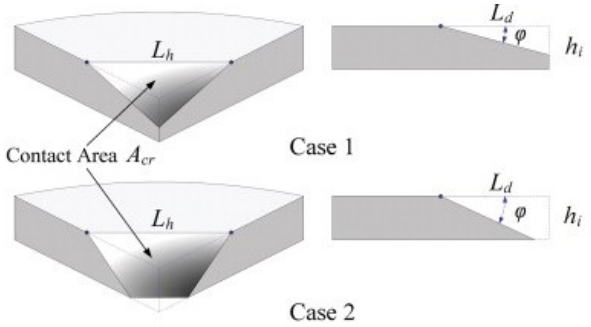

Figure 3.3: Idealized contact interferences (Tan, et al., 2013)

3/ Determination of local crushing force:

Once this contact area determined, it is possible to calculate the local crushing force resulting from the ice-structure interaction. In (Tan, et al., 2013), the model applied to calculate the local crushing force is the one proposed by (Riska, 1995) based on the concept of average contact pressure:

$$F_{cr} = p_{av} A_{cr} \quad [47]$$

With: p_{av}**:** *Average contact pressure*

A_{cr}**:** *Contact area*

p_{av} depends on several parameters such as the ice properties or the temperature but more importantly on the contact area magnitude and this dependency – known as (*p-a*) curve- exhibits a power law:

$$p_{av} = k A_{cr}^{n} \quad [48]$$

With *k* and *n* empirical parameters.

4/ Determination of contact forces:

Knowing the local crushing forces, it is then possible to derive an expression for the contact forces. The contact loads are finally obtained by integrating the local forces over all the contact zones.

5/ Bending failure criterion:

From crushing and friction action, a vertical force will be acting on the ice edge. This force will be increasing till it exceeds the bearing capacity of the ice edge P_f leading to bending failure. Here, the bending failure criterion applied is a dynamic bending failure criterion developed from finite element calculations and curve fitting. Additionally, we assume that once the ice is broken it is washed away from the structure before the next contact event occurrence.

6/ Ice breaking pattern determination:

As explained in 2.1, when ice breaks radial and circumferential cracks appear. In the present numerical procedure the bending crack is idealized as a circular arc. Based on this

assumption, the size of the broken ice flow can be estimated. This calculation involves the concept of characteristic breaking length, mentioned in 2.2. Here, the characteristic breaking length is derived based on static theory for an elastic plate. Based on the size of the broken ice flow, the new ice edge geometry can be known and it can be updated for the next time step. An example of simulated icebreaking pattern can be seen in Figure 3.4 below (the axis conventions used here are the same as the one used in the HAWC2):

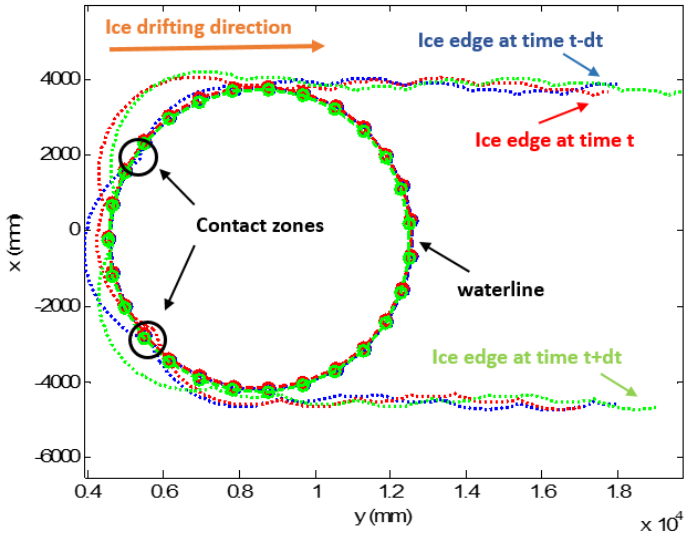

Figure 3.4: Example of simulated icebreaking pattern between a WT and ice edge

The code developed by Xiang Tan is calibrated based on full scale measurements for a particular ship and the original code is developed for ice-ship interaction. However, the bending failure phenomenon is quite similar to the ice-structure failure for wind turbine. So it is also applicable to our case. See (Tan, et al., 2013) and (Su, et al., 2011) for more details concerning the calculation process.

The coordinates system utilized in this study is illustrated in Figure 3.5 as per the main dimensions of the floater part where the ice loads will act. It is not represented on the following figure but the structure is fitted with a 45º inverted ice-breaking cone with a width at the waterline of 8m. This cone is considered as a rigid body.

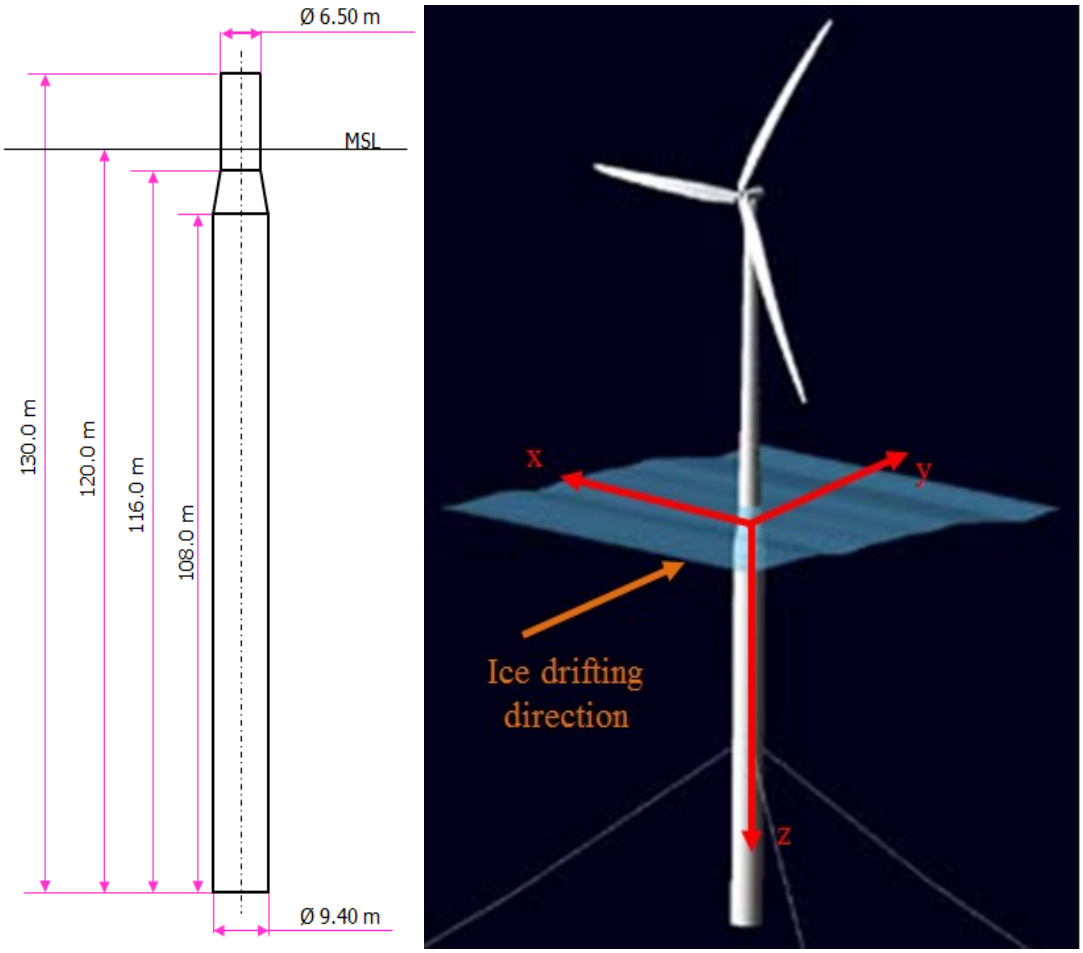

Figure 3.5: Coordinates system used and main dimensions of the floater

The dimensions of the cone geometry are not detailed more as the constant frame angle and the waterline width are sufficient inputs for the various calculations. However, it should be noted that the cone was designed by Wei Shi in a previous study and the cone size was chosen according to the diameter, frame angle, and model test from (Barker, et al., 2005) and (Gravesen, et al., 2005). These dimensions are summarized in Table 3.4.

Table 3.4: Cone dimensions based on (Barker, et al., 2005) and (Gravesen, et al., 2005) model tests

Parameter	Value
Cone angle	45°
Volume	225.344 m^3
Mass	540 825.175 kg
Center of gravity	Z_g=1.907 m

It should be noted that the axis used in the Fortran code and the ones used in HAWC2 are different. So, to use the DLL in HAWC2 a decomposition and transformation of the loads obtained should be performed as follows (also illustrated in Figure 3.6):

$$\begin{cases} F(1) = -Fcrbrk(2) \\ F(2) = -Fcrbrk(1) \\ F(3) = -Fcrbrk(3) \\ M(1) = -Fcrbrk(5) \\ M(2) = -Fcrbrk(4) \\ M(3) = -Fcrbrk(6) \end{cases} \quad [49]$$

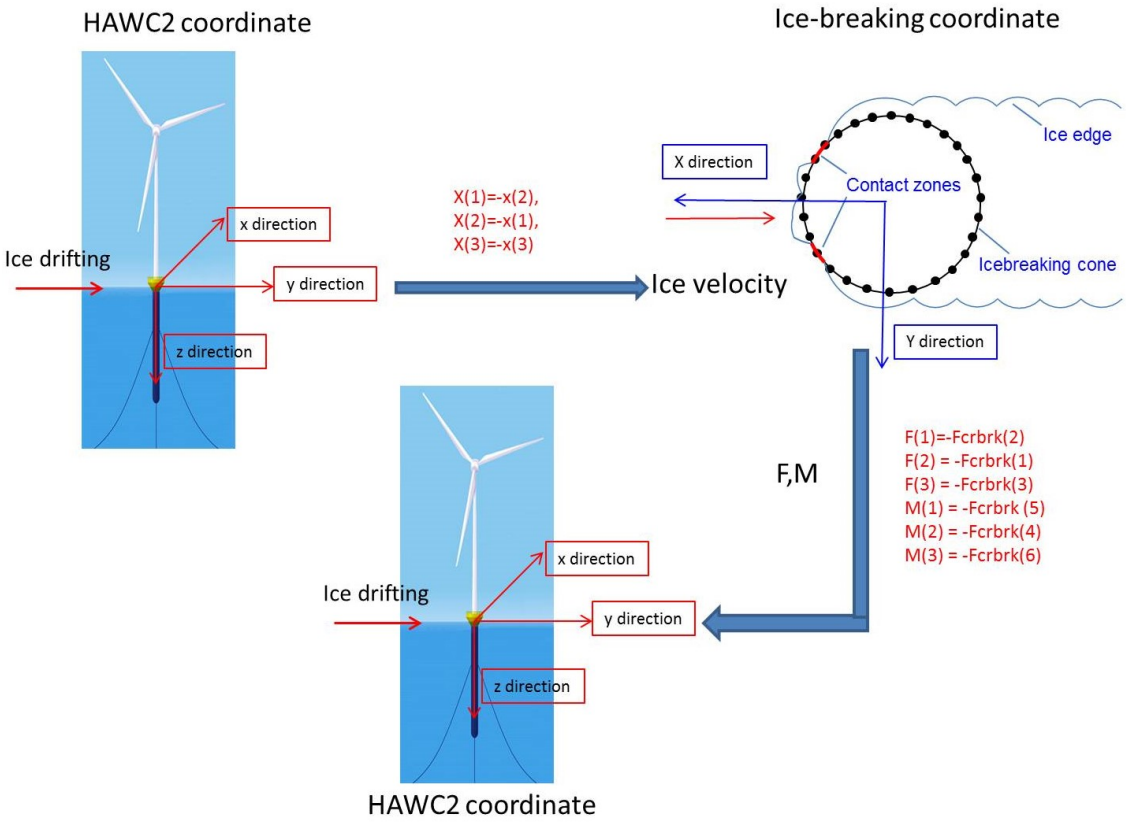

Figure 3.6: Representation of the different axis conventions used in this work

3.4. Aero-hydro-servo-elastic model

The software exploited to run the analysis is HAWC2. As explained in (Larsen, et al., 2007):

"It is an aeroleastic code intended for calculating wind turbine response in time domain and has a structural formulation based on multi-body dynamics. It has been developed within the years 2003-2006 at the aeroelastic design research programme at Risoe, National laboratory Denmark.

The structural part of the code is based on a multibody formulation where each body is an assembly of timoshenko beam elements. The formulation is general which means that quite complex structures can be handled and arbitrary large rotations of the bodies can

be handled. The turbine is modeled by an assembly of bodies connected with constraint equations, where a constraint could be a rigid coupling, a bearing, a prescribed fixed bearing angle etc. The aerodynamic part of the code is based on the blade element momentum theory, but extended from the classic approach to handle dynamic inflow, dynamic stall, skew inflow, shear effects on the induction and effects from large deflections. Several turbulence formats can be used. Control of the turbine is performed through one or more DLL's (Dynamic Link Library). The format for these DLL's is also very general, which means that any possible output sensor normally used for data file output can also be used as a sensor to the DLL. This allows the same DLL format to be used whether a control of a bearing angle, an external force or moment is placed on the structure."

So it is possible to directly run the aerodynamic problem using the features of the software. However, the ice loads have to be implemented through an additional DLL file that will be called in the HAWC2 input file. This way, at each time step, the ice loads are going to be estimated by referring to the DLL file and applied on the structure.
The HAWC2 input file (*.htc*) is divided in different sections defining the structure, assumptions, loads and calculations methods applied. The process is summarized in Figure 3.7 which presents an example of floating energy device modeled in HAWC2:

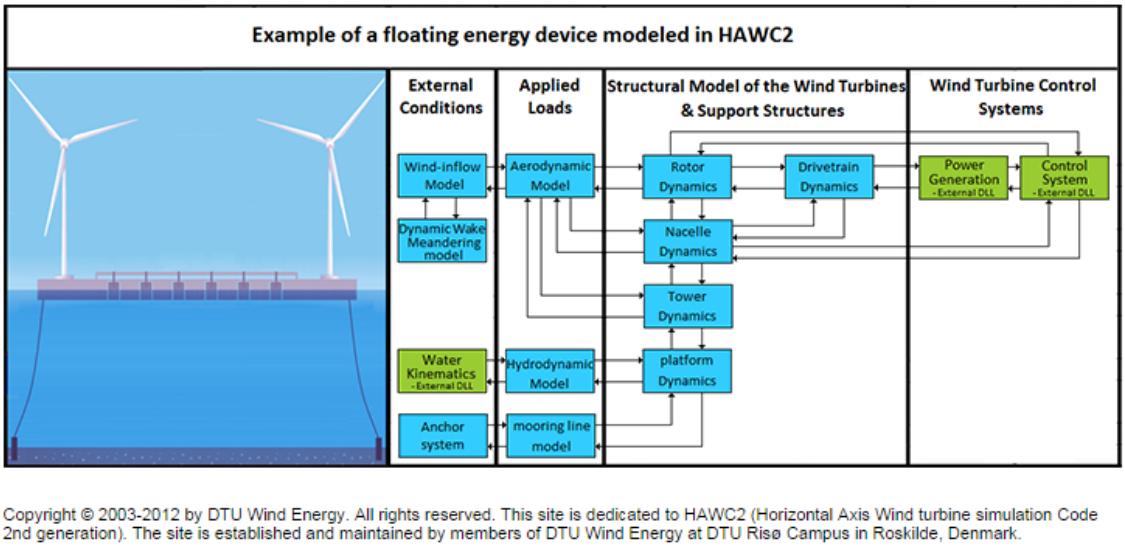

Figure 3.7: Example of floating energy device modeled in HAWC2 (from http://www.hawc2.dk)

The control feature of the wind turbine i.e. the turbine speed and pitch are described using a DLL file. This topic will only be shortly treated in the present paper.

3.4.1. Simulation

The main characteristics of the simulation are selected there as, for example, the type of solver used, the simulation length or convergence criterions to apply. The main parameters of interest here are:

- Simulation length (*time_stop*) is chosen around 3000s with no wind and 1500s with wind to have sufficient damping of the transient state. The results presented respectively do not take into account the first 1600s and the first 900s where strong transient state can be observed and the ice loads ramp force is applied;
- Time increment (*deltat*) should be set equal to the one employed in the ice loads calculation algorithm (here respectively 0.001s and 0.0005s);
- The solver is based on Newmark method, a numerical integration method to solve differential equation widely used in numerical evaluation of the dynamic response of structures and solids. The parameters are fixed as the default ones and should ensure stability of the method;
- To obtain convergence, the convergence limits that must be obtained at every time step are set in HAWC2 as follows:
    - *epsresq*, residual on internal-external forces =5000
    - *epsresd*, residual on increment = 1.0
    - *epsresg*, residual on constraint equations = 1E-7 %

They have been selected upon recommendations from the software developers in DTU for cases involving floating structures.

3.4.2. Structural input

The structure is defined as multibody where each body is an assembly of timoshenko beam elements. The bodies are here assumed rigid but a flexible configuration can be implemented with HAWC2 code. The different bodies are defined along with their relative orientation and the constraints linking them. Various modeling features are moreover available such as bearing or joints to obtain a complete WT model.

3.4.3. Aerodynamics

As explained in (Larsen, et al., 2007), "*The aerodynamic part of the code is based on the blade element momentum theory, but extended from the classic approach to handle dynamic inflow, dynamic stall, skew inflow, shear effects on the induction and effects from large deflections. Several turbulence formats can be used. This module set up parameters for the aerodynamic specification of the rotor. It is also possible to submit aerodynamic forces to other structures as example the tower or nacelle*".

We can note that in the present case:

- Prandtl tip-loss model is applied to correct the assumption of an infinite number of blades from BEM theory and allows computing a rotor with a finite number of blades. It will thus lead to a correction of the vortex system in the wake –different for an infinite and a finite number of blades (Hansen, 2008);
- MHH Beddoes method as dynamic stall model. This model takes into account attached flow, leading edge separation and compressibility effects, and also corrects the drag and moments coefficients (Hansen, 2008).

The dynamic inflow model takes into account the time delay between the induced velocities attain the equilibrium. This time lag is due to vorticity being shed and convected downstream. Finally, a correction should be applied to mitigate the fact that when the axial induction factor becomes greater than 0.4 the simple momentum theory is no longer valid (Hansen, 2008).

The software can simulate constant wind but also turbulence. It can be noted that, in the present case, the tower shadow is modelled using a potential flow model. And, in this model the shadow source is moved and rotated in space as the tower coordinate system is moving and rotating. As explained in (Karimirad, 2013), this is not the case in all codes. Indeed, in FAST the tower shadow is considered fixed at the mean position of the structure. And those differences in the implementation of the tower shadow can be of significance when considering a floating wind turbine with a tower moving in space, as it is the case here.

As explained in (Larsen, et al., 2007), "*with this module it is possible to apply aerodynamic drag forces at a given number of structures*." However, the aerodynamic drag was no taken into account in the OC3 project so we will not take it into account here.

Finally, the control feature of the wind turbine i.e. the turbine speed and pitch are described using a DLL file. As explained in (Jonkman, 2010) and (Karimirad, 2013), the control system constituted of a conventional variable-speed generator-torque and PI collective blade-pitch controllers for the NREL 5MW wind turbine tuned to avoid the potential for negative damping occurring with this type of systems and would trigger large resonant motions. The control strategy implemented can then be divided in 3 distinctive zones represented in Figure 3.8 (Karimirad, 2013), (Gao, et al., 2014):

- At below rated speeds: the generator torque is controlled to maintain the turbine at the maximum possible efficiency by increasing the rotor speed for increasing wind speed;
- At above rated speeds: the blades are feathered by the control system to always maintain a constant power output and reduce the loads on the wind turbine;
- Around the rated power: the controller will either behave as in the below or the above rated speeds zone. It will be determined by the relative wind velocity.

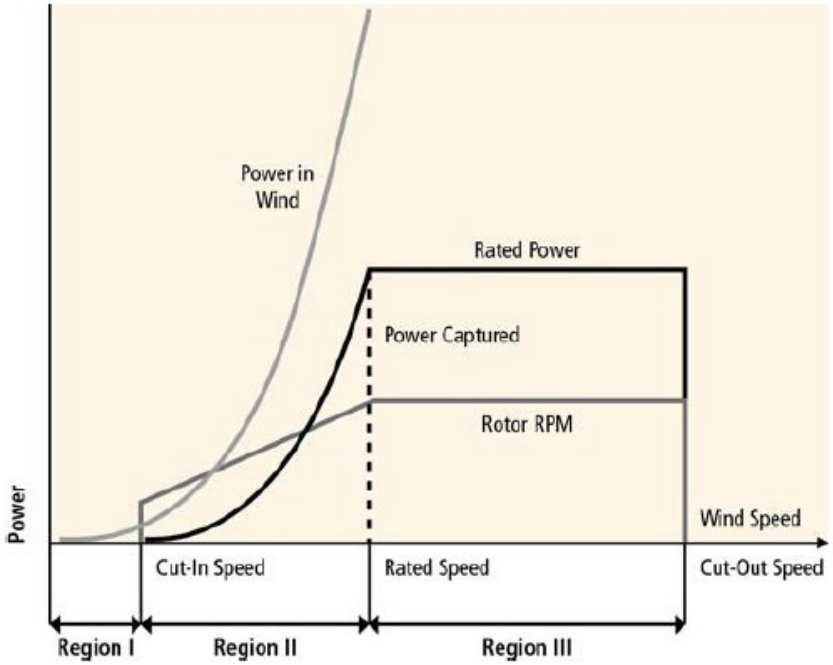

Figure 3.8: Conceptual power curve of a variable-speed pitch-regulated wind turbine (Gao, et al., 2014)

3.4.4. Hydrodynamics

The hydrodynamic loads calculations are based on the pressure integration method coupled to the Morison's equation (Faltinsen, 1990):

$$dF = \frac{1}{2}\rho C_D D dz (u - \dot{\eta}_1)|u - \dot{\eta}_1| \quad [50]$$

With: ρ = *density of sea water*

D= *Cylinder diameter*

C_D= *viscous coefficient on the specific direction that has projected area* Ddz

u = *Undisturbed fluid velocity*

$\dot{\eta}_1$ = *Velocity of the body*

It gives a simplified formula of the wave loads when viscous effects matter. Moreover, it is adapted to slender structures. Such structures have small dimensions compared to the wavelength.

The water kinematic is implemented using external DLLs. Current influence will be taken into account as it will play a role in the prediction of ice movement and pressure (ISO/FDIS19906, 2010) [A.6.4.3 p136]. HAWC2 can also simulate different type of waves:

- Linear airy waves ;
- Irregular airy waves: Directional spreading, Jonswap's spectrum;
- Deterministic irregular airy waves;
- Wheeler stretching for load application points.

However, we will consider that there is no wave in the case of an ice-covered sea. This decision is not following the recommendation of (ISO/FDIS19906, 2010) [A.6.4.1 p134]. Indeed, even if the loads due to wave are significantly reduced in presence of ice conditions, they still have to be considered using theoretical models for wave attenuation in ice covered seas. However, this work aim is to provide a first model to compare ice loads and aerodynamics loads. So, for the sake of simplicity and clear comparison, wave loads will not be included in the present analysis. It can however be justified by the fact that they are expected to be significantly less important than ice or aerodynamic loads.

3.4.5. Soil module

As explained in (Larsen, et al., 2007), the interaction between the bottom foundation and the soil is modelled with a set of spring-damper forces attached to a main body. The wind turbine is moored by a system of three catenary lines. The mooring lines tension is calculated using an additional DLL file and represented as external forces and moments transferred at each time step by the DLL (Karimirad, 2013). The calculations are made using a quasi-static approach. The development of the solution of the inelastic cable line (catenary) equations is presented, for example, in (Faltinsen, 1990) [Chapter 8]. For more details on the mooring system properties see (Jonkman, 2010).

3.5. Cases studied

In the present study, we are interested by the influence of the ice velocity and ice thickness in the ice-structure interaction. Here, we will study the coupled actions of ice and wind i.e. the ice/structure interactions are considered. So, contrary to the uncoupled analysis where the ice loads were imported directly as time-series data to the structure node using DLL, they are now calculated at each iteration. And the dynamic motions of the spar are taken into account. The results are obtained for a rigid model and not a flexible one. However, as explained in (Karimirad, et al., July 2012) a rigid model is accurate enough for a first study of the phenomenon:

"For floating wind turbines, the motions and structural responses, such as the nacelle surge motion and acceleration as well as the bending moment and shear force at the tower–substructure interface, are dominated by rigid body motions rather than elastic deformations (Karimirad, et al., 2009)*,* (Karimirad, et al., January 2012) *and* (Karimirad, et al., April 2011)*. Nacelle surge is the fore-aft displacement of the nacelle. However, the local responses of the rotor, such as the blade structural responses, are affected by the aero-elasticity. Hence, the rigid body formulation of floating wind turbines is accurate enough to be used in place of the multi-body elastic formulation to analyze the general motions and structural responses with an acceptable accuracy."*

In all the LCs comporting only ice, the wind turbine is under parked conditions. In the numerical model, the calculations are done for ice speed ranging from 0.3 m/s to 0.5 m/s and ice thicknesses from 0.1m to 0.8m (Baltic Sea ice thickness range suggested by ISO standards (ISO/FDIS19906, 2010)).

Different simulation configurations are applied and are described in the following paragraphs. Figure 3.9 below shows the flowchart of the numerical procedure developed in (Shi, et al., November 24-26, 2014) and applied here.

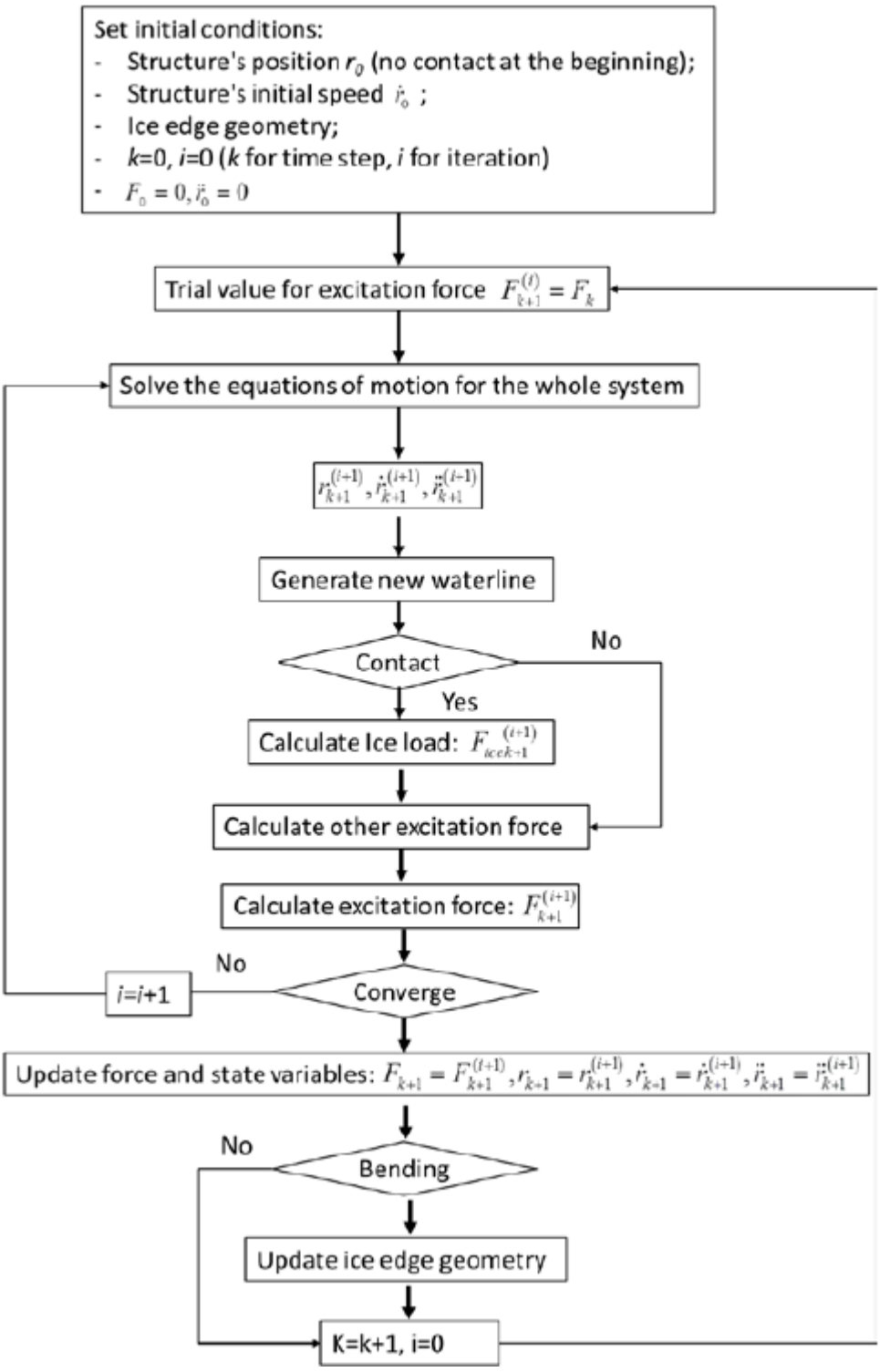

Figure 3.9: Flowchart of the numerical procedure (Shi, et al., November 24-26, 2014)

3.5.1. Only ice loads

In a first time, the only loads considered are the ice loads. The model applied simulates the ice sheet with a constant ice thickness and a constant ice drifting speed.

Numerical problems were encountered in previous attempts aiming at coupling the ice loads module to a global aerodynamic model of a floating wind turbine. To remedy to these problems, the ice loads introduced in the present work are selected based on an uncoupled analysis made in a previous study.

In this previous work, the ice loads were directly included in the model and taken into account in a decoupled analysis. Here, the ice loads are introduced as a ramp function as coupled loads and analyzing the results from the previous study the ramp duration and final value can be selected (1). The final value of the ramp is fixed as the mean value of the ice loads obtained in the decoupled analysis realized in a previous work. This way, the loads introduction is smoothed and the transient state is reduced in magnitude and time. Then, convergence can be attained in a reasonable time.

As we can see from Figure 3.10 and Figure 3.11, the mean fore-aft force obtained in the case of the uncoupled analysis are comprised in the range going from 0 to 120 kN. Moreover, they can vary quite a lot from one case to another so the ramp will have to be adjusted case by case to ensure convergence.

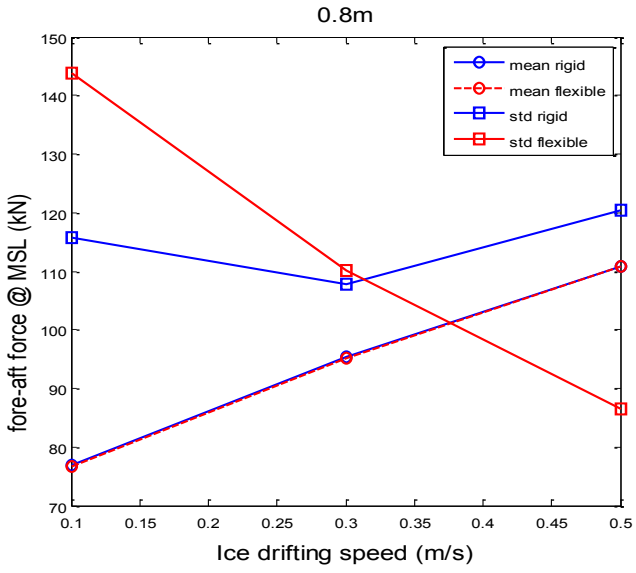

Figure 3.10: Statistical characteristics of the fore-aft force at the MSL with different ice speeds (uncoupled analysis)

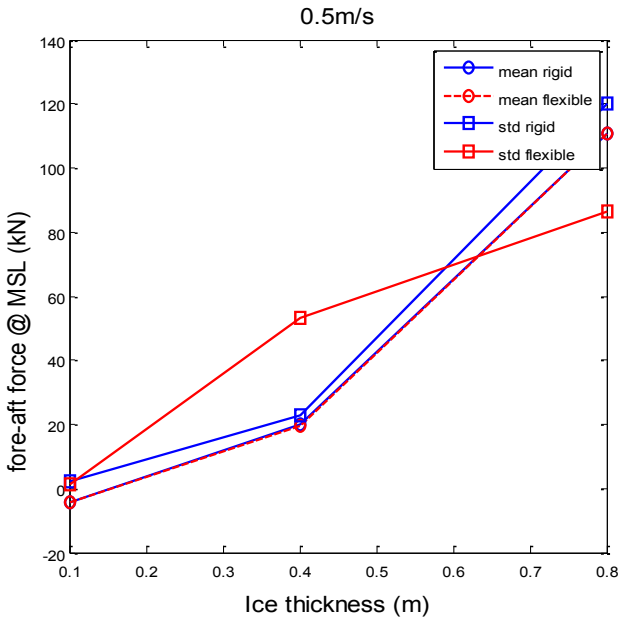

Figure 3.11: Statistical characteristics of fore-aft force at the MSL with different ice thicknesses (uncoupled analysis)

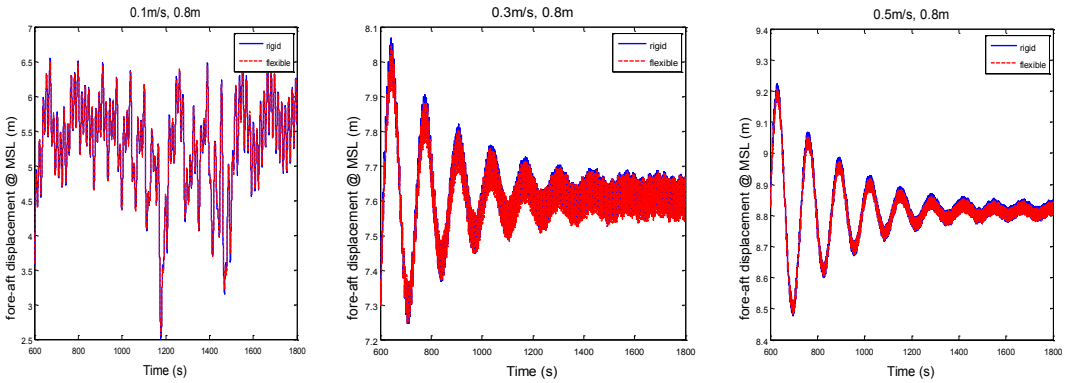

Figure 3.12: Time series of the fore-aft displacements at the MSL for with different ice speeds (uncoupled analysis)

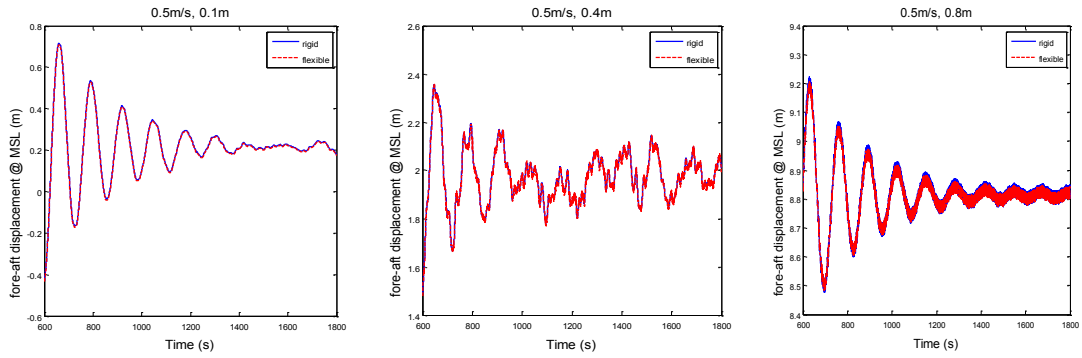

Figure 3.13: Time series of the fore-aft displacements at the MSL for with different ice thicknesses (uncoupled analysis)

In the uncoupled analysis study, the ramp function introducing the ice loads had a total duration of 150s. From Figure 3.12 and Figure 3.13, we can see that the transient time is quite important and the steady state is only reached around 1200s, in this case. So, in order to obtain convergence in the case of a coupled analysis, it has been decided that the

ramp function will be applied on an extended duration and the value selected was finally 1000s. This way, the transient state response will be reduced along with the oscillation amplitude before reaching the equilibrium position. And so, it will ensure a faster convergence of the solution.

In Figure 3.14, the piece of FORTRAN code concerned is presented. As we can see, for the time between 0 and 1000s, the fore-aft force and moment are enforced on the structure and their values are manually chosen. And the process is illustrated in Figure 3.15 where the case depicted is an ice sheet with a drifting speed of 0.5 m/s and a thickness of 0.1 m. The ramp is introduced in the time between 0 and 1000s as a linear function as in Figure 3.14. And, in Figure 3.15, the final value of the FA force is 9.9496 kN and the final value of the FA moment is 35.1104 kNm.

```
!************************************
!************************************
IF (T.LT.1000) then
       F(1)=0
       F(2)=110.8*T      !9.9496*T
       F(3)=0
       M(1)=5102*T       !35.1104*T
       M(2)=0
       M(3)=0
           write(*,301)   T
       301 format('time=',f10.3)
else

write(*,300)   T
300 format('time=',f10.3)
!************************************
```

Figure 3.14: Ramp function as introduced in the ice loads DLL

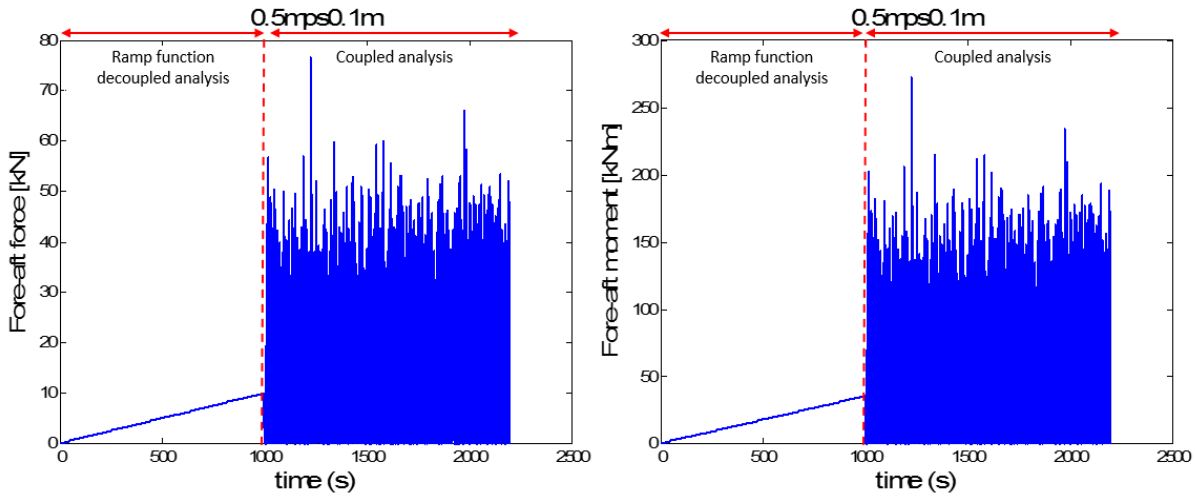

Figure 3.15: Introduction of ice loads via a ramp function (ice load case: 0.5 mps, 0.1m)

The ramp function is applied on both FA force and moment and not only on the FA force because F_y and M_x are the largest ones among the six component. And, the large input of moment M_x will also cause a sudden increase of motion.

However, in some of the studied cases, this strategy is not enough to ensure convergence. This is the case for the following ice load cases:

- 0.1 mps and 0.4 m;
- 0.5 mps and 0.8m.

It should be noted that convergence problems where already encountered when modelling a monopile submitted to ice loads and convergence was really hard to attain for the case 0.1 mps 0.8m due to slow speed combined with very thick ice. In this case, the ice keep pushing the structure without breaking and the equilibrium position is thus hard to reach. In these cases the following error message is displayed by the compiler:

Forrtl: severe <161>: Program Exception – array bounds exceeded

Image	***PC***	***Routine***	***Line***	***Source***
coupled_spar_0.5m_coupled.90	***055219FA***	***forcedll***	***1250***	

So, an additional condition was added to the algorithm to ensure convergence (2), that is:

Between the end of the ramp function at 1000s and 1100s, the algorithm calculates the ice load $F_{y,i}$ (only for F_y force and not M_x moment), and compares it with the final value from ramp function ($F_{y,mean}$) – obtained thanks to the decoupled analysis. Then the algorithm sets the value of F_y as described in equation [51]:

$$F_y = \begin{cases} F_{y,mean}, if\ the\ relative\ error\ is\ larger\ than\ 5\% \\ F_{y,i}, \quad otherwise \end{cases} \quad [51]$$

This strategy can reduce the transient at 1000s and then allows to reach convergence for all the load cases without the need to specifically tune the ice loads ramp for each and every cases.

This fact is highlighted with Figure 3.16, Figure 3.17, Figure 3.18 and Figure 3.19. Here, we compare 2 cases:

- The figures in blue represent the result for the ice load case 0.5mps 0.8m when only using a ramp function to introduce the ice loads. In this case, the analysis does not reach the end (stops at 2122s instead of 2200s).
- The figures in green represent the result for the ice load case 0.5mps 0.8m when using a ramp function to introduce the ice loads and monitoring the maximal ice load FA force between 1000 and 1100s. In this case, the analysis reaches the end.

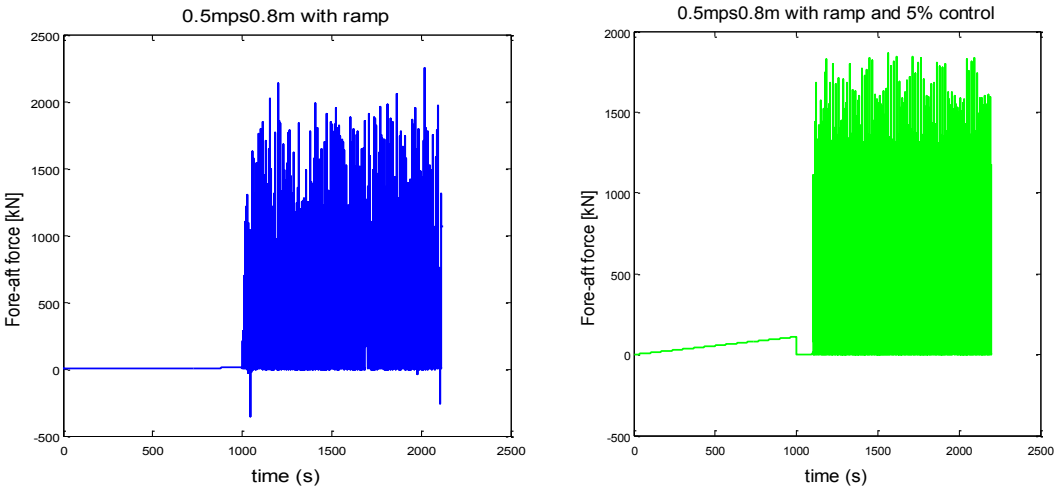

Figure 3.16: Comparison of FA forces when using (green) and not using (blue) a load restriction between 1000 and 1100s (load case: 0.5mps 0.8m)

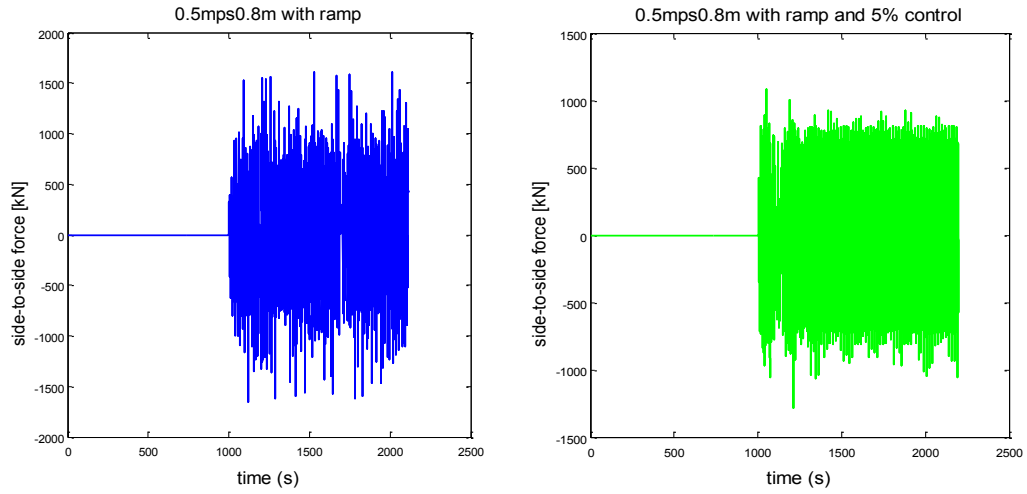

Figure 3.17: Comparison of SS forces when using (green) and not using (blue) a load restriction between 1000 and 1100s (load case: 0.5mps 0.8m)

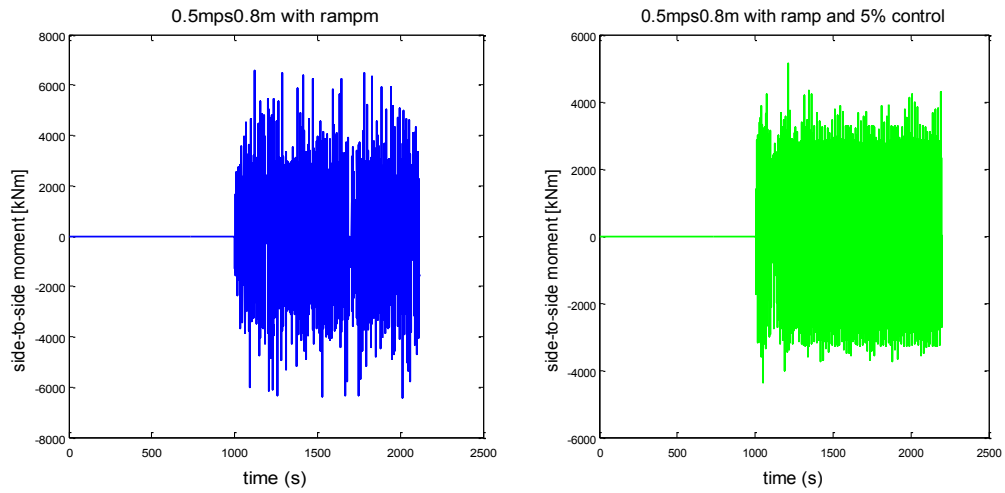

Figure 3.18: Comparison of SS moments when using (green) and not using (blue) a load restriction between 1000 and 1100s (load case: 0.5mps 0.8m)

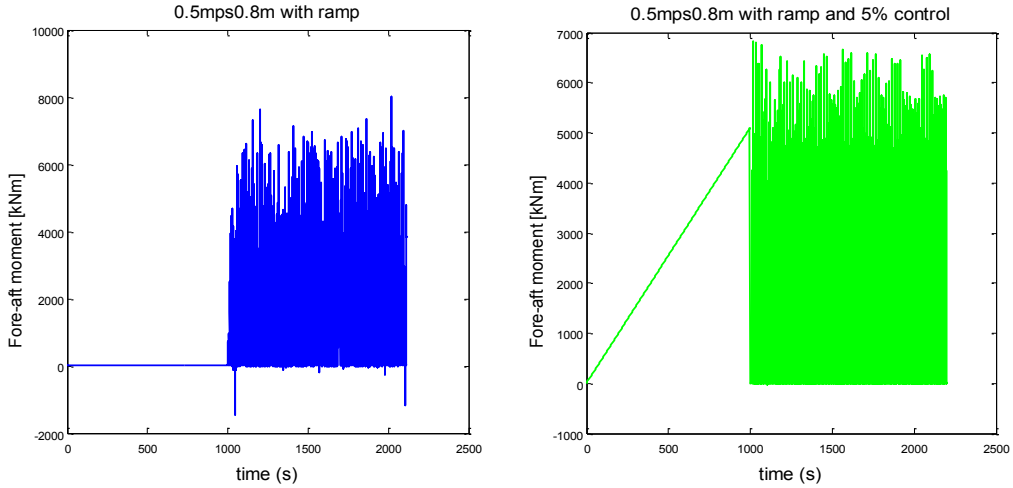

Figure 3.19: Comparison of FA moments when using (green) and not using (blue) a load restriction between 1000 and 1100s (load case: 0.5mps 0.8m)

We can see in Figure 3.16, Figure 3.17, Figure 3.18 and Figure 3.19 that by applying the additional control strategy, the maximal FA and SS forces and moments reached are smaller. Moreover, the oscillations are less pronounced. So the equilibrium position is reached more easily which allows to obtain a successful simulation.

However, in some of the studied cases (0.1mps 0.4m for example), this strategy is not enough to ensure convergence. So, in these cases, a 3rd strategy is implemented (3). This strategy is based on a progressive introduction of the ice thickness using a ramp function as shown in Figure 3.20. It thus simulates a progressive increase of the ice thickness that results in a smoother transient state for the structure and by consequence a converging simulation.

```
If (T.LT.1100) then
hi=0.0008d0*(T-1000.0)
else
hi=0.8d0
endif
```

Figure 3.20: Ice thickness progressive increase as introduced in the ice loads DLL

In the presented case, the ice thickness is increased between 1000s and 1100s linearly from 0 to 0.8 m.

The design loads are summarized in Table 3.5 below. As convergence was never achieved despite all the efforts for the load cases 0.1mps 0.4m, it was decided to implement the load case 0.4mps 0.4m instead to study the ice drifting speed influence.

Table 3.5: Summary of the design load cases

LC #	LC name	turbine wind speed [m/s]	ice speed [m/s]	Ice thickness [m]	Analysis type
1	0_ice_mono_0.1mps0.4m_coupled_no_wind_rigid	no wind	0.3	0.4	Coupled / rigid structure
2	0_ice_mono_0.3mps0.4m_coupled_no_wind_rigid	no wind	0.4	0.4	Coupled/ rigid structure
3	0_ice_mono_0.5mps0.1m_coupled_no_wind_rigid	no wind	0.5	0.1	Coupled / rigid structure
4	0_ice_mono_0.5mps0.4m_coupled_no_wind_rigid	no wind	0.5	0.4	Coupled / rigid structure
5	0_ice_mono_0.5mps0.8m_coupled_no_wind_rigid	no wind	0.5	0.8	Coupled / rigid structure

Moreover, as explained in this section, the ice loads are introduced as a ramp function and the final value of the ramp is fixed as the mean value of the ice loads obtained in the decoupled analysis realized in a previous work. The results obtained in the decoupled analysis are summarized in Table 3.6 and the final value applied for the ramp function in each case is detailed in Table 3.7.

Table 3.6: Mean fore-aft forces and moments obtained with a decoupled analysis

LC #	LC name	mean FA force [kN]	mean FA moment [kNm]
1	0_ice_mono_0.3mps0.4m_decoupled_no_wind_rigid	16.12	-470.1
2	0_ice_mono_0.4mps0.4m_decoupled_no_wind_rigid	65	2600
3	0_ice_mono_0.5mps0.1m_decoupled_no_wind_rigid	-4.03	-1642
4	0_ice_mono_0.5mps0.4m_decoupled_no_wind_rigid	20.23	-230.3
5	0_ice_mono_0.5mps0.8m_decoupled_no_wind_rigid	110.95	5047.5

Table 3.7: Ramp function applied in the coupled analysis (fore-aft force and moment)

LC #	LC name	Applied FA force [kN]	Applied FA moment [kNm]
1	0_ice_mono_0.3mps0.4m_coupled_no_wind_rigid	16.12	-470.1
2	0_ice_mono_0.4mps0.4m_coupled_no_wind_rigid	70.0	3000
3	0_ice_mono_0.5mps0.1m_coupled_no_wind_rigid	-4.03	-1642
4	0_ice_mono_0.5mps0.4m_coupled_no_wind_rigid	9.950	35.11
5	0_ice_mono_0.5mps0.8m_coupled_no_wind_rigid	110.5	5102

Finally, Table 3.8 summarizes the strategies employed in each case to attain convergence of the simulation.

Table 3.8: Summary of the convergence strategy implemented in each case

LC #	LC name	Strategy		
		(1)	**(2)**	**(3)**
1	0_ice_mono_0.3mps0.4m_decoupled_no_wind_rigid	X		
2	0_ice_mono_0.4mps0.4m_decoupled_no_wind_rigid	X		
3	0_ice_mono_0.5mps0.1m_decoupled_no_wind_rigid	X		
4	0_ice_mono_0.5mps0.4m_decoupled_no_wind_rigid	X		
5	0_ice_mono_0.5mps0.8m_decoupled_no_wind_rigid	X	X	

3.5.2. Both ice and wind loads

Constant ice thickness and constant wind speed

For the case with both ice and wind, the main issue was to ensure convergence and overcome problems due to the ice-structure overlapping procedure. Indeed, as explained in §3.3, the algorithm is looking for overlap in the structure definition and the ice edge to determine if there is contact or not and from there calculate the contact forces. And, it turns out that when considering both wind and ice the oscillations of the structure are quite important and can pose a problem for the contact detection sequence. Thus, in a first time, the following procedure was implemented in order to ensure convergence of the analysis:

1. Run the test without ice and only wind loads to find the static equilibrium position (x_1,y_1);
2. Use the previous result to shift the ice initial geometry by x_1 and y_1;
3. Run the simulation with both ice and wind loads.

To first find the static position with only wind we run 3000s simulations with constant wind speeds. Due to time limitations, only 3 wind speeds are considered that are 8, 11.4 and 18 mps. This way, we have a case involving an under rated wind speed, another one

at the rated speed and finally, one at an above rated speed. The results are summarized in Table 3.9 below:

Table 3.9: Static position of the WT only submitted to wind loads (HAWC2 conventions)

LC #	Wind speed [mps]	Static equilibrium position (x_1,y_1) [m]
1	8	(-0.115412;.57)
2	11.4	(-0.234;24.76)
3	18	(-0.3821; 11.73)

Special care should be taken when positioning the structure at the start of the simulation. Problems were encountered at the time step ice was introduced. Indeed, the structure and the ice sheet were already overlapping and the DLL code could not handle this configuration resulting in the simulation failing. To solve this problem, the code was completed by Wei Shi. The enhancements are the following:

- During the first 100s only wind is introduced. During this time the structure position is monitored and recorded – which was not done earlier.
- At 100s, the ice is introduced. This is done without using a ramp for the ice forces or moments. Moreover, the initial conditions are written depending on the recorded position of the structure. This way any overlapping at the time of introduction of the ice is avoided.

Additionally, the time step was reduced and was set to 0.0005s instead of the 0.001s previously used. Indeed, even if 0.001s time step gives accurate results with only ice (see §4.2.2), the program was crashing due to too big overlaps that cannot be solved by the DLL. The reason for these problems is most likely that the algorithm was designed for an ice breaking ship. In this configuration, the oscillations and variations of relative speed between the ship and the ice sheet are relatively small. However, in the present case, due to the wind action and the nature of the structure – a spar floating wind turbine – the oscillations of the structure and thus its relative speed compared to the ice sheet are presenting large variations. By reducing the time step, we will then reduce the time available to create an overlap and as a consequence the overlap magnitude.

In this configuration, the simulations run successfully with rated wind speed – 11.4 mps - for approximately 1400-1500s, depending on the cases. This is a good start but as can

be seen in Figure 3.21, strong transient effects due to the wind action are still ongoing at the time of introduction of ice. From the plot with only wind considered we can see that the transient effects are still ongoing till 500-600s. Moreover, from the plot with ice and wind loads, we can see that the additional transient effect due to ice is small compare to the one due to wind. Thus, it was decided to run new simulations introducing the ice at 500s. This way, the structure will have reached the mean position due to wind loads and ice loads introduction should not lead to important transient.

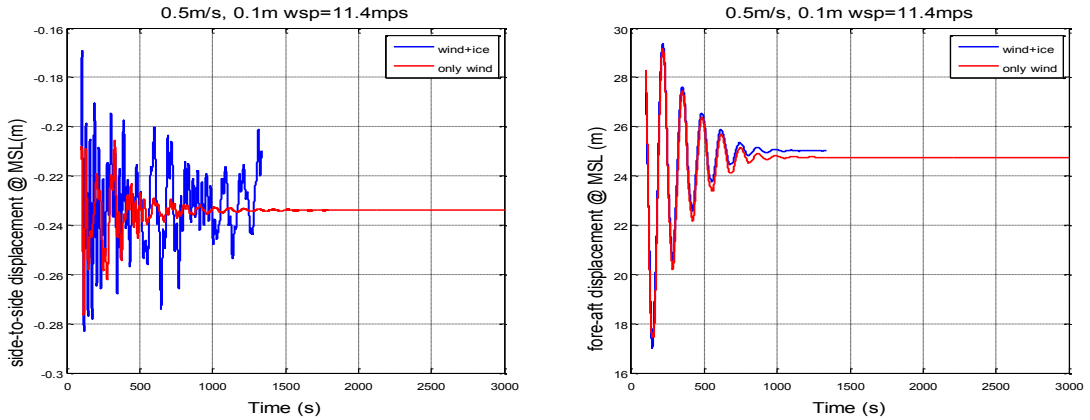

Figure 3.21: Time series of the side-to-side and fore-aft displacements at the MSL for an ice sheet 0.1m thick, drifting at 0.5mps with a wind speed of 11.4mps

In this configuration, the simulations stop at around 1800s. It is an improvement but it is still not enough if we need to study the results after removing the transient part. Thus, to overcome this problem, the solution chosen is to run 2 simulations with effective length of 600s and different initial conditions. Then the statistical results - mean and std – are studied. The ice loads are introduced at respectively 500s and 520s and the simulation runs for an additional 1000s. Randomness will consequently be introduced in the simulations. The first 500s/520s before the introduction of ice and the next 400s containing transient effects are not accounted for (as decided based on Figure 3.22). Thus we will have 600s of effective simulation as wanted.

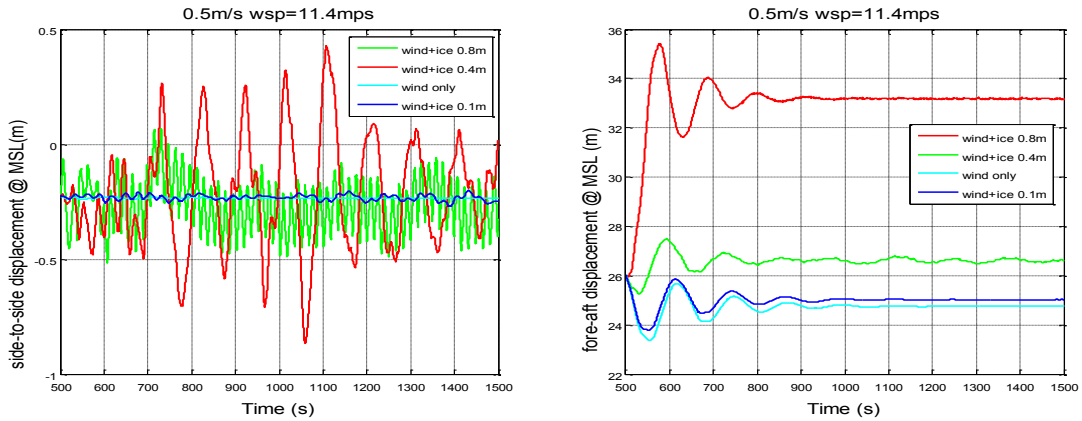

Figure 3.22: Time series of the side-to-side and fore-aft displacements at the MSL for an ice sheet 0.4m thick, drifting at 0.5mps with a wind speed of 11.4mps

Random variation of ice thickness and turbulent wind

Concerning turbulent wind, HAWC2 is already fitted with turbulent features. More information can be found in (Larsen, et al., 2007).

Randomness can be introduced in 2 ways for the ice conditions. First, by changing the time of introduction of the ice loads or the initial conditions for ice in simulations comporting already wind. This is the method described in the previous paragraph. Secondly, the ice properties can be randomized as explained in §2.5. In this case, there is still to define the length of the generated ice sheet. A total simulation length of 1800s seems to give sufficiently accurate results once the transient effects have been removed. So knowing the ice drifting speed, the total ice field length can be estimated. As an example we can do it for an ice sheet drifting with a velocity equals to 0.5mps. Then:

$$L_B = time * drifting\ velocity = 1800 * 0.5 = 900\ m$$

So, the generated ice sheet should be 900m long in this case. Now the sampling interval should be chosen. In (Su, et al., 2011) and (Su, et al., 2011), 25m, 50m and 100m intervals are tested. However, the ice sheet considered is 10 km long. Following this logic, we should test here intervals of 0.225m, 0.450m and 0.900m.

4. Simulation and Results

4.1. Eigenfrequency analysis

First an eigenfrequency analysis is run to determine the natural frequencies and natural modes of the structure studied. The natural frequencies and mode shapes of 17 lowest modes are given in Figure 4.1 and Table 4.1 below. The eigenvalue calculation is run using HAWC2 functionalities. The analysis is done for the total system including external systems attached, such as mooring lines and the constraint equations are also fully included in the analysis (Larsen, et al., 2007). The system is described as a flexible model to run the calculation. And, the structure is not submitted to wind and placed in still water. Moreover, the platform, tower drivetrain and blades are enabled for the analysis to match the conditions implemented in (Jonkman, et al., 2010).

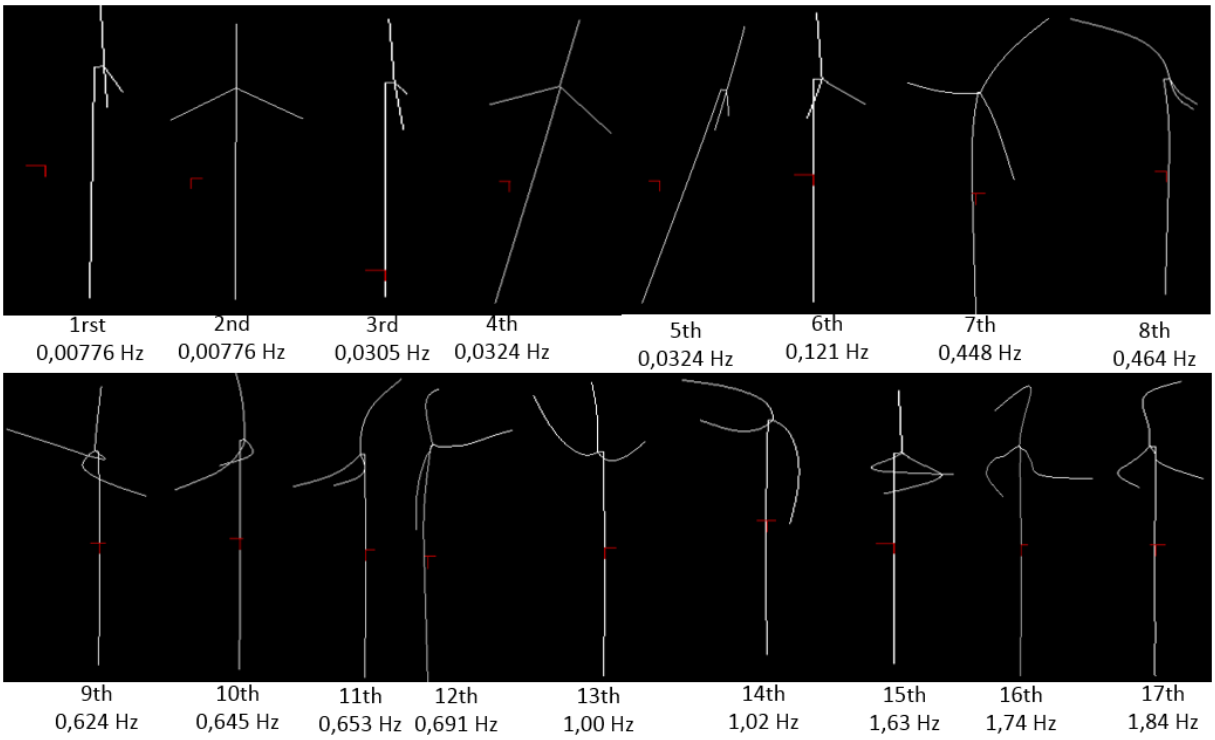

Figure 4.1: Natural frequencies and mode shapes of 20 lowest modes

Table 4.1: Full system eigenmodes

#	Full system eigenmodes	Natural frequency [Hz]	Period [s]
1	Platform Surge	7,76E-03	128,842735
2	Platform Sway	7,76E-03	128,842735
3	Platform Heave	3,05E-02	32,7653997
4	Platform Roll	3,24E-02	30,8451573
5	Platform Pitch	3,24E-02	30,8451573

6	Platform Yaw	1,21E-01	8,26173166
7	1st Tower Side-To-Side	4,48E-01	2,22983836
8	1st Tower Fore-Aft	4,64E-01	2,15364537
9	1st Blade Asymmetric Flapwise Yaw	6,23E-01	1,60392641
10	1st Blade Asymmetric Flapwise Pitch	6,45E-01	1,54932109
11	1st Blade Collective Flap	6,53E-01	1,53061771
12	1rst Drivetrain Torsion	6,91E-01	1,44720732
13	1st Blade Asymmetric Edgewise Pitch	1,00E+00	0,9967804
14	1st Blade Asymmetric Edgewise Yaw	1,02E+00	0,98280098
15	2nd Blade Asymmetric Flapwise Yaw	1,63E+00	0,61309447
16	2nd Blade Asymmetric Flapwise Pitch	1,74E+00	0,57347999
17	2nd Blade Collective Flap	1,84E+00	0,54329224

The results obtained should be considered carefully as the full system eigen analysis was implemented recently in HAWC2. And, for some of the eigenfrequencies an abnormal damping was obtained which, most probably, is due to a bug of HAWC2. However, the whole analysis is in good agreement with the results obtained in the OC3 task (Jonkman, et al., 2010) and presented in Figure 4.2.

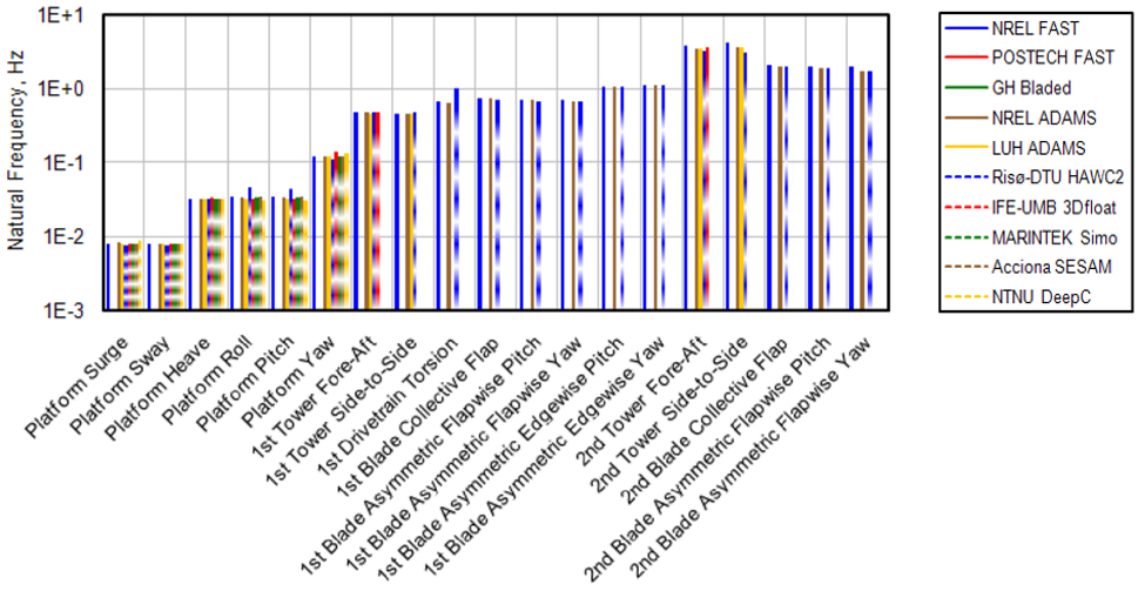

Figure 4.2: Full-system hydro-elastic natural frequencies from (Jonkman, et al., 2010)

It should be noted that "t*he designation of "pitch" and "yaw" in the asymmetric flapwise and edgewise blade modes identifies coupling of the blade motions with the nacelle-pitching and nacelle-yawing motions, respectively"* (Jonkman, et al., 2010). And, for example, asymmetric flapwise yaw can be described as such: *"vertically positioned blade remains stationary, while the two other blades flap out of phase with each other. These*

blade motions couple with the torsion of the tower and—in Phase IV—the yaw of the platform (both being rotations about the tower centerline)" (Jonkman, et al., 2010).

The eigenfrequencies displaying abnormal damping values were the ones related to heave, pitch and roll. Thus, an additional decay test was realized to confirm the results obtained. The settings applied are the followings:

inipos 0.0(sway) 0.0(surge) 120.0 (heave) ;
body_eulerang 0.0(roll) 0.0(pitch) 0.0 (yaw);

And, for each test, the initial conditions were modified as follows:

- Platform Heave = +5m, Other = 0;
- Platform Roll = -10deg, Other = 0;
- Platform Pitch = 10deg, Other = 0.

The heave decay test results are displayed in Figure 4.3. It is possible to compare them with the results obtained by (Jonkman, et al., 2010) and displayed in Figure 4.2 and Figure 4.4. On the first hand, comparing Figure 4.3 and Figure 4.4, we can see that the behavior of the structure are concurring. On the second hand, comparing Figure 4.3 and Figure 4.2 we can see that the eigenfrequency for the heave motion is obtained equal to 0.03052 Hz and is in agreement with the results obtained by (Jonkman, et al., 2010).

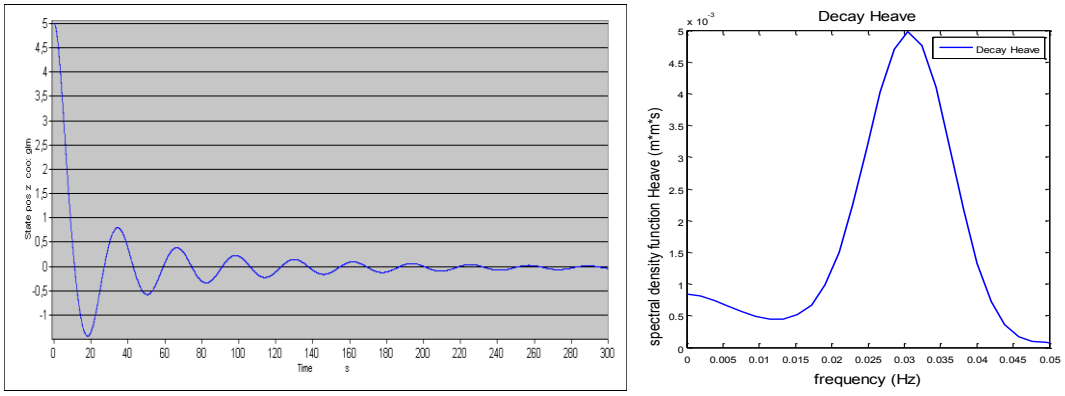

Figure 4.3: Free decay in platform heave in still water and no wind conditions (Heave)

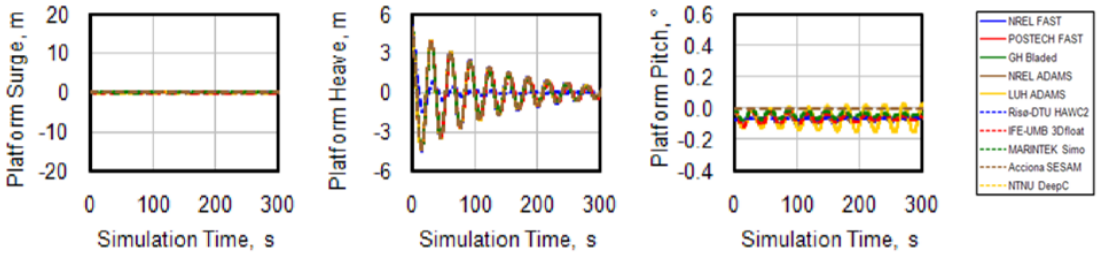

Figure 4.4: Free decay in platform heave in still water and no wind conditions (Jonkman, 2010)

The same test is then conducted to establish the eigenfrequency for the pitch and roll motions. They were both found equals to 0.0324 Hz. Moreover, the eigenfrequencies obtained for pitch and roll are concurring with the results from Figure 4.2.

4.2. Convergence study

For the different cases of ice loads, there are different parameters we can act upon to avoid numerical problems when coupling the ice load module to a global aerodynamic model of wind turbine. We should thus perform a convergence study to tune the analysis settings to obtain reliable results. The different parameters identified for the convergence study are the following:

- Initial conditions and transient phases i.e. the ice loads ramp duration and final value;
- Time steps;
- Simulation length.

However, as we do not take into account the transient state in the results but only the steady state, a different ramp function will not change the results consequently. So the convergence study will be focused on the variation of the time step and simulation length.

We will present results only for parameters of influence considering only ice influence. Thus, results for parameters such as SS moments, SS displacements or roll motions where mean value is close to 0 will not be presented.

4.2.1. Simulation length influence

Concerning the simulation length influence, the first 1600s are not be taken into account to get rid of the transient effects. The simulations are run for different ice cases for 3 different simulation lengths equals to 2200s, 2600s and 3000s. Then the stability of the statistical results are assessed. The settings of the simulations are summarized in Table 4.2. The time step is set to 0.001s for all the simulations.

Table 4.2: Convergence study – simulation length influence

LC #	LC name	Simulation length [s]	Effective length [s]
1.1.	0_ice_mono_0.5mps0.1m_decoupled_no_wind_rigid	2200	600
1.2.	0_ice_mono_0.5mps0.1m_decoupled_no_wind_rigid	2600	1000
1.3.	0_ice_mono_0.5mps0.1m_decoupled_no_wind_rigid	3000	1400
1.4.	0_ice_mono_0.5mps0.8m_decoupled_no_wind_rigid	2200	600
1.5.	0_ice_mono_0.5mps0.8m_decoupled_no_wind_rigid	2600	1000
1.6.	0_ice_mono_0.5mps0.8m_decoupled_no_wind_rigid	3000	1400

The results obatined are presented in Figure 4.5 to Figure 4.8 and Figure B. 1 to Figure B. 4 placed in Appendix B for readibility. When we only compare 2200s and 3000s simulations, the simulations agree globally quite well for the FA forces, moments and displacements at MSL. The maximal error for these parameters does not exceed 4% in STD except for the FA displacements where it reaches 20% for a 0.1m thick ice. For the pitch the error always exceed 40% for the STD values but the mean values are concurring well.

After a complete analysis, it seems that the statistical results are not stable between 3000s simulations and 2200s ones. It might be due to the fact that for the 2200s simulations only 600s are effectively exploited. It is, it seems, not enough to give reliable statistical results and some resonant phenomenom between the different eigenfrequencies of the system might be missed. However, when comparing 2600s long simulation results and 3000s long ones we can observe that the results are converging. Indeed, the errors drops under 10% for all the parameters except for pitch STD (25.9%). However, in all of these cases, the difference is quite significantly reduced compared to 2200s long simulations and the error in mean value is under 10% for all the parameters. So, it seems that 3000s simulations give rather stable results but longer simulation time should be implemented if technical means and time allow it. It is not the case for the present project as 3000s simulations with a time step of 0.001s already took from 3 to 4 days. Indeed, usually, the effective simulation time is around 1h and represent 30 to 50 sway motion cycles.

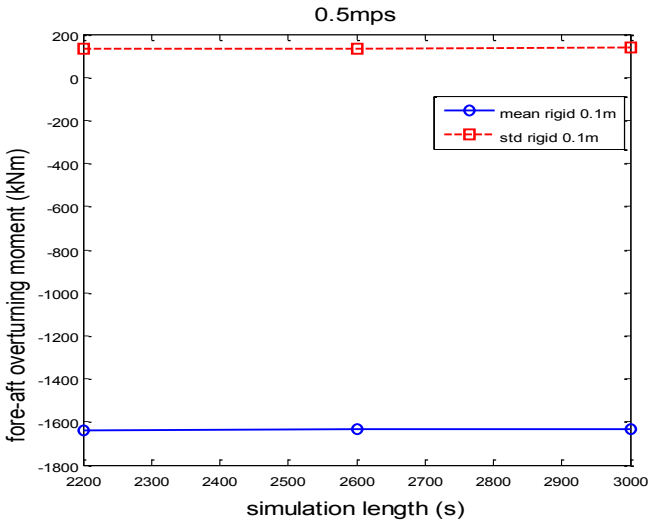

Figure 4.5: Comparison of statistical characteristics of the fore-aft over-turning moment at the MSL with ice thickness of 0.1m and constant ice drifting speed of 0.5mps for simulation of different length

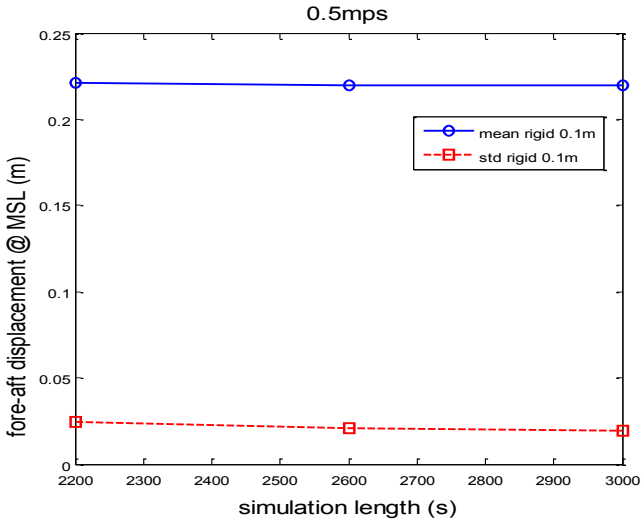

Figure 4.6: Comparison of statistical characteristics of the fore-aft displacements at the MSL with different ice thicknesses and constant ice drifting speed of 0.5mps for simulation of different length

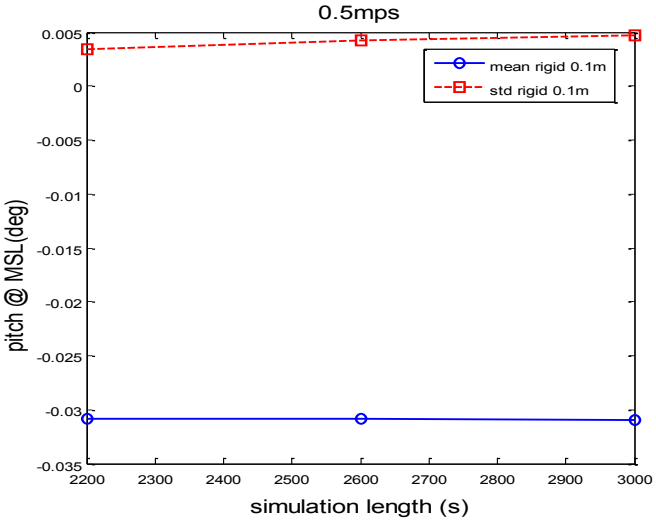

Figure 4.7: Comparison of statistical characteristics of the pitch at the MSL with different ice thicknesses and constant ice drifting speed of 0.5mps for simulation of different length

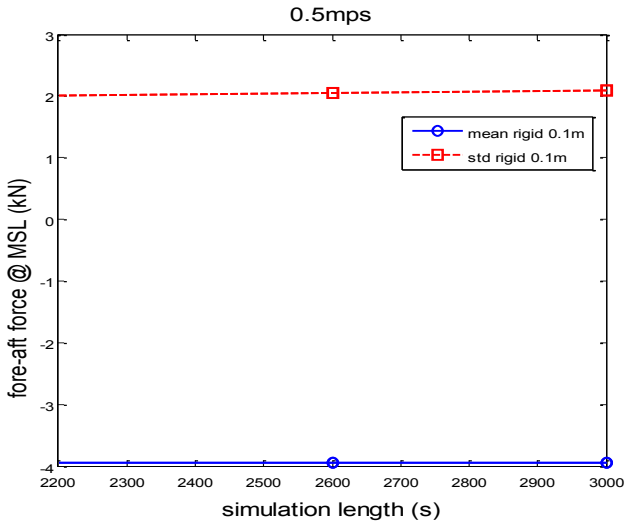

Figure 4.8: Comparison of statistical characteristics of the fore-aft force at the MSL with different ice thicknesses and constant ice drifting speed of 0.5mps for simulation of different length

4.2.2. Time step influence

Concerning the time step, the one applied in all the simulations presented above is equal to 0.001s. This time step should be the same in both HAWC2 and the DLL file. To test the stability of the results obtained, we will study the impact of a different time step on the statistical results. To restrain this study, it has been chosen to focus on cases with the same ice drifting speed but different ice thickness. The extreme cases are the only one considered. The settings of the simulations are summarized in Table 4.3. The simulation length is set to 3000s and the first 1600s are not taken into account to get rid of the transient effects. So the effective simulation length is finally of 1400s.

Table 4.3: Convergence study – time step influence

LC #	LC name	Time step [s]
2.1.	0_ice_mono_0.5mps0.1m_decoupled_no_wind_rigid	0.0005
2.2.	0_ice_mono_0.5mps0.1m_decoupled_no_wind_rigid	0.001
2.3.	0_ice_mono_0.5mps0.1m_decoupled_no_wind_rigid	0.002
2.4.	0_ice_mono_0.5mps0.1m_decoupled_no_wind_rigid	0.005
2.5.	0_ice_mono_0.5mps0.8m_decoupled_no_wind_rigid	0.0005
2.6.	0_ice_mono_0.5mps0.8m_decoupled_no_wind_rigid	0.001
2.7.	0_ice_mono_0.5mps0.8m_decoupled_no_wind_rigid	0.002
2.8.	0_ice_mono_0.5mps0.8m_decoupled_no_wind_rigid	0.005

It should be noted that convergence problem were encountered for the load cases 2.1 and 2.5 due to the small time step applied. The simulations stopped prematurely respectively at 2237s and 2431s. It was however decided to use the results obtained as the simulation time was judged long enough to give satisfying results – respectively 637s and 831s of effective simulation time.

The results of this study are shown in Figure 4.9 to Figure 4.12 and Figure C. 1 to Figure C. 4 placed in Appendix C for readability. On one hand, when we only compare simulations with 0.005s and 0.001s time step, the simulations agree globally quite well for the FA forces, moments and displacements at MSL. The maximal error for these parameters does not exceed 2% both in STD and mean. On the other hand, for the pitch at MSL the error always exceed 40% for the STD values.

So, it seems that the statistical results are not stable between simulations with time step of 0.005s and 0.001s ones. It might be due to the fact that for the 0.005s time step is not accurate enough given the rapid changes in motions of the spar wind turbine. It is, it seems, not enough to give reliable statistical results. However, when comparing simulations with 0.002s and 0.001s time step we can observe that the results are converging quite well when decreasing the time step. Indeed, the errors drop significantly for all the parameters. So, it seems that simulations with 0.001s time step give rather stable results and the error in mean value is under 10% for all the parameters. But, smaller simulation time step should be implemented if technical means and time allow it. It is not the case for the present project as 3000s simulations with a time step of 0.001s already took from 3 to 4 days.

Moreover, 0.0005s time step is also included in the analysis as it is utilized in the simulations including both wind and ice. As can be seen in Figure 4.9 to Figure 4.12 and Figure C. 1 to Figure C. 4, the statistical results are stable between simulations with time step of 0.002s and 0.0005s ones and simulations with time step of 0.001s and 0.0005s ones. The error in mean values is in these cases always inferior to 3% for both load cases – 0.5mps 0.1m and 0.5mps 0.8m.

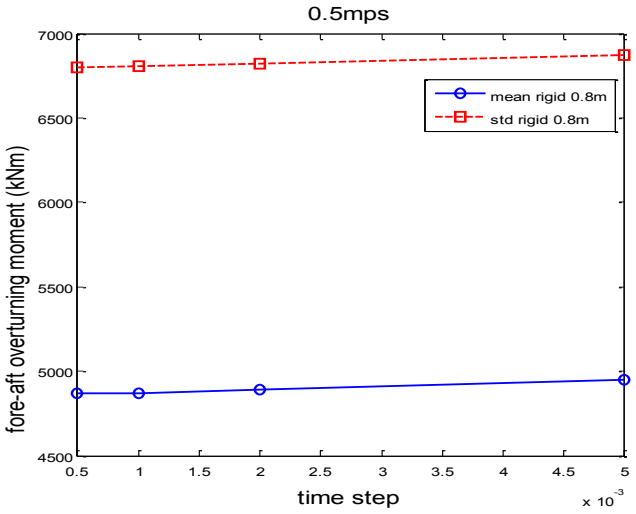

Figure 4.9: Comparison of statistical characteristics of the fore-aft over-turning moment at the MSL with constant ice thicknesses of 0.8m and ice drifting speed of 0.5mps for different time steps

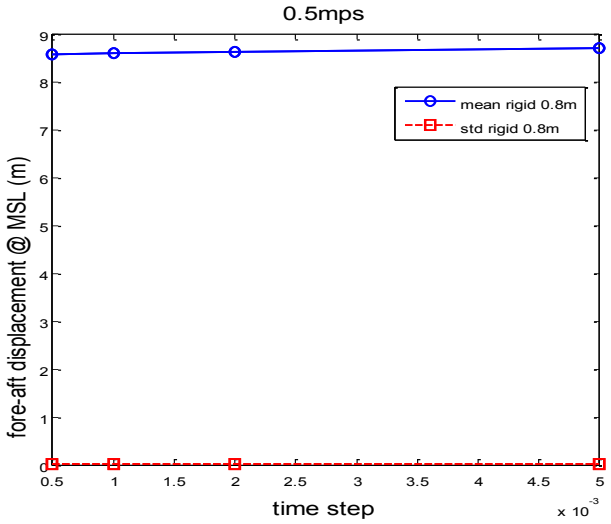

Figure 4.10: Comparison of statistical characteristics of the fore-aft displacements at the MSL with constant ice thicknesses of 0.8m and ice drifting speed of 0.5mps for different time steps

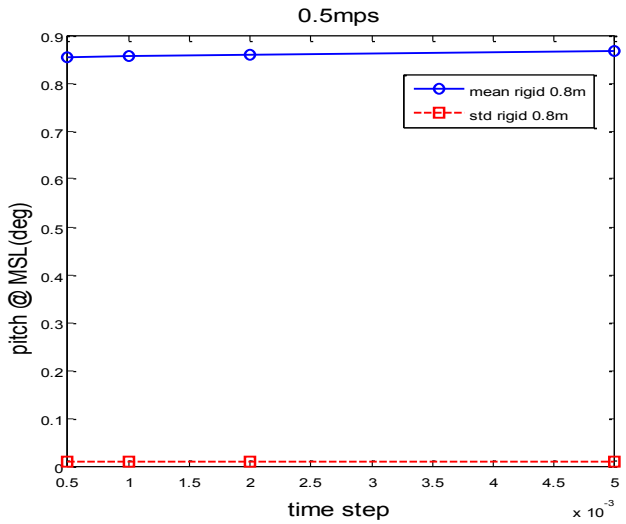

Figure 4.11: Comparison of statistical characteristics of the pitch at the MSL with constant ice thicknesses of 0.8m and ice drifting speed of 0.5mps for different time steps

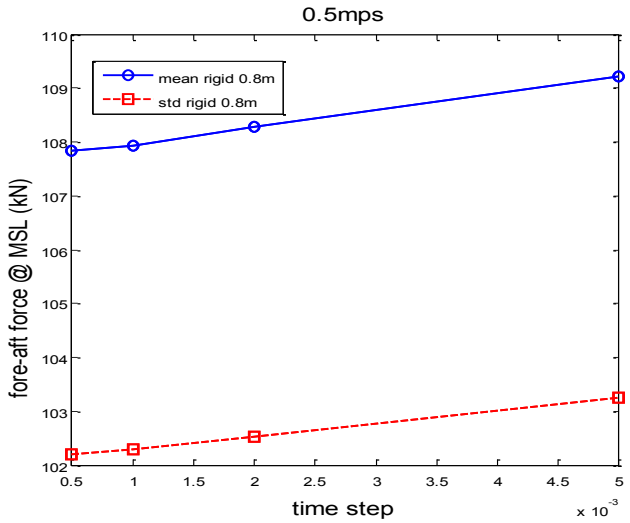

Figure 4.12: Comparison of statistical characteristics of the fore-aft force at the MSL with constant ice thicknesses of 0.8m and ice drifting speed of 0.5mps for different time steps

4.3. Comparison between the decoupled and coupled models

In the following section, we are comparing the results obtained with 2 different models:

- The coupled model implemented so far in this work;
- The decoupled model developed before the coupled one using the same algorithm with the difference that the ice loads series are read and thus the model does not take into account the ice-structure interactions.

Additionally, the initial conditions are the same but, as soon as the 2nd time step is reached, the conditions applied on the turbine are already different. So, the results should be compared carefully and are considered in a qualitative and statistical way.

The results for the decoupled model are based on 1800s simulations and only take into account the output from 1200 to 1800s to avoid the transient state. For the coupled model, however, the time series are based on 2200s simulations where the first 1600s are not included in the interpretation. This way, we have 600s of effective time series for both models. The time series are included to give an overview of the difference in shape of the solicitations. And, as they represent different time intervals and different conditions for the same time step they should be considered with caution and not compared time step to time step. Table 4.4 summarized the load cases implemented in the analysis.

Table 4.4: Load cases to investigate the differences in coupled and decoupled models.

LC #	turbine wind speed [m/s]	ice speed [m/s]	Ice thickness [m]
3.1.	no wind	0.5	0.1
3.2.	no wind	0.5	0.4
3.3.	no wind	0.5	0.8

4.3.1. Moment at MSL

Figure 4.13, Figure 4.14 and Figure 4.15 present the time series of the side-to-side and fore-aft overturning moment at the MSL for different ice thicknesses. These figures moreover compare results obtained from a previous decoupled analysis to the results obtained with the new coupled model developed. We can observe that we have sensibly the same type of response with short oscillations.

In the case of the fore-aft moment, for both the coupled and the decoupled model, we observe 5s periodic loads in the case of a rigid structure. The highest loads have a period around 60s. The statistical analysis in Figure 4.16 shows that globally the mean and standard deviation obtained are concurring. It shows that with increasing thickness we have increasing mean FA moment. This increase is expected. Indeed, thicker ice will induce a bigger contact area and thus higher loads. The maximal difference is obtained for an ice thickness of 0.4 m where the results differ from around 67% in mean and 16% in standard deviation. Finally, the decoupled analysis seems to give more conservative results for increasing ice thickness. However, it cannot be fully affirmed from the present cases considered.

For the side-to-side overturning moment, the results shape is identical for coupled and decoupled analysis. That is, the mean value is approximately the same for all ice thicknesses and the response oscillates around the zero value due to the symmetry of the structure. But, the amplitude will increase with increasing ice thickness. So, the ice-structure interaction is more significant for thicker ice. However, the value of the standard deviation change drastically from decoupled and coupled analysis. This difference moreover grows bigger for increasing ice thickness and raises from 5% for 0.1 m thick ice to 40% for 0.8m thick ice.

These results seems to be concurring with the properties of the different models. Indeed, the decoupled model does not take into account the interaction ice-structure. And, as the ice loads are introduced only in the FA direction, the SS moments will be underestimated

in the decoupled model. However, in the coupled model they will be more important due to the interaction ice-structure. Thus, some energy is dampened in SS motions and moments and, as a consequence, the FA moments are smaller in the coupled simulation.

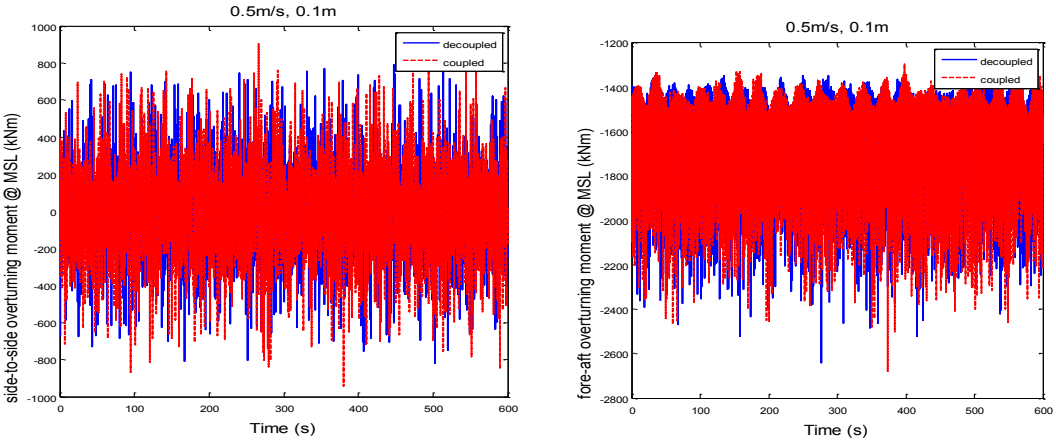

Figure 4.13: Time series of the side-to-side and fore-aft overturning moment at the MSL for LC 3.1 for a decoupled vs. a coupled analysis

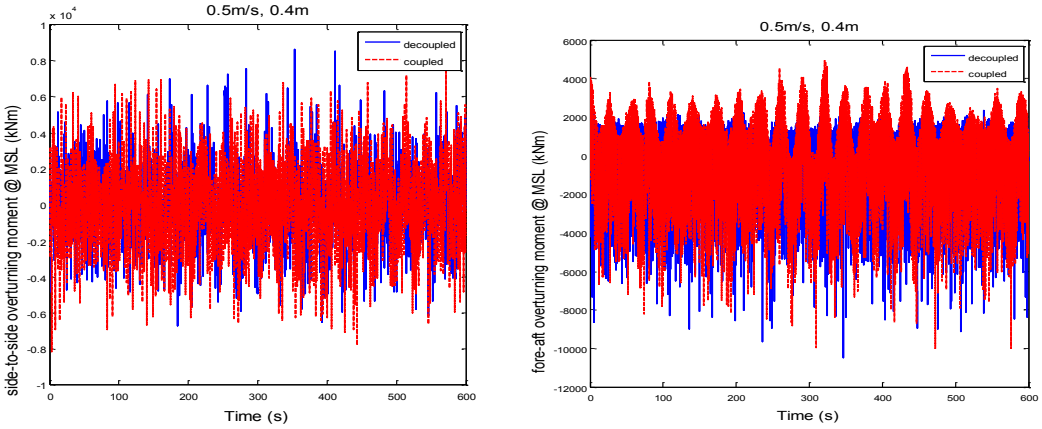

Figure 4.14: Time series of the side-to-side and fore-aft overturning moment at the MSL for LC 3.2 for a decoupled vs. a coupled analysis

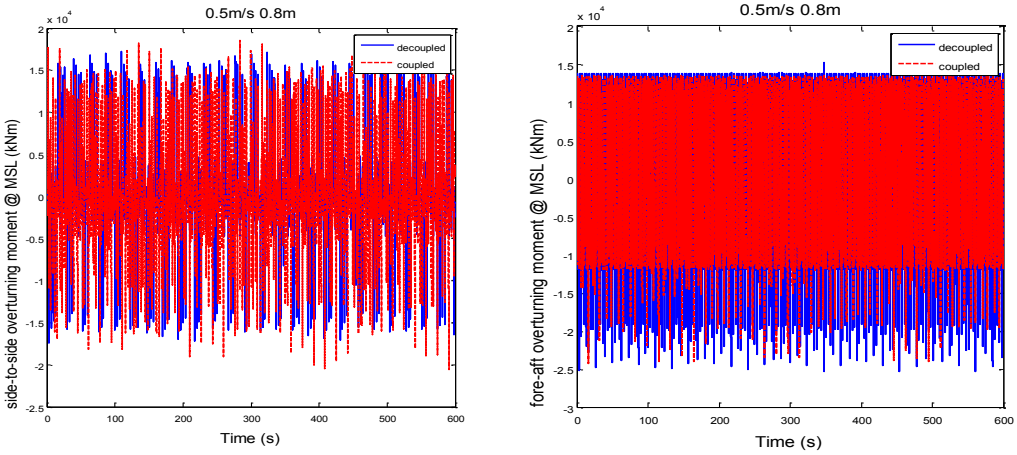

Figure 4.15: Time series of the side-to-side and fore-aft overturning moment at the MSL for LC 3.3 for a decoupled vs. a coupled analysis

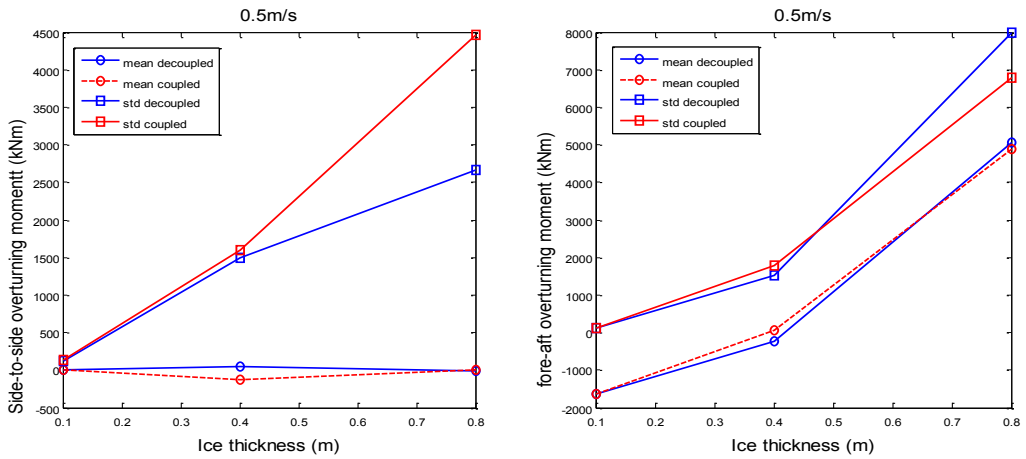

Figure 4.16: Statistical characteristics of the side-to-side and fore-aft over-turning moment at the MSL with different ice thicknesses and constant ice drifting speed (0.5mps) for a decoupled vs. a coupled analysis

Figure 4.17 shows the spectrum of the side-to-side overturning moment at the MSL with different ice thicknesses for both coupled and decoupled analysis from time series in Figure 4.13, Figure 4.14 and Figure 4.15. The global behavior is the same for both models i.e. the response shows larger amplification in both cases for increasing ice thickness and the process becomes wide-banded. In the case of the decoupled model, the process presents a wider band but a smaller response amplitude than for the coupled one. In this case, the same peaks are represented by the 2 models but the low frequency ones have more influence in the case of the coupled response. For the 0.8m thick ice we can observe that the peaks are appearing by pair in the decoupled model with a recurring pattern: the 1st peak is occurring later than for the coupled model while the second one is appearing before. These 2 peaks present an approximately constant difference of 0.08Hz and the pair of peaks appears with a period of 0.3 Hz.

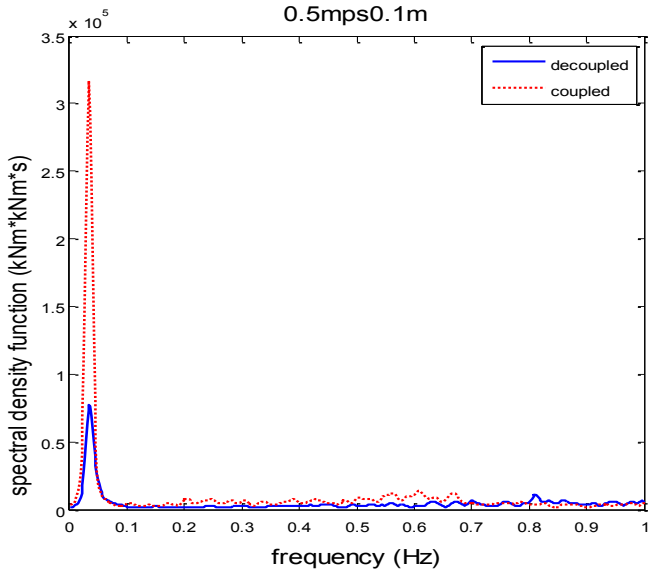

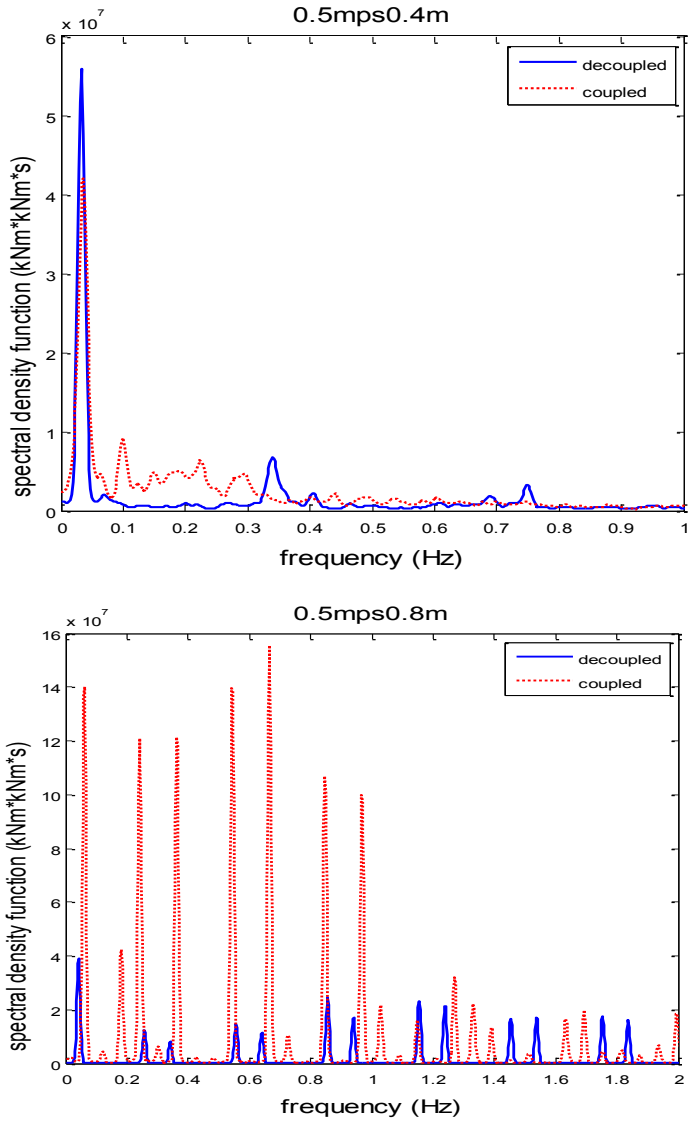

Figure 4.17: Spectrum of the side-to-side overturning moment at the MSL with different ice thicknesses and constant ice drifting speed (0.5mps) for a decoupled vs. a coupled analysis

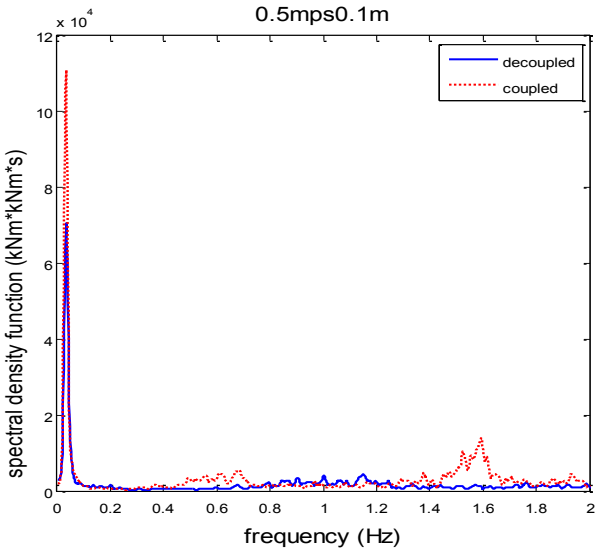

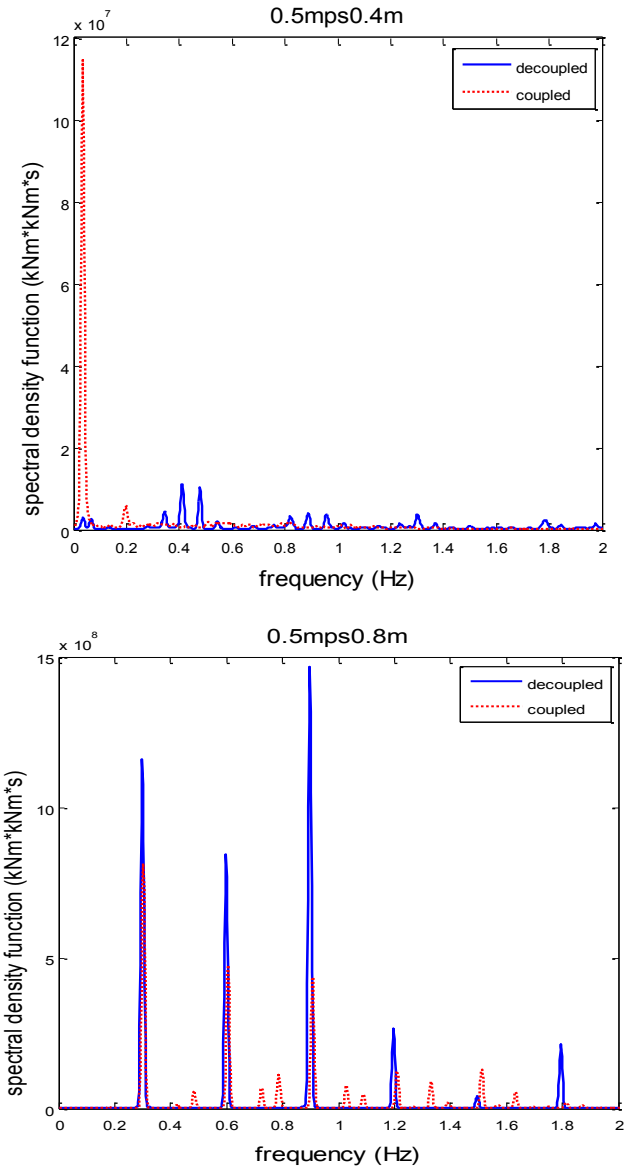

Figure 4.18: Spectrum of the fore-aft overturning moment at the MSL with different ice thicknesses and constant ice drifting speed (0.5mps) for a decoupled vs. a coupled analysis

Figure 4.18 shows the spectrum of the fore-aft overturning moment at the MSL with different ice thicknesses from time series in Figure 4.13, Figure 4.14 and Figure 4.15. With increasing ice thickness, the response shows larger amplification in both cases and the excited modes are concurring. For larger ice thickness, the process becomes wide-banded. In the case of the decoupled model, the process excites less frequencies than the coupled model where modes with a smaller influence appear more frequently. However, the response amplitude is larger than for the coupled model except for the 0.4m thick ice where the amplitude for the decoupled response is negligible compared to the one obtained with the coupled model. It is in agreement with the observations made on the time series.

4.3.2. Displacement at MSL

Figure 4.19, Figure 4.20 and Figure 4.21 present the time series of the side-to-side and fore-aft displacement at the MSL for different ice thicknesses. The displacement patterns produced by the 2 models are quite similar. The structure will be pushed away in the fore-aft direction due to the ice loading. The statistical results (Figure 4.22) shows that with increasing ice thickness the structure will be pushed further away. Also, with increasing thickness, the oscillation in SS direction will be restrained. The behavior observed between coupled and decoupled models seems to be in accordance with the observations made for the moment at MSL with more important displacements in the SS direction and smaller ones in the FA direction for the coupled model. Lastly, for increasing thickness, the structure is oscillating faster but the general slope of the curve is unchanged. So, it seems that the structure is hitting the ice sheet more often before the occurrence of the ice breaking event.

We also observe that in the case of the SS displacement, the trend of the mean value is diverging between the coupled and the decoupled model. More results are necessary to state on this divergence. However, its origin can come from the difference in properties of the 2 models and more precisely the fact that the interaction ice-structure are not taken into account in the decoupled model. Moreover, we can see that only 4-5 cycles of low-frequency motions are enclosed in the effective simulation time and it is not sufficient for a thorough analysis. Longer simulations would give a better understanding and more reliable results.

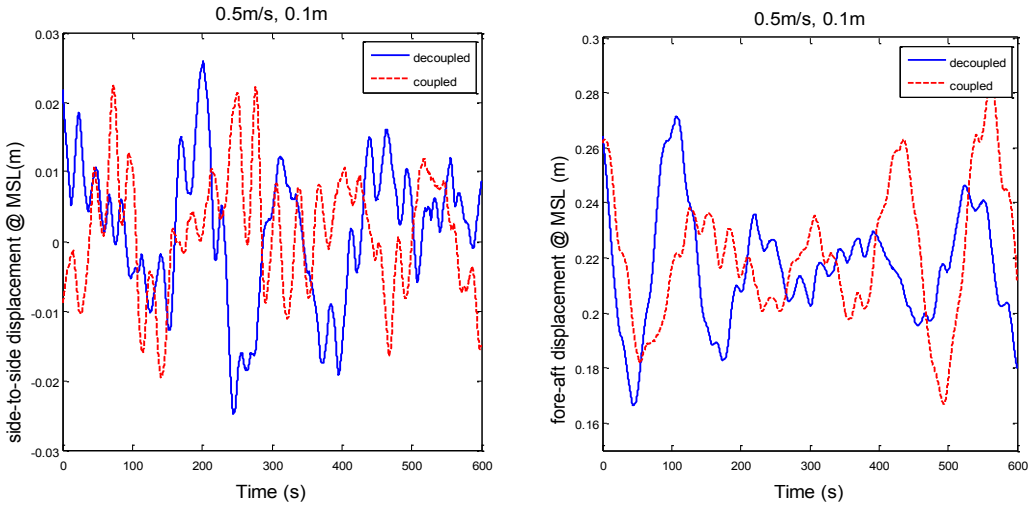

Figure 4.19: Time series of the side-to-side and fore-aft displacements at the MSL for LC3.1 for a decoupled vs. a coupled analysis

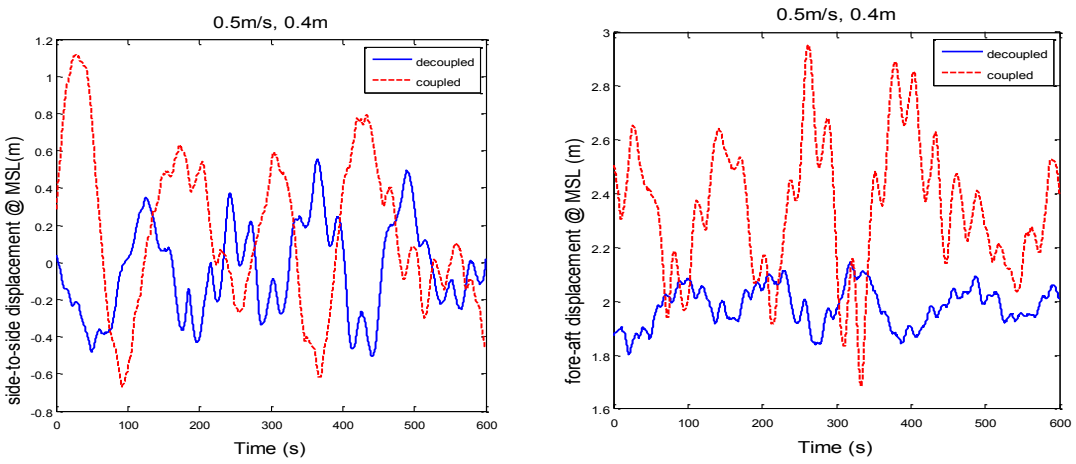

Figure 4.20: Time series of the side-to-side and fore-aft displacements at the MSL for LC3.2 for a decoupled vs. a coupled analysis

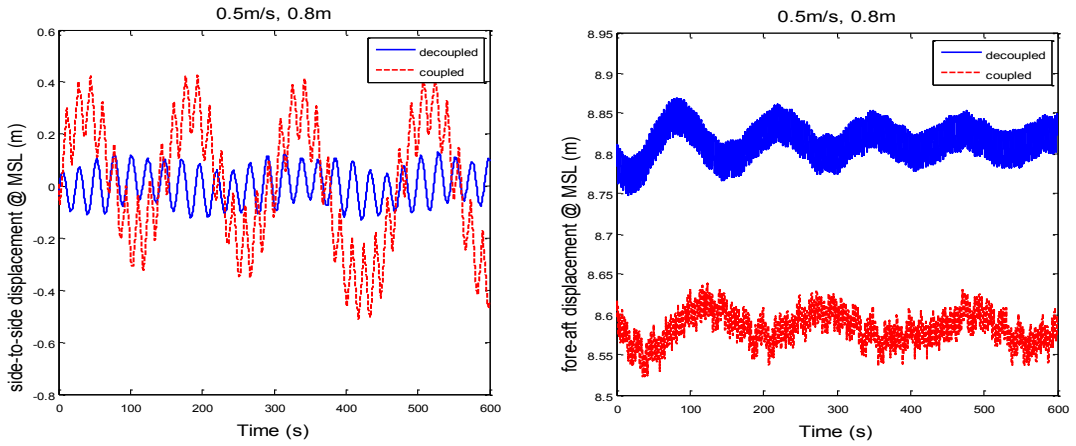

Figure 4.21: Time series of the side-to-side and fore-aft displacements at the MSL for LC3.3 for a decoupled vs. a coupled analysis

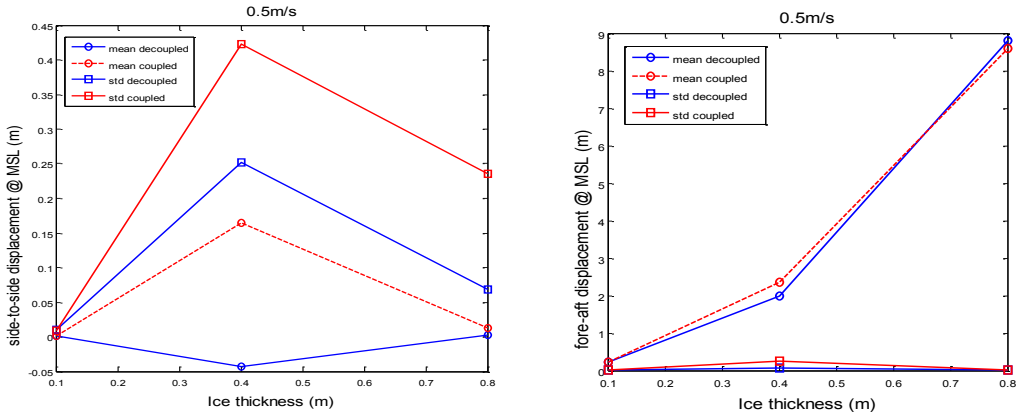

Figure 4.22: Statistical characteristics of the side-to-side and fore-aft displacements at the MSL with different ice thicknesses and constant ice drifting speed (0.5mps) for a decoupled vs. a coupled analysis

Figure 4.23 shows the spectrum of the side-to-side overturning moment at the MSL with different ice thicknesses for both coupled and decoupled analysis from time series in Figure 4.19, Figure 4.20 and Figure 4.21. The response presents 2 main peaks for all the ice sheets tested. For the thickest ice case, the peaks are observed at 0.0019Hz and

0.061Hz which might correspond to excitation of a combination of yaw and roll/pitch motions. For the 2 other cases, the peaks are observed at around 0.0057 Hz and 0.035 Hz which might correspond respectively to excitation of sway mode and the response to roll motions. So, for both coupled and decoupled analysis the same peaks are observed. However, the amplitude of the response is more important for the coupled analysis.

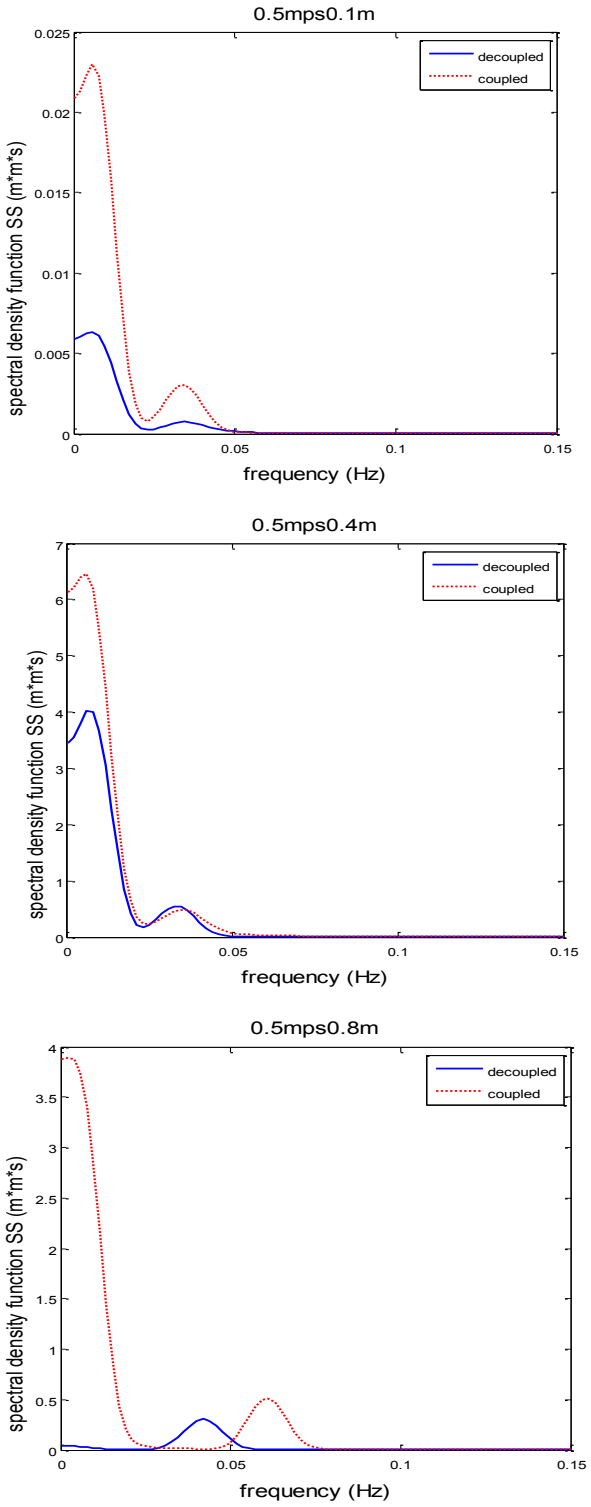

Figure 4.23: Spectrum of the side-to-side displacements at the MSL with different ice thicknesses and constant ice drifting speed (0.5mps) for a decoupled vs. a coupled analysis

Figure 4.24 shows the spectrum of the fore-aft overturning moment at the MSL with different ice thicknesses for both coupled and decoupled analysis from time series in Figure 4.19, Figure 4.20 and Figure 4.21. The response presents 2 main peaks for the intermediate case tested and only one for the 2 other cases. For the intermediate ice case, the peaks are observed at around 0.0057 Hz and 0.035 Hz which might correspond respectively to excitation of surge mode and the response to pitch motions. For the 2 other cases, one peak is observed really close to 0 but it is hard to tell which mode is responsible for this response seeing the eigenfrequency analysis results. The response amplitude is more important for the decoupled model for the 0.1 and 0.8m thick ice while it is smaller for the 0.4m thick ice than for the coupled model. It is in accordance with the observations made with the time series. Moreover, the peaks are occurring for the same frequencies in the 2 models.

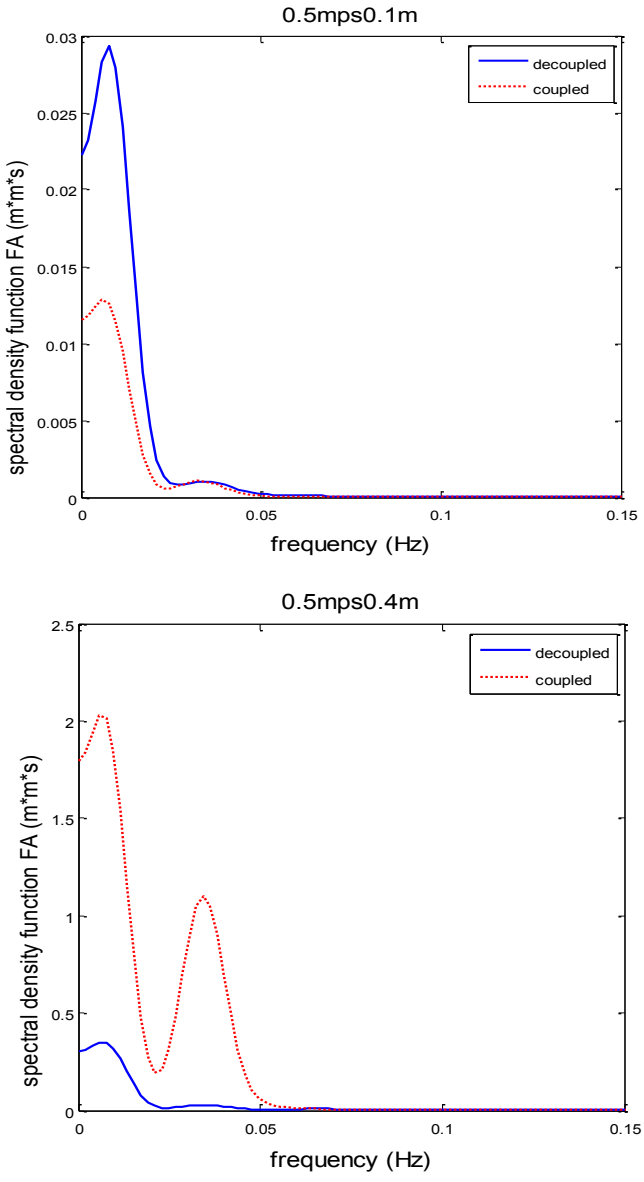

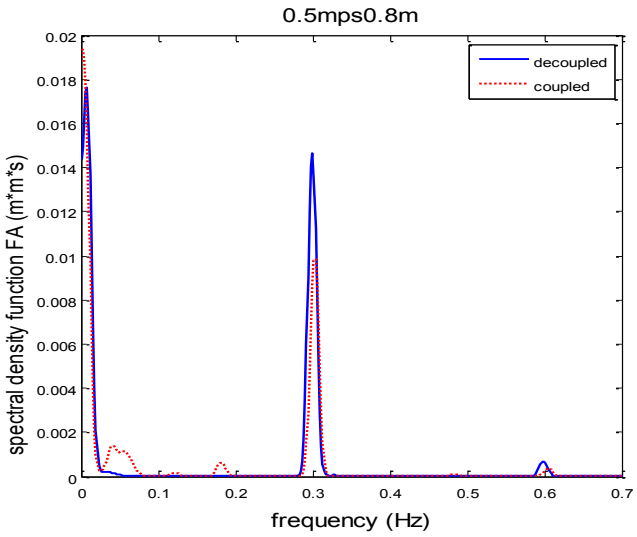

Figure 4.24: Spectrum of the fore-aft displacements at the MSL with different ice thicknesses and constant ice drifting speed (0.5mps) for a decoupled vs. a coupled analysis

4.3.3. Roll and pitch motions at MSL

Figure 4.25, Figure 4.26, Figure 4.27 and Figure 4.28 describe the behavior of pitch and roll angles for increasing ice thickness for both the coupled and the decoupled models. Contrary to displacements graphs, roll and pitch present a satisfying number of cycles in the effective simulation time. This is due to the difference in eigenperiod for the different motions – 128.8s for surge/sway vs. 30.8s for roll/pitch. The observations made from these figures corroborate the observations made with the displacement curves. Indeed, the platform will be more pitched toward the –y-direction. So the structure will be pushed in the y-direction by the ice cover and thus pitched toward the –y-direction. Moreover, the pitch will oscillate with an higher frequency with increasing ice drifting speed i.e. the cycle formed by contact-ice failure-new contact is shortened due to the increased ice thickness. However, it is more difficult to state on the dependency to the ice thickness for the side-to-side oscillations. For the roll motion mean value, the same divergence in behavior is observed than in the case of the mean value for the SS displacements and it also seems to be concurring with the restrictions in displacements observed for thicker ice sheets.

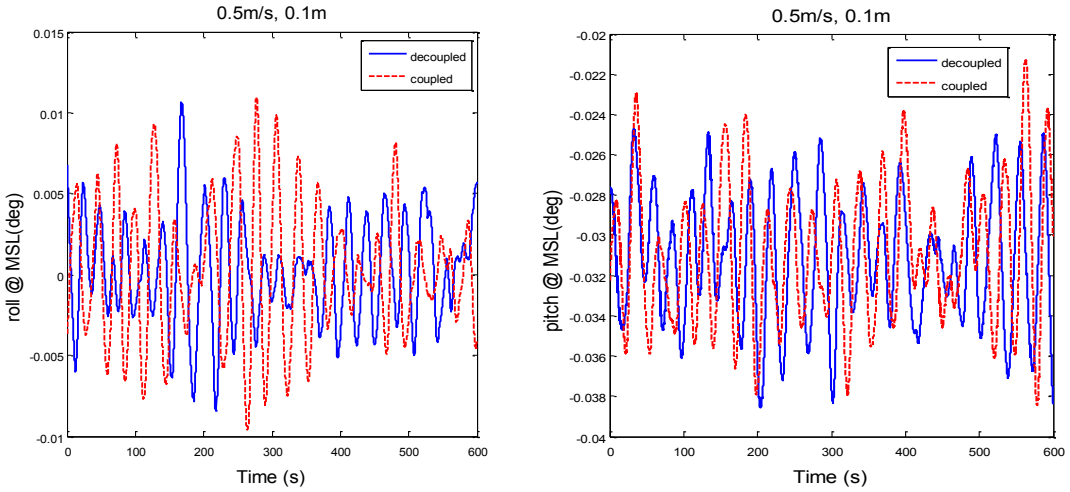

Figure 4.25: Time series of the roll and pitch motions at the MSL for LC3.1 for a decoupled vs. a coupled analysis

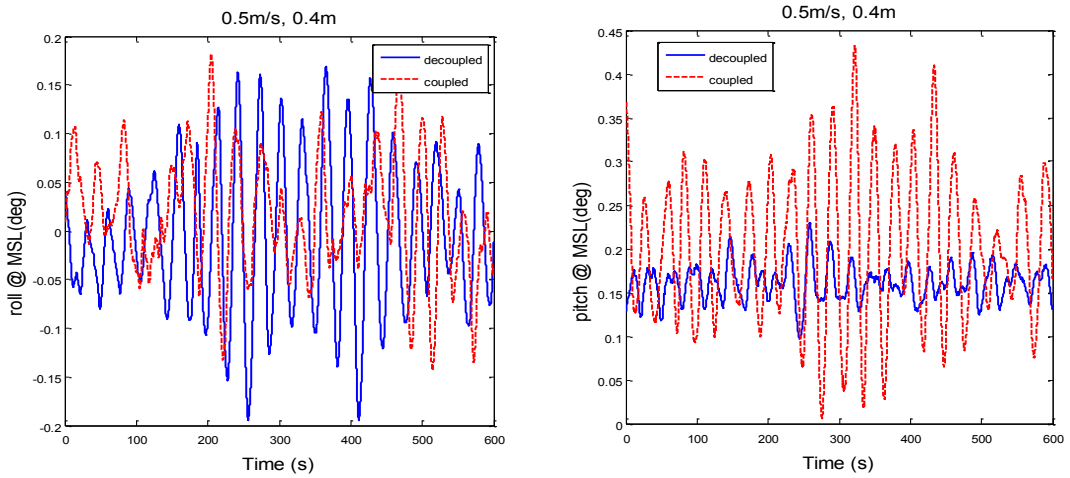

Figure 4.26: Time series of the roll and pitch motions at the MSL for LC3.2 for a decoupled vs. a coupled analysis

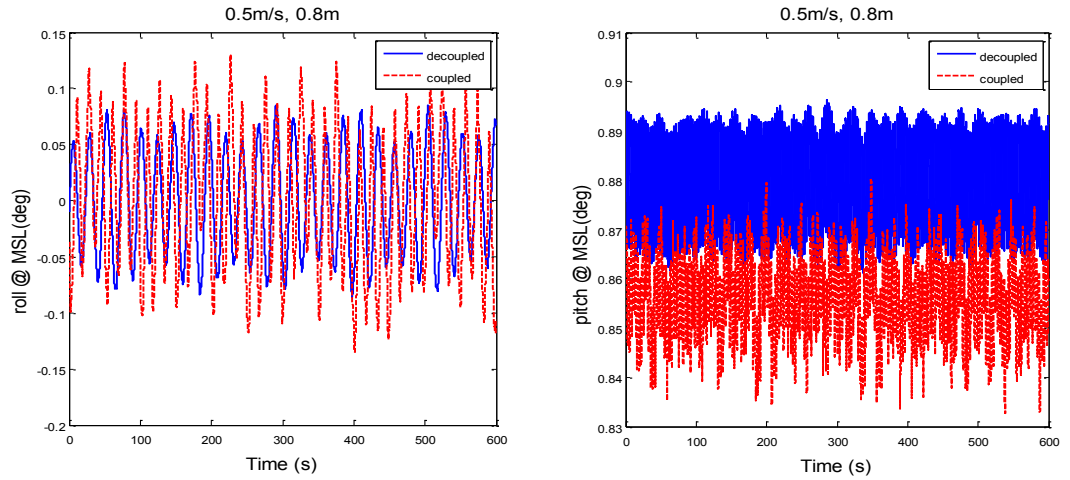

Figure 4.27: Time series of the roll and pitch motions at the MSL for LC3.3 for a decoupled vs. a coupled analysis

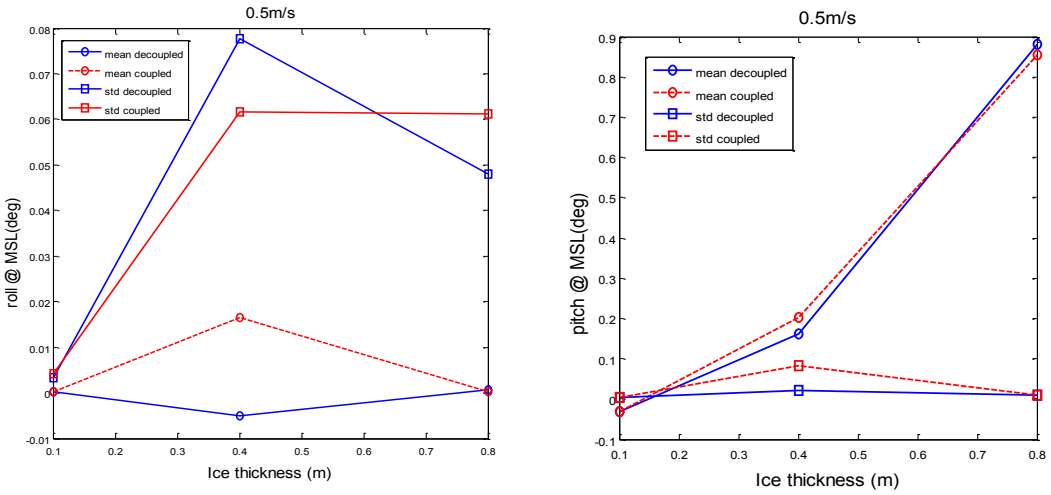

Figure 4.28: Statistical characteristics of roll and pitch motions at the MSL with different ice thicknesses and constant ice drifting speed (0.5mps) for a decoupled vs. a coupled analysis

4.3.4. Fore-aft force at MSL

Figure 4.29, Figure 4.31 and Figure 4.33 present the time series of the fore-aft force at the MSL for different ice thicknesses. With increasing ice thickness, the fore-aft force at MSL increases as shown by the statistical results (Figure 4.35). This increase in loading is also expected as thicker ice will induce a bigger contact area and thus higher loads. The general conclusions are the same as the ones drawn in section 4.3.1 due to the proportionality between the FA moments and forces. However, the maximal difference between the coupled and the decoupled models is obtained for the load case 0.5mps 0.4m and is slightly higher than for the FA moment concerning the standard deviation – around 18% instead of 16% - and quite smaller concerning the difference in mean value – around 20% instead of 67%.

Figure 4.30, Figure 4.32 and Figure 4.34 are zooms of respectively Figure 4.29, Figure 4.31 and Figure 4.33. These zooms are encompassing period range of 130s – roughly the highest eigenperiod of the structure. As explained in the introduction of §4.3, as soon as the first time step is solved, the conditions are different for the coupled and the decoupled model. Moreover the time interval are not the same due to different transient periods. So, the aim of these zooms is to spot comparable events for the FA force displayed in the decoupled and the coupled models and spot the differences between the models.

Figure 4.30 shows the comparison between similar events for a 0.1m thick ice sheet drifting at 0.5mps. Globally the curves display the same shape with oscillations

encompassed roughly between -10 kN and 0 kN with higher negative peaks. The maximal peak magnitude is quite similar between the decoupled and the coupled models – respectively -20.4kN vs. -19.56 kN. Moreover, the curves display oscillation with a period of approximately 30s. This is concurring with the pitch eigenperiod found with the eigenanalysis (cf. §4.1).

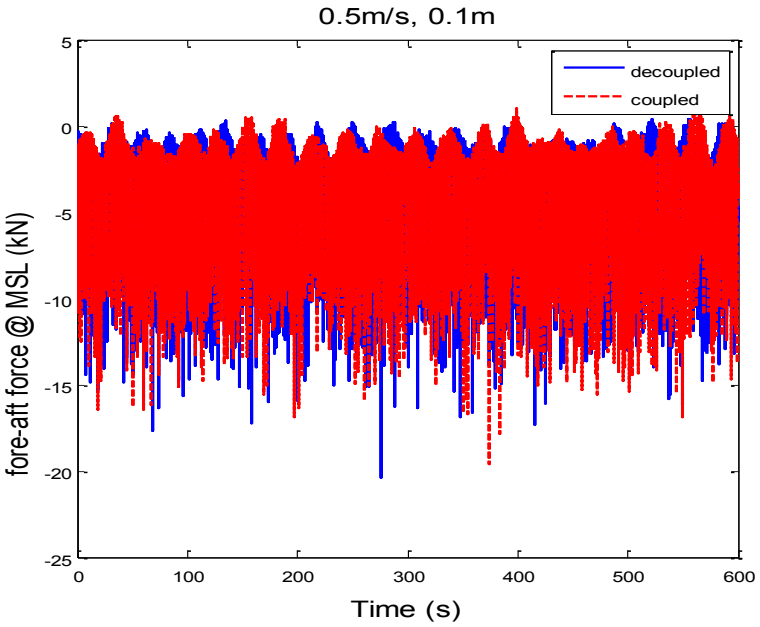

Figure 4.29: Time series of the fore-aft force at the MSL for LC3.1 for a decoupled vs. a coupled analysis

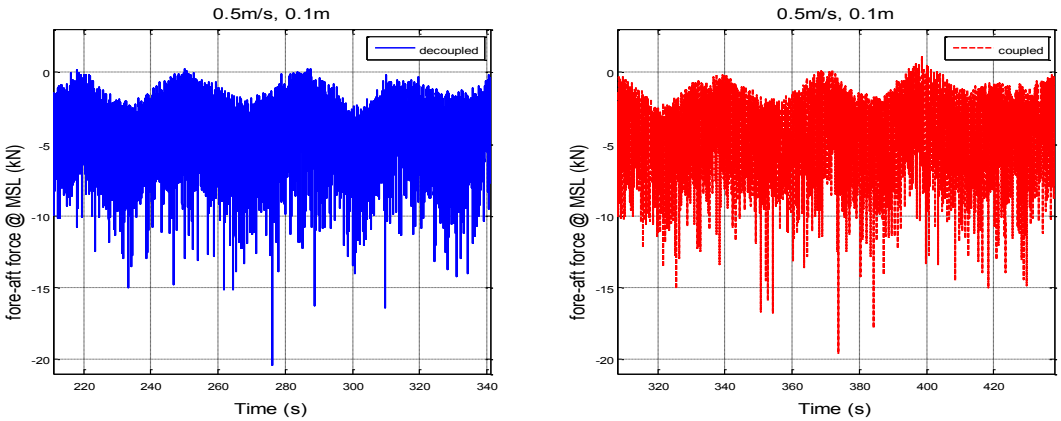

Figure 4.30: Zoom in on time series of the fore-aft force at the MSL for LC3.1 for a decoupled vs. a coupled analysis

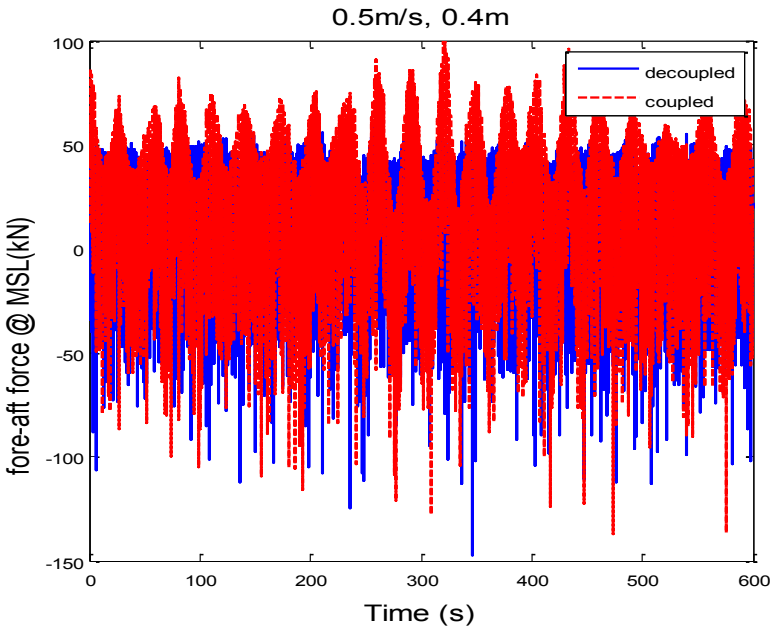

Figure 4.31: Time series of the fore-aft force at the MSL for LC3.2 for a decoupled vs. a coupled analysis

Figure 4.32 shows the comparison between similar events for a 0.4m thick ice sheet drifting at 0.5mps. Here, the differences between the 2 models are more noticeable. Indeed, the same magnitude is displayed for the maximum peaks but the oscillations range in the coupled model results are more important. For the decoupled model, the oscillations are mainly included in the interval [-50;50] kN while for the coupled model the range is [-50; 100] kN. The period of oscillation seems to be the same as observed in Figure 4.30. However, the oscillation period is hard to estimate for the decoupled model results.

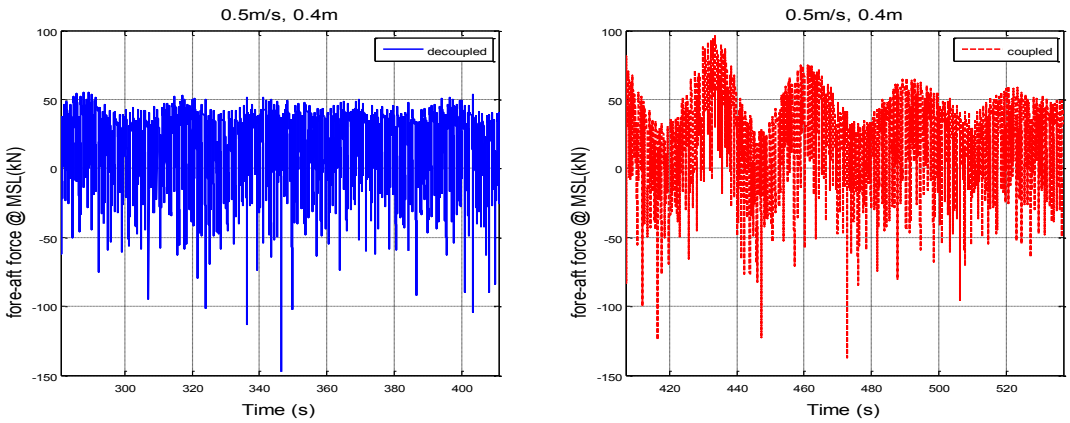

Figure 4.32: Zoom in on time series of the fore-aft force at the MSL for LC3.2 for a decoupled vs. a coupled analysis

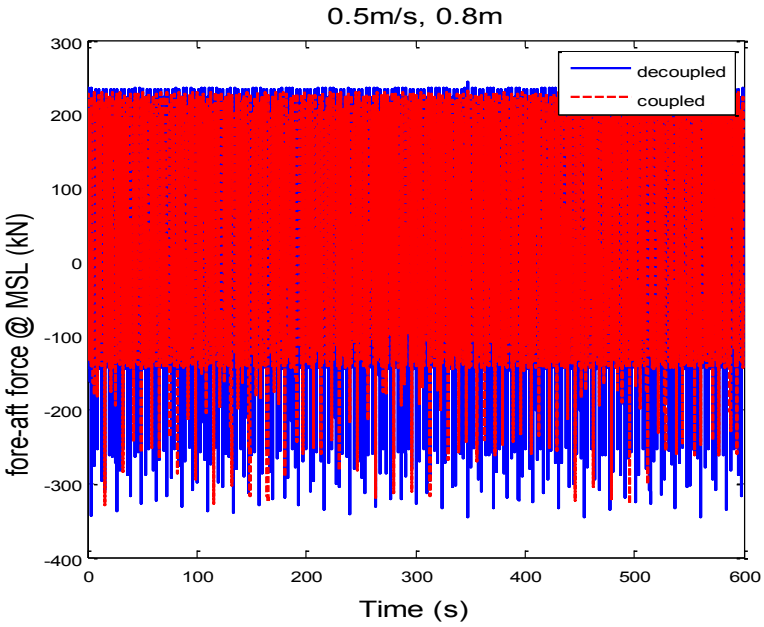

Figure 4.33: Time series of the fore-aft force at the MSL for LC3.3 for a decoupled vs. a coupled analysis

Figure 4.34 shows the comparison between similar events for a 0.8m thick ice sheet drifting at 0.5mps. As previously, we can observe comparable shapes encompassed in the range [-100; 200] kN. However, in this case, the decoupled analysis presents a larger density of higher peaks. Moreover, in this case, with thick ice, the pitch oscillation period is not easily discernable. The structure motions should thus be restrained by the ice sheet.

Finally, the 2 models seems to display relatively close static behaviors. However, there is some differences in the dynamic outputs. This could lead to important differences in long term design and results for fatigue study.

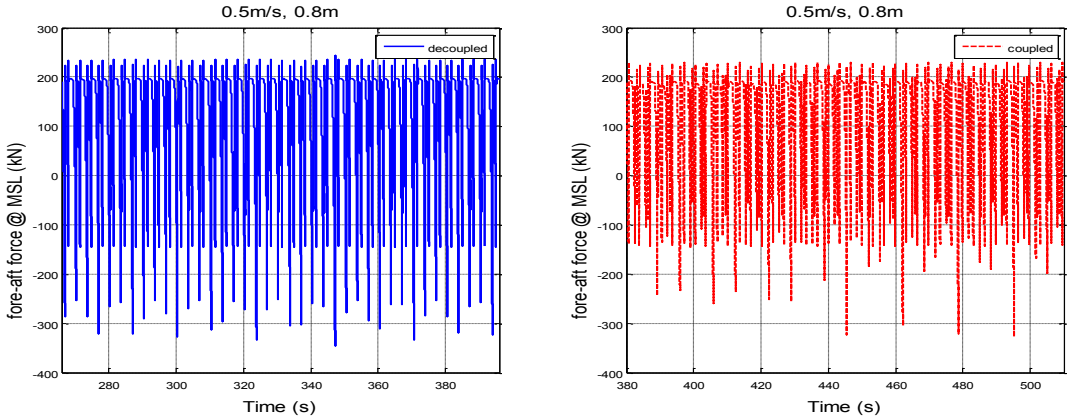

Figure 4.34: Zoom in on time series of the fore-aft force at the MSL for LC3.3 for a decoupled vs. a coupled analysis

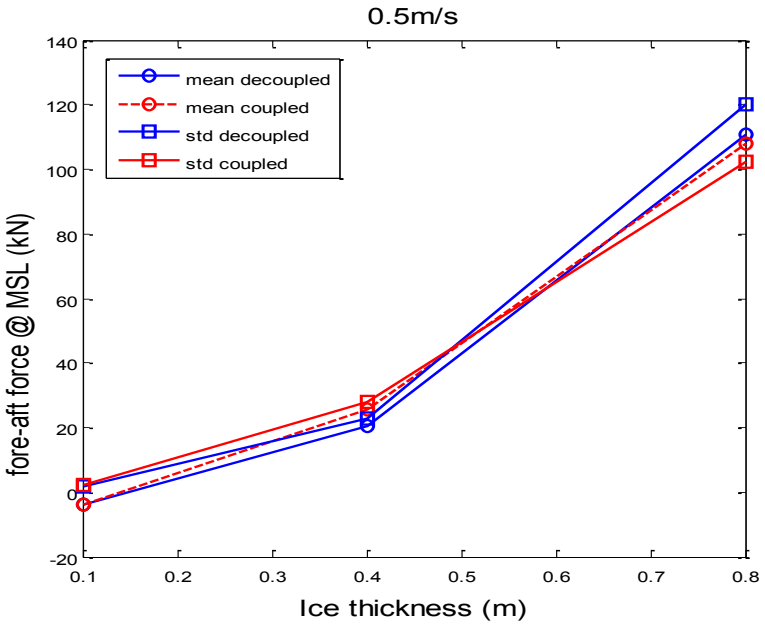

Figure 4.35: Statistical characteristics of the fore-aft force at the MSL with different ice thicknesses and constant ice drifting speed (0.5mps) for a decoupled vs. a coupled analysis

Figure 4.36 shows the spectrum of the fore-aft force at MSL corresponding to the time series displayed in Figure 4.29, Figure 4.31 and Figure 4.33. As observed in section 4.3.4, with increasing ice thickness, the response shows larger amplification. It confirms the influence of the ice thickness. The spectra obtained is quite similar to the one displayed by fore-aft overturning moment at the MSL (See Figure 4.18). The same modes are excited and the order of magnitude in the response between the different cases is similar. The only difference is the amplitude obtained for the same case between the FA moment and the FA force responses. Indeed, the amplitude is approximately 4.10^3 to 5.10^3 times higher in the case of the FA moment response.

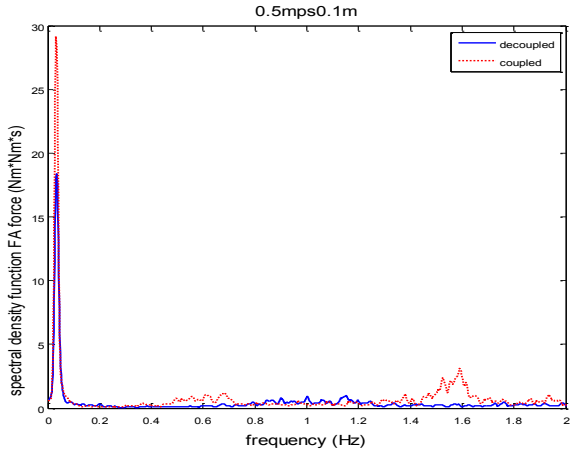

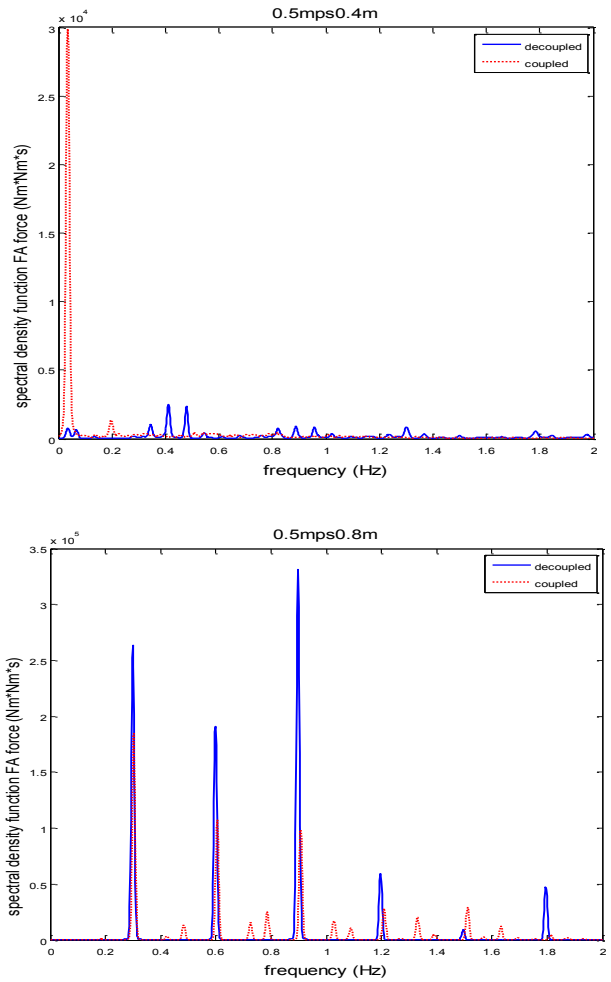

Figure 4.36: Spectrum of the fore-aft force at the MSL with different ice thicknesses and constant ice drifting speed (0.5 mps) for a decoupled vs. a coupled analysis

4.3.5. Fore-aft velocity at MSL

Figure 4.37, Figure 4.38 and Figure 4.39 present the time series of the fore-aft velocity at the MSL for different ice thicknesses. The statistical results (Figure 4.40) show that with increasing ice thickness, the fore-aft velocity will increase. It is linked to the increase in loads due to a larger contact area. It also highlights that the FA velocity at MSL will oscillate approximately at the same mean value in the coupled and decoupled models. However, the standard deviation will be way higher in the case of the coupled model. This must one more time be due to the fact that the decoupled model does not take into account the ice-structure interaction. Thus, the FA velocity at MSL is not properly estimated in the decoupled model. It should be noted that for the FA velocity the difference between the coupled and the decoupled are really high – at least 25% difference on the mean values. It is directly related to the definition of the decoupled model that does not take into account the ice-structure interactions. So the FA speed predicted by the

decoupled model will be quite off compared to a reliable coupled model and more generally to reality.

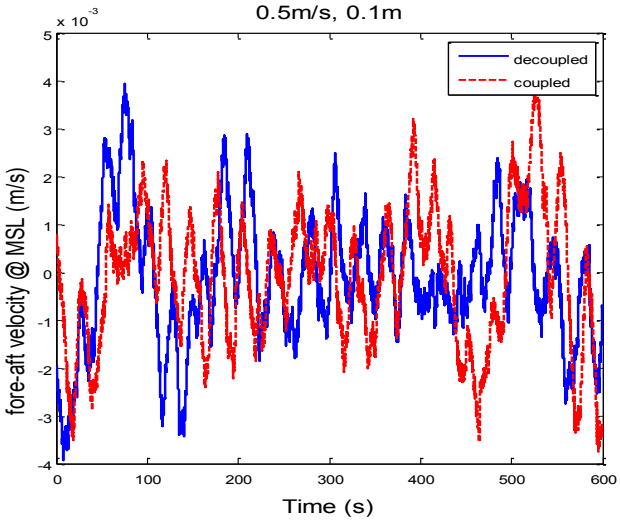

Figure 4.37: Time series of the fore-aft velocity at the MSL for LC3.1 for a decoupled vs. a coupled analysis

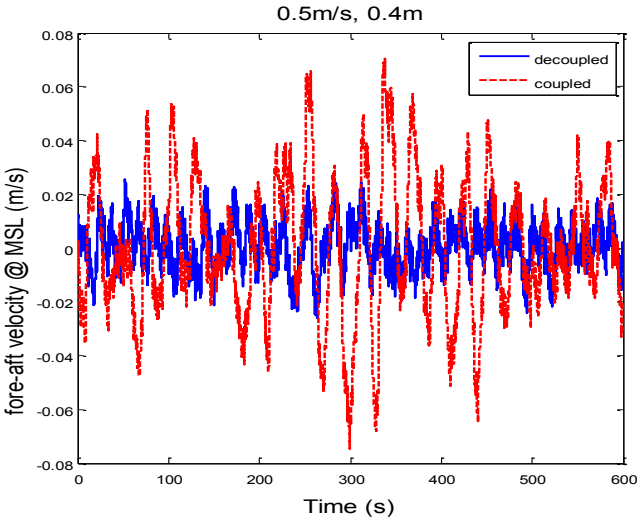

Figure 4.38: Time series of the fore-aft velocity at the MSL for LC3.2 for a decoupled vs. a coupled analysis

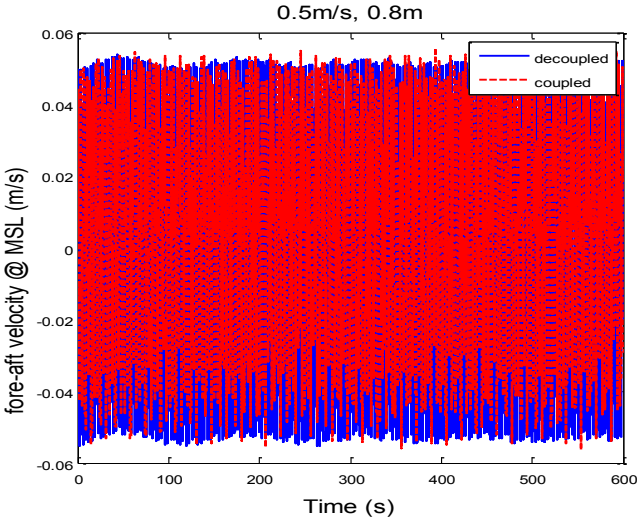

Figure 4.39: Time series of the fore-aft velocity at the MSL for LC3.3 for a decoupled vs. a coupled analysis

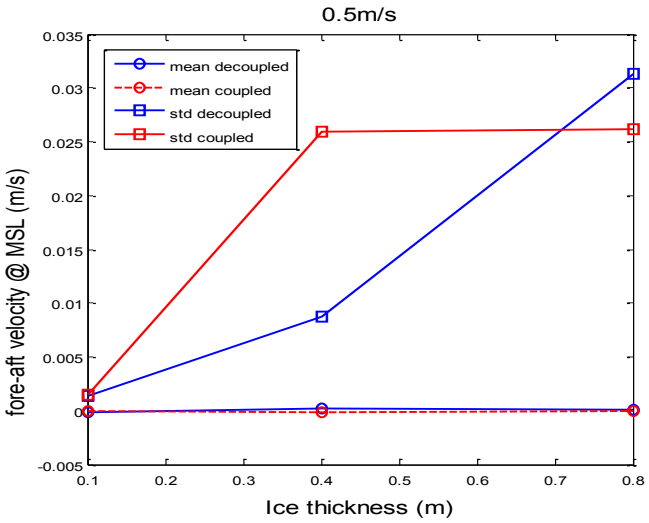

Figure 4.40: Statistical characteristics of the fore-aft velocity at the MSL with different ice thicknesses and constant ice drifting speed (0.5 mps) for a decoupled vs. a coupled analysis

4.4. Ice breaking pattern

In this section we are going to observe the ice breaking patterns obtained for different load cases. First, Figure 4.41 shows the initial relative position of the wind turbine and the incoming ice sheet. We can see that the ice is border is shaped like an idealized circular arcs as implemented in the bending crack model (Tan, et al., 2013). The ice sheet is modelled as a rectangle with a length of 16m and a width of 9m. At the initial time, the structure is not in contact with the ice sheet. Moreover, the ice sheet part that will be in contact with the structure once the ice will start to drift is purposefully shaped with a width smaller than the structure diameter. This way, it is ensured that the contact between the ice and the structure will occur. The axis conventions used here are the same as the one used in the HAWC2.

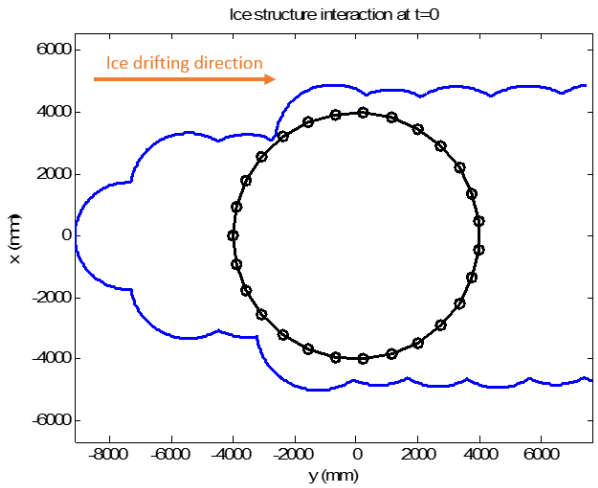

Figure 4.41: Ice-structure initial position (cases with no wind)

It is intended to compare the ice breaking patterns obtained for different ice conditions. To do so, on the first hand, the structure position is obtained from the initial conditions modified using the data on displacements of the structure. On the second hand, the DLL outputs the ice shape at the final time of the simulation only. So, it will be necessary to run simulations with different lengths to obtain the relative position of the structure and the ice sheet at different time steps. It is possible to proceed this way as no randomness is introduced in the simulations. The transient period at the beginning of each simulations should be avoided to provide representative displacements of the structure. Thus, the results will be plotted starting after 1600s – time where it was established that the transient effects have vanished for the LC involving only ice. So the first step was to determine the cases and the simulation lengths for each cases. It was chosen to study 6 different LCs: 4.1, 4.2, 4.3 and 4.4 without wind while 4.5 and 4.6 include wind (see numbering Table 4.5 below). This way, using LCs 4.1 and 4.3 it is possible to compare the influence of drifting speed on the ice breaking pattern while with cases 4.2, 4.3 and 4.4 the influence of the ice thickness can be highlighted. Finally, LCs 5 and 6 give an idea of the influence of wind on the ice breaking pattern by comparing them with LC 3. Once the cases chosen, it is then possible to determine the simulation length for each case using equations [1] and [2]. This will give an approximate estimation that will save time in simulations. For the LC 4.6 the simulation length was chosen based on the displacement curve (see Figure 3.22) to be in a zone of important motions. The different results and simulations settings are summarized in Table 4.5. The time steps is chosen to limit the number of simulations per cases to maximum 4. This decision is due to the limited time provided for the study.

Table 4.5: Simulation settings for ice breaking pattern observation

LC #	LC name	Estimated period from eq. [1] and [2] [s]	Chosen time period/time step [s]
4.1.	0_ice_mono_0.3mps0.4m_decoupled_no_wind_rigid	5.3-9.3s	9s/3s
4.2.	0_ice_mono_0.5mps0.1m_decoupled_no_wind_rigid	0.8-1.4 s	2s/1s
4.3.	0_ice_mono_0.5mps0.4m_decoupled_no_wind_rigid	3.2-5.6s	6s/2s
4.4.	0_ice_mono_0.5mps0.8m_decoupled_no_wind_rigid	6.4-11.2s	12s/4s
4.5.	0_ice_mono_0.5mps0.4m_decoupled_11.4mps_rigid	3.2-5.6s	6s/2s
4.6.	0_ice_mono_0.5mps0.4m_decoupled_11.4mps_rigid	3.2-5.6s	72s/36s

Figure 4.42 shows the simulated ice breaking pattern obtained for 0.4 m thick ice with a drifting speed of 0.5mps. Figure 4.43 shows the same plot but decomposed in several images for a better readability. The simulations are extending from 1605 to 1611s with a time step of 2s. We can see that during this interval the structure is pushed in the negative

–x direction and in the negative –y direction. It is both visible in Figure 4.42 and by comparing plots for t=1605s and t=1611s in Figure 4.43.

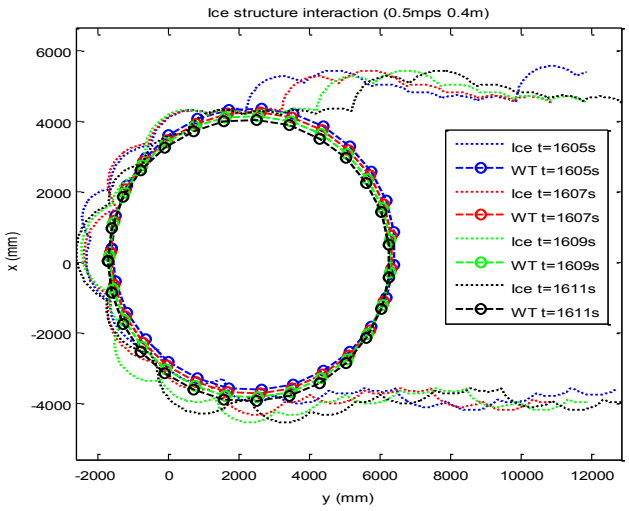

Figure 4.42: Simulated ice breaking pattern for LC 4.3

In Figure 4.43, the different contact zones are highlighted and the interaction areas numbered to follow more easily their respective movements. We can see that the ice is mainly interacting with the part of the structure that has the larger projected width. There, the ice is seen as overlapping the structure – actually it is only in contact with it – till the breaking failure is reached. Then, the ice breaks and a circular arc pattern appears. At the same time, the ice is dragged along the structure due to ice drift. After the ice has passed the structure first half it is not interacting anymore with it due to the structure shape. The radius of the breaking patterns seems to be bigger in the front part of the structure i.e. between -20° and 20°. In this area, the contact force must be more pronounced as it is harder for the ice to drift along the structure to be washed away.

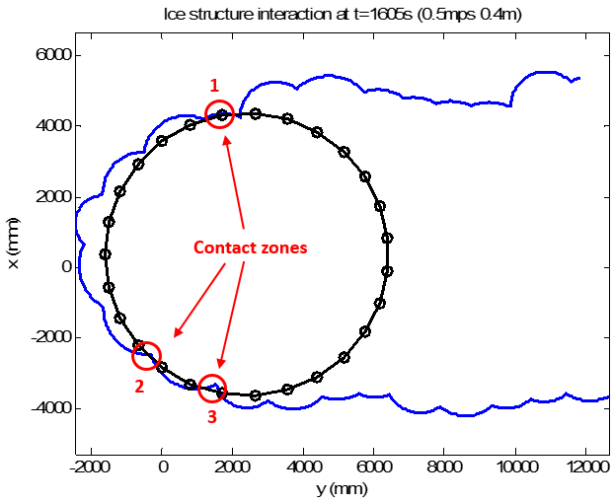

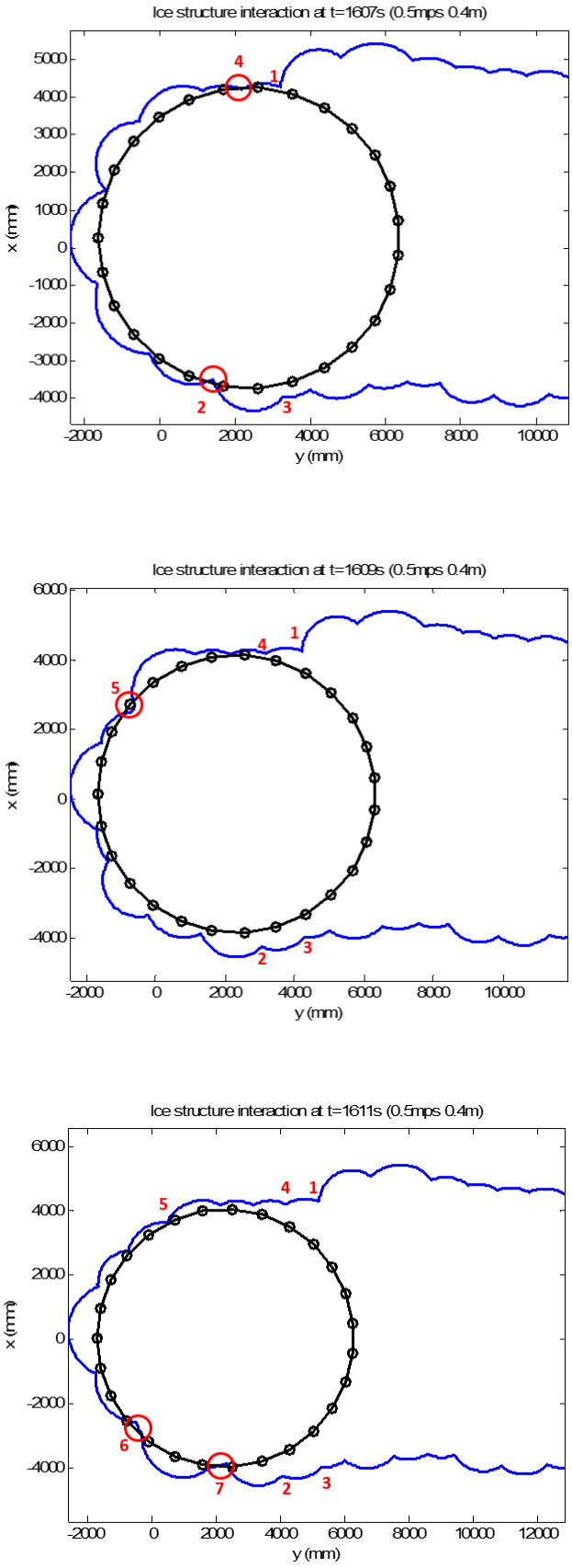

Figure 4.43: Decomposed simulated ice breaking pattern for LC 4.3

Figure 4.44 shows the ice breaking patterns for a 0.1m thick ice sheet drifting with a velocity of 0.5mps. We can see that in this case the ice breaking pattern is quite different. Indeed, almost the whole half of the cylinder is in contact with the ice sheet while in the previous case the contact areas where reduced to a few point. And, the radii of the circular arcs modelling the bending cracks are significantly reduced. So, as the ice is thinner, a bigger zone of contact in the (x;y) plane is needed to have the same contact area and thus reach the bending failure criterion. Moreover we can see that the ice trail behind the structure is tighter and fits within the 8m diameter of the structure while in the previous case it was enclosed in a nearly 10m wide area. It is linked to the fact that for thinner ice the displacement of the structure are quite reduced. As a consequence the ice channel opened is less wide.

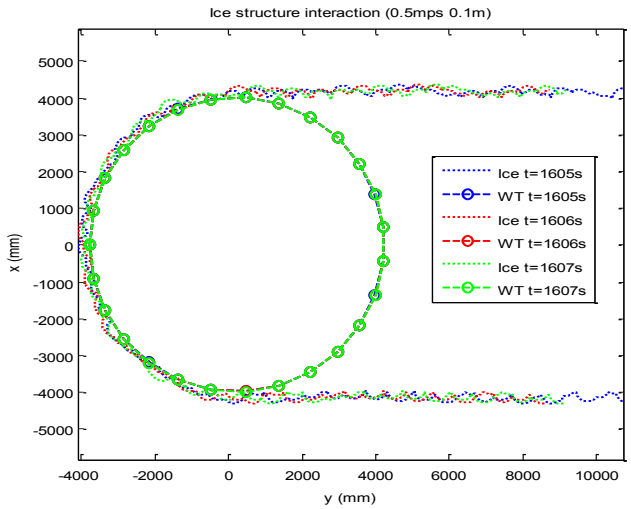

Figure 4.44: Simulated ice breaking pattern for LC 4.2

Figure 4.45 shows the ice breaking patterns for a 0.8m thick ice sheet drifting with a velocity of 0.5mps. We can see that in this case the channel opened behind the structure is one more time tighter than for a 0.4m thick ice sheet drifting with a velocity of 0.5mps. The structure is less oscillating (see §4.6.2) leading to an almost straight 8.5 meter wide channel. However, the channel opened is wider than for the case depicted in Figure 4.44. It must be due to the shape of the ice breaking pattern. Indeed, in this case, the ice sheet is interacting with the left half of the structure through maximum 3 bending cracks. The radius of these cracks is bigger than in the 2 previous cases and the contact zones are reduced to maximum 3 areas at a time numbered 1, 2 and 3 on Figure 4.45. The ice breaking events are occurring alternatively in zone 1, 2 and 3. For example, at t=1605s, the ice is close to the structure in zone 1. Thus, the breaking event will occurr there and

can be seen at t=1609s. At the same time the ice has gotten closer to the structure in zones 2 and 3 and at t=1613s we can note a breaking event in zone 3 and partly in zone 2. Finally, at t=1613s the ice has gotten closer to the structure in zone 2 and at t=1617s the breaking event can be seen there. This highlights the dynamic effect of ice breaking on the structure. Indeed, the floater will be submitted to dynamic loads due to the periodical ice breaking. These loads will result in dynamic motions of the spar and also introduce dynamic tension in mooring lines.

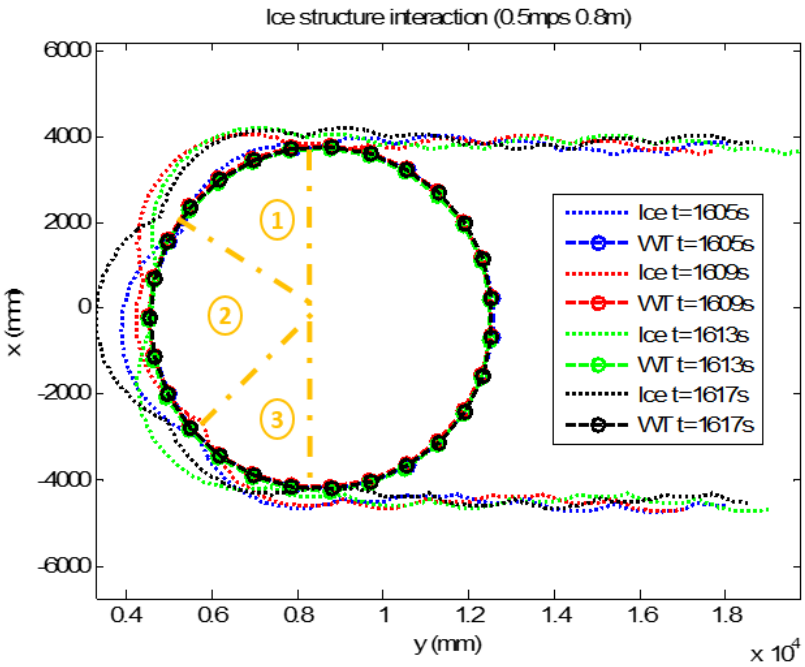

Figure 4.45: Simulated ice breaking pattern for LC 4.4

Figure 4.46 shows the ice breaking patterns for a 0.4m thick ice sheet drifting with a velocity of 0.3mps. We can see that in this case the ice breaking pattern is quite similar to the one observed for a 0.4m thick ice sheet drifting with a velocity of 0.5mps. Indeed, the number of contact areas and the radii of the circular arcs modelling the bending cracks are significantly close to the one observed in this previous case. Moreover, we can see that the ice trail behind the structure is tighter than for the LC 4.4 but wider than for the LCs 4.3 and 4.5 and fits within a nearly 8.5-9m wide area. So it seems that the strongest influence on the ice breaking pattern as a whole comes from the ice thickness while the ice drifting speed will mainly influence the ice breaking period.

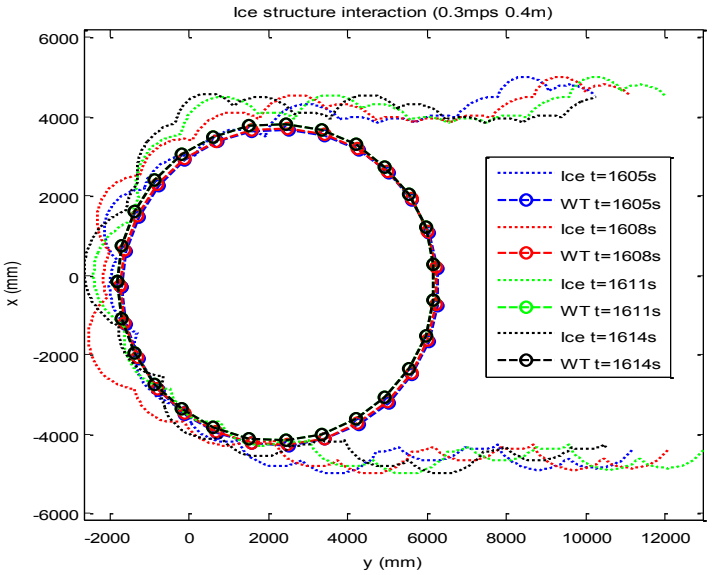

Figure 4.46: Simulated ice breaking pattern for LC 4.1

Figure 4.47 and Figure 4.48 show the ice breaking patterns for a 0.4m thick ice sheet drifting with a velocity of 0.5mps. Moreover, the structure is submitted to wind loads acting with a constant speed of 11.4mps. Figure 4.47 is enclosed in an interval similar to the one applied in Figure 4.42 while Figure 4.48 represents purposefully a longer interval where the structure presents large motions (as can be seen in Figure 3.22). From Figure 4.47, we can see that the structure displacements are less important than for LC 4.3 in the same time interval. Moreover, as also highlighted more clearly in Figure 4.48, these displacements are mainly in the fore-aft direction while for LC 4.3 side-to-side and fore-aft displacements were mixed. The ice breaking pattern seems quite similar to the one presented in the case without wind whether it is in the number of contact zones or the radii of the bending cracks. The only noticed difference is the ice breaking period. Indeed, by studying a particular contact zone, it seems that in case 4.5 the breaking event will occurs after 5 to 6s while in case 4.4 it occurs after around 4s. One explanation that comes in mind by looking at Figure 4.48 is that the wind tends to push the structure in the same direction as the ice drift in the simulated cases. Thus, it will take more time to reach the breaking failure criterion considering the same ice conditions. However, it is hard to conclude based on these cases alone. More cases should be tested applying different wind speed to get a better understanding of the situation. However, the time allocated to this work did not allowed further investigations.

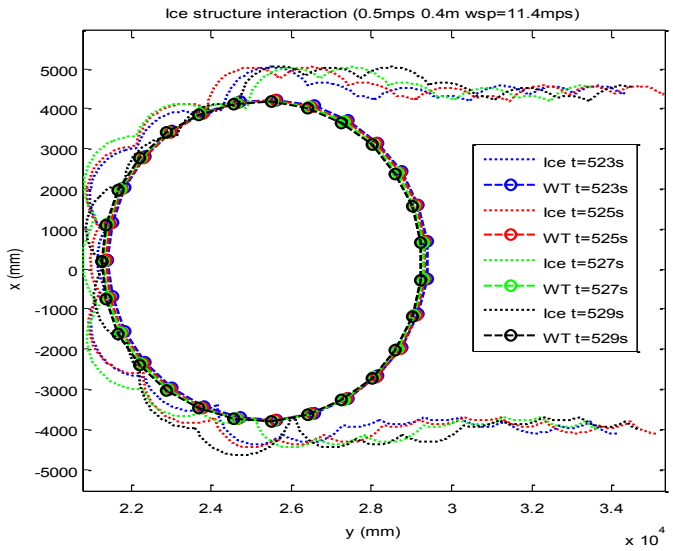

Figure 4.47: Simulated ice breaking pattern for LC 4.5

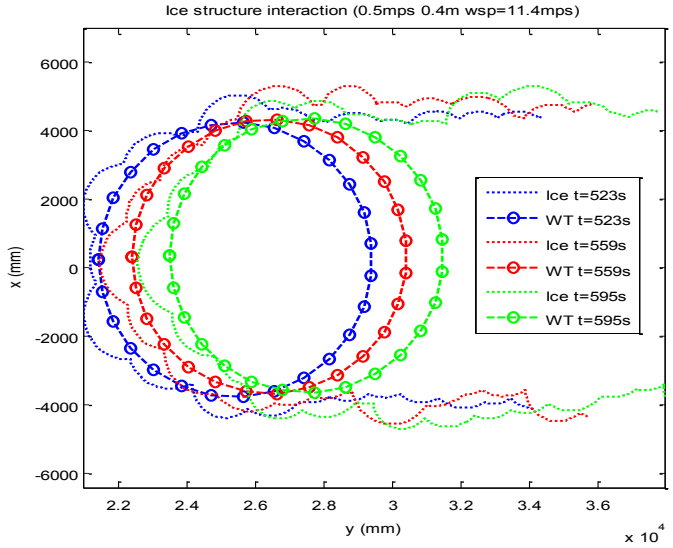

Figure 4.48: Simulated ice breaking pattern for LC 4.6

4.5. Influence of ice drifting speed

Three cases were chosen to investigate the influence of ice drifting speed on the structural behavior of the overall wind turbine. The wind turbine is under parked conditions for the 3 LCs. The ice field with a thickness of 0.4m has a drifting speed of 0.3 m/s, 0.4 m/s and 0.5m/s, respectively. A rigid wind turbine is studied for each load case. An overview for the cases is given in Table 4.6.

Table 4.6: Load cases to investigate the effect of ice drifting speed.

LC #	turbine wind speed [m/s]	ice speed [m/s]	Ice thickness [m]
5.1.	no wind	0.3	0.4
5.2.	no wind	0.4	0.4
5.3.	no wind	0.5	0.4

The time series are based on 3000s simulations where the first 1600s are not included in the interpretation in order to avoid transient effects that will distort the results.

4.5.1. Moment at MSL

Figure 4.49 and Figure 4.50 present the time series and statistical characteristics of the side-to-side and fore-aft overturning moment at the MSL for different ice drifting speeds when the coupled model is applied. In the case of the fore-aft moment, the statistical analysis shows that with increasing drifting speed the variation of the mean FA moment is not straight forward. Indeed, the intermediate case i.e. 0.4mps 0.4m the mean and the STD value are inferior to the ones for the extreme cases. So, it seems that this configuration is less critical for the structure.

For the side-to-side overturning moment, the mean value is approximately the same for all ice speeds and the response oscillates around the zero value due to the symmetry of the structure. But, as previously, the amplitude will be slightly smaller for the intermediate case.

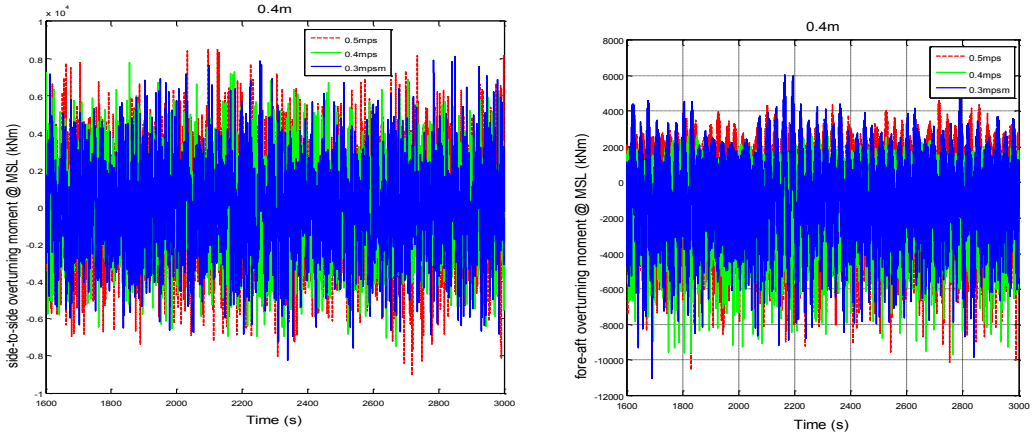

Figure 4.49: Time series of the side-to-side and fore-aft overturning moment at the MSL for LC5.1, 5.2 and 5.3

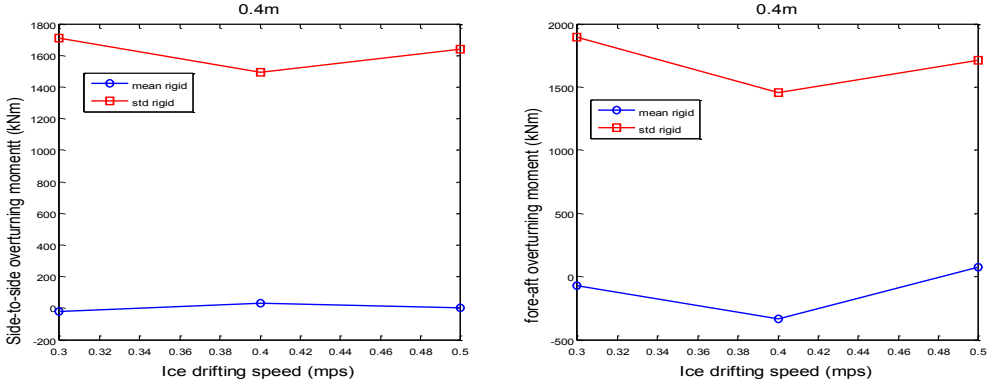

Figure 4.50: Statistical characteristics of the side-to-side and fore-aft over-turning moment at the MSL with different ice drifting speeds and constant ice thickness of 0.4m

Figure 4.51 shows the spectrum of the side-to-side overturning moment at the MSL with different ice drifting speeds. The response shows larger amplification for decreasing ice drifting speed. The roll mode is involved in all the cases (0.03Hz). Moreover, a wider peak is observed in all the case but its frequency decreases as the ice velocity decrease as it is mentioned in §2.4 (0.25Hz for 0.3mps, 0.28Hz for 0.4mps and 0.32Hz for 0.5mps). These peaks are linked to the 1st tower SS mode.

Figure 4.52 shows the spectrum of the fore-aft overturning moment at the MSL with different ice drifting speeds. The response shows larger amplification 0.3mps and the smallest amplification is displayed with 0.4mps which agrees with the observations made on the time series. One main mode (0.034Hz) is involved in all the cases. This excitation is linked to the pitch mode. Moreover, in the intermediate case, 2 additional peaks can be seen (0.33Hz and 0.38Hz) and are linked with the 1st tower FA mode.

Ice drifting speed does not seem to have a significant influence on the dynamic response.

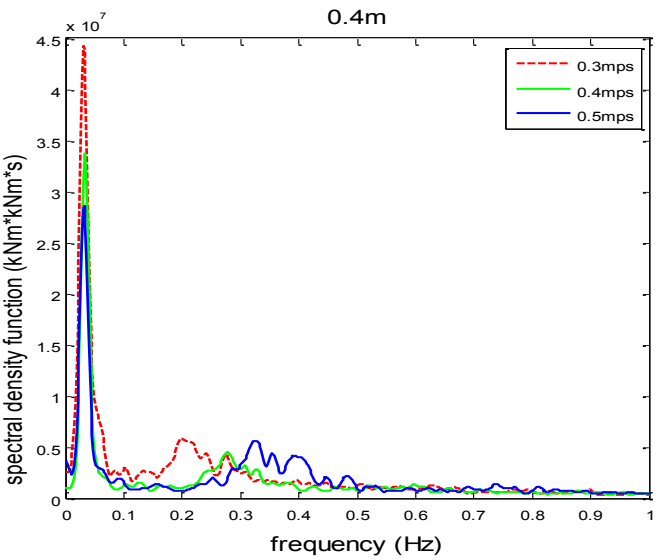

Figure 4.51: Spectrum of the side-to-side overturning moment at the MSL with different ice drifting speeds and constant ice thickness (0.4m)

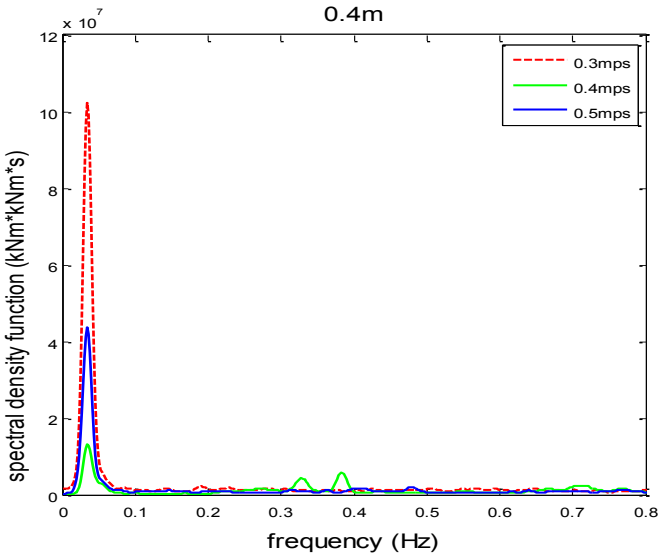

Figure 4.52: Spectrum of the fore-aft overturning moment at the MSL with different ice drifting speeds and constant ice thickness (0.4m)

4.5.2. Displacement at MSL

Figure 4.53 presents the time series of the side-to-side and fore-aft displacement at the MSL for different ice drifting speeds. The structure is pushed away in the fore-aft direction due to the ice loading. The statistical results (Figure 4.54) shows that the structure mean position does not vary a lot for varying ice drifting speed and the structure will be pushed by approximately 2m. The FA displacements present higher amplitudes for the 3mps case. There, it seems that the structure will have less freedom to oscillate in the SS direction. However, overall the variations observed are not important and the ice drifting speed does not seem to influence strongly the structure motions. Moreover, we can see that only few cycles of low-frequency motions are enclosed in the effective simulation time and it is not sufficient for a thorough analysis. Longer simulations would give a better understanding and more reliable results.

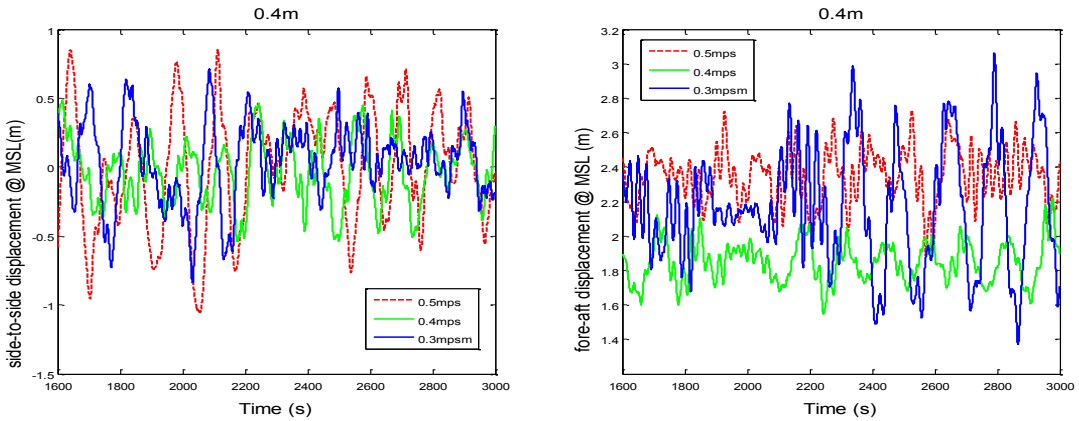

Figure 4.53: Time series of the side-to-side and fore-aft displacements at the MSL for LC 5.1, 5.2 and 5.3

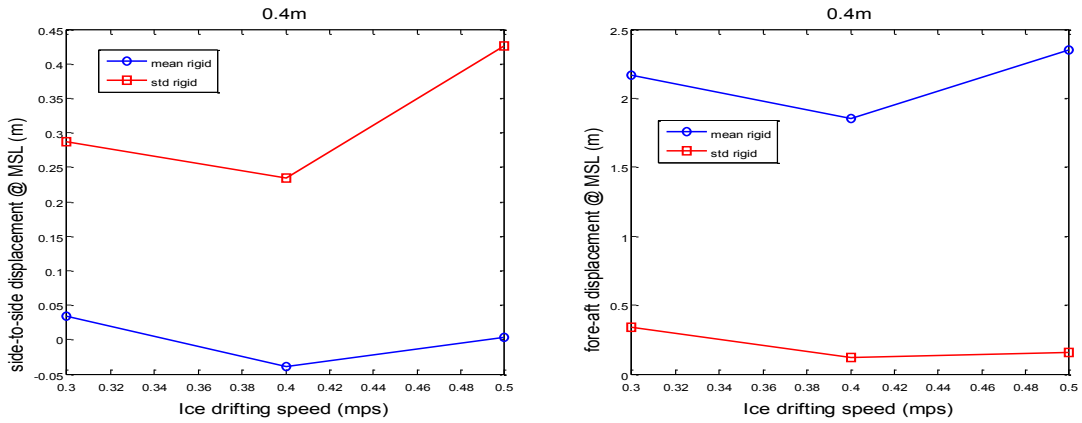

Figure 4.54: Statistical characteristics of the side-to-side and fore-aft displacements at the MSL with different ice drifting speeds and constant ice thickness of 0.4m

Figure 4.55 and Figure 4.56 show the spectrum of the side-to-side and fore-aft displacements at the MSL with different ice drifting speeds. First, in both cases, the spectrum is in accordance with the observations made on the time series.

In the case of the SS displacements, the response presents 1 main peak for all the ice sheets tested. These peaks are observed at 0.0057Hz for the slowest ice drifting speed and 0.0076Hz for the 2 other cases. These peaks are corresponding to the sway mode identified in the eigenfrequency analysis. Moreover a peak with small amplitude and a large range can be observed in all the cases around 0.03Hz. This can be due to an excitation of the roll mode.

In the case of the FA displacements, the response presents 2 main peaks (0.0057Hz and 0.034Hz for 0.3mps and 0.0076Hz and 0.034Hz for the 2 other cases). These peaks correspond respectively to the surge and the pitch mode.

These observations are backed up by comments in (Jonkman, et al., 2010):

"*Unless large loads are applied to the platform to react with the rapidly increasing mooring loads, the platform will tend to pitch as it translates in surge and will tend to roll as it translates in sway*".

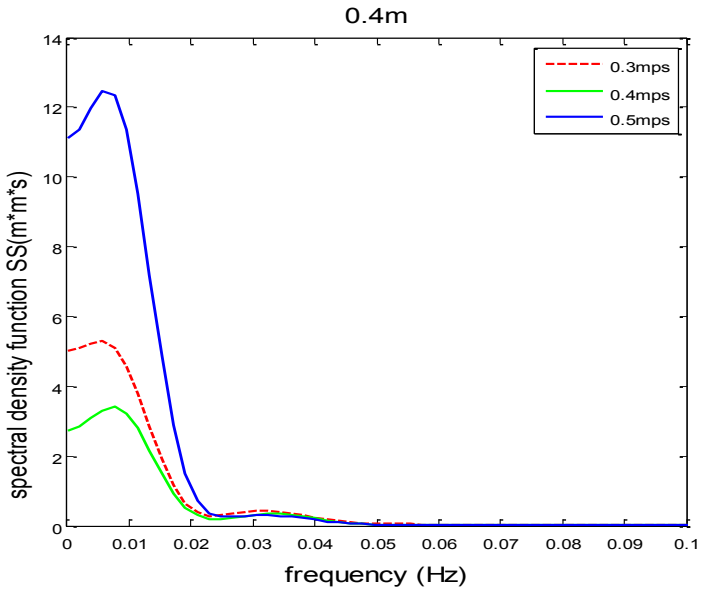

Figure 4.55: Spectrum of the side-to-side displacement at the MSL with different ice drifting speeds and constant ice thickness (0.4m)

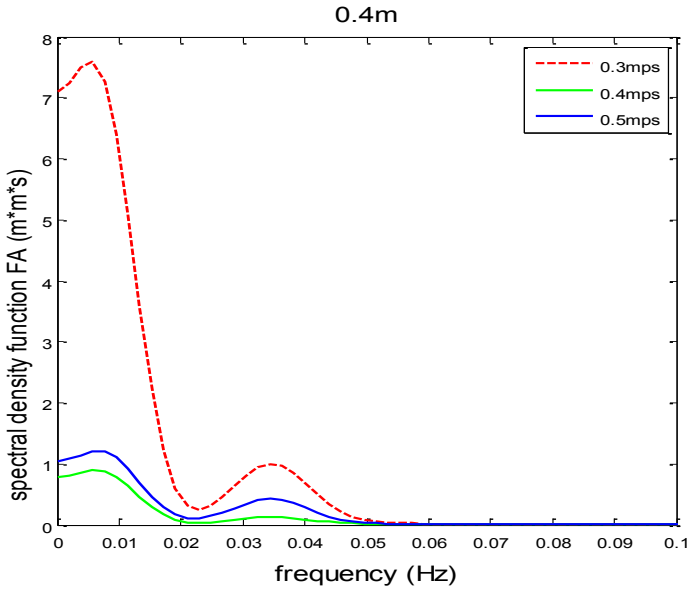

Figure 4.56: Spectrum of the fore-aft displacement at the MSL with different ice drifting speeds and constant ice thickness (0.4m)

4.5.3. Roll and pitch motions at MSL

Figure 4.57 and Figure 4.58 describe the behavior of pitch and roll angles for increasing ice drifting speed. The observations made from these figures corroborate the observations made with the displacement curves. The frequency of pitch and roll does not seem to vary much in the different configuration and is close to the natural period identified in the eigenfrequency analysis. One more time, the ice drifting speed does not seem to play a major role in the motion response.

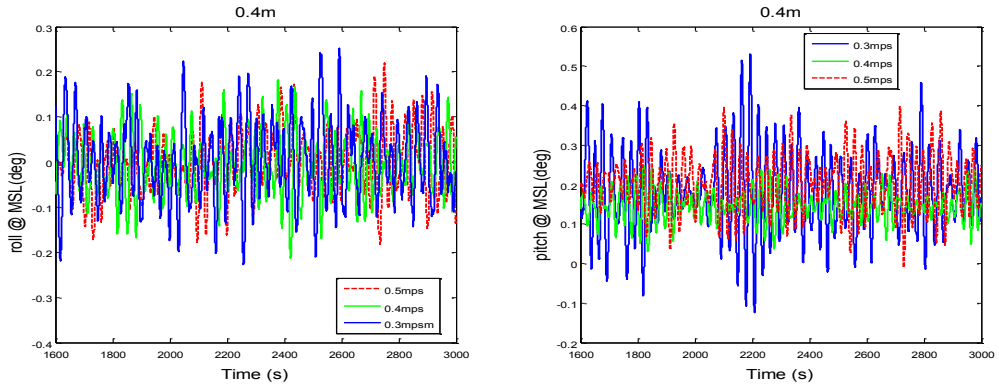

Figure 4.57: Time series of the roll and pitch at the MSL for LC 5.1, 5.2 and 5.3

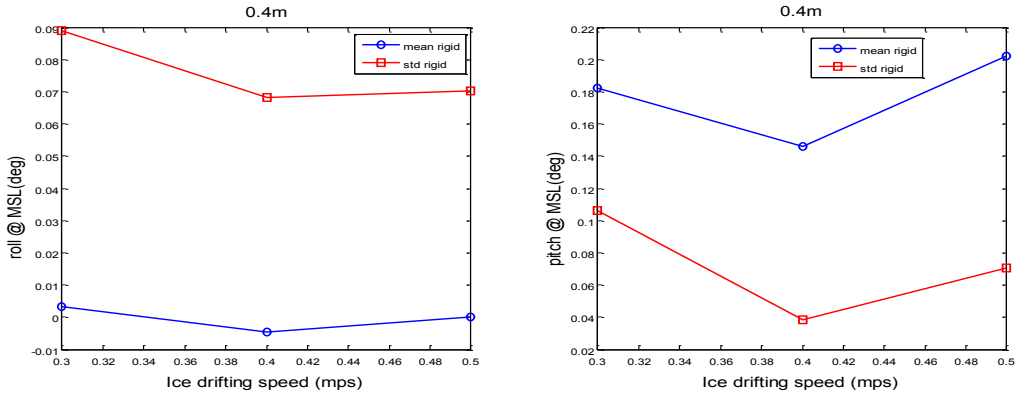

Figure 4.58: Statistical characteristics of the roll and pitch at the MSL with different ice drifting speeds and constant ice thickness of 0.4m

4.5.4. Fore-aft force at MSL

Figure 4.59 present the time series of the fore-aft force at the MSL for different ice drifting speeds. With increasing ice drifting speed, the fore-aft force at MSL does not significantly vary as shown by the statistical results (Figure 4.60). The general conclusions are the same as the ones drawn in section 4.5.1 due to the proportionality between the FA moments and forces.

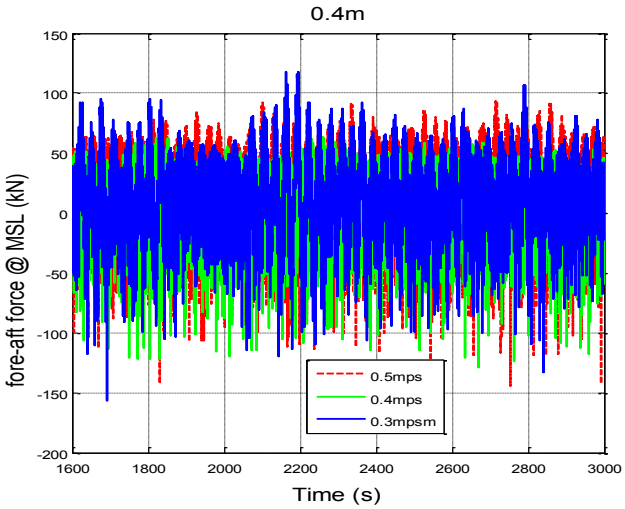

Figure 4.59: Time series of the fore-aft force at the MSL for LC 5.1, 5.2 and 5.3

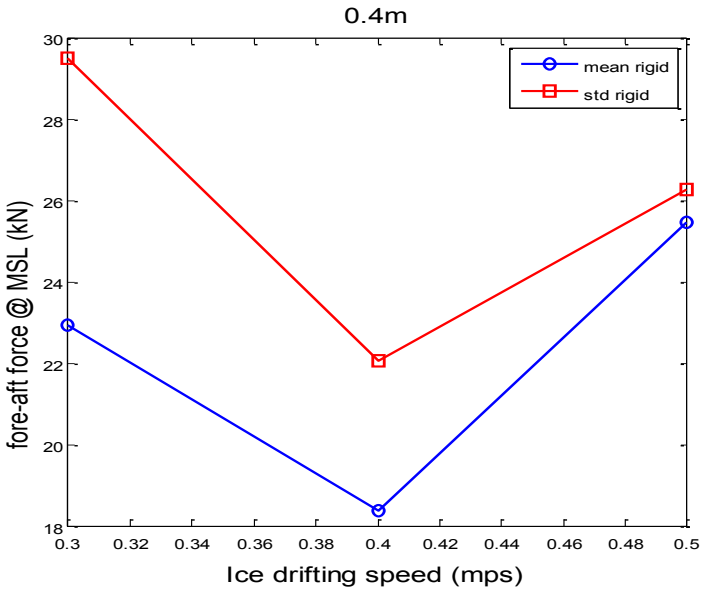

Figure 4.60: Statistical characteristics of the fore-aft force at the MSL with different ice drifting speeds and constant ice thickness of 0.4m

Figure 4.61 shows the spectrum of the fore-aft fore at MSL corresponding to the time series displayed in Figure 4.59. The response shows the largest amplification with a drifting speed of 0.3mps. The spectrum obtained is quite similar to the one displayed by fore-aft overturning moment at the MSL (See Figure 4.52). The same modes are excited and the order of magnitude in the response between the different cases is similar. The only difference is the amplitude obtained for the same case between the FA moment and the FA force responses. Indeed, the amplitude is approximately 4.10^3 times higher in the case of the FA moment response.

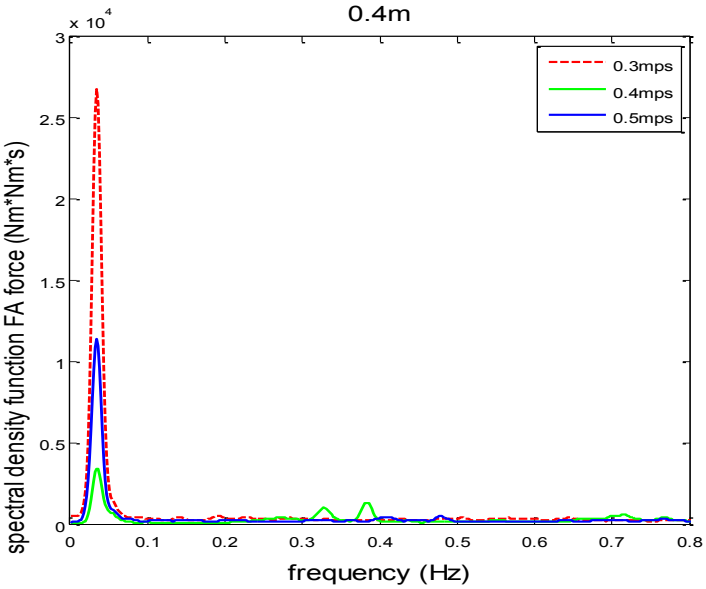

Figure 4.61: Spectrum of the fore-aft force at the MSL with different ice drifting speeds and constant ice thickness (0.4m)

4.5.5. Fore-aft velocity at MSL

Figure 4.62 present the time series of the fore-aft velocity at the MSL for different ice drifting speeds. The statistical results (Figure 4.63) show that with decreasing ice drifting speed, the fore-aft velocity amplitude will increase. It also highlights that the FA velocity at MSL will oscillate at approximately the same mean value in each case. However, the FA velocity seems to be reaching a maximum STD of around 0.03mps for a drifting speed of 0.3mps i.e. 10% of the ice sheet drifting velocity. And for the 2 other cases, the maximum reached is around 4% of the ice drifting speed.

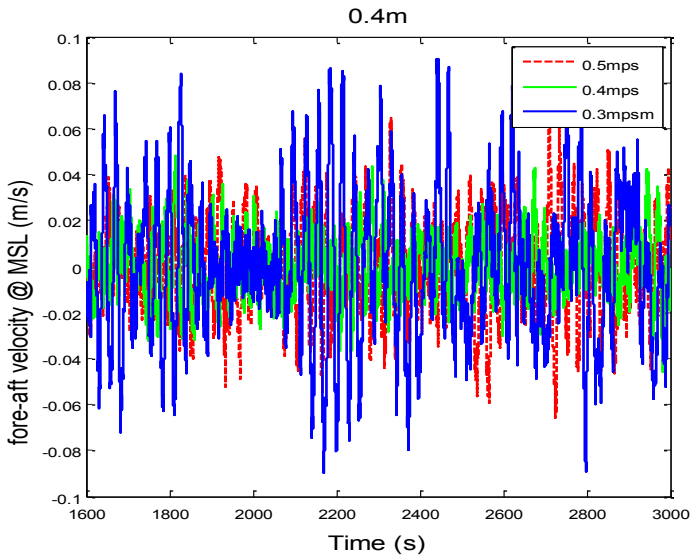

Figure 4.62: Time series of the fore-aft velocity at the MSL for LC 5.1, 5.2 and 5.3

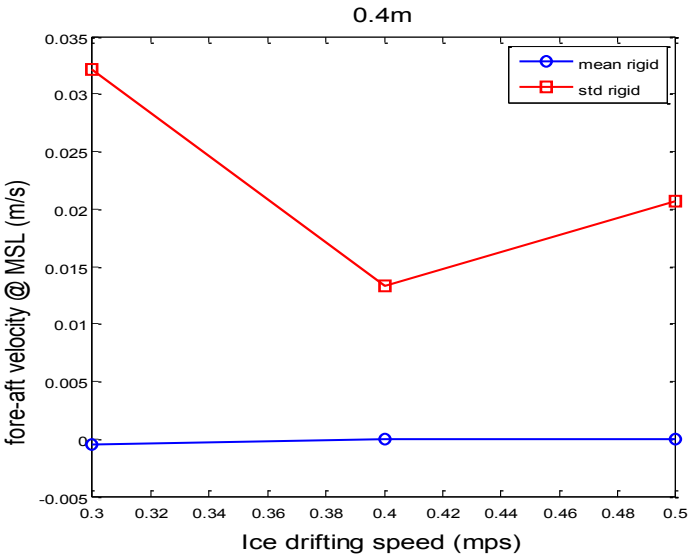

Figure 4.63: Statistical characteristics of the fore-aft velocity at the MSL with different ice drifting speeds and constant ice thickness of 0.4m

4.6. Influence of ice thickness

Three cases were chosen to investigate the influence of the ice thickness on the structural behavior of the overall wind turbine. The wind turbine is under parked conditions for the 3 LCs. The ice field with a drifting speed of 0.5m/s has a thickness of 0.1m, 0.4m and 0.8m, respectively. A rigid wind turbine is studied for each load case. An overview for the cases is given in Table 4.7.

Table 4.7: Load cases to investigate the effect of ice thickness.

LC #	turbine wind speed [m/s]	ice speed [m/s]	Ice thickness [m]
6.1.	no wind	0.5	0.1
6.2.	no wind	0.5	0.4
6.3.	no wind	0.5	0.8

The time series are based on 3000s simulations where the first 1600s are not included in the interpretation in order to avoid transient effects that will distort the results.

4.6.1. Moment at MSL

Figure 4.64 and Figure 4.65 present the time series and statistical characteristics of the side-to-side and fore-aft overturning moment at the MSL for different ice thicknesses when the coupled model is applied. In the case of the fore-aft moment, the statistical analysis shows that with increasing thickness we have increasing mean FA moment. This increase is expected. Indeed, thicker ice will induce a bigger contact area and thus higher loads.

For the side-to-side overturning moment, the mean value is approximately the same for all ice thicknesses and the response oscillates around the zero value due to the symmetry of the structure. But, the amplitude will increase with increasing ice thickness. So, the ice-structure interaction is more significant for thicker ice.

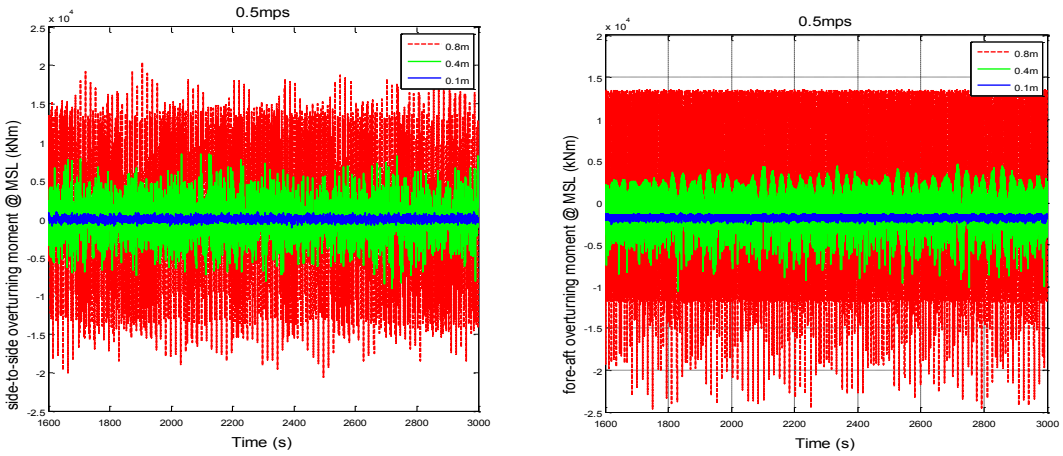

Figure 4.64: Time series of the side-to-side and fore-aft overturning moment at the MSL for LC6.1, 6.2 and 6.3

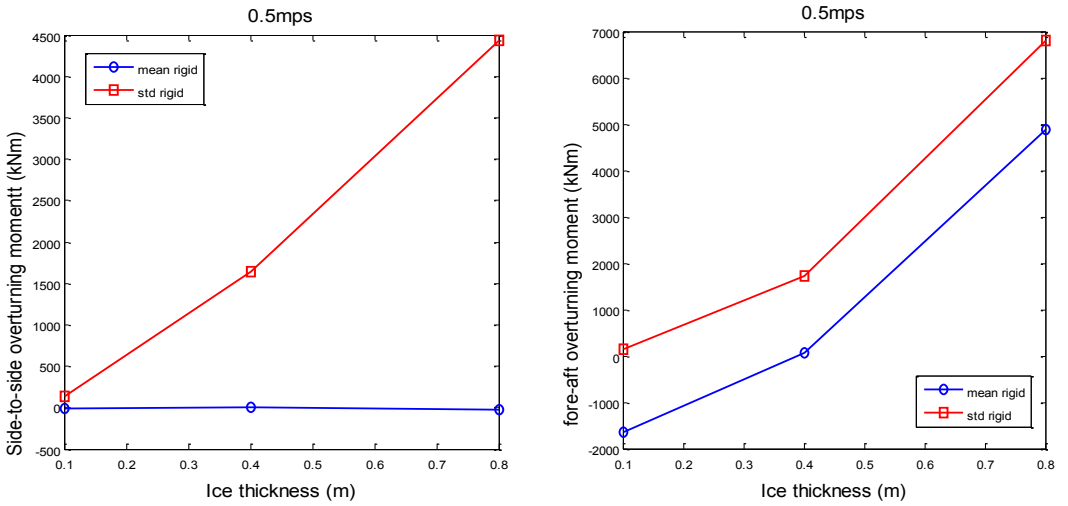

Figure 4.65: Statistical characteristics of the side-to-side and fore-aft over-turning moment at the MSL with different ice thicknesses and constant ice drifting speed of 0.5mps

Figure 4.66 shows the spectrum of the side-to-side overturning moment at the MSL with different ice thicknesses. The response shows larger amplification for increasing ice thickness. 1 mode (0.034Hz) and 2 modes (0.036Hz and 0.099Hz) are respectively involved for ice thicknesses of 0.1m and 0.4m. In the case of 0.1m thick ice, the excitation is linked to the roll mode. Same goes for 0.4m thick ice with an additional contribution of the yaw mode which can be combined with the pitch mode (same frequency as roll) to give SS motions. For larger ice thickness, the process becomes wide-banded and 7 peaks of comparable importance can be observed (0.061 Hz, 0.24Hz, 0.36Hz, 0.54Hz, 0.67Hz, 0.85Hz, and 0.97Hz). So, several modes of the structure are involved in the response for thick ice and it is hard to discern the different modes respective influence.

Figure 4.67 shows the spectrum of the fore-aft overturning moment at the MSL with different ice thicknesses. With increasing ice thickness, the response shows larger

amplification. It confirms the influence of the ice thickness. And, the pitch mode (0.03 Hz) is involved for the case 0.1m and 0.4m. Moreover, for both 0.4m and 0.8m thick ice a peak at 0.3Hz is observed. This could be due to a combination of platform yaw and the 1st tower SS mode that will result in a component in FA direction. For larger ice thickness, the process becomes wide-banded and 3 major peaks can be identified for the thicker ice sheet case (0.8m) that are 0.30Hz, 0.60Hz and 0.91Hz. The 2 last ones can be identified as contributions from modes 8 and 13.

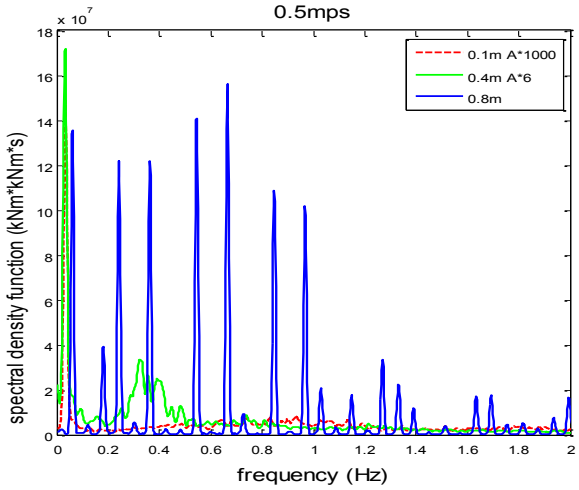

Figure 4.66: Spectrum of the side-to-side overturning moment at the MSL with different ice thicknesses and constant ice drifting speed (0.5mps)

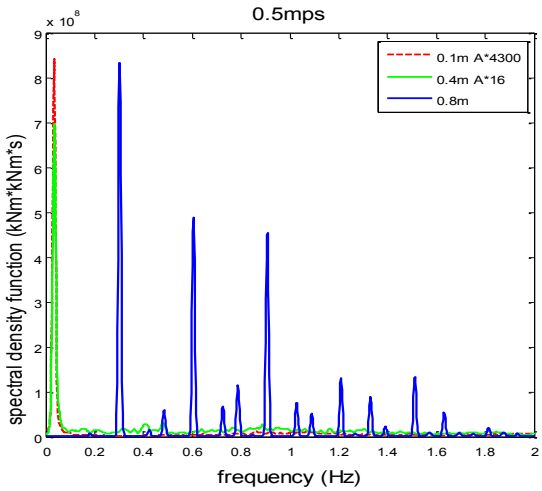

Figure 4.67: Spectrum of the fore-aft overturning moment at the MSL with different ice thicknesses and constant ice drifting speed (0.5mps)

4.6.2. Displacement at MSL

Figure 4.68 presents the time series of the side-to-side and fore-aft displacement at the MSL for different ice thicknesses. The structure is pushed away in the fore-aft direction due to the ice loading. The statistical results (Figure 4.69) shows that with increasing ice thickness the structure will be pushed further away. Also, with increasing thickness, the

oscillation in SS direction will be restrained and displacements for 0.4m thick ice will be more important than for 0.8m thick ice. Moreover, both for FA and SS displacements, the oscillations around the mean value are more pronounced for the intermediate case 0.5mps 0.4 m. So, it seems that for thicker ice the displacements of the wind turbine are restrained in both directions. Moreover, we can see that only few cycles of low-frequency motions are enclosed in the effective simulation time and it is not sufficient for a thorough analysis. Longer simulations would give a better understanding and more reliable results.

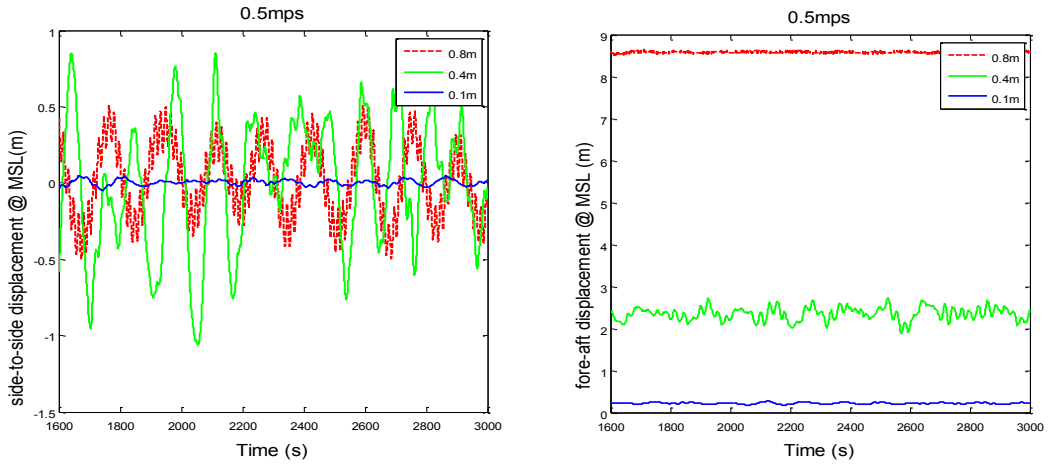

Figure 4.68: Time series of the side-to-side and fore-aft displacements at the MSL for LC 6.1, 6.2 and 6.3

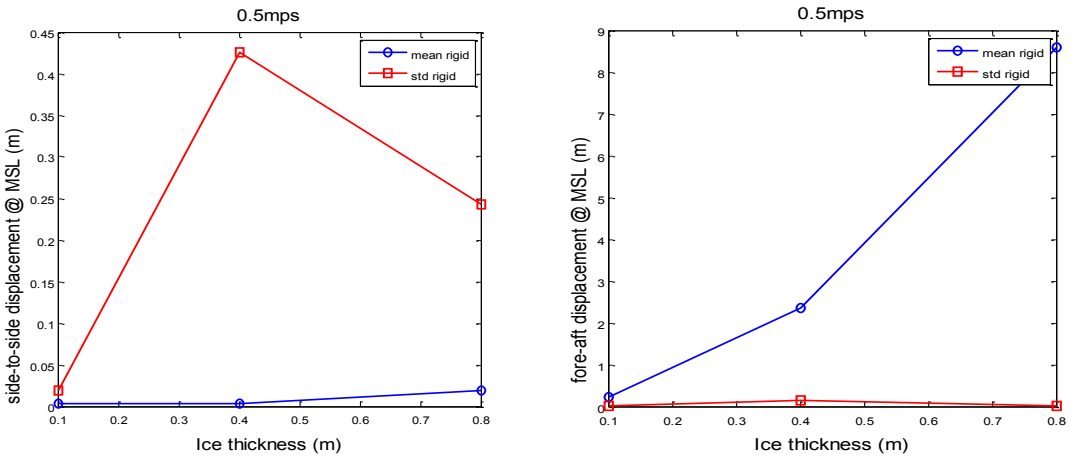

Figure 4.69: Statistical characteristics of the side-to-side and fore-aft displacements at the MSL with different ice thicknesses and constant ice drifting speed of 0.5mps

Figure 4.70 shows the spectrum of side-to-side and the fore-aft displacements at the MSL with different ice thicknesses. First, in both cases, the spectrum is in accordance with the observations made on the time series i.e. the oscillations around the mean value are more pronounced for the intermediate case 0.5mps 0.4 m.

In the case of the SS displacements, the response presents 2 main peaks for all the ice sheets tested. For the thickest ice case, the peaks are observed at 0.0019Hz and 0.061Hz

which might correspond to excitation of a combination of yaw and roll/pitch motions. For the 2 other cases, the peaks are observed at around 0.0057 Hz and 0.035 Hz which might correspond respectively to excitation of sway mode and the response to roll motions.

In the case of the FA displacements, the response presents 2 main peaks for the intermediate case tested and only one for the 2 other cases. For the intermediate ice case, the peaks are observed at around 0.0057 Hz and 0.035 Hz which might correspond respectively to excitation of surge mode and the response to pitch motions. For the 2 other cases, one peak is observed really close to 0 but it is hard to tell which mode is responsible for this response seeing the eigenfrequency analysis results.

These observations are backed up by comments in (Jonkman, et al., 2010):

"*Unless large loads are applied to the platform to react with the rapidly increasing mooring loads, the platform will tend to pitch as it translates in surge and will tend to roll as it translates in sway*".

So, this coupling in modes can be at the origin of the difficulty to identify a specific modes in the case of FA and SS displacements.

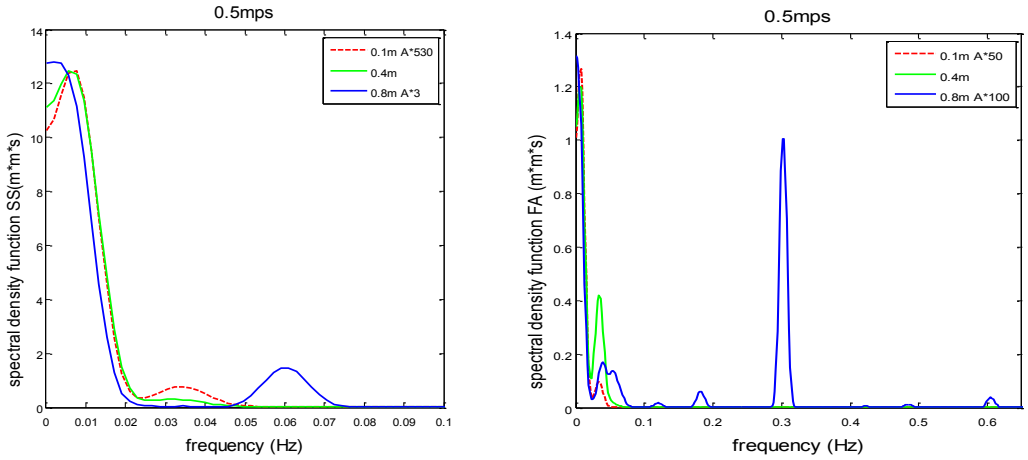

Figure 4.70: Spectrum of the side-to-side and fore-aft displacements at the MSL with different ice thicknesses and constant ice drifting speed (0.5 mps)

4.6.3. Roll and pitch motions at MSL

Figure 4.71 and Figure 4.72 describe the behavior of pitch and roll angles for increasing ice thickness. The observations made from these figures corroborate the observations made with the displacement curves. Indeed, the platform will be more pitched toward the

–y-direction. So the structure will be pushed in the y-direction by the ice cover and thus pitched toward the –y-direction. Moreover, the pitch will oscillate with an higher frequency with increasing ice thickness i.e. the cycle formed by contact-ice failure-new contact is shortened due to the increased ice thickness. For thinner ice, the oscillation period will be close to the eigenfrequency of the motion and for increasing ice it will decrease away from the natural frequency value. Besides, as per the SS displacements, the roll motions are restrained for the thickest ice sheet. And, the roll motions also have a smaller period with increasing ice thickness.

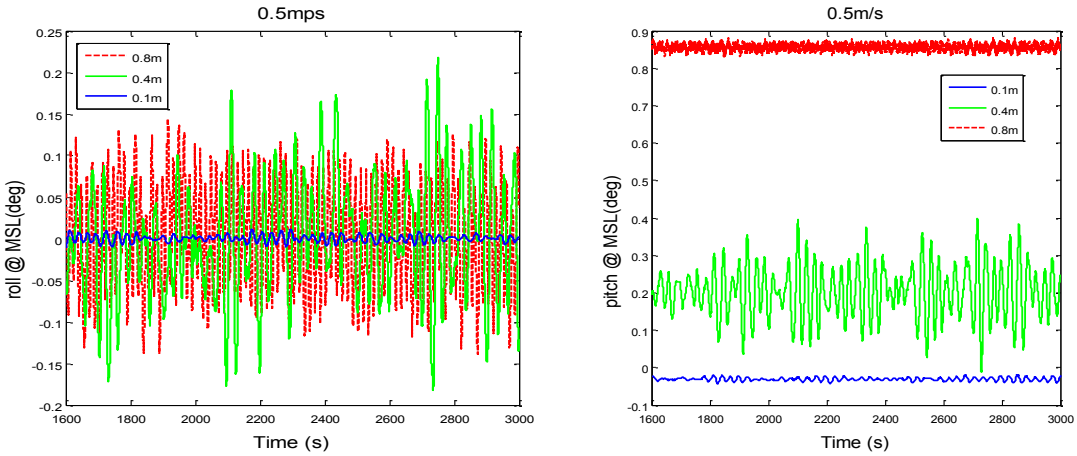

Figure 4.71: Time series of the roll and pitch motions at the MSL for LC 6.1, 6.2 and 6.3

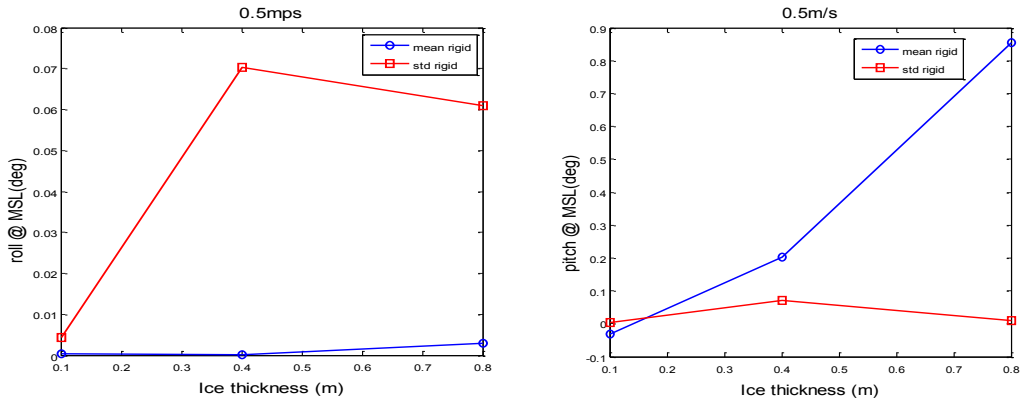

Figure 4.72: Statistical characteristics of the roll and pitch at the MSL with different ice thicknesses and constant ice drifting speed of 0.5mps

4.6.4. Fore-aft force at MSL

Figure 4.73 present the time series of the fore-aft force at the MSL for different ice thicknesses. With increasing ice thickness, the fore-aft force at MSL increases as shown by the statistical results (Figure 4.74). This increase in loading is also expected as thicker ice will induce a bigger contact area and thus higher loads. The general conclusions are the same as the ones drawn in section 4.6.1 due to the proportionality between the FA moments and forces.

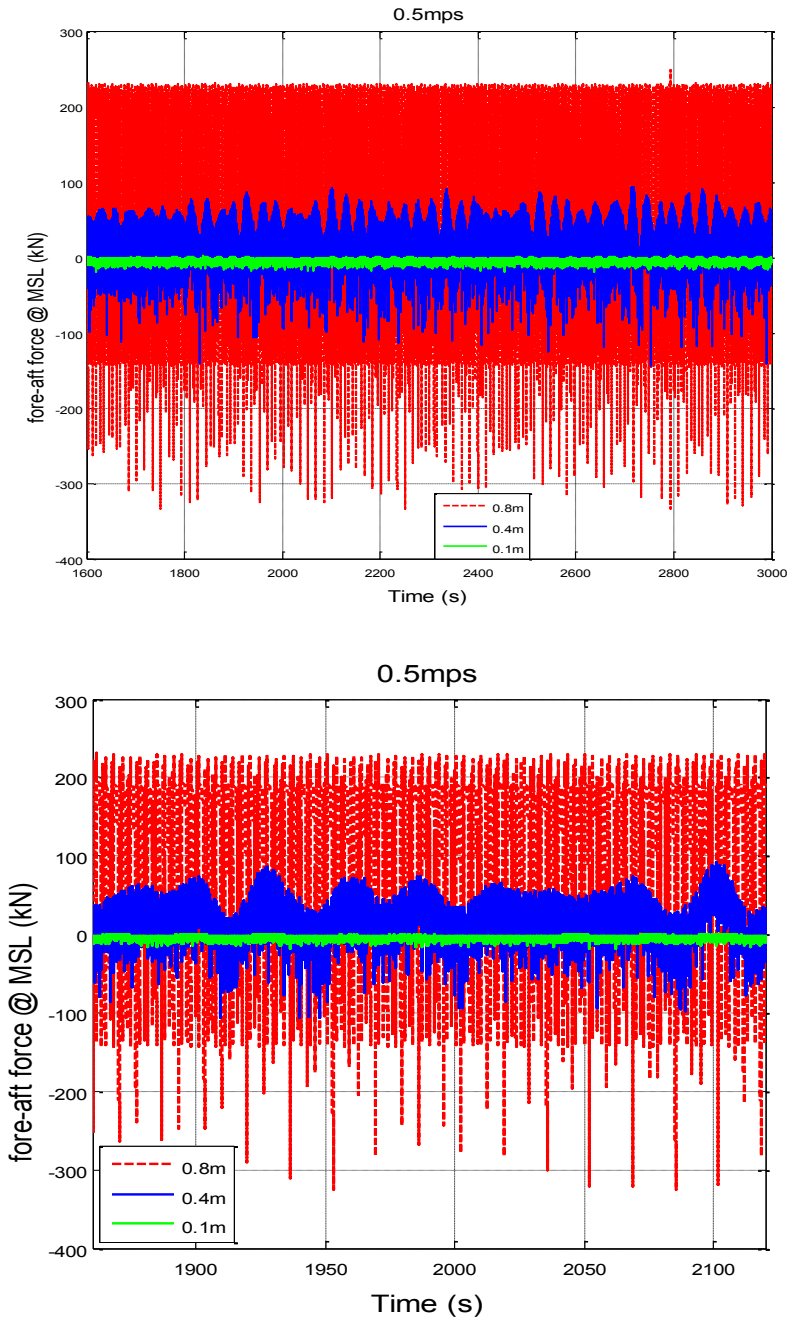

Figure 4.73: Time series of the fore-aft force at the MSL for LC 6.1, 6.2 and 6.3

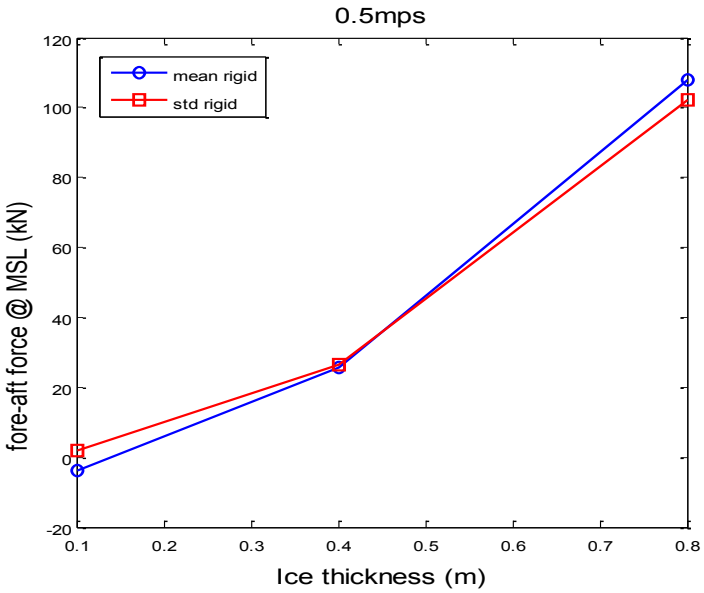

Figure 4.74: Statistical characteristics of fore-aft force at the MSL with different ice thicknesses and constant ice drifting speed of 0.5mps

Figure 4.75 shows the spectrum of the fore-aft fore at MSL corresponding to the time series displayed in Figure 4.73. With increasing ice thickness, the response shows larger amplification. It confirms the influence of the ice thickness. The spectra obtained is quite similar to the one displayed by fore-aft overturning moment at the MSL (See Figure 4.67). The same modes are excited and the order of magnitude in the response between the different cases is similar. The only difference is the amplitude obtained for the same case between the FA moment and the FA force responses. Indeed, the amplitude is approximately 4.10^3 to 5.10^3 times higher in the case of the FA moment response.

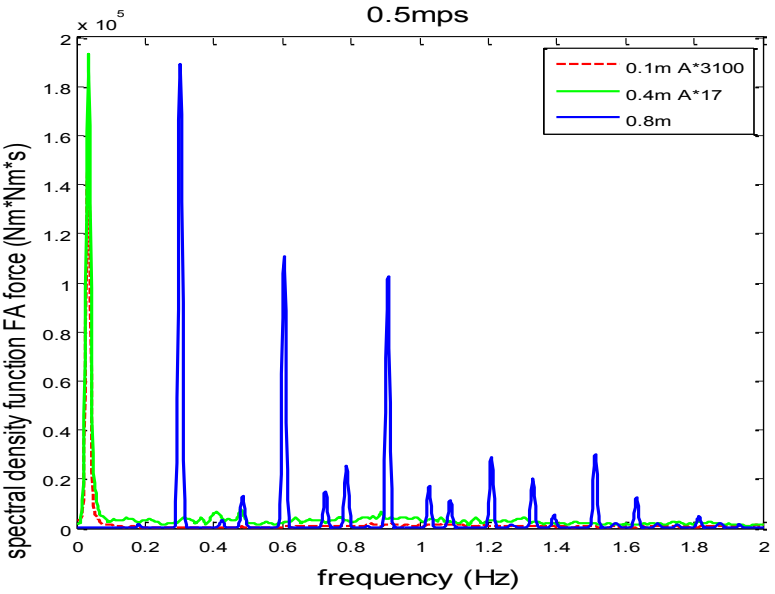

Figure 4.75: Spectrum of the fore-aft force at the MSL with different ice thicknesses and constant ice drifting speed (0.5 mps)

4.6.5. Fore-aft velocity at MSL

Figure 4.76 present the time series of the fore-aft velocity at the MSL for different ice thicknesses. The statistical results (Figure 4.77) show that with increasing ice thickness, the fore-aft velocity amplitude will increase. It is linked to the increase in loads due to a larger contact area. It also highlights that the FA velocity at MSL will oscillate approximately the same mean value in each case. However, the FA velocity seems to be reaching a maximum for an STD of around 0.05mps i.e. 10% of the ice sheet drifting velocity.

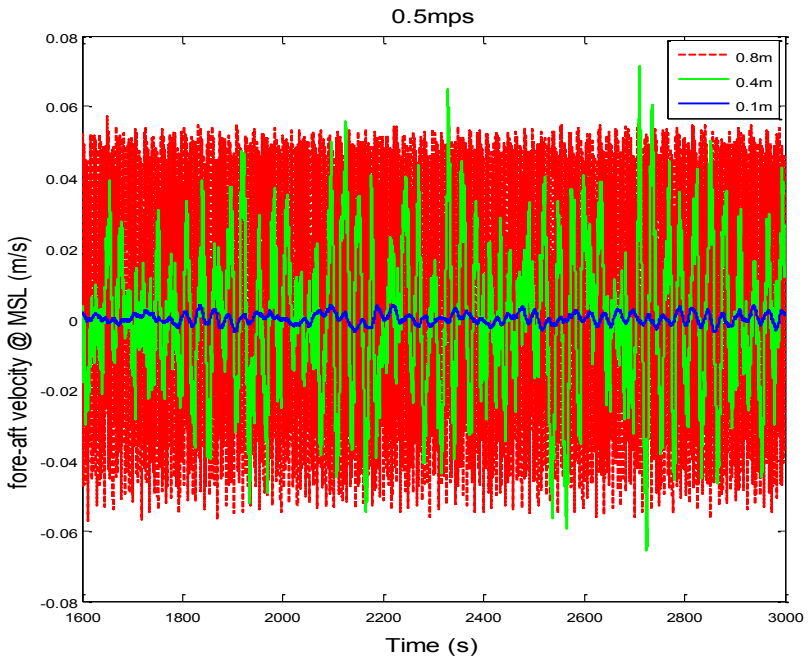

Figure 4.76: Time series of the fore-aft velocity at the MSL for LC 6.1, 6.2 and 6.3

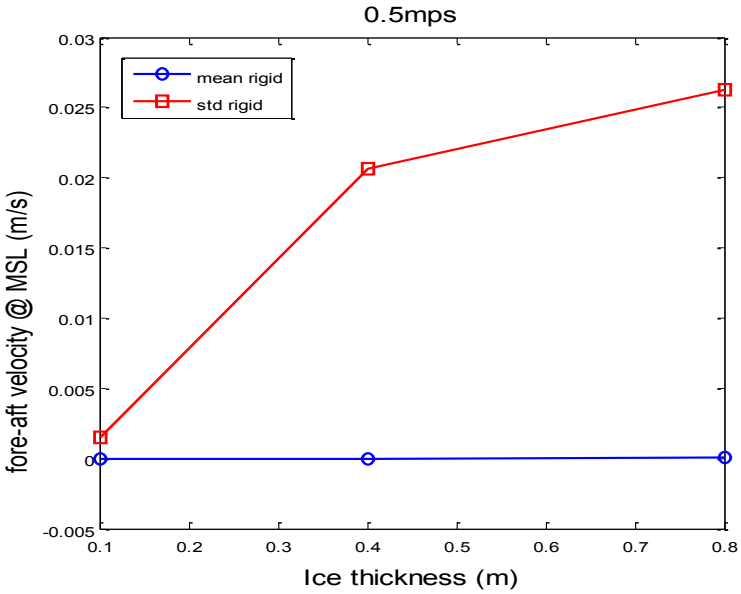

Figure 4.77: Statistical characteristics of fore-aft velocity at the MSL with different ice thicknesses and constant ice drifting speed of 0.5mps

4.7. Comparison of aerodynamic and ice loads

To compare aerodynamic and ice loads, 2 simulations are run with effective length of 600s and different initial conditions. Then the statistical results are studied - mean and standard deviation. Indeed, randomness will consequently be introduced in the simulations. The ice loads are introduced at respectively 500s and 520s and the simulation is run for an additional 1000s. The first 500s/520s before the introduction of ice and the next 400s including transient effects will not be included in the analysis. Thus we will have 600s of effective simulation as wanted.

LC #	turbine wind speed [m/s]	ice speed [m/s]	Ice thickness [m]
7.1.	11.4	0.3	0.4
7.2.	11.4	0.4	0.4
7.3.	11.4	0.5	0.1
7.4.	11.4	0.5	0.4
7.5.	11.4	0.5	0.8
7.6.	11.4	0	0

4.7.1. Moments at MSL and tower top

Figure 4.78, Figure 4.79, Figure D. 4 and Figure D. 5 present statistical characteristics of the side-to-side and fore-aft overturning moment at the MSL and the tower top for different ice thicknesses and ice drifting speeds when the coupled model is applied.

For the fore-aft overturning moments, it is visible that they are way higher at the MSL than at the tower top. The shape displayed by the curves in Figure 4.78 and Figure D. 4 is significantly different from the ones displayed when only ice loads are applied (see Figure 4.50 and Figure 4.67). Here, the statistical results show a high mean with small oscillations around it while with only ice loads the mean value was close to 0 with large oscillations around it. The statistical analysis shows that with increasing speed we have increasing mean FA moment. This increase is expected. Indeed, thicker ice will induce a bigger contact area and thus higher loads. And, this phenomenon was already observed previously in this work. From the statistical plots, the influence of the ice action seems minimal compared to the role played by the wind loads. The increase in loads due to the ice action is more noticeable at the tower top for both varying ice thickness and ice drifting speed – respectively a maximum of +3% vs. +1.3% and +15.8% vs. +6.4%.

For the side-to-side overturning moments, it is visible that they are also higher at the MSL than at the tower top. They moreover present larger oscillations at the MSL than at the tower top.

One more time, it can be noted that the ice drifting has almost no influence on the results while an increasing ice thickness will trigger higher FA moments and larger oscillations in the SS moments value.

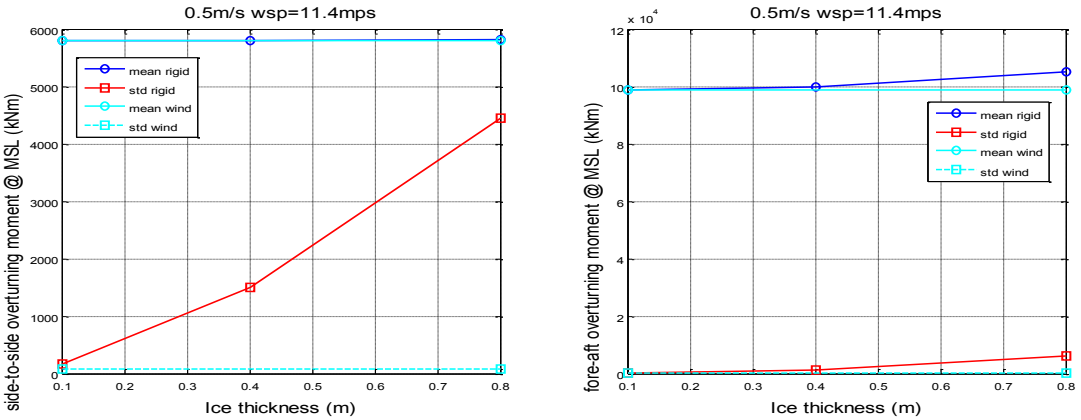

Figure 4.78: Statistical characteristics of the side-to-side and fore-aft over-turning moment at the MSL with different ice thicknesses and constant ice drifting speed of 0.5mps and wind rated speed

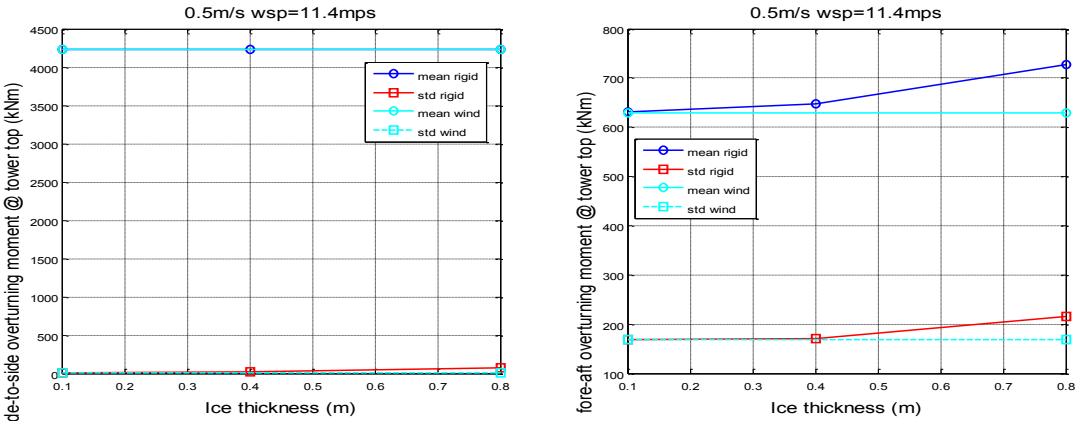

Figure 4.79: Statistical characteristics of the side-to-side and fore-aft over-turning moment at the tower top with different ice thicknesses and constant ice drifting speed of 0.5mps and wind rated speed

4.7.2. Displacements at MSL and tower top

Figure 4.80 to Figure 4.82, Figure D. 1 to Figure D. 3 and Figure D. 6 to Figure D. 11 present the time series and statistical characteristics of the side-to-side and fore-aft displacement at the MSL and at the tower top for different ice thicknesses and drifting speeds.

The fore-aft and the side-to-side displacements at MSL and tower top curves presents the same shape. This is true for both varying ice drifting speed and varying ice thickness. In all these cases, the curves present larger displacements at the tower top and the STD is reduced at the MSL compared to cases with only ice loads (see Figure 4.54 and Figure 4.69). Moreover, in the cases comporting both wind and ice loads, the ice action is of the same magnitude as in the cases with only ice loads. The FA displacements curves show almost no oscillations and a high mean value while the SS displacements curves present a small mean value with oscillations of the same magnitude around it.

FA displacements are increasing for increasing ice drifting speed while the SS displacements are decreasing. Additionally, the ice thickness has still an important impact on the results and FA displacements significantly increase for increasing ice thickness. Finally, in the case of the FA displacements, the wind loads have a predominant action compared to ice loads. Moreover, we can see that only few cycles of low-frequency motions are enclosed in the effective simulation time and it is not sufficient for a thorough analysis. Longer simulations would give a better understanding and more reliable results.

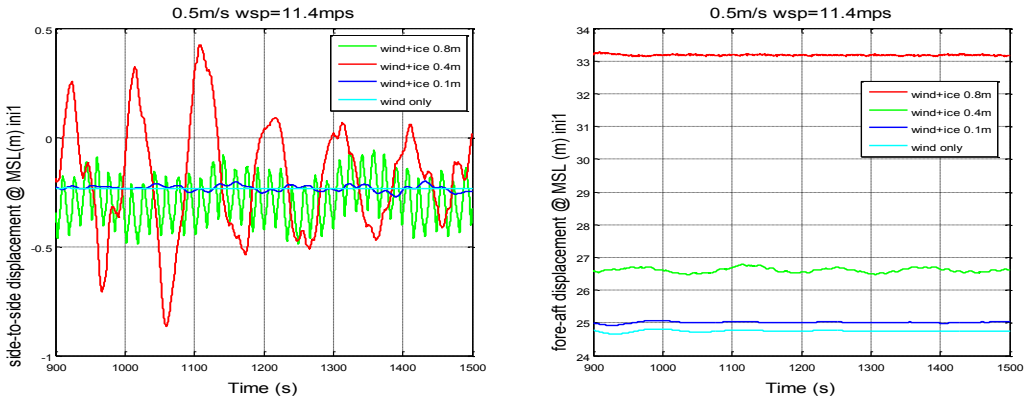

Figure 4.80: Time series of the side-to-side and fore-aft displacements at the MSL for LCs 7.3, 7.4 and 7.5 (initial conditions 1)

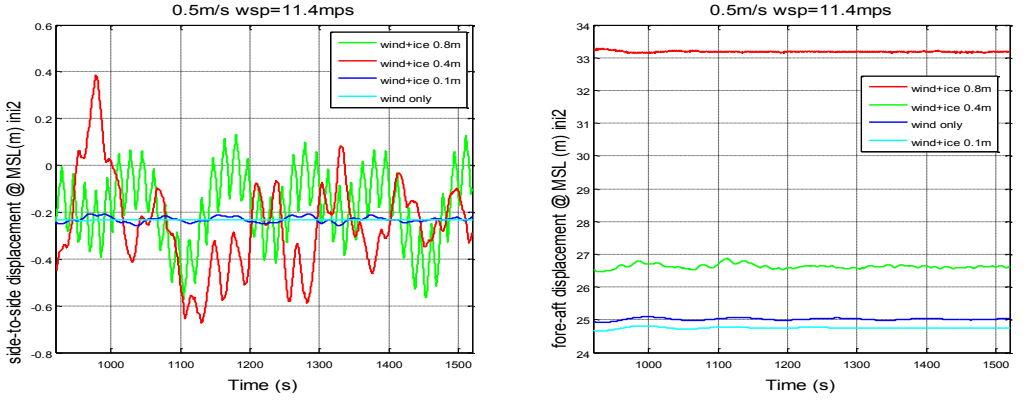

Figure 4.81: Time series of the side-to-side and fore-aft displacements at the MSL for LCs 7.3, 7.4 and 7.5 (initial conditions 2)

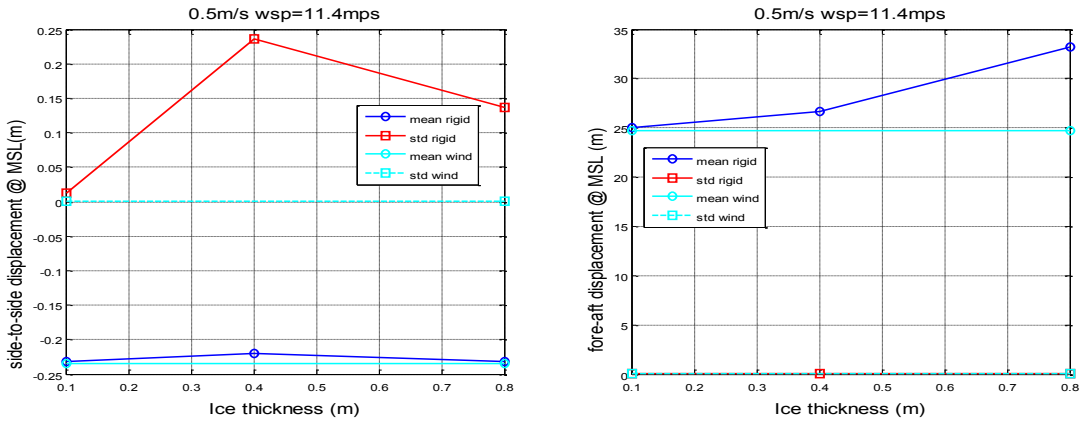

Figure 4.82: Statistical characteristics of the side-to-side and fore-aft displacements at the MSL with different ice thicknesses and constant ice drifting speed of 0.5mps and wind rated speed

4.7.3. Roll and pitch motions at MSL

Figure 4.83 to Figure 4.85 and Figure D. 12 to Figure D. 14 present the time series and statistical characteristics of the roll and pitch motions at the MSL for different ice thicknesses and drifting speeds.

The roll and pitch motions seem steady for varying ice drifting speed while for increasing ice thickness the pitch mean value increases. The roll mean value is also varying but it is quite case dependent. Compared to the LCs with only wind, for the roll motions, the mean value is approximately the same while the oscillations around the mean value are larger. Thus, ice loads will trigger periodical loading. The pitch presents here almost no oscillation. Compared to the LCs with only ice loads (see Figure 4.58 and Figure 4.72), the oscillations around the mean value are reduced for both pitch and roll motions.

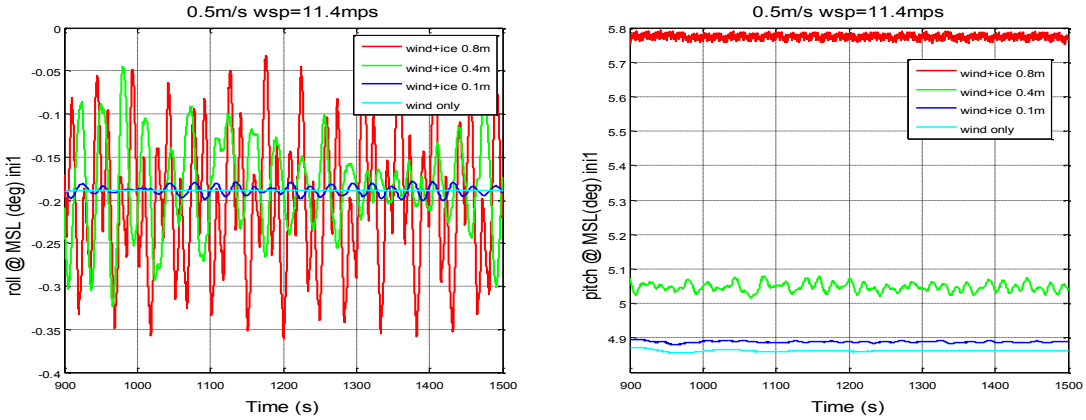

Figure 4.83: Time series of the roll and pitch motions at the MSL for LCs 7.3, 7.4 and 7.5 (initial conditions 1)

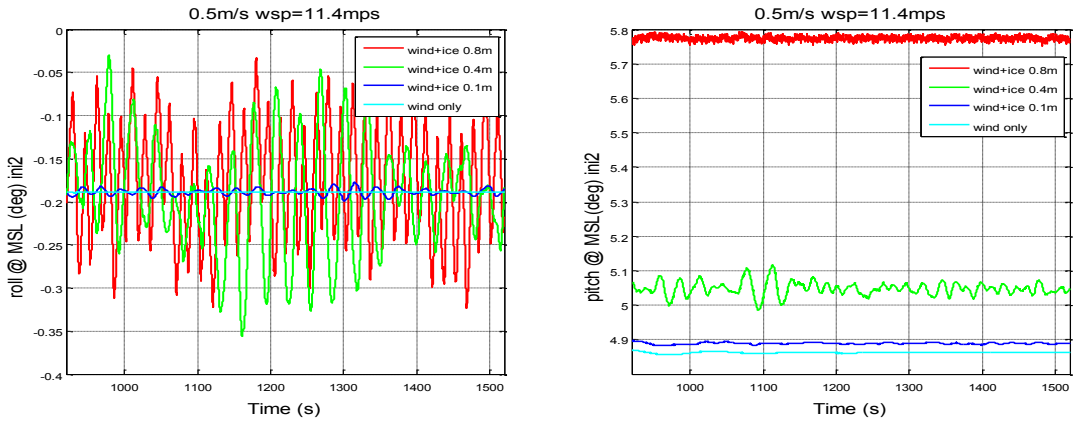

Figure 4.84: Time series of the roll and pitch motions at the MSL for LCs 7.3, 7.4 and 7.5 (initial conditions 2)

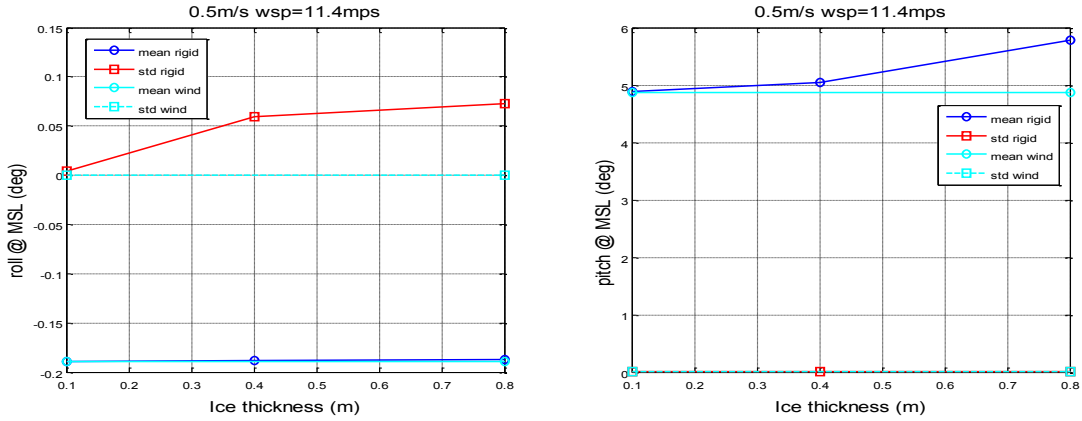

Figure 4.85: Statistical characteristics of the roll and pitch at the MSL with different ice thicknesses and constant ice drifting speed of 0.5mps and wind rated speed

4.7.4. Fore-aft force at MSL and tower top

Figure 4.86 and Figure D. 15 present the statistical characteristics of the fore-aft at the MSL and the tower top for different ice thicknesses and drifting speeds.

The fore-aft force presents the same shape at both the tower top and at the MSL i.e. it displays a high mean value and almost no oscillations around this mean. Thus, the results are steadier than with only ice loads contribution. The fore-aft value is higher at the MSL as the ice is not directly interacting with the structure at the tower top. By comparing the present plots to Figure 4.60 and Figure 4.74 an important increase of the FA force magnitude due to the wind contribution is noticeable.

Figure D. 15 shows relatively stable results thus it highlight the fact that the ice drifting has a relatively small influence on the dynamic response. On the contrary, as already pinpointed in §4.6, for increasing ice thickness the FA force will increase whether it is at the MSL or at the tower top. This increase in loading is expected as thicker ice will induce

a bigger contact area and thus higher loads. This increase is more significant at the MSL (11%) than at the tower top (5%) due to direct interaction with the ice sheet.

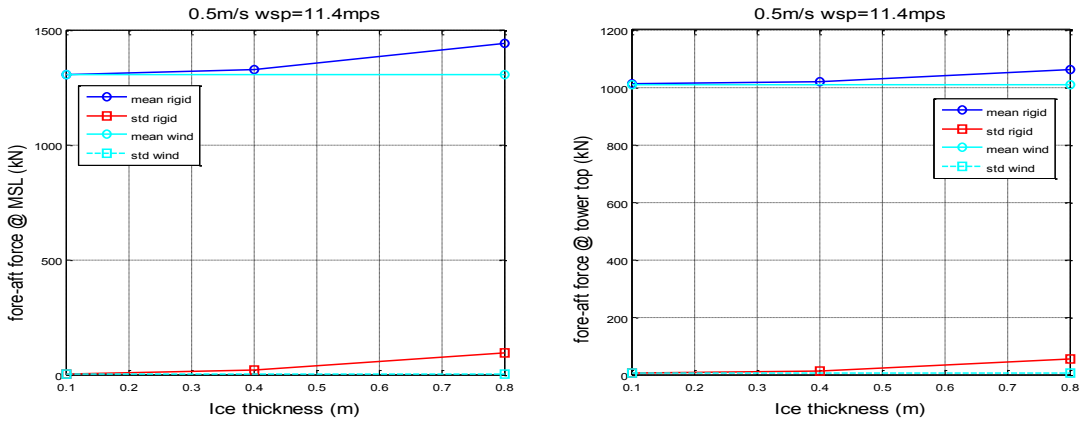

Figure 4.86: Statistical characteristics of fore-aft force at the MSL and tower top with different ice thicknesses and constant ice drifting speed of 0.5mps and wind rated speed

4.7.5. Fore-aft velocity at MSL

Figure 4.87 and Figure D. 16 present the statistical characteristics of the fore-aft at the MSL for different ice thicknesses and drifting speeds.

The shape observed is similar to the one displayed in Figure 4.63 and Figure 4.77 with oscillation around a null mean value. We can note that the insertion of wind loads leads to smaller oscillations around the mean value.

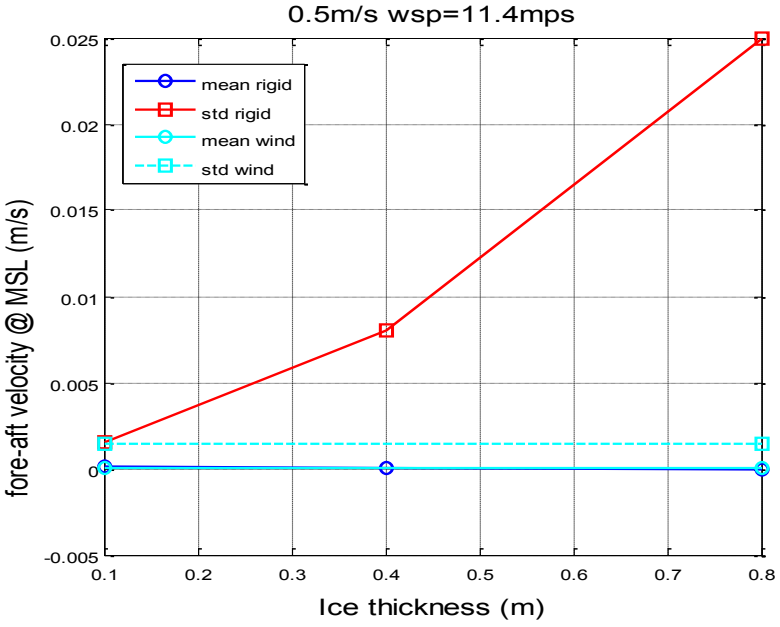

Figure 4.87: Statistical characteristics of fore-aft velocity at the MSL with different ice thicknesses and constant ice drifting speed of 0.5mps and wind rated speed

4.7.6. Aerodynamic thrust

Figure 4.88 and Figure D. 17 present the statistical characteristics of the thrust for different ice thicknesses and drifting speeds.

The thrust obtained is relatively stable regardless of the ice conditions. It slightly decreases due to the presence of ice and for increasing ice thickness the thrust decreases. Moreover, the thrust displayed for LC 7.3 (0.5mps 0.1m) is the same as the one displayed in LC 7.6 i.e. without ice loads. Additionally, in LC 7.1 (0.3mps 0.4m) the thrust output is almost equal to the one obtained without ice loads and does not vary much. Thus, one more time, the predominance of the ice thickness on the dynamic response over the ice drifting speed is visible.

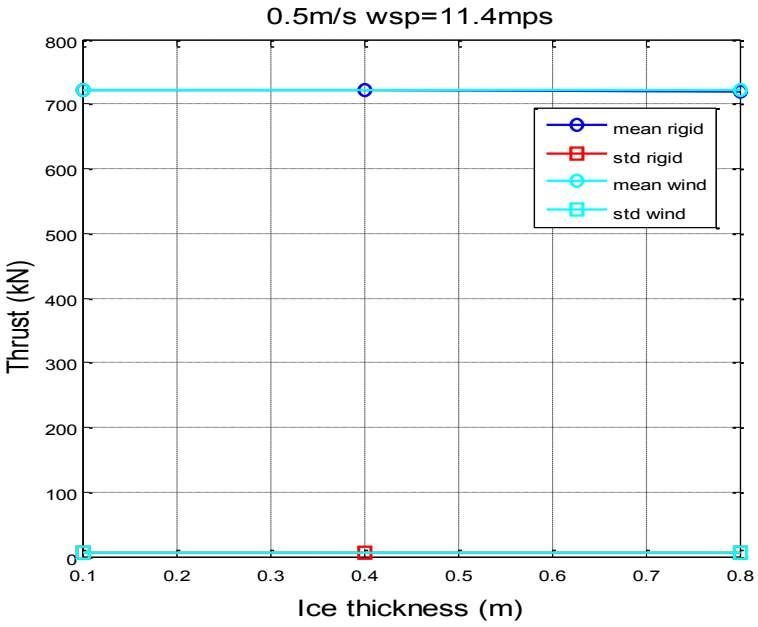

Figure 4.88: Statistical characteristics of the aerodynamic thrust with different ice thicknesses and constant ice drifting speed of 0.5mps and wind rated speed

5. Discussion

Eigenfrequency analysis and convergence study on time domain simulations

After conducting an eigenvalue analysis and a convergence study, knowledge was acquired on the model and the simulations settings. It was decided that the accuracy offered by effective 1400s long simulations with a time steep of 0.001s was satisfying considering the time dedicated per analysis. However, longer simulations should be run if possible. Indeed, usually the effective simulation time is around 1h to encompass at least 30 to 50 sway motion cycles - 2.5 time longer than the one implemented here. Using the identified settings, it was then possible to run several types of simulations.

Coupled vs. Uncoupled time domain simulations

First, the comparison between the coupled model implemented in this work and a decoupled model shows that globally the curves output have the same shape for both time series and statistical results. However, they present differences in magnitude. Indeed, larger differences are observed between decoupled analysis and coupled analysis with high drifting speed or large ice thickness as also highlighted in (Shi, et al., November 24-26, 2014). In the mentioned work, a monopile-type offshore wind turbine is studied applying the same models as in this work. Additionally, contrary to (Shi, et al., November 24-26, 2014) where *"in most LCs, decoupled analysis presents lower structural response"* it is difficult here to identify a clear trend in the difference in results.

Influence of ice thickness and ice drifting speed

Simulation including only ice loads – with constant ice properties - have highlighted the influence of the ice drifting speed and thickness in the ice breaking pattern and the structural responses. As it was already presented in various works such as (ISO/FDIS19906, 2010), (Barker, et al., 2005), (Hetmanczyk, et al., 2011) and (Shi, et al., November 24-26, 2014), increasing ice thickness induces increasing loads. It is explained by the fact that an increasing ice thickness will increase the contact area, and consequently induces higher ice loads. However, a trend is hardly discernable for the influence of ice drifting speed based on the cases run in this work. And, ice drifting speed has a less significant influence on the dynamic response than ice thickness. Finally, in the different load cases, no mode is dominating the response and the excited modes highly depend on the load case.

Coupled analysis considering both ice and aerodynamic loads

Several simulations have been performed including both ice and wind loads. The wind loads were introduced through a constant wind set at the rated speed of the wind turbine. Thus, the influence of the ice loads in the wind turbine working conditions can be studied. The initial transient observed is reduced compared to the transient state observed for simulations comporting only ice loads. This is explained in (Jonkman, et al., 2010) by the damping effect triggered by the aerodynamic loading on the structure. Moreover, as in the previous set of simulations the predominance of the ice thickness over the ice drifting speed in the dynamic response is visible. The wind has a predominant influence on the loads. But, ice loads participate to the dynamic component of the response by causing amplified oscillations around the mean value. Thus, this could have a significant influence in the lifetime of the wind turbine by accelerating fatigue damages. However, the power production does not seems to be significantly impacted, at the rated speed at least.

Recommendation for future work

During this work, the model was enhanced and will allow for further work on the topic. Indeed, so far the coupled simulations with both ice and wind were only possible with a bottom fixed wind turbine. And, for a spar wind turbine, the ice loads were only available in a decoupled model which did not include wind. Thus, it was the occasion to gain essential knowledge on the simulation parameters to implement, to draw the actual limitations encountered with the model applied, to identify the problems to assess in the future and a first step in the collection of data on the topic. Moreover, only a limited number of results were obtained for simulations comporting both wind and ice loads due to technical problems with the coupling of the aero-servo-hydro-elastic model and the ice module. Different strategies were tested to remedy to the issues occurring during this work which was a time consuming process. So, in the future, more load cases comporting both wind and ice loads should be implemented. Additionally, in the scope of this work, a mention is made to performing analyses with both ice and wind turbine loads considering random variation of ice thickness as well as turbulent wind field. Due to time limitations it was not possible to extend the work this far and this should be assessed in a future work. To do so, it seems possible to use a method close to the one applied in (Su, et al., 2011). As of now it is not possible to employ the results obtained for design purpose due to the non-realistic conditions applied in the model.

6. Conclusion

The principal aim of this work is to develop the study of coupled dynamic analysis when both wind and ice loads are applied on a spar floating wind turbine. It can be summarized as follows:

- Ice loads model coupled to HAWC2 for spar floating wind turbine analysis;
- Eigenfrequency analysis;
- Convergence study on time domain simulations: simulation steps and length;
- Coupled vs. Uncoupled time domain simulations;
- Influence of ice thickness and ice drifting speed;
- Coupled analysis considering both ice and aerodynamic loads.

To do so, a semi-empirical ice module was coupled to an aero-servo-hydro-elastic model. The ice loads were obtained using a Fortran code, while the global responses of the spar floating wind turbine were obtained in HAWC2 using the time series of ice loads as input. The ice loads are calculated by defining the ice sheet and structure geometry at the waterline and then integrating the contact forces over the waterline. Moreover, waves were not included in the model considering that they are negligible in case of ice covered sea. The wind turbine model exploited here corresponds to Phase IV – Floating spar buoy described in OC3 i.e. a NREL offshore 5-MW wind turbine installed on a floating spar-buoy in deep water (320 m). The NREL 5 MW model is an upwind, variable-speed, collective pitch controlled horizontal axis wind turbine (HAWT). The wind turbine is considered as a rigid body and the 6 DOFs of the body are included in the analysis. Besides, the structure is fitted with an inverted ice-breaking cone. Thus, it is assumed that the only ice breaking mode occurring is flexural failure.

The resulting model was studied prior to simulations via an eigenfrequency analysis and a convergence study to respectively identify the structure natural frequencies and modes and to investigate the effect of time step and simulation length. From then on it was possible to run simulations in ice conditions corresponding to the ones encountered in the Baltic Sea (ISO/FDIS19906, 2010). The goal of these simulations was to identify the ice drifting speed and thickness influence – this was done without including wind in the

simulations – and to study the combined action of wind and ice loads on the structure. Moreover, the results obtained using a decoupled and a coupled model were compared.

The comparison between the coupled model implemented in the present work and the decoupled model used before shows that they present differences in magnitude but comparable output shapes. Indeed, larger differences are observed between decoupled analysis and coupled analysis with high drifting speed or large ice thickness but it is difficult here to identify a clear trend in the difference in results.

Next, simulation including only ice loads – with constant ice properties - have highlighted the influence of the ice drifting speed and thickness on the ice breaking pattern and the structural responses. It was observed that increasing ice thickness induces increasing loads. It is explained by the fact that an increasing ice thickness will increase the contact area, and consequently induces higher ice loads. However, a trend is hardly discernable for the influence of ice drifting speed based on the cases run in this work. And, ice drifting speed has a less significant influence on the dynamic response than ice thickness.

Then, several simulations have been performed including both ice and wind loads. The wind loads were introduced through a constant wind set at the rated speed of the wind turbine. Thus, the influence of the ice loads in the wind turbine working conditions can be studied. The initial transient observed is reduced compared to the transient state observed for simulations comporting only ice loads. Moreover, as in the previous set of simulations the predominance of the ice thickness over the ice drifting speed in the dynamic response is visible. The wind has a predominant influence on the loads. But, ice loads participate to the dynamic component of the response by causing amplified oscillations around the mean value. Thus, this could have a significant influence in the lifetime of the wind turbine by accelerating fatigue damages. However, the power production does not seems to be significantly impacted, at the rated speed at least.

During this work, the model was enhanced and will allow for further work on the topic. Indeed, it is now possible to simulate a coupled analysis including both wind and ice loads for a spar floating wind turbine which was not the case before with the Fortran module used. Thus, essential knowledge was gain concerning the simulation parameters to implement.

In the future, more load cases should be run with both ice and wind loads. Indeed, only a limited number of results were obtained due to technical problems with the coupling of the aero-servo-hydro-elastic model and the ice module.

Additionally, in the scope of this work, a mention is made to performing analyses with both ice and wind turbine loads considering random variation of ice thickness as well as turbulent wind field. Due to time limitations it was not possible to extend the work this far and this should be assessed in a future work. Then fatigue and energy production study should be performed to quantify the impact of the ice loads on the wind turbine lifetime and efficiency. As of now it is not possible to employ the results obtained for design purpose due to the non-realistic conditions applied in the model.

The model can also be enhanced in 2 ways:

- Even if a rigid model is accurate enough for a first study of the phenomenon, implementing the structure as a flexible model will give more accurate results;
- The point of contact at the waterline between the structure and the ice sheet is fixed. It does not account for the structure body motions which can affect the accuracy of the results. Taking into account the body motions at the waterline can thus be a possible expansion of the work.

It is hard to find other coupled analysis model comporting both wind and ice loads to compare the results obtained here. One solution could be to verify the model based on standards and guidelines or to compare it with a model developed in another university. Finally, a last option could be to validate the results by comparing them to physical response data from actual measurements (model tests or full scale data) as envisaged in Offshore Code Comparison Collaboration Continuation, with Correlation (OC5) project (Robertson, et al., June 8–13, 2014). However, the OC5 initiative is still not taking into account the ice loads. Thus, it will not be possible to validate the present model by mean of this workshop.

References

Biswajit, Baju and Van-Nguyen, Dinh. 2013. *On the Modeling of Spar-type Floating Offshore Wind Turbines.* 2013.

Arany, László, et al. 2014. Simplified critical mudline bending moment spectra of offshore wind turbine support structures. *Wind Energy.* Wiley Online Library, 2014.

Barker, Anne, et al. 2005. Ice loading on Danish wind turbines Part 1: Dynamic model tests. *Cold Regions Science and Technology.* Elsevier, 2005, 41.

Blenkarn, K. A.,. 1970. *Measurement and analysis of ice forces on Cook inlet structures.* s.l. : Proceedings of 2nd Offshore Technology Conference, Houston, TX, Vol. 2, pp. 365–378., 1970.

DNV-OS-J101, Det Norske Veritas 2014. May, 2014. DNV-OS-J101 Offshore Standard: Design of Offshore Wind Turbine Structures. May, 2014.

Faltinsen, O. M. 1990. *Sea Loads on ships and offshore structures.* s.l. : Cambridge University Press, 1990.

Gao, Zhen and Bachinsky, Erin. 2014. *Integrated dynamic analysis of wind turbines - Lecture Notes.* 2014.

Gravesen, Helge and Kärnä, Tuomo. 2009. *Ice loads for offshore wind turbines in the southern Baltic Sea.* Luleå, Sweden : Proceedings of the 20th International Conference on Port and Ocean Engineering under Arctic Conditions, 2009.

Gravesen, Helge, et al. 2005. Ice loading on Danish wind turbines: Part 2. Analyses of dynamic model test results. *Cold Regions Science and Technology.* Elsevier, 2005, 41.

Greco, Marilena. 2012. *TMR 4215: Sea Loads - Lecture notes (NTNU).* 2012.

Hansen, Martin O. L. 2008. *Aerodynamics of wind turbines, second edition.* London-Washington, DC : earthscan, 2008. 978-1-84407-438-9.

Heinonen, Jaakko, Hetmanczykl, Sebastian and Strobel, Michael. 2011. *Introduction of ice loads in overall simulation of offshore wind turbines.* Montréal : Proceedings of the 21st International Conference on Port and Ocean Engineering under Arctic Conditions, 2011.

Hendrikse , Hayo, Renting, Frank W. and Metrikine , Andrei V. 2014. *Analysis of the fatigue life of offshore wind turbine generators under combined ice- and aerodynamic loading.* San Francisco, California, USA : Proceedings of the ASME 2014 33rd International Conference on Ocean, Offshore and Arctic Engineering OMAE2014, 2014.

Hetmanczyk, Sebastian, Heinonen, Jaakko and Strobel, Michael. 2011. *Dynamic Ice Load Model in Overall Simulation of Offshore Wind Turbines.* Maui, Hawaii, USA : ISOPE 2011, Twenty-First International Offshore and Polar Engineering Conference. , 2011.

ISO/DIS19906. 2008. International Standard for Petroleum and natural gas industries-Arctic offshore structures. *Technical Committee ISO/TC 67, Materials, equipment and offshore structures for petroleum, petrochemical and natural gas industries, Subcommittee SC 7, Offshore structures.* 2008.

ISO/FDIS19906. 2010. Petroleum and natural gas industries - Arctic offshore structures. 2010.

Jonkman, J. and Musial, W. 2010. *Offshore Code Comparison Collaboration (OC3) for IEA Task 23 Subtask 2 Offshore Wind Technology and Deployment Final Report.* 2010.

Jonkman, J. 2010. *Definition of the Floating System for Phase IV of OC3.* 2010. Technical Report NREL/TP-500-47535.

Karimirad, Madjid and Moan, Torgeir. July 2012. A simplified method for coupled analysis of floating offshore wind turbines. *Marine Structures.* July 2012, Vol. 27.

—. April 2011. Extreme dynamic structural response analysis of catenary moored spar wind turbine in harsh environmental conditions. *Journal of Offshore Mechanics and Arctic Engineering (JOMAE), ASME.* April 2011, Vol. 133.

—. January 2012. Feasibility of the Application of aSpar-type Wind Turbine at a Moderate Water Depth. *Energy Procedia.* January 2012, Vol. 24.

—. January 2012. Wave and wind induced dynamic response of catenary moored spar wind turbine. *Journal of Waterway, Port, Coastal, and Ocean Engineering.* January 2012, Vol. 138.

Karimirad, Madjid. 2013. Modeling aspects of a floating wind turbine for coupled wave–wind-induced dynamic analyses. *Renewable energy.* 2013, Vol. 53.

Karimirad, Madjid, et al. 2011. Hydroelastic code-to-code comparison for a tension leg spar-type floating wind turbine. *Marine Structures.* 2011, Vol. 24.

Karimirad, Madjid, Gao, Zhen and Moan, Torgeir. 2009. *Dynamic Motion Analysis of Catenary Moored Spar Wind Turbine In Extreme Environmental Condition.* Sweden : Offshore Wind Conference 2009, 2009.

Kärnä, T. and Kolari, K. 2004. *Mitigation of dynamic ice actions on offshore wind turbines.* Austria : Proceedings of the Third European Conference on Structural Control, 3ECSC, 2004.

Karna, T. and Turunen, R. 1990. *A straightforward technique for analyzing structural response to dynamic ice action.* Houston, USA : Proceedings of the 9th Offshore Mechanics and Arctic Engineering Conference, 1990. vol. 4, pp. 135– 142..

Kärnä, Tuomo and Jochmann, Peter. *Field observations of ice failure modes.*

Kujala, Pentti. 2013. *Lecture notes Kul-24.3500 Winter Navigation (Aalto University).* 2013.

—. 1994. On the Statistics of Ice Loads on Ship Hull in the Baltic. *Mechanical Engineering Series No. 116, Ship Laboratory, Helsinki University of Technology, Finland.* 1994.

—. 1996. Semi-empirical Evaluation of Long Term Ice Loads on a Ship Hull. *Marine Structures.* Elsevier, 1996, 9.

Kujala, Pentti, Mazaheri, Arsham and Sormunen, Otto . 2013. *Lecture Notes Kul-24.4200 Introduction to Risk Analysis of Structures (Aalto University).* 2013.

Langen, Ivar and Sigbjörnsson, Ragnar. 1977. *Dynamisk analyse av konstruksjoner.* 1977.

Larsen, Torben Juul and Hansen, Anders Melchior. 2007. *How 2 HAWC2, the user's manual.* 2007.

Määttänen, M. 1999. *Numerical model for ice-induced vibration load lock-in and synchronization.* Potsdam/New York/Usa : Proceedings of the 14th International Symposium on Ice, 1999.

Määttänen, Mauri. 1999. *Ice and offshore wind turbines in the gulf of Bothnia.* Espoo : Proceedings of the 15th International conference on port and ocean engineering under arctic conditions, 1999.

Mroz, Arkadiusz, Holnicki-Szulc, Jan and Kärna, Tuomo. 2008. Mitigation of ice loading on off-shore wind turbines: Feasibility study of a semi-active solution. *Computers & structures.* Elsevier, 2008, 86.

Muliawan, Made Jaya, Karimirad, Madjid and Moan, Torgeir. 2012. Dynamic response and power performance of a combined Spar-type floating wind turbine and coaxial floating wave energy converter. *Renewable Energy.* Elsevier, 2012, 50.

Popko, Wojciech. 2014. *Comparison of full-scale and numerical model dynamic responses of Norströmsgrund lighthouse.* San Francisco, California, USA : Proceedings

of the ASME 2014 33rd International Conference on Ocean, Offshore and Arctic Engineering OMAE2014, 2014.

Popko, Wojciech, et al. 2012. *State-of-the-art Comparison of Standards in Terms of Dominant Sea Ice Loads for Offshore Wind Turbine Support Structures in the Baltic Sea.* Rhodes : Proceedings of the Twenty-second (2012) International Offshore and Polar Engineering Conference, 2012.

Qu, Yan, et al. 2006. A random ice force model for narrow conical structures. *Cold regions science and technology.* Elsevier, 2006, 45.

Riska, Kaj. 1995. Models of ice-structure contact for engineering applications. 1995, Vol. 42.

Robertson, A., et al. June 8–13, 2014. *Offshore Code Comparison Collaboration Continuation Within IEA Wind Task 30: Phase II Results Regarding a Floating Semisubmersible Wind System.* San Francisco, California : International Conference on Ocean, Offshore and Arctic Engineering, June 8–13, 2014.

Schreck, S. October 2004. *Integrated wind energy / desalination system.* s.l. : NREL, October 2004. Tech. Rep. NREL/SR-50039485.

Shi, Wei, et al. November 24-26, 2014. *Study on the effect of ice-structure interaction on the dynamic response of offshore wind turbine.* Lisbon, Portugal : Proceedings of the first International Conference on Renewable Energies Offshore (RENEW2014), November 24-26, 2014.

Su, Biao, Riska, Kaj and Moan, Torgeir. 2011. Numerical study of ice-induced loads on ship hulls. *Marine Structures.* Elsevier, 2011, 24.

Su, Biao, Riska, Kaj and Moan, Torgeir. 2011. Numerical simulation of local ice loads in uniform and randomly varying ice conditions. *Cold Regions Science and Technology.* Elsevier, 2011, 65.

Tan, Xiang, et al. 2013. A six-degrees-of-freedom numerical model for level ice-ship interaction. *Cold Regions Science and Technology.* Elsevier, 2013, 92.

Xu, Ning and Yue, Qianjin. 2014. Dynamic Ice Force Analysis on a Conical Structure Based on Direct Observation and Measurement. *Journal of Offshore Mechanics and Arctic Engineering.* 2014, Vol. 136.

Xu, Ning, Yue, Qianjin and Guo, Fengwei. 2010. *Mitigating Ice-induced Vibration by Adding Ice-breaking Cone.* Beijing : Proceedings of the Twentieth (2010) International Offshore and Polar Engineering Conference, 2010.

Yu, Bingbin , et al. 2013. *A surface ice module for wind turbine dynamic response simulation using fast.* Nantes, France : Proceedings of the ASME 2013 32nd International Conference on Ocean, Offshore and Arctic Engineering, 2013.

Yu, Bingbin and Karr, Dale G. 2014. *An ice-structure interaction model for non-simultaneous ice failure.* Houston, Texas, USA : Arctic Technology Conference, 2014.

Yu, Bingbin, Karr, Dale G. and Sirnivas, Senu. 2014. *Ice non simultaneous failure, bending and floe impact modeling for simulating wind turbine dynamics using FAST.* San Francisco : Proceedings of the ASME 2014 33rd International Conference on Ocean, Offshore and Arctic Engineering, 2014.

Ziemer, Gesa and Evers, Karl-Ulrich. 2014. *Ice model tests with a compliant cylindrical structure to investigate ice-induced vibrations.* San Francisco, California, USA : Proceedings of the ASME 2014 33rd International Conference on Ocean, Offshore and Arctic Engineering OMAE2014-24011, 2014.

Appendix

A. Example of HAWC2 htc file

```
;0_ice_mono_0.1mps0.8m_decoupled_no_wind_rigid, 03-11-13, Larh
begin Simulation;
 time_stop 1000 ;
  solvertype   1 ;    (newmark)
  on_no_convergence continue ;
;  convergence_limits 100 1.0 1E-7 ;
  logfile ./log/0_ice_mono_0.1mps0.8m_decoupled_no_wind_rigid.log ;
;  animation ./anim/0_ice_mono_0.1mps0.8m_decoupled_no_wind_rigid.dat;
;
  begin newmark;
    deltat    0.001;
  end newmark;
end simulation;
;
begin new_htc_structure;
;  beam_output_file_name  ./log/0_ice_mono_0.1mps0.8m_decoupled_no_wind_rigid_beam.dat;
Optional - Calculated beam properties of the bodies are written to file
;  body_output_file_name  ./log/0_ice_mono_0.1mps0.8m_decoupled_no_wind_rigid_body.dat;                  Optional
- Body initial position and orientation are written to file
;  struct_inertia_output_file_name ./log/0_ice_mono_0.1mps0.8m_decoupled_no_wind_rigid_struct.dat;
;  body_eigenanalysis_file_name ./eigenfrq/0_ice_mono_0.1mps0.8m_decoupled_no_wind_rigid_body_eigen.dat;
;  structure_eigenanalysis_file_name ./eigenfrq/0_ice_mono_0.1mps0.8m_decoupled_no_wind_rigid_strc_eigen.dat;
;-------------------------------------------------------------------------------------------------------------------------------------------
-------------------
;
  begin main_body;
    name        floater ;
    type        timoschenko ;
    nbodies     1 ;
    node_distribution     c2_def ;
    damping   0.0 0.0 0.0 1.0E-3 1.0E-3 1.0E-3 ;
    begin timoschenko_input;
      filename ./data/floater.txt ;
      set 1 2 ;
    end timoschenko_input;
    begin c2_def;              Definition of centerline (main_body coordinates)
      nsec 8 ;
      sec    1 0.0 0.0    0.00     0.0 ;  Bottom of floater
      sec    2 0.0 0.0  -30.00     0.0 ;  COG
      sec    3 0.0 0.0  -50.00     0.0 ;  Anchor point (located 70.0 m below SWL)
      sec    4 0.0 0.0  -60.00     0.0 ;
      sec    5 0.0 0.0 -108.00     0.0 ;  Start of conical section
      sec    6 0.0 0.0 -116.00     0.0 ;  End of cinocal section
      sec    7 0.0 0.0 -120.00     0.0 ;  Water line
      sec    8 0.0 0.0 -130.00     0.0 ;  Top of floater, interface to tower
    end c2_def ;
  end main_body;
;
  begin main_body;
    name        tower ;
    type        timoschenko ;
    nbodies     1 ;
    node_distribution     c2_def ;
    damping   0.0 0.0 0.0 2.59E-3 2.59E-3 1.0E-3 ;
    begin timoschenko_input;
      filename ./data/Reinforced_80m_Tower_st.txt ;
      set 1 2 ;
    end timoschenko_input;
    begin c2_def;              Definition of centerline (main_body coordinates)
      nsec 11 ;
      sec    1 0.0 0.0    0.00  0.0 ; Tower bottom
      sec    2 0.0 0.0   -7.76  0.0 ;
```

```
    sec    3 0.0 0.0  -15.52  0.0 ;
    sec    4 0.0 0.0  -23.28  0.0 ;
    sec    5 0.0 0.0  -31.04  0.0 ;
    sec    6 0.0 0.0  -38.80  0.0 ;
    sec    7 0.0 0.0  -46.56  0.0 ;
    sec    8 0.0 0.0  -54.32  0.0 ;
    sec    9 0.0 0.0  -62.08  0.0 ;
    sec   10 0.0 0.0  -69.84  0.0 ;
    sec   11 0.0 0.0  -77.60  0.0 ; Tower top
   end c2_def ;
  end main_body;
;
  begin main_body;
   name       towertop ;
   type       timoschenko ;
   nbodies    1 ;
   node_distribution    c2_def ;
;   damping_posdef   9.025E-06 9.025E-06 8.0E-05 8.3E-06 8.3E-06 8.5E-05 ;
   damping_posdef  0.0  0.0  0.0  3.00E-05  3.00E-05  2.00E-04  ;
   concentrated_mass 2 0.0  1.9 0.21256 2.4E5 1741490.0  1.7E5 1741490.0 ;  Nacelle mass and inertia
            begin timoschenko_input;
    filename ./data/NREL_5MW_st.txt ;
    set 2 2 ;
   end timoschenko_input;
   begin c2_def;             Definition of centerline (main_body coordinates)
    nsec 2;
    sec 1 0.0 0.0 0.0       0.0 ; x,y,z,twist
    sec 2 0.0 0.0 -1.96256  0.0 ;
   end c2_def ;
  end main_body;
;
  begin main_body;
   name       shaft ;
   type       timoschenko ;
   nbodies    1 ;
   node_distribution    c2_def ;
;  damping_posdef  7.00E-3  7.00E-03  7.00E-02  3.48E-04  3.48E-04  1.156E-03 ;
            damping_posdef  0.0 0.0 0.0 4.65E-04  4.65E-04  7.0725E-03 ; "tuned by Anyd 23/5/13 to 31.45 log decr.
damping for free free with stiff rotor and tower"
            concentrated_mass 1 0.0 0.0 0.0 0.0 0.0 0.0 5025497.444 ;generator equivalent slow shaft
   concentrated_mass 5 0.0 0.0 0.0 56780 0.0 0.0 115926 ; hub mass and inertia;
            begin timoschenko_input;
    filename ./data/NREL_5MW_st.txt ;
    set 3 2 ;
   end timoschenko_input;
   begin c2_def;             Definition of centerline (main_body coordinates)
    nsec 5;
    sec 1 0.0 0.0 0.0     0.0 ; Tower top x,y,z,twist
    sec 2 0.0 0.0 1.0     0.0 ;
    sec 3 0.0 0.0 2.0     0.0 ;
    sec 4 0.0 0.0 3.1071  0.0 ; Main bearing
    sec 5 0.0 0.0 5.0191  0.0 ; Rotor centre
   end c2_def ;
  end main_body;
;
  begin main_body;
   name       hub1 ;
   type       timoschenko ;
   nbodies    1 ;
   node_distribution    c2_def ;
   damping_posdef  0.0  0.0  0.0  3.00E-06  3.00E-06  2.00E-05;
            begin timoschenko_input;
    filename ./data/NREL_5MW_st.txt ;
    set 4 2 ;
   end timoschenko_input;
   begin c2_def;             Definition of centerline (main_body coordinates)
    nsec 2;
```

```
     sec 1 0.0 0.0 0.0     0.0 ; x,y,z,twist
     sec 2 0.0 0.0 1.5   0.0 ;
   end c2_def ;
  end main_body;
;
  begin main_body;
    name          hub2 ;
    copy_main_body hub1;
  end main_body;
;
  begin main_body;
    name          hub3 ;
    copy_main_body hub1 ;
  end main_body;
;
  begin main_body;
    name        blade1 ;
    type        timoschenko ;
    nbodies     9 ;
    node_distribution    c2_def;
;   damping   3.5e-2 5.5e-4 5.0e-4 3.0e-4 0.5e-3 5.5e-3  ;
    damping_posdef   0.0 0.0 0.0 1.41E-03 2.39E-03 4.5E-05 ;
    begin timoschenko_input ;
      filename ./data/NREL_5MW_st.txt ;
      set 5 2 ;               set subset
    end timoschenko_input;
    begin c2_def;             Definition of centerline (main_body coordinates)
      nsec 19 ;
            sec 1                 0.0000          0.0000          0.000           0.000           ;
            x.y.z. twist
            sec 2                 -0.0027         0.0006          1.367           -13.308         ;
            sec 3                 -0.1057         0.0250          4.100           -13.308         ;
            sec 4                 -0.2501         0.0592          6.833           -13.308         ;
            sec 5                 -0.4592         0.1086          10.250          -13.308         ;
            sec 6                 -0.5699         0.1157          14.350          -11.480         ;
            sec 7                 -0.5485         0.0983          18.450          -10.162         ;
            sec 8                 -0.5246         0.0832          22.550          -9.011          ;
            sec 9                 -0.4962         0.0679          26.650          -7.795          ;
            sec 10                -0.4654         0.0534          30.750          -6.544          ;
            50% blade radius
            sec 11                -0.4358         0.0409          34.850          -5.361          ;
            sec 12                -0.4059         0.0297          38.950          -4.188          ;
            sec 13                -0.3757         0.0205          43.050          -3.125          ;
            sec 14                -0.3452         0.0140          47.150          -2.319          ;
            sec 15                -0.3146         0.0084          51.250          -1.526          ;
            sec 16                -0.2891         0.0044          54.667          -0.863          ;
            sec 17                -0.2607         0.0017          57.400          -0.370          ;
            sec 18                -0.1774         0.0003          60.133          -0.106          ;
            sec 19                -0.1201         0.0000          61.500          -0.000          ;
   end c2_def ;
  end main_body;
;
  begin main_body;
    name          blade2 ;
    copy_main_body blade1;
  end main_body;
;
  begin main_body;
    name          blade3 ;
    copy_main_body blade1 ;
  end main_body;
;------------------------------------------------------------------------------------------------------------------------------------------
------------------
  begin orientation;
;
    begin base;
      body floater;
```

```
    inipos 0.0 0.0 120.0 ;
    body_eulerang 0.0 0.0 0.0;
  end base;
;
  begin relative;
    body1  floater last;
    body2  tower 1;
    body2_eulerang 0.0 0.0 0.0;
  end relative;
;
  begin relative;
    body1  tower last;
    body2  towertop 1;
    body2_eulerang 0.0 0.0 0.0;
  end relative;
;
  begin relative;
    body1  towertop last;
    body2  shaft 1;
    body2_eulerang 90.0 0.0 0.0;
    body2_eulerang 5.0 0.0 0.0;    5 deg tilt angle
    body2_ini_rotvec_d1 0.0 0.0 -1.0 0.5 ; body initial rotation velocity x,y,z,angle velocity[rad/s]  (body 2
coordinates)
  end relative;
;
  begin relative;
    body1  shaft last;
    body2  hub1 1;
    body2_eulerang -90.0 0.0 0.0;
    body2_eulerang 0.0 180.0 0.0;
    body2_eulerang 2.5 0.0 0.0;      2.5deg cone angle
  end relative;
;
  begin relative;
    body1  shaft last;
    body2  hub2 1;
    body2_eulerang -90.0 0.0 0.0;
    body2_eulerang 0.0 60.0 0.0;
    body2_eulerang 2.5 0.0 0.0;      2.5deg cone angle
  end relative;
;
  begin relative;
    body1  shaft last;
    body2  hub3 1;
    body2_eulerang -90.0 0.0 0.0;
    body2_eulerang 0.0 -60.0 0.0;
    body2_eulerang 2.5 0.0 0.0;      2.5deg cone angle
  end relative;
;
  begin relative;
    body1  hub1 last;
    body2  blade1 1;
    body2_eulerang 0.0 0.0 0;
  end relative;
;
  begin relative;
    body1  hub2 last;
    body2  blade2 1;
    body2_eulerang 0.0 0.0 0.0;
  end relative;
;
  begin relative;
    body1  hub3 last;
    body2  blade3 1;
    body2_eulerang 0.0 0.0 0.0;
  end relative;
;
```

```
  end orientation;
;------------------------------------------------------------------------------------------------------------------------
------------------
begin constraint;
;
;   begin fix0;  fixed to ground in translation and rotation of node 1
;     body floater;
;   end fix0;
;
   begin fix1;  fixed relative to other body in translation and rotation
     body1 floater last;
     body2 tower 1;
   end fix1;
;
    begin fix1;
                          body1 tower last ;
                          body2 towertop 1;
                        end fix1;
;
   begin bearing1;                    free bearing
    name  shaft_rot;
     body1 towertop last;
     body2 shaft 1;
     bearing_vector 2 0.0 0.0 -1.0;       x=coo (0=global.1=body1.2=body2) vector in body2 coordinates where the
free rotation is present
   end bearing1;
;
;    begin fix1;
;                         body1 towertop last ;
;                         body2 shaft 1;
;                       end fix1;
;
    begin fix1;
                          body1 shaft last ;
                          body2 hub1 1;
                        end fix1;
;
    begin fix1;
                          body1 shaft last ;
                          body2 hub2 1;
                        end fix1;
;
    begin fix1;
                          body1 shaft last ;
                          body2 hub3 1;
                        end fix1;
;
   begin bearing2;
     name pitch1;
     body1 hub1 last;
    body2 blade1 1;
                                bearing_vector 2 0.0 0.0 -1.0;
  end bearing2;
;
   begin bearing2;
     name pitch2;
     body1 hub2 last;
     body2 blade2 1;
                                bearing_vector 2 0.0 0.0 -1.0;
   end bearing2;
;
   begin bearing2;
     name pitch3;
     body1 hub3 last;
     body2 blade3 1;
                                bearing_vector 2 0.0 0.0 -1.0;
   end bearing2;
```

```
;
end constraint;
;
end new_htc_structure;
;-------------------------------------------------------------------------------------------------------------------------------------------------------
 continue_in_file ./htc/mooring.inc ;
;-------------------------------------------------------------------------------------------------------------------------------------------------------
begin hydro;
  begin water_properties;
    rho 1025 ; kg/m^3
    gravity 9.816 ; m/s^2
    mwl 0.0 ;
    mudlevel 320.0 ;
             water_kinematics_dll ./wkin_dll.dll   ./htc_hydro/reg_airy_h6_t10.inp ;
 end water_properties;
;
  begin hydro_element;
    mbdy_name floater ;
    update_states 1;
    buoyancy 1;
    hydrosections auto 4 ; distribution of hydro calculation points from sec 1 to nsec
    nsec 7; z      Cm                          Cd      A      Aref   width    dr/dz         Cd_a_(quad) Cm_a Cd_a_lin Aif
 sec        0.000              0.969954 0.600      69.398    69.398    9.400       0.000 69.398 2.0 ;
 sec        107.999            0.969954 0.600      69.398    69.398    9.400       0.000 ;
 sec        108.001            0.969954 0.600      69.398    69.398    9.400      -0.181 ;
 sec        115.999            0.969954 0.600      33.183    33.183    6.500      -0.181 ;
 sec        116.000            0.969954 0.600      33.183    33.183    6.500       0.000 ;
 sec        120.000            0.969954 0.600      33.183    33.183    6.500       0.000 ;
 sec        130.000            0.969954 0.600      33.183    33.183    6.500       0.000 ;
  end hydro_element;
;
end hydro;
;-------------------------------------------------------------------------------------------------------------------------------------------------------
begin wind ;
  density                1.225 ; to be checked
  wsp                    0.001  ;
  tint                  0.0;
  horizontal_input       1     ;           0=false, 1=true
  windfield_rotations     0.0  0.0  0.0 ;    yaw, tilt, rotation
  center_pos0             0.0 0.0 -90.00 ;
  shear_format            1  0.14  ;0=none,1=constant,2=log,3=power,4=linear
  turb_format            0     ;  0=none, 1=mann,2=flex
  tower_shadow_method     3     ;  0=none, 1=potential flow, 2=jet
;  scale_time_start       0 ;
;  wind_ramp_factor   0.0 [t0] [wsp factor] 1.0 ;
;  [gust] iec_gust [gust_type] [gust_A] [gust_phi0] [gust_t0] [gust_T] ;
;
  begin mann;
    filename_u    ./turb/dummyu.bin ;
    filename_v    ./turb/dummyv.bin ;
    filename_w    ./turb/dummyw.bin ;
    box_dim_u    8192 0.0 ;
    box_dim_v    32 4.6875;
    box_dim_w    32 4.6875;
    std_scaling   1.0 0.7 0.5 ;
  end mann;
;
  begin tower_shadow_potential_2;
    tower_mbdy_link tower;
    nsec  2;
    radius      0.0  3.0 ;
    radius     77.6 1.935 ;
  end tower_shadow_potential_2;
end wind;
```

```
;
;-------------------------------------------------------------------------------------------------------------------------------------------
------------------
;
begin aero ;
  nblades  3;
  hub_vec shaft -3 ;         rotor rotation vector (normally shaft composant directed from pressure to sustion side)
  link 1 mbdy_c2_def blade1;
  link 2 mbdy_c2_def blade2;
  link 3 mbdy_c2_def blade3;
  ae_filename         ./data/NREL_5MW_ae.txt;
  pc_filename         ./data/NREL_5MW_pc.txt;
  induction_method   1 ;     0=none, 1=normal
  aerocalc_method    1 ;     0=ingen aerodynamic, 1=med aerodynamic
  aerosections       30 ;
  ae_sets            1 1 1;
  tiploss_method     1 ;     0=none, 1=prandtl
  dynstall_method    2 ;     0=none, 1=stig øye method,2=mhh method
end aero ;
;
; begin aerodrag ;  aerodynamic drag was no used in the OC3 project but should be turned on in other simulations
  ; begin aerodrag_element ;
    ; mbdy_name tower;
    ; aerodrag_sections uniform 10 ;
    ; nsec 2 ;
    ; sec 0.0 0.6 6.0 ;  tower bottom
    ; sec 87.6 0.6 3.87 ;  tower top
  ; end aerodrag_element;
; ;
  ; begin aerodrag_element ;        Nacelle drag side
    ; mbdy_name shaft;
    ; aerodrag_sections uniform 2 ;
    ; nsec 2 ;
    ; sec 0.0   0.8 10.0 ;
    ; sec 5.02  0.8 10.0 ;
  ; end aerodrag_element;
; end aerodrag
;
;-------------------------------------------------------------------------------------------------------------------------------------------
------------------
begin dll;
  begin hawc_dll;
    filename  ./control/bladed2hawc.dll ;
    dll_subroutine regulation ;
    arraysizes  15 15 ;
    ;deltat  0.02;
    begin output;
      general time ;                                                                    1
      constraint bearing2 pitch1 1;  angle and angle velocity written to dll                                  2,3
      constraint bearing2 pitch2 1;  angle and angle velocity written to dll                                  4,5
      constraint bearing2 pitch3 1;  angle and angle velocity written to dll                                  6,7
      constraint bearing2 shaft_rot 1; angle and angle velocity written to dll  (slow speed shaft)                    8,9
      wind free_wind 1 0.0 0.0 -90.0; local wind at fixed position: coo (1=global,2=non-rotation rotor coo.), pos x, pos
y, pos z   10,11,12
      general constant 97.0 ;              generator exchange ratio                                  13
    end output;
;
    begin actions;
      body moment_ext shaft 1 3;
    end actions;
  end hawc_dll;
;
  begin hawc_dll;
    filename  ./control/pitchservo_pos.dll ;
    dll_subroutine servo ;
    arraysizes  15 15 ;
    ;deltat    0.02 ;
```

```
   begin output;
     general time ;                                          1
     dll inpvec 1 2;                                         2
     dll inpvec 1 3;                                         3
     dll inpvec 1 4;                                         4
     constraint bearing2 pitch1 1;  angle and angle velocity written to dll      5,6
     constraint bearing2 pitch2 1;  angle and angle velocity written to dll      7,8
     constraint bearing2 pitch3 1;  angle and angle velocity written to dll      9,10
   end output;
;
   begin actions;
     body bearing_angle pitch1;
     body bearing_angle pitch2;
     body bearing_angle pitch3;
   end actions;
  end hawc_dll;
;
   begin hawc_dll;
    filename  ./control/damper.dll ;
    dll_subroutine damp ;
    arraysizes  15 15 ;
    begin output;
      general time ;                                         1
      general constant 5.0;
      general constant 10.0;
      general constant -1.0E1 ;
      mbdy state vel towertop 1 1.0 tower;
    end output;
;
    begin actions;
       mbdy force_ext towertop 2 1 towertop;
    end actions;
  end hawc_dll;
;
  begin type2_dll;
    name gear;
    filename  ./control/hss_convert.dll ;
    arraysizes_init  3 1 ;
    arraysizes_update  2 2 ;
    begin init;
      constant 1 1.0 ;     number of used sensors - in this case only 1
      constant 2 1000;     unit conversion factor
    end init;
    begin output;
      mbdy momentvec shaft 1 1 shaft # only 3;
    end output;
;
    begin actions;
      mbdy moment_ext towertop 2 3 shaft;
    end actions;
  end type2_dll;
;
end dll;
;-------------------------------------------------------------------------------------------------------------------------------------------------------
-------------------
;-----------------------------------------------------
begin force;
begin dll;
dll ./uncoupled.dll;
update ForceDLL;
mbdy floater;
node 7;
end dll;
end force;
;-------------------------------------------------------------------------------------------------------------------------------------------------------
-------------------
;
```

```
begin output;
  filename ./res/0_ice_mono_0.1mps0.8m_decoupled_no_wind_rigid ;
  data_format  hawc_binary;
  time 400.0 1000.0 ;
  buffer 1 ;
;
 general time;
  mbdy momentvec tower 1 1 tower  # Tower bottom;
  mbdy forcevec  tower 1 1 tower  # Tower botttom;
  wind free_wind 1 0.0 0.0 -90.4; local wind at fixed position: coo (1=global,2=non-rotation rotor coo.), pos x, pos y,
pos z
  mbdy state pos floater 1 0.0 global # Position floater bottom;
  mbdy state pos floater 7 1.0 global # Position floater top;
  mbdy state pos floater 7 0.0 global # Position floater MSL;
  mbdy state vel floater 7 0.0 global # Velocity floater MSL;
  mbdy state acc floater 7 0.0 global # Acceleration floater MSL;
  mbdy state_rot eulerang_xyz floater 7 0.0 global # rotation floater MSL;
  mbdy state_rot omega floater 7 0.0 global # rotation floater MSL;
  mbdy state_rot omegadot floater 7 0.0 global # rotation velocity floater MSL;
  mbdy momentvec floater 7 1 floater # moment floater MSL;
  mbdy forcevec  floater 7 1 floater # force floater MSL;
  mbdy state pos tower 1 0.0 global # Position tower bottom;
  mbdy state pos towertop   1 1.0 global # tower top position ;
  mbdy state vel towertop   1 1.0 global # Velocity tower top;
  mbdy forcevec tower 1 1  tower # tower base flange ;
  mbdy momentvec tower 1 1  tower # tower base flange ;
  mbdy momentvec towertop  1 1 towertop # # yaw bearing ;
  mbdy forcevec  towertop  1 1 towertop # yaw bearing ;
  mbdy momentvec shaft 4 1  shaft # main bearing ;
  mbdy momentvec hub1 1  2 hub1  # blade 1 root ;
  mbdy momentvec blade1 10 1 local # blade 1 50% local e coo ;
  mbdy forcevec  hub1 1  2 hub1  # blade 1 root ;
  mbdy momentvec hub2 1  2 hub2  # blade 2 root ;
  mbdy momentvec hub2 1  2 hub2  # blade 3 root ;
  mbdy state pos tower   9 1.0 global # tower top flange position ;
  mbdy state pos blade1  18 1.0 hub1 # blade 1 tip pos ;
  mbdy state pos blade2  18 1.0 hub2 # blade 2 tip pos ;
  mbdy state pos blade3  18 1.0 hub3 # blade 3 tip pos ;
  mbdy state pos blade1  18 1.0 global # blade 1 tip pos ;
  mbdy state_rot proj_ang blade1  18 1.0 blade1 only 3 # blade 1 tip twist;
  aero thrust;
  hydro water_surface 0.0 0.0 ;        x,y   gl. pos
;
  dll inpvec 1 5 # Gen speed fast;
  dll inpvec 1 6 # Mgen fast;
  dll inpvec 1 7 # F;
  dll inpvec 1 8 # Mechanical power generator [kW];
  dll inpvec 1 9 # Electrical power generator [kW];
;
end output;
exit;
```

B. Convergence study: simulation length

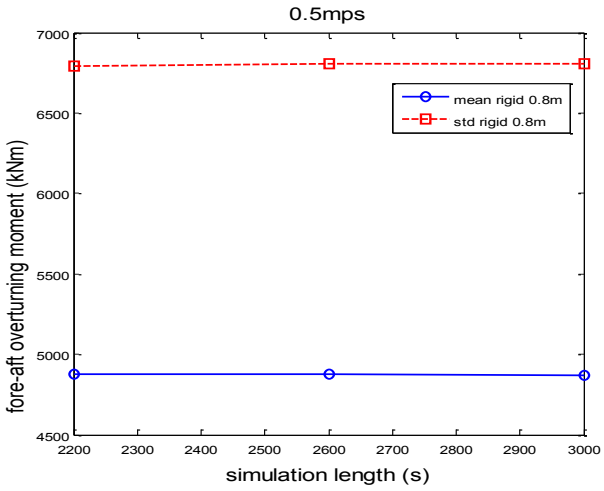

Figure B. 1: Comparison of statistical characteristics of the fore-aft over-turning moment at the MSL with ice thickness of 0.8m and constant ice drifting speed of 0.5mps for simulation of different length

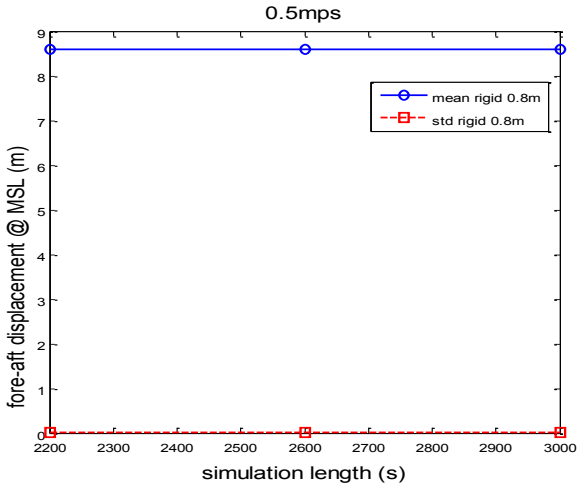

Figure B. 2: Comparison of statistical characteristics of the fore-aft displacements at the MSL with ice thickness of 0.8m and constant ice drifting speed of 0.5mps for simulation of different length

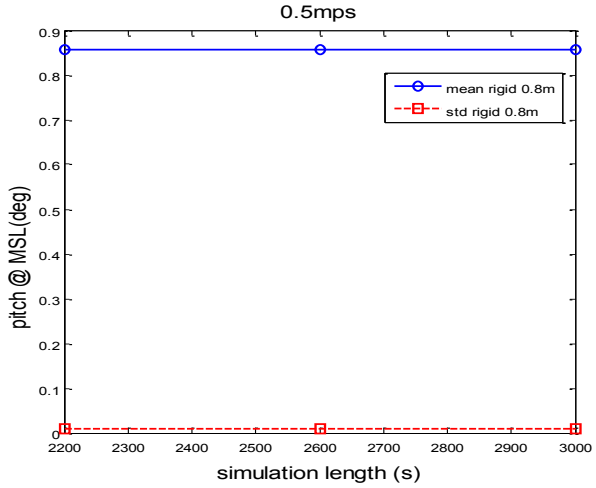

Figure B. 3: Comparison of statistical characteristics of the pitch at the MSL with ice thickness of 0.8m and constant ice drifting speed of 0.5mps for simulation of different length

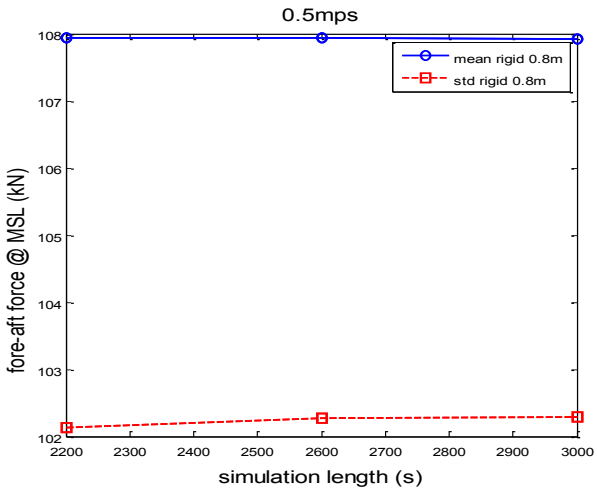

Figure B. 4: Comparison of statistical characteristics of the fore-aft force at the MSL with ice thickness of 0.8m and constant ice drifting speed of 0.5mps for simulation of different length

C. Convergence study: Time step

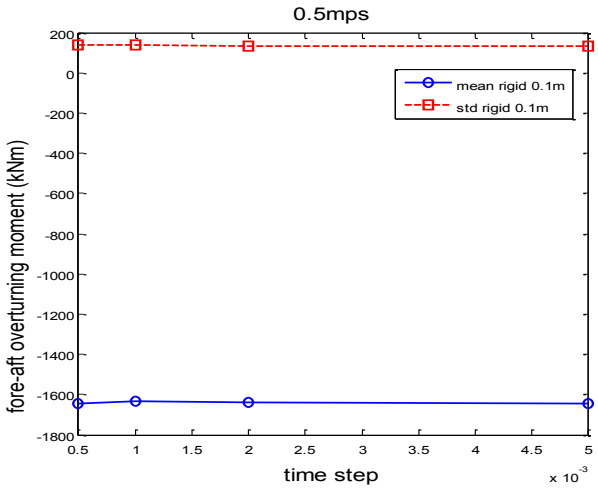

Figure C. 1: Comparison of statistical characteristics of the fore-aft over-turning moment at the MSL with constant ice thicknesses of 0.1m and ice drifting speed of 0.5mps for different time steps

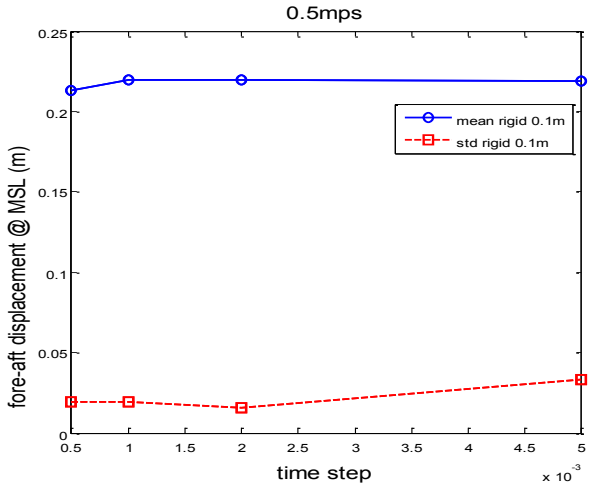

Figure C. 2: Comparison of statistical characteristics of the fore-aft displacement at the MSL with constant ice thicknesses of 0.1m and ice drifting speed of 0.5mps for different time steps

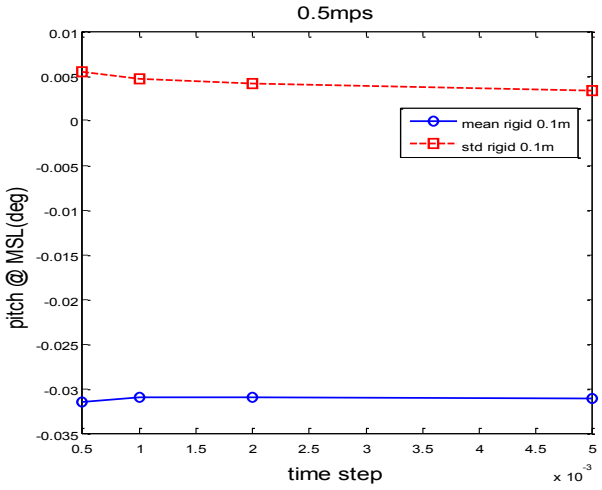

Figure C. 3: Comparison of statistical characteristics of the pitch at the MSL with constant ice thicknesses of 0.1m and ice drifting speed of 0.5mps for different time steps

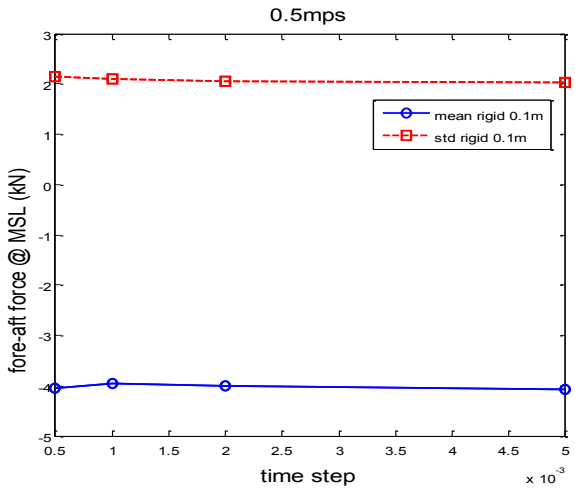

Figure C. 4: Comparison of statistical characteristics of the fore-aft force at the MSL with constant ice thicknesses of 0.1m and ice drifting speed of 0.5mps for different time steps

D. Comparison of aerodynamic and ice loads

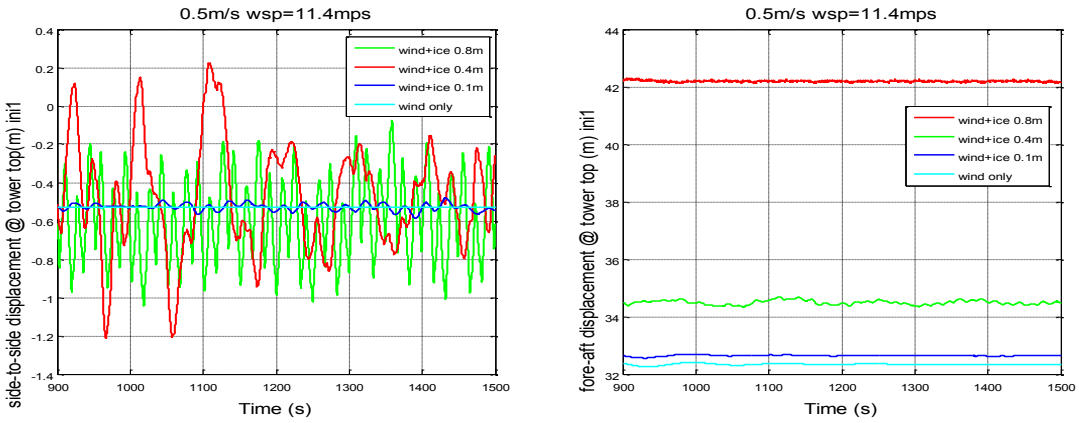

Figure D. 1: Time series of the side-to-side and fore-aft displacements at the tower top for LCs 7.3, 7.4 and 7.5 (initial conditions 1)

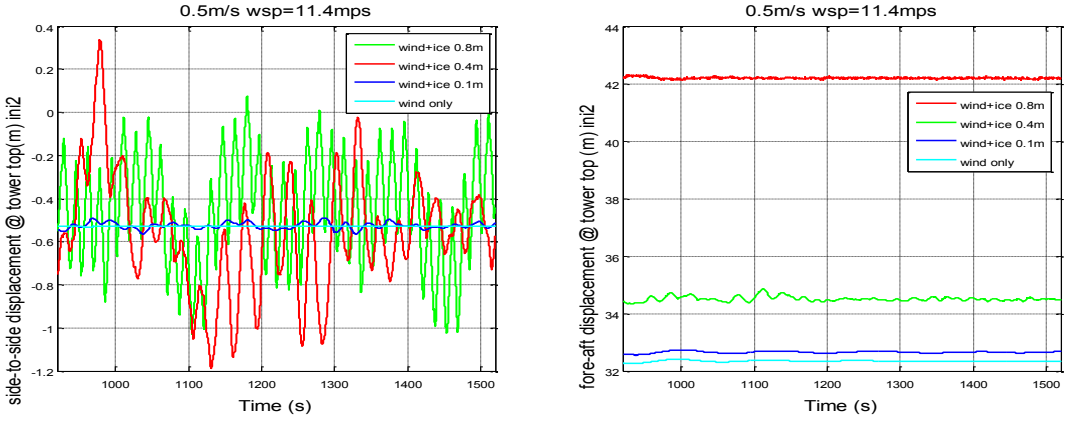

Figure D. 2: Time series of the side-to-side and fore-aft displacements at the tower top for LCs 7.3, 7.4 and 7.5 (initial conditions 2)

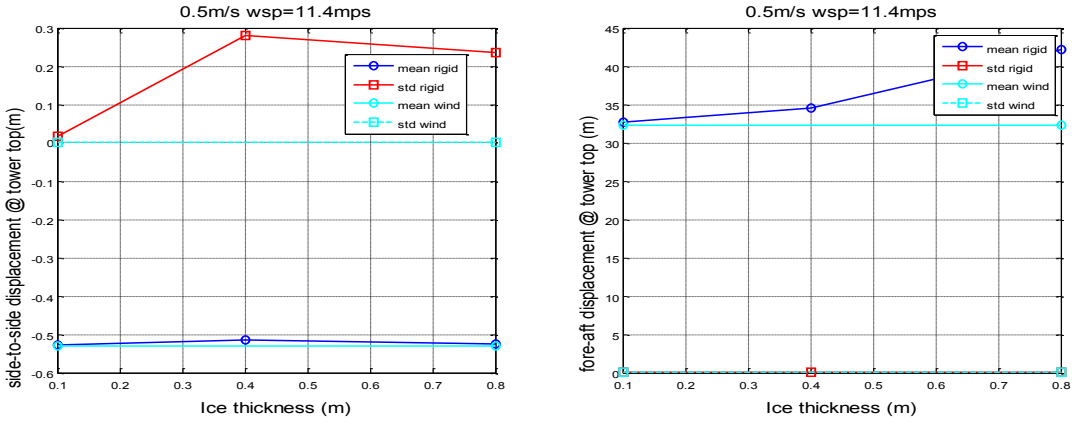

Figure D. 3: Statistical characteristics of the side-to-side and fore-aft displacements at the tower top with different ice thicknesses and constant ice drifting speed of 0.5mps and wind rated speed

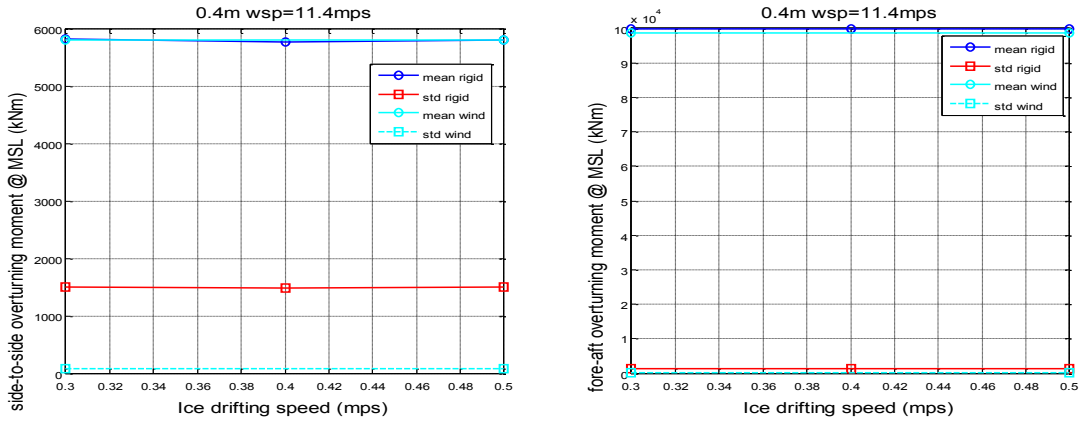

Figure D. 4: Statistical characteristics of the side-to-side and fore-aft over-turning moment at the MSL with different ice drifting speeds and constant ice thickness of 0.4m and wind rated speed

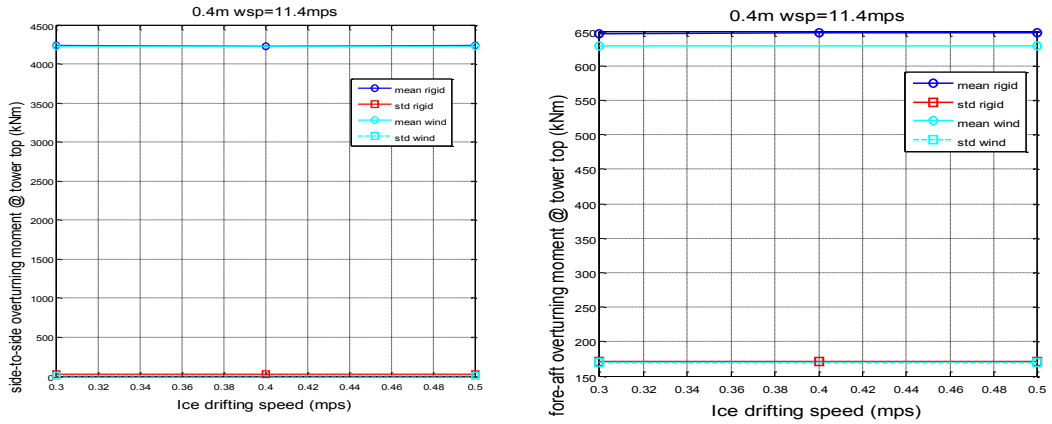

Figure D. 5: Statistical characteristics of the side-to-side and fore-aft over-turning moment at the tower top with different ice drifting speeds and constant ice thickness of 0.4m and wind rated speed

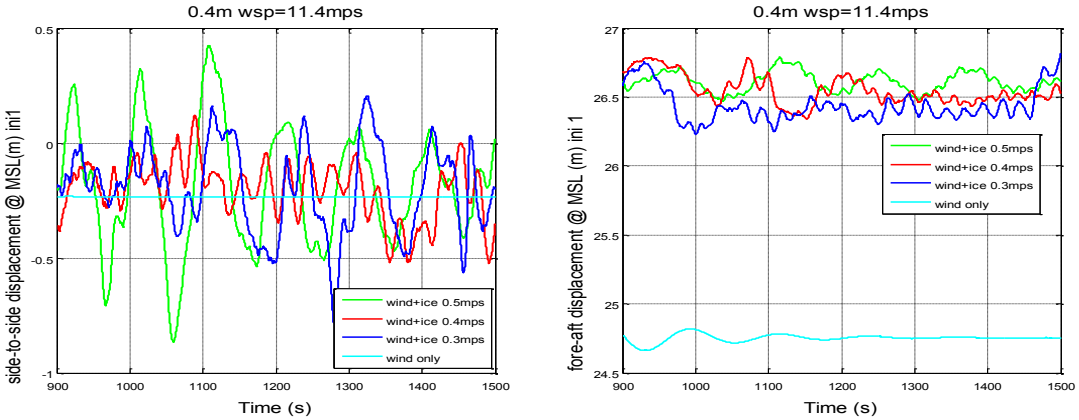

Figure D. 6: Time series of the side-to-side and fore-aft displacements at the MSL for LCs 7.1, 7.2 and 7.4 (initial conditions 1)

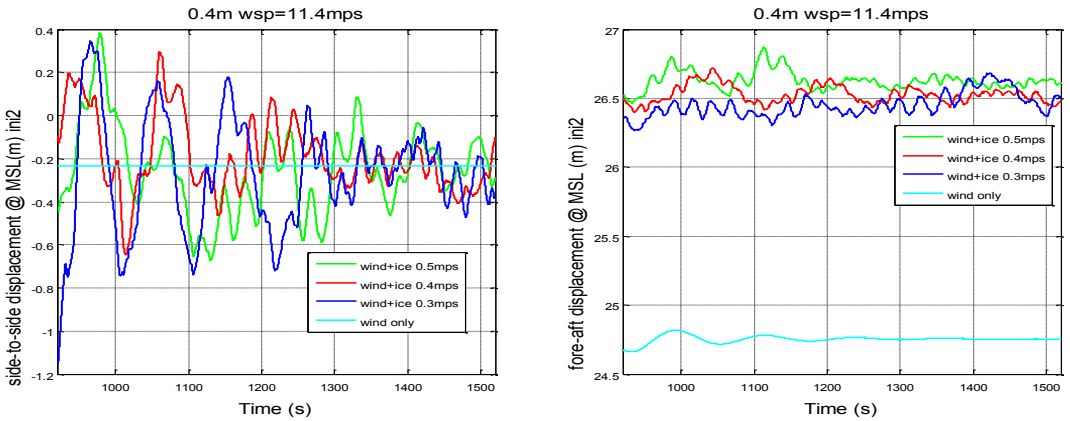

Figure D. 7: Time series of the side-to-side and fore-aft displacements at the MSL for LCs 7.1, 7.2 and 7.4 (initial conditions 2)

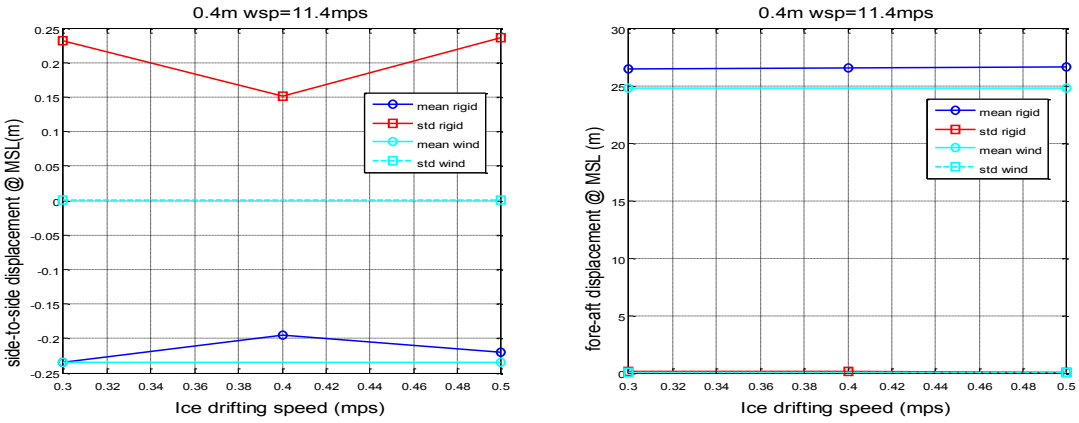

Figure D. 8: Statistical characteristics of the side-to-side and fore-aft displacements at the MSL with different ice drifting speeds and constant ice thickness of 0.4m and win rated speed

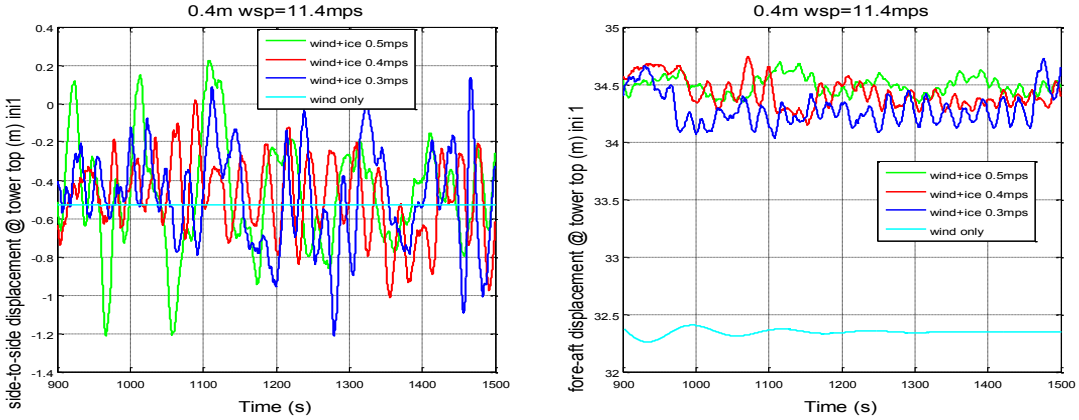

Figure D. 9: Time series of the side-to-side and fore-aft displacements at the tower top for LCs 7.1, 7.2 and 7.4 (initial conditions 1)

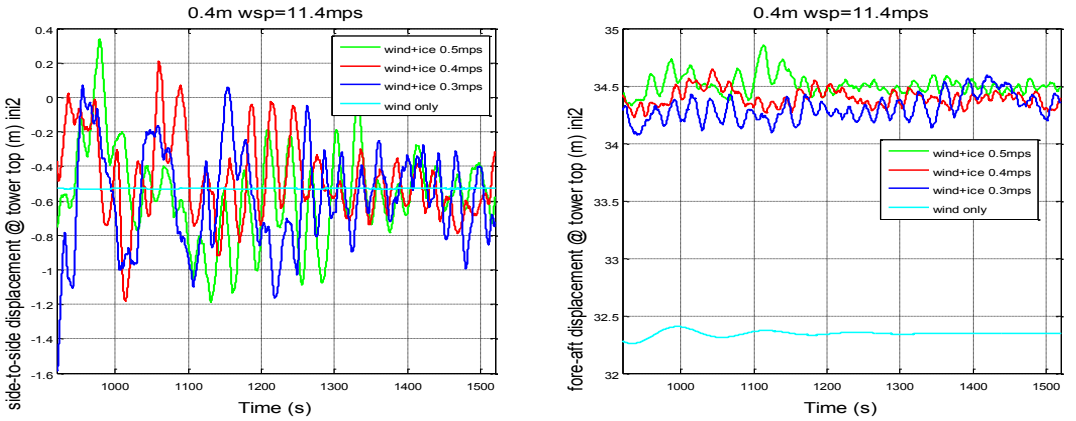

Figure D. 10: Time series of the side-to-side and fore-aft displacements at the tower top for LCs 7.1, 7.2 and 7.4 (initial conditions 2)

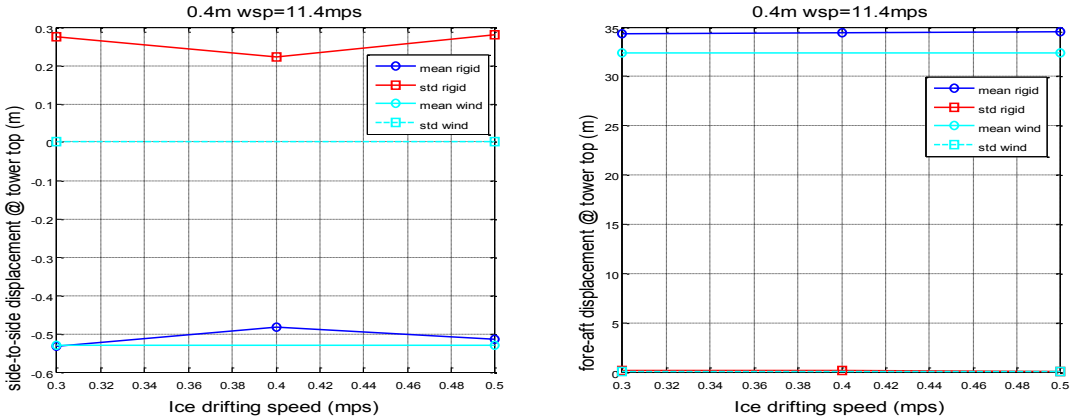

Figure D. 11: Statistical characteristics of the side-to-side and fore-aft displacements at the tower top with different ice drifting speeds and constant ice thickness of 0.4m and wind rated speed

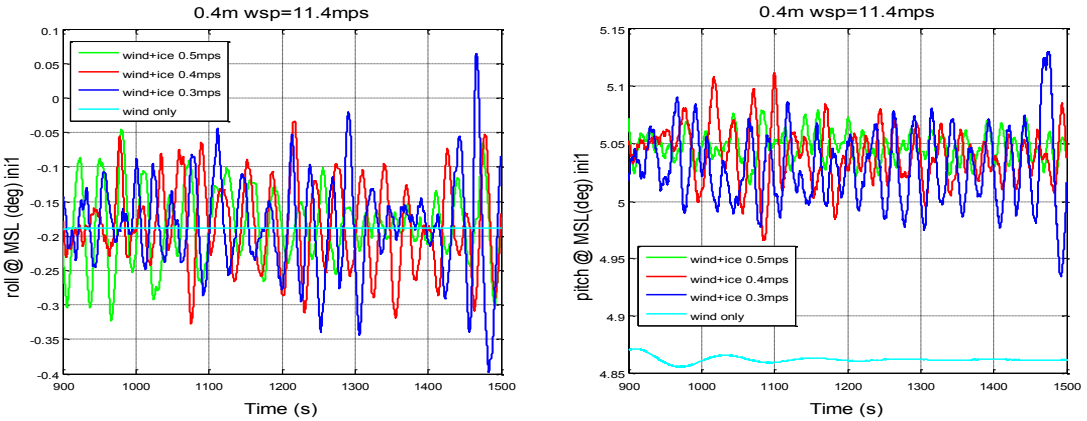

Figure D. 12: Time series of the roll and pitch at the MSL for LCs 7.1, 7.2 and 7.4 (initial conditions 1)

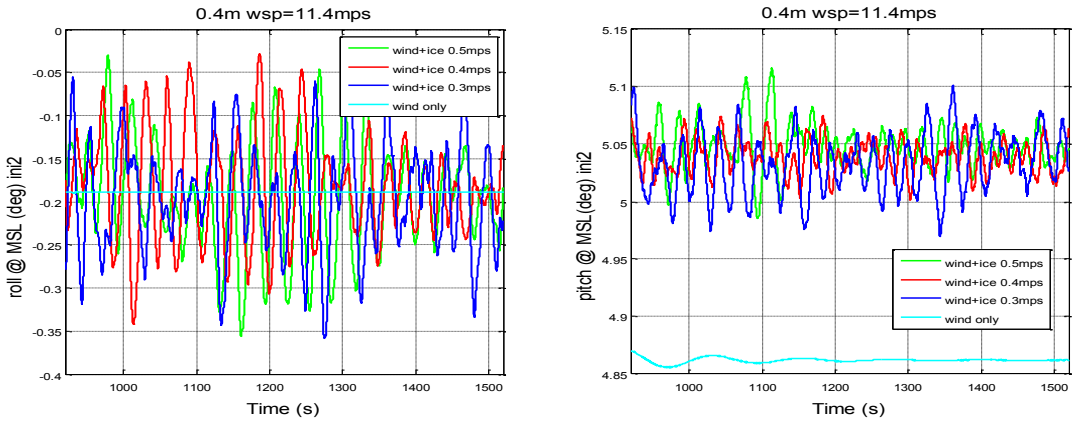

Figure D. 13: Time series of the roll and pitch at the MSL for LC LCs 7.1, 7.2 and 7.4 (initial conditions 2)

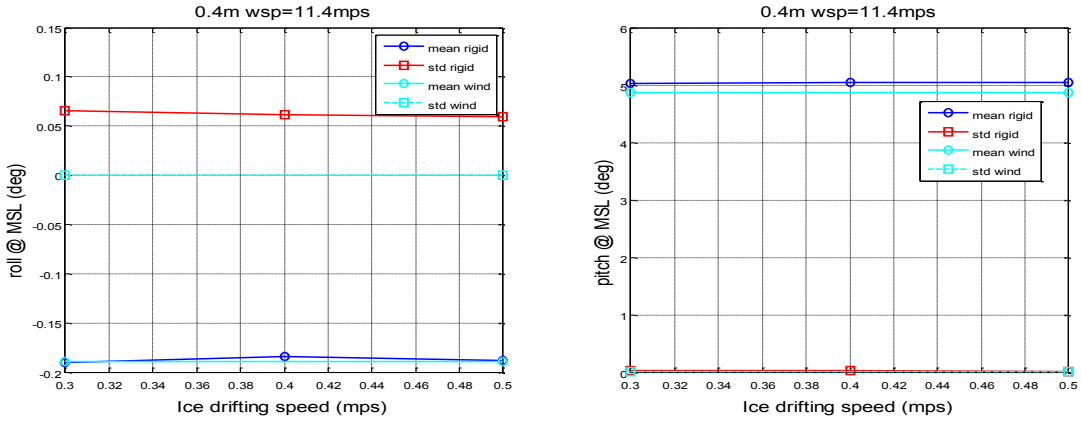

Figure D. 14: Statistical characteristics of the roll and pitch at the MSL with different ice drifting speeds and constant ice thickness of 0.4m and wind rated speed

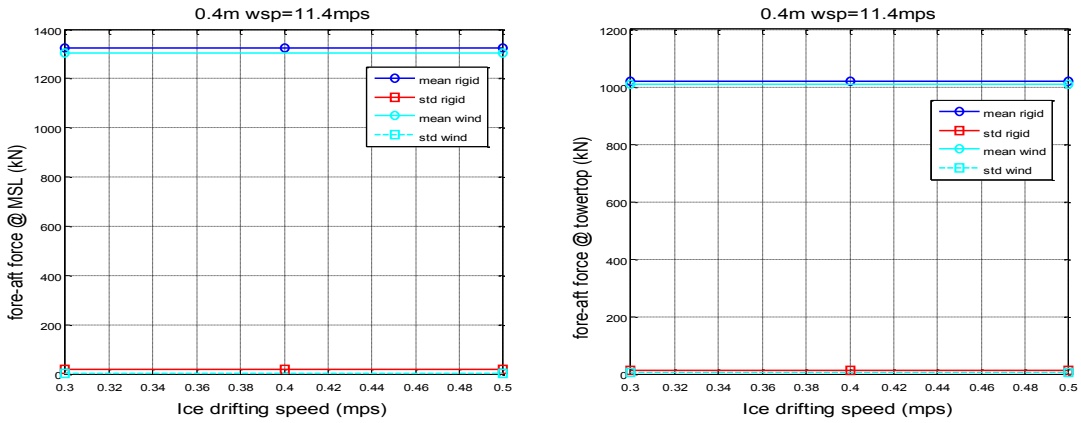

Figure D. 15: Statistical characteristics of the fore-aft force at the MSL and tower top with different ice drifting speeds and constant ice thickness of 0.4m and wind rated speed

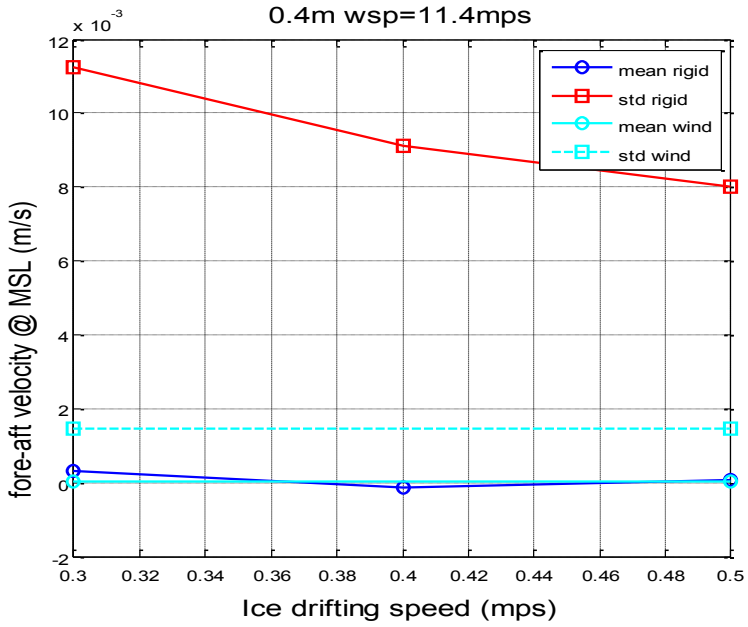

Figure D. 16: Statistical characteristics of the fore-aft velocity at the MSL with different ice drifting speeds and constant ice thickness of 0.4m and wind rated speed

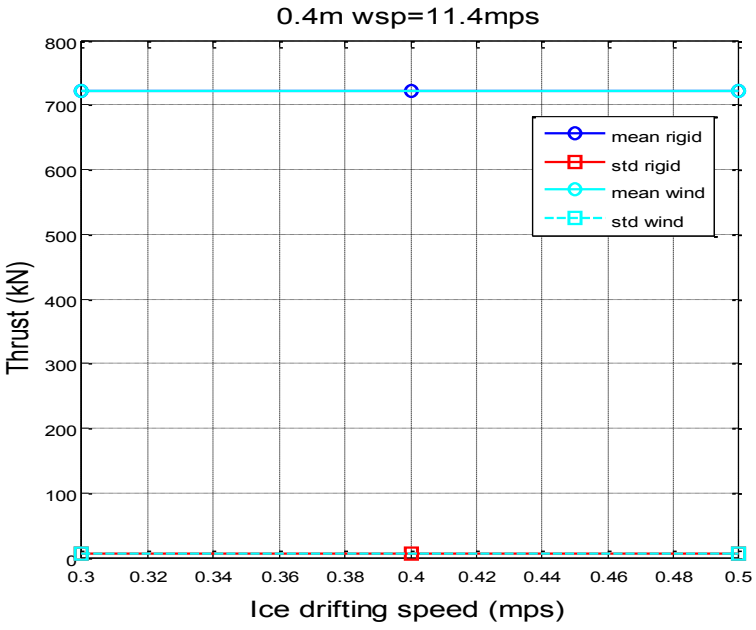

Figure D. 17: Statistical characteristics of the aerodynamic thrust with different ice drifting speeds and constant ice thickness of 0.4m and wind rated speed